

Ultrafast X-ray Spectroscopies of Transition Metal Complexes Relevant for Catalysis

Dissertation zur Erlangung des Doktorgrades
an der Fakultät für Mathematik, Informatik und Naturwissenschaften
Fachbereich Physik
der Universität Hamburg

vorgelegt von
Alexander Britz
aus Erlangen

Hamburg
2016

Gutachter der Dissertation:

Prof. Dr. Christian Bressler

Prof. Dr. Wilfried Wurth

Gutachter der Disputation:

Prof. Dr. Christian Bressler

Prof. Dr. Nils Huse

Prof. Dr. Daniela Pfannkuche

Prof. Dr. Angel Rubio

Prof. Dr. Wilfried Wurth

Datum der Disputation:

10. Januar 2017

Vorsitzende des Prüfungsausschusses:

Prof. Dr. Daniela Pfannkuche

Vorsitzender des Promotionsausschusses:

Prof. Dr. Wolfgang Hansen

Dekan der Fakultät für Mathematik,
Informatik und Naturwissenschaften:

Prof. Dr. Heinrich Graener

Abstract

Transition metal (TM) complexes are ubiquitous in both technological and biological catalytic systems. For a detailed understanding of their reactivity, a knowledge of the fundamental processes during chemical reactions is crucial. These primary processes involve correlated changes in spin state, molecular orbitals as well as the geometric structure of the reactant and occur on femtosecond (fs) time- and Ångström (Å) length scales. Using optical laser pump – X-ray spectroscopic probe techniques the aforementioned dynamics of solvated TM complexes can be tracked with 100-picosecond(ps)-resolution at synchrotrons and 100-fs-resolution at X-ray Free Electron Lasers (XFELs). Time-resolved (TR) hard X-ray absorption (XAS) and emission (XES) spectroscopy is exploited to site-selectively probe the optically induced changes in structure and molecular orbitals of TM complexes with high relevance for catalysis.

A novel setup for TR XAS at PETRA III has been implemented, consisting of a repetition-rate-tunable synchronized MHz fiber amplifier laser and a data acquisition (DAQ) strategy which is capable of measuring multi-photon events with single photon resolution at MHz repetition rates. This system permits measuring TR XAS with signal-to-noise ratios comparable to those of static measurements.

We have probed the optically induced changes in the unoccupied orbitals of an iridium photosensitizer (IrPS) by measuring its TR X-ray absorption near edge structure (XANES). Monitoring the IrPS in a fully functioning system for photocatalytic hydrogen generation allowed following the electron transfer from an electron donor to the optically excited IrPS*. Furthermore, we have characterized the excited state spin and structure of a possible candidate towards low-spin Fe(II) photosensitizers via TR XES and the TR extended X-ray absorption fine structure (EXAFS).

Finally we have investigated an octahedral high-valent Fe(V) complex, which is formed via UV flash photolysis from its Fe(III) precursor. The ultrafast high-valent Fe(V) formation was monitored using TR XANES at the SACLA XFEL with ~ 300 fs resolution and the formation was found to occur on the same timescale or faster than the temporal resolution. TR XES was employed to identify a ~ 40 -ps-lived pentacoordinated intermediate state in a competing ligand exchange reaction channel.

Kurzfassung

Übergangsmetallkomplexe sind allgegenwärtig in technologischen und biologischen Katalysesystemen. Für ein detailliertes Verständniss ihrer Reaktivität sind die Kenntnisse der fundamentalen Prozesse chemischer Reaktionen unabdingbar. Diese beinhalten korrelierte Änderungen des Spinzustandes, der Molekülorbitale sowie der geometrischen Struktur des Reaktants und finden auf der Femtosekunden (fs) Zeit- und der Ångström (Å) Längenskala statt. Die Abbildung dieser Dynamiken in gelösten Übergangsmetallkomplexen werden durch Experimente mit optischen Anregungspulsen und röntgenspektroskopischen Abfragetechniken ermöglicht, wobei die Zeitauflösung 100 Pikosekunden (ps) an Synchrotronen und 100 fs an Röntgen-Freie-Elektronen-Lasern (XFELs) beträgt. Die optisch induzierten Änderungen der Molekülorbitale und der Struktur von katalytisch relevanten Übergangsmetallkomplexen werden hier mittels zeitaufgelöster harter Röntgenabsorptions- und Emissionsspektroskopie elementspezifisch erforscht.

Ein neuartiger Experimentieraufbau für zeitaufgelöste Röntgenabsorptionsspektroskopie wurde realisiert. Dieser besteht aus einem Faserlaser mit einstellbarer MHz Repetitionsrate und einem Datenaquisitionssystem, welches Mehrphotonenereignisse einzelphotonenaufgelöst bei MHz Wiederholungsraten detektieren kann. Erst hierdurch wurden zeitaufgelöste Röntgenabsorptionmessungen mit Signal-zu-Rausch Verhältnissen, die denen von statischen Experimenten entsprechen, möglich.

Ferner wurden die Änderungen der unbesetzten Molekülorbitale eines Iridium-Photosensibilisators (IrPS) bestimmt, indem die Röntgenabsorptions-Nahkantenstruktur (XANES) gemessen wurde. Der IrPS wurde auch als Teil eines vollständigen Systems zur photokatalytischen Wasserspaltung untersucht. So konnte der Elektronentransfer von einem Elektronendonator zum optisch angeregten IrPS* verfolgt werden. Des Weiteren wurde der Spin und die Struktur des angeregten Zustands eines möglichen Kandidaten in der Entwicklung Eisen(II)-basierter Photosensibilisatoren mittels zeitaufgelöster Röntgenemissionsspektroskopie und der kantenfernen Feinstruktur des Röntgenabsorptionsspektrums (EXAFS) charakterisiert.

Zuletzt wurde ein oktahedrischer hochvalenter Fe(V) Komplex erforscht, der durch optische Anregung seines Fe(III) Vorgängers im UV Spektralbereich erzeugt wird. Sein ultraschneller Entstehungsprozess konnte am SACLA XFEL mit etwa 300 fs Auflösung beobachtet werden. Die Entstehungszeit des Fe(V) läuft auf dieser Grössenordnung oder schneller ab. Zudem konnte mittels zeitaufgelöster Röntgenemissionsspektroskopie ein 40-ps-lebiger pentakoordinierter Zwischenzustand in einer Ligandenaustauschreaktion identifiziert werden, die mit dem Reaktionsweg zum Fe(V) konkurriert.

Contents

Abstract	III
Kurzfassung	V
1 Introduction	1
2 Photophysics and Photochemistry of Transition Metal Complexes	5
2.1 Introduction	5
2.2 Transition Metal Complexes and the Role of the d-Orbitals	7
2.3 Optical Excitation	9
2.4 Excited State Decay	12
2.5 Numerical Example: Optical Excitation of an Example Molecule	14
2.6 Summary and Conclusions	15
3 Experimental Methodology - Time-resolved X-ray Spectroscopy	17
3.1 Interaction of X-rays with Matter	17
3.2 X-ray Absorption Spectroscopy	19
3.2.1 Pre-edge Peaks to Extract Chemical Information	20
3.2.2 X-ray Absorption Near Edge Structure (XANES)	21
3.2.3 Extended X-ray Absorption Fine Structure (EXAFS)	23
3.3 X-ray Absorption Spectroscopy Measurement Techniques	25
3.3.1 Transmission Measurement of X-ray Absorption Spectra	25
3.3.2 Total Fluorescence Yield Measurement of X-ray Absorption Spectra	27
3.3.3 Signal-to-Noise of Transient X-ray Absorption Spectra	29
3.4 X-ray Emission Spectroscopy of Transition Metal Complexes	32
3.4.1 3d Transition Metal Complexes - $K\alpha$ X-ray Emission Spectroscopy .	32
3.4.2 3d Transition Metal Complexes - $K\beta$ X-ray Emission Spectroscopy .	33
3.4.3 3d Transition Metal Complexes - Valence-to-Core X-ray Emission Spectroscopy	34
3.4.4 5d Transition Metal Complexes - $L\alpha$ X-ray Emission Spectroscopy .	34
3.4.5 Time-resolved X-ray Emission Spectroscopy	34
3.5 X-ray Emission Measurement Techniques	35
3.6 Advanced X-ray Spectroscopies: RXES, HERFD	37
3.6.1 Resonant X-ray Emission Spectroscopy	37

3.6.2	High-Energy Resolution Fluorescence Detection XAS	37
3.7	X-ray Sources: From Synchrotrons to XFELs	39
3.7.1	Synchrotrons	39
3.7.2	X-ray Free Electron Lasers (XFELs)	41
3.8	Experimental Setups for Combined Time-resolved X-ray Absorption and Emission Spectroscopy and X-ray Diffuse Scattering	44
3.8.1	Experimental Setup	45
3.8.2	Synchrotrons: Beamline 7ID-D at the Advanced Photon Source . . .	45
3.8.3	Synchrotrons: Dynamics Beamline P01 at PETRA III	47
3.8.4	X-ray Free Electron Lasers: SACLA	47
4	Time-resolved X-ray Absorption Spectroscopy at PETRA III	49
4.1	Introduction	49
4.2	Experimental Approach for Implementing MHz Pump-Probe Experiments in the Hard X-ray Domain at P01 Beamline of PETRA III	51
4.2.1	The PETRA III SR Source for Pump-Probe Studies	51
4.2.2	The Dynamics Beamline P01	52
4.2.3	The Liquid Jet Flat Sheet Target	53
4.2.4	Multi-MHz Fiber Amplifier Laser System	53
4.2.5	Spatial and Temporal Overlap of X-ray and Laser Beams	54
4.2.6	X-Ray Fluorescence Detection Strategy	55
4.2.7	Synchronization and Data Acquisition Strategy at MHz repetition Rates	57
4.3	Results: Signal Statistics and Time-resolved XAS Measurements	59
4.3.1	Detector Signal Statistics	60
4.3.2	Linearity of APD and Dynamic Range	64
4.3.3	High Signal Quality for Measuring a Spin Transition Process: Sol- vated $[\text{Fe}(\text{bpy})_3]^{2+}$	67
4.3.4	TR XANES of Weakly Excited Aqueous $[\text{Co}(\text{CN})_6]^{3+}$	69
4.4	Summary and Outlook	72
5	Iridium Photosensitizer for Solar Hydrogen Generation	75
5.1	Introduction – $[\text{Ir}(\text{ppy})_2(\text{bpy})]^+$	75
5.2	Results - Picosecond-resolved X-ray Spectroscopy	79
5.2.1	Experimental Conditions	79
5.2.2	Static $L\alpha$ X-ray Emission Spectroscopy	80
5.2.3	Time-resolved L_3 -Edge X-ray Absorption Spectroscopy	80
5.2.4	Time-resolved L_2 -Edge Total Fluorescence Yield XANES	83
5.2.5	Time-resolved XAS of Fully Functioning Photocatalytic System . . .	84
5.3	Analysis and Discussion	87
5.3.1	XANES Analysis	87

5.3.2	Determination of Excited State Fraction	92
5.3.3	Electron Transfer Rates from TEA to IrPS*	94
5.4	Summary	95
6	Towards an Iron-based Photosensitizer	97
6.1	Introduction - $[\text{Fe}(\text{dcpp})_2]^{2+}$	97
6.2	Picosecond-resolved X-ray Spectroscopies of $[\text{Fe}(\text{dcpp})_2]^{2+}$	100
6.2.1	Experimental Conditions	100
6.2.2	K-edge X-ray Absorption Spectroscopy	101
6.2.3	X-ray Emission Spectroscopy	103
6.3	Analysis and Discussion	107
6.3.1	Analysis of X-ray Emission Spectra	107
6.3.2	EXAFS analysis	109
6.3.3	Discussion of EXAFS Refined Structures and Comparison to Simulation	116
6.3.4	Excited State Lifetime	116
6.3.5	Comparison to $[\text{Fe}(\text{terpy})_2]^{2+}$	118
6.4	Summary	120
7	Direct Observation of Ultrafast High-valent Iron Formation	121
7.1	Introduction - $\textit{trans}[(\text{cyclam})\text{Fe}^{\text{III}}(\text{N}_3)_2]^+$	121
7.2	Results I - Picosecond-resolved X-ray Spectroscopy	124
7.2.1	APS XAS Measurements	124
7.2.2	PETRA III XAS Measurements	129
7.2.3	Picosecond XAS Analysis	131
7.3	Results II - Femtosecond-resolved X-ray Spectroscopy	137
7.3.1	TR XAS after 266 nm Excitation	138
7.3.2	Femtosecond XAS Analysis	141
7.3.3	TR XES after 355 nm Excitation	147
7.4	Summary	151
8	General Conclusions and Outlook	153
8.1	Summary and Conclusions	153
8.2	Perspectives and Outlook	155
A	MHz DAQ at P01 User's Guide	157
A.1	Preparing Input Signals for MHz DAQ	157
A.2	Software Starting Procedure	159
A.3	Parameters of the Karabo project for data acquisition	161
A.4	TCP/IP server to connect MHz DAQ with SPOCK	162
B	Iridium L₃-edge - Gaussian vs. Lorentzian Broadening	165

C	Supplementary Info - SACLA Experiments	167
C.1	Dispersive Pulse Broadening and Spot Size Measurements	167
C.2	Low vs. High Laser Intensity	170
C.3	Channel Cut Si(111) Monochromator and Timing Tool Correction	172
D	FEFF Input File for $[\text{Fe}(\text{dcp})_2]^{2+}$ Ground State	175
	Bibliography	177
	Acknowledgements	193
	List of Publications	195

1 Introduction

Chemistry traditionally treats reactions on a macroscopic scale as the transformation from an ensemble of reactants to an ensemble of products. This approach obviously lacks an understanding of the individual temporal and spatial evolution of the electronic orbitals and atomic nuclei, which could be seen as the smallest entities of chemical reactions. Making the dream of a real time observation of molecules during the ongoing process of a chemical reaction come true is extremely challenging. It requires accessing the overwhelmingly fast femtosecond (fs) time- and incredibly small Ångström (Å) spatial domains.

The making and breaking of chemical bonds happen on the femtosecond ($1 \text{ fs} = 10^{-15} \text{ s}$) timescale [1]. The wave packet motion on the molecular potential energy surface can be considered one of the fastest chemical processes, thus setting the standard of required temporal resolution when measuring the dynamics of chemical reactions. Although diffusion driven chemical processes can be slower and the lifetimes of metastable states can even expand into the second timescale, a knowledge of the ultrafast primary processes is inevitable to understand the efficiencies of chemical reactions. These primary processes happening in the sub nanoseconds ($= \text{ns} = 10^{-9} \text{ s}$) regime can be accessed with pump-probe techniques. A first pulse (= pump) is used to electronically excite the system and after a certain delay a second, synchronized pulse (= probe) is used to probe the transient state of the system. The temporal resolution of such a pump-probe experiment is limited by the duration of the two pulses as well as the temporal jitter in their synchronization, caused e.g. by mechanical instabilities.

The use of femtosecond optical laser pulses both for pumping and probing to study femtosecond chemical dynamics started in the 1980's, giving birth to the field of femtochemistry [2, 3]. Nowadays, femtosecond transient absorption spectroscopy from the mid-IR to the UV regime has become a standard tool in chemical dynamics research [4, 5] and setups can be bought commercially [6]. The complexity of all-optical pump probe experiments has increased tremendously. For example femtosecond-resolved fluorescence measurements are used to detect the radiative decay of extremely short-lived excited states [7, 8]. Multi-dimensional spectroscopies consisting of a pump-probe scheme with sequences of more than two pulses can be used to understand correlations of spectral features [9, 10]. The THz spectral regime is used to study the ultrafast processes of strong electric fields interacting with matter [11]. Furthermore, the XUV spectral regime is exploited via high-harmonic generation, which allows for attosecond ($= \text{as} = 10^{-3} \text{ fs}$) resolution and can be used to study electron dynamics [12, 13]. These all-optical techniques are only sensitive to valence

electronic states and transitions amongst these are typically very broad. Their interpretation is often very ambiguous and the molecular structure is not directly accessible with these methods.

To directly observe the molecular structure during a chemical reaction, where the relevant length scales are the size of atoms or molecular bond distances which are on the order of 1 Å ($=10^{-10}$ m), structural techniques are required to replace the optical probe. Here, pulses of either particles or short-wavelength photons (X-rays) can be used, with the most straightforward experimental approach being to probe the molecular structure by means of scattering techniques. This has succeeded with ultrafast electron diffraction [14] and ultrafast X-ray scattering [15].

As an alternative approach ultrafast X-ray absorption spectroscopy (XAS) [16–18] has been implemented, which combines the advantage of X-rays being sensitive to the structure with those of spectroscopies, i.e. being also sensitive to the electronic orbitals. This electronic sensitivity is not restricted to the valence shells, but extends to the core-shells, which for different atomic species are well separated, leading to the element specificity of XAS. By tuning the incident X-ray energy to the respective absorption edge, the electronic structure of a certain atom and the geometric structure in its close vicinity can be probed. This atom could be the transition metal (TM) center of a solvated coordination complex. Here we focus on the hard X-ray regime (typically the photon energy range of ~ 5 keV to ~ 20 keV), where many TM absorption edges can be found. Measuring the energy dependent absorption cross section delivers X-ray absorption spectra. The region close to the absorption edge, called X-ray absorption near edge structure (XANES) and the range further above the absorption edge, called extended X-ray absorption fine structure (EXAFS) are analyzed. TR XANES has been exploited to measure electronic [19–21] and structural [19, 22, 23] changes of TM chromophores in solution. Changes in the distances of the absorbing atom to its nearest neighbors have been quantified with \sim picometer ($= 1$ pm $= 0.01$ Å) resolution using TR EXAFS [22–25].

Later TR XAS has been complemented by TR X-ray emission spectroscopy (XES) [26, 27], which can be exploited as a spin sensitive tool. Combining both with TR X-ray diffuse scattering (XDS) in a single setup [28, 29] to benefit from XDS to also monitor the solute-solvent interactions has followed. A crucial technological improvement was the transition from kHz [26, 30] to MHz [27, 31–33] repetition rate experiments. This development boosted the achievable signal-to-noise ratios of TR experiments close to those of static ones, and ultimately enables the study of relevant molecular complexes instead of model systems. The combined XAS, XES and XDS setups come now close to being the ultimate molecular camera, as with its joined observables they allow to monitor all relevant observables of chemical reactivity: changes in spin (via XES) and electronic (via XANES and XES) states and the structure (via XANES, EXAFS and XDS) of the solute molecules as well as their interplay with the solvent environment (via XDS).

The aforementioned setups have all first been implemented at Synchrotrons, limiting the

temporal resolution to ~ 100 ps. Very soon though, the regime of ~ 100 fs temporal resolution has been reached using femtosecond slicing schemes (with incredibly low photon fluxes of ~ 10 per pulse) at the same facilities [34–36]. The real revolution came with the implementation of XAS, XES and XDS [37–42] at X-ray Free Electron Lasers (XFELs), which deliver unprecedented X-ray intensities with $\sim 10^{12}$ photons in < 100 fs pulses [43–45] in the hard X-ray regime.

This thesis aims to apply ultrafast X-ray spectroscopies to relevant questions in technological (photo-) catalysis with the extension to systems of fundamental interest for enzyme catalysis. In these biological catalytic systems, TM complexes play a key role (see e.g. the manganese cluster in photosystem II [46]). Furthermore, a huge amount of technological applications to exploit solar activity in order to solve the urging human need for energy involve TM complexes. Here, examples include photosensitizers in dye-sensitized solar cells [47] or both photosensitizers and catalysts in homogeneous catalytic system for solar hydrogen generation [48, 49].

TR XAS, XES and XDS have been found as a suitable probe for (photo-)catalytically relevant molecular systems in solution phase [21, 40, 50, 51]. They are able to capture the light induced correlated electronic and nuclear changes on the relevant timescales down to 100-fs resolution and due to the element specificity of XAS and XES they are ideally suited to site-selectively probe the relevant transition metal centers in the liquid environment of a solution. Nevertheless, these studies mainly focused on model systems. Here we aim for pushing the limits further towards applying TR XAS and XES to answer fundamental questions in the chemistry of TM complexes relevant for technological as well as biological catalysis.

In chapter 2 the photophysics and photochemistry of TM complexes is introduced, which is needed to understand the principal photoexcitation and the subsequent relaxation mechanisms. In the following chapter 3 the experimental methodology of time-resolved X-ray spectroscopies is explained. In chapter 4 an experimental setup at the P01 beamline of PETRA III is described, which has been developed as a part of this thesis in order to maximize the signal-to-noise ratio in TR XAS measurements by fully exploiting the high X-ray photon flux at synchrotrons [33]. This is required to study dilute (biological) samples and those with very weak time-resolved modulations.

The next two chapters represent 100-ps-resolved synchrotron studies of TM complexes relevant for photocatalytic process. In chapter 5 the investigation of an iridium photosensitizer [48], for solar hydrogen generation is presented, including also the measurements in the fully functioning photocatalytic system [49]. The following chapter 6 summarizes the study on a possible candidate towards iron based photosensitizers [52], in order to replace expensive and rare ruthenium or iridium based systems. Here the structure and spin of the energetically lowest lying excited state are meticulously characterized to assess the capabilities of this candidate complex towards a new class of iron based photosensitizer.

In the last chapter 7, combined synchrotron and XFEL studies were used to monitor the ~ 300 fs to >30 ns timescale photochemical reactions of an iron compound [53] relevant for biological catalysis. The investigated system forms a high-valent Fe(V) complex after photoexcitation. Fe(V) complexes are of vital interest for the understanding of the Cytochrome P450 class of enzymes [54], which are involved in the catalytic metabolism of xenobiotics and the here investigated model complex is the first one to allow for the detection of octahedral Fe(V) at biological conditions (room temperature, solution phase). Using combined fs XAS and XES, the ultrafast process of Fe(V) formation is directly probed along with a second competing reaction pathway, consisting of a ligand exchange mechanism.

2 Photophysics and Photochemistry of Transition Metal Complexes

This chapter introduces the photophysical and photochemical processes of $3d$ (Iron) and $5d$ (Iridium) transition metal complexes with (approximately) octahedral symmetry.

2.1 Introduction

The transition metals are the elements of groups 3 to 12 [55] between scandium and copernicium, see periodic table in Fig. 2.1. They are characterized by their incomplete d sub-shell, respectively their capability to form cations with incomplete d sub-shells [56]. These can form transition metal (TM) complexes when they bind further groups of atoms, so-called ligands, via a coordinate bond. In such a coordinate bond the central atom (here the TM) acts as an electron acceptor and the ligands (= the electron-pair donors) bind to this central atom by donating a lone electron-pair to the central atom [57].

IUPAC Periodic Table of the Elements

Key:																			
atomic number																			
Symbol																			
name																			
standard atomic weight																			
1 H hydrogen [1.007, 1.009]																18 He helium 4.003			
3 Li lithium [6.938, 6.997]	4 Be beryllium 9.012													5 B boron [10.80, 10.83]	6 C carbon [12.00, 12.02]	7 N nitrogen [14.00, 14.01]	8 O oxygen [15.99, 16.00]	9 F fluorine 19.00	10 Ne neon 20.18
11 Na sodium 22.99	12 Mg magnesium [24.30, 24.31]													13 Al aluminum 26.98	14 Si silicon [28.08, 28.09]	15 P phosphorus 30.97	16 S sulfur [32.05, 32.08]	17 Cl chlorine [35.44, 35.46]	18 Ar argon 39.95
19 K potassium 39.10	20 Ca calcium 40.08	21 Sc scandium 44.96	22 Ti titanium 47.87	23 V vanadium 50.94	24 Cr chromium 52.00	25 Mn manganese 54.94	26 Fe iron 55.85	27 Co cobalt 58.93	28 Ni nickel 58.69	29 Cu copper 63.55	30 Zn zinc 65.38(2)	31 Ga gallium 69.72	32 Ge germanium 72.63	33 As arsenic 74.92	34 Se selenium 78.97	35 Br bromine [79.90, 79.91]	36 Kr krypton 83.80		
37 Rb rubidium 85.47	38 Sr strontium 87.62	39 Y yttrium 88.91	40 Zr zirconium 91.22	41 Nb niobium 92.91	42 Mo molybdenum 95.95	43 Tc technetium	44 Ru ruthenium 101.1	45 Rh rhodium 102.9	46 Pd palladium 106.4	47 Ag silver 107.9	48 Cd cadmium 112.4	49 In indium 114.8	50 Sn tin 118.7	51 Sb antimony 121.8	52 Te tellurium 127.6	53 I iodine 126.9	54 Xe xenon 131.3		
55 Cs caesium 132.9	56 Ba barium 137.3	57-71 lanthanoids	72 Hf hafnium 178.5	73 Ta tantalum 180.9	74 W tungsten 183.8	75 Re rhenium 186.2	76 Os osmium 190.2	77 Ir iridium 192.2	78 Pt platinum 195.1	79 Au gold 197.0	80 Hg mercury 200.6	81 Tl thallium [204.3, 204.4]	82 Pb lead 207.2	83 Bi bismuth 209.0	84 Po polonium	85 At astatine	86 Rn radon		
87 Fr francium	88 Ra radium	89-103 actinoids	104 Rf rutherfordium	105 Db dubnium	106 Sg seaborgium	107 Bh bohrium	108 Hs hassium	109 Mt meitnerium	110 Ds darmstadtium	111 Rg roentgenium	112 Cn copernicium	113 Uut ununtrium	114 Fl flerovium	115 Uup ununpentium	116 Lv livermorium	117 Uus ununseptium	118 Uuo ununoctium		
57 La lanthanum 138.9	58 Ce cerium 140.1	59 Pr praseodymium 140.9	60 Nd neodymium 144.2	61 Pm promethium	62 Sm samarium 150.4	63 Eu europium 152.0	64 Gd gadolinium 157.3	65 Tb terbium 158.9	66 Dy dysprosium 162.5	67 Ho holmium 164.9	68 Er erbium 167.3	69 Tm thulium 168.9	70 Yb ytterbium 173.0	71 Lu lutetium 175.0					
89 Ac actinium	90 Th thorium 232.0	91 Pa protactinium 231.0	92 U uranium 238.0	93 Np neptunium	94 Pu plutonium	95 Am americium	96 Cm curium	97 Bk berkelium	98 Cf californium	99 Es einsteinium	100 Fm fermium	101 Md mendelevium	102 No nobelium	103 Lr lawrencium					

INTERNATIONAL UNION OF PURE AND APPLIED CHEMISTRY

For notes and updates to this table, see www.iupac.org. This version is dated 8 January 2016. Copyright © 2016 IUPAC, the International Union of Pure and Applied Chemistry.

Figure 2.1: Periodic table of the elements where the transition metals can be found in groups 3 to 12 (Fig. reproduced with permission from [58], copyright © 2016 International Union of Pure and Applied Chemistry).

The total number of donor atoms which are bound to the central transition metal is called the coordination number [55]. As all reactant complexes discussed in this thesis are hexacoordinated, we focus here on the description of coordination complexes with coordination number 6. Due to the six-fold coordination, the symmetry around the transition metal center is (approximately) octahedral (O_h).

Typical examples of ligands are ammonia (NH_3), carbonyl (CO), cyanide (CN^-), but also single atoms, e.g. N^- , as well as larger molecules are common ligands. Here polydentate ligands, which bind to the coordination center with more than one donor atom, play an important role (these are often called chelating ligands) [55]. Depending on the number of donor atoms, these ligands are termed bidentate (2 donor atoms), tridentate (3 donor atoms) and so on. Examples of bidentate ligands in this thesis are phenylpyridine (=ppy) and bipyridine (=bpy) in $[\text{Ir}(\text{ppy})_2(\text{bpy})]^+$ (see Chapter 5). Tridentate ligands are terpyridine (=terpy) in $[\text{Fe}(\text{terpy})_2]^{2+}$, di(carboxypyridyl)pyridine (=dcp) in $[\text{Fe}(\text{dcp})_2]^{2+}$ and di(vinylpyridyl)pyridine (=dvpp) in $[\text{Fe}(\text{dvpp})_2]^{2+}$ (see Chapter 6). A tetradentate ligand is cyclam in *trans*[(cyclam) $\text{Fe}^{\text{III}}(\text{N}_3)_2]^+$ (see Chapter 7). Often, the transition metal complex has a net charge, which is compensated by a counterion. Common counterions include (PF_6) and Cl. In solution this counterion is detached, resulting in a TM complex ion.

TM complexes are ubiquitous in biology and have been found increasingly interesting for industrial applications. The most prominent examples of TM complexes in biology include the heme cofactors of hemoglobin [59] and myoglobin [60], which consist of Fe embedded in tetradentate porphyrin ligands. Another important example is the Mn cluster as the active catalytic site in the oxygen evolving complex of photosystem II (PSII). [46] A very promising example for technological application is the use of TM complexes as photosensitizers (PS) for photocatalytic hydrogen or electricity generation, e.g. Ruthenium based complexes are used in dye-sensitized solar cells (DSSC) [47].

These examples are merely a small selection of transition metal complexes, but it is clear that they are highly relevant as functional complexes in both biology and technological applications. Furthermore, they appear extremely important especially as catalytically active centers and it is the goal of this thesis to understand the primary steps of their catalytic activity.

Many of the aforementioned catalytic reactions are initiated by absorption of an optical photon, e.g. photocatalytic electricity generation in DSSC or oxygen generation in PSII, and are thus ideally suited for pump-probe experiments. This has been applied in this thesis to understand the photocatalytic activity of already applicable photosensitizers as well as candidates for new (and cheaper) photosensitizers. We can also contribute to the understanding of not intrinsically optically induced catalytic activity of TM by mimicking the activation of the TM complex with optical light or by replacing the TM catalysts by a photoactive model complex. This has been applied in this thesis to advance the understanding of a catalytic step of cytochrome P450 [54], an enzyme which is responsible for drug metabolism.

2.2 Transition Metal Complexes and the Role of the d-Orbitals

The valence orbitals of transition metals are the d -orbitals. The five different d -orbitals sketched in Cartesian coordinates are shown in Fig. 2.2. In gas phase, these five atomic orbitals are degenerate and can allocate ten electrons. While the two orbitals $d_{x^2-y^2}$ and d_{z^2} are aligned along the coordinate axes, the lobes of the three orbitals d_{xy} , d_{xz} and d_{yz} are allocated between the coordinate axes [55].

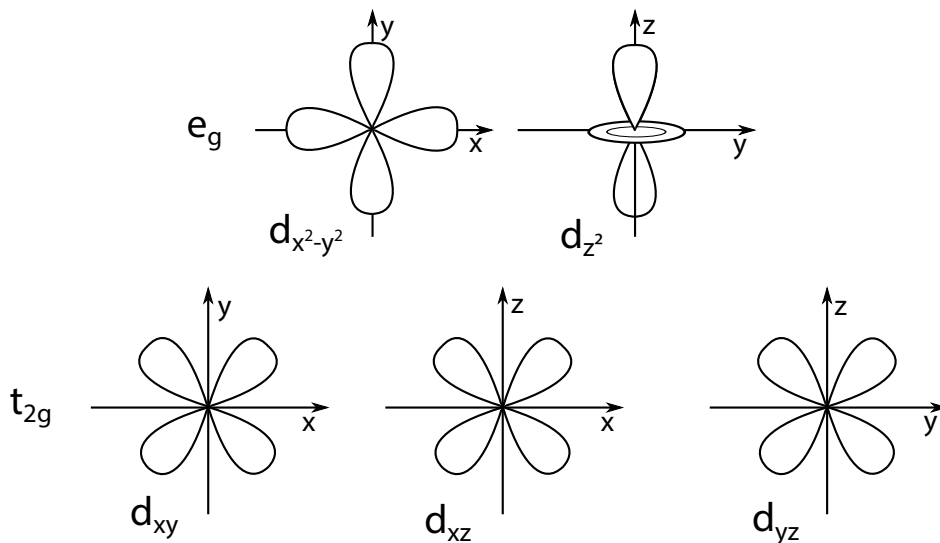
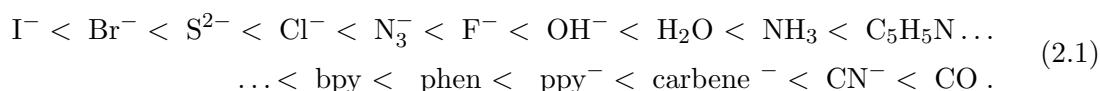


Figure 2.2: Sketch of the five d -orbitals which in octahedral symmetry split into two subsets: e_g (two-fold degenerate) and t_{2g} (three-fold degenerate).

In an octahedral, i.e. hexa-coordinated, complex the six donor atoms of the ligands are situated on the x , y , and z axis. The orbitals of the donor atoms interact mainly with the two d -orbitals which point along the Cartesian coordinates ($d_{x^2-y^2}$ and d_{z^2}). This lifts the degeneracy of the d -orbitals and splits them into the subsets t_{2g} (d_{xy} , d_{xz} and d_{yz}) and e_g ($d_{x^2-y^2}$ and d_{z^2}). The t_{2g} subset is further termed non-bonding while the e_g subset is called anti-bonding. The amount of the splitting is described in ligand field theory by the parameter of the ligand field strength $10Dq$ [62]. The spectrochemical series describe the relation of $10Dq$ and the ligand species as well as the central atom [55]. The colloquially termed "stronger" ligands lead to an increased ligand field strength compared to the "weaker" ligands. An example selection of ligands (from [63], where also a more comprehensive list can be found) ordered in terms of the $10Dq$ they exert is given by



Furthermore, $10Dq$ increases with increasing period of the atom, i.e. of $5d$ complexes it is larger than of $4d$ complexes which is again larger than of $3d$ complexes [55].

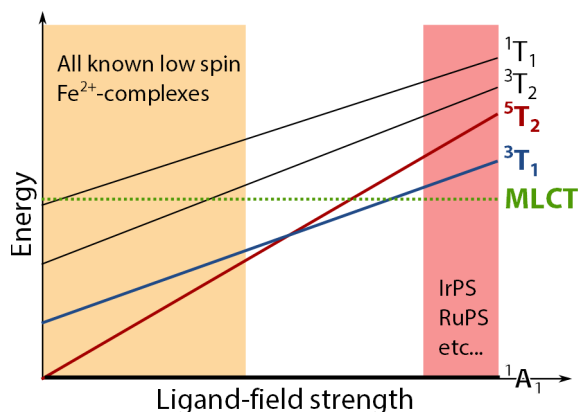


Figure 2.3: Simplification of the low spin region of the Tanabe-Sugano diagram of an octahedral $3d^6$ transition metal complex, showing the ligand field excited state energy compared to the 1A_1 ground state. For comparison, the tentative position of the metal-to-ligand charge transfer (MLCT) states have been added. For further comparison, the region where the RuPS and IrPS ($4d$ respectively $5d$ transition metal complexes) can be found is schematically shown as a shaded red area, yielding MLCT states at lower energies than the ligand-field states (Fig. as in [52]).

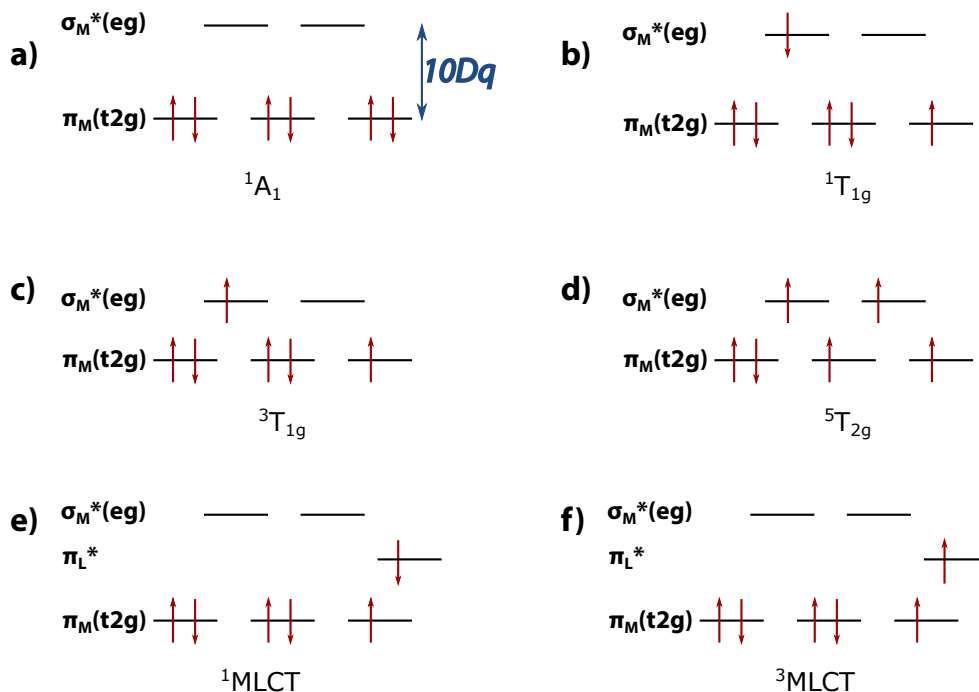


Figure 2.4: Simplified orbital diagrams of octahedral d^6 transition metal complex in singlet metal centered ground state (a), singlet metal centered excited state (b), triplet metal centered state (c), quintet metal centered state (d) (as in [61]). For comparison, the singlet MLCT (e) and triplet MLCT (f) are shown in a simplified analogous scheme.

The occupation of the d -orbitals is clearly dependent on the ligand field splitting. If we consider a d^6 transition metal in the case of no ligand field (and thus degenerate d -orbitals), the occupation of the orbitals will be, due to the electron-electron repulsion and Hund's rule, such that the spin is maximized. Consequently, four d -orbitals will be singly occupied, leading to a $S=2$ quintet state (see Fig. 2.4d). This quintet state is termed 5T_2 and is the ground state in the weak ligand-field case, where the spin pairing energy is larger than the ligand-field strength. As the ligand-field strength increases, the $S=0$ singlet state (1A_1), in which all six electrons are located in the t_{2g} orbitals, comes closer in energy to the 5T_2 . Eventually, when the ligand-field strength surpasses the spin pairing energy, the 1A_1 state becomes the ground state. The orbital ordering of these ligand field states as a function of the ligand-field strength is commonly plotted as the Tanabe-Sugano diagram. A very simplified version of a Tanabe-Sugano diagram, limited to only the low spin ground state region, is shown in Fig. 2.3 (here the crossing point between the 5T_2 and 1A_1 is the left-most point).

The Jahn-Teller theorem states that a molecular configuration without degenerate orbitals is preferred over a state with such a degeneracy [55]. The Jahn-Teller effect results in the distortion of the octahedral symmetry, e.g. along one axis of the molecule, and ultimately removes the degeneracy of each of the t_{2g} and e_g subsets, and can be caused e.g. by an uneven occupation of two e_g orbitals [57]. Such a Jahn-Teller distorted state can also result from ligand constraints, e.g. due to chelation [55]. An example are the Jahn-Teller distorted ground states of $[\text{Fe}(\text{terpy})_2]^{2+}$ [25] and $[\text{Co}(\text{terpy})_2]^{2+}$ [42], which show contracted axial bond lengths compared to the equatorial ones due to the steric constraints exerted by the tri-dentate terpyridine ligands (see also Chapter 6, where the $[\text{Fe}(\text{terpy})_2]^{2+}$ molecular structure is compared to the one of $[\text{Fe}(\text{dcpp})_2]^{2+}$).

2.3 Optical Excitation

Up to here our description has been limited to the atomic orbitals of the transition metal. However, when forming a complex, the atomic orbitals of the TM center mix with the ligand orbitals, giving rise to molecular orbitals.

An example of a simplified molecular orbital diagram for an octahedral d^n TM complex is presented in Fig. 2.5. The molecular orbitals can be grouped into $\pi_M(t_{2g})$, $\sigma_M^*(e_g)$, and σ_M^* with mainly metal character and σ_L , π_L and π_L^* with mainly ligand character [61]. In the ground state configuration of this complex, the σ_L and π_L orbitals are fully occupied and the n valence electrons are distributed over $\pi_M(t_{2g})$ and $\sigma_M^*(e_g)$, while the rest of the orbitals are not occupied [61]. The highest occupied molecular orbital is called HOMO, the lowest unoccupied one LUMO.

The possible electronic excitations correspond to promoting one electron to a vacancy in a higher lying orbital. We can distinguish four types of excitations: i) metal-to-ligand charge transfer (MLCT) excitation corresponding to an electron transfer from a mainly

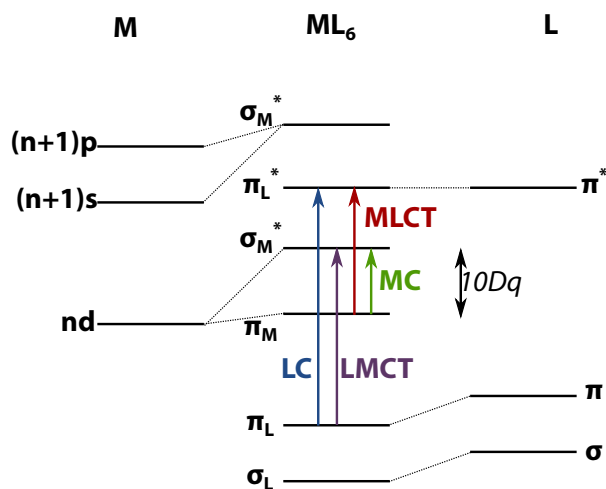


Figure 2.5: Molecular orbital digramm of an octahedral transition metal complex. One example of each of the four possible types of transitions, metal-to-ligand charge transfer (MLCT), ligand-to-metal charge transfer (LMCT), ligand centered (LC) and metal centered (MC) are shown (Fig. based on [61, 64]).

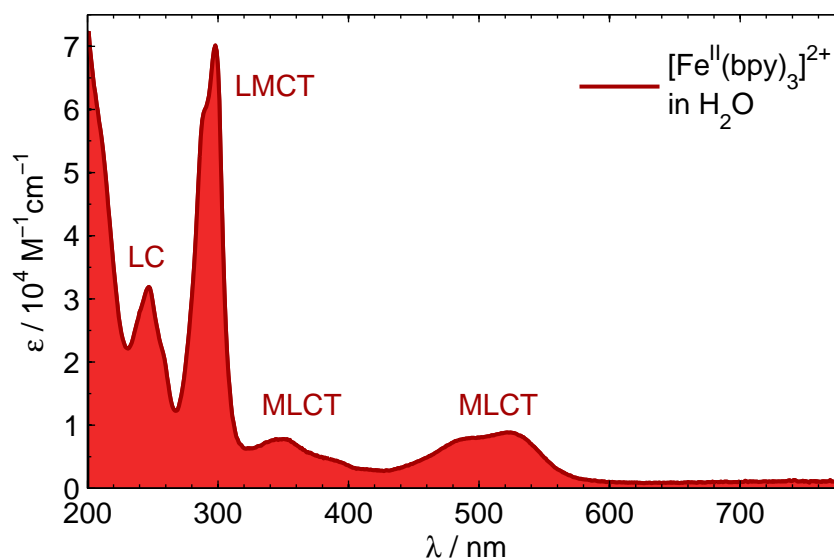


Figure 2.6: Static UV-vis absorption spectrum of $[\text{Fe}(\text{bpy})_3]^{2+}$ in H_2O . The visible discrete peaks can be assigned to transitions of ligand-centered (LC), ligand-to-metal charge transfer (LMCT) and metal-to-ligand charge transfer (MLCT) type, the herein presented assignment follows the description in Ref. [65].

metal- to a mainly ligand-orbital, ii) ligand-to-metal charge transfer (LMCT) excitation for a transfer from a mainly ligand- to a mainly metal-orbital, iii) ligand centered (LC) transitions from one ligand orbital to another ligand orbital and iv) metal centered (MC) transitions from one metal orbital to another metal orbital.

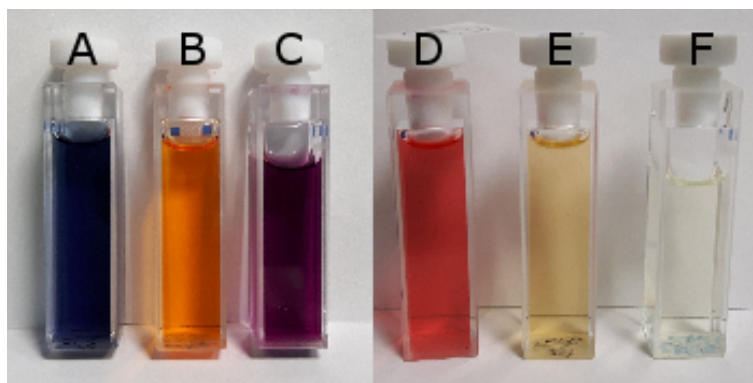


Figure 2.7: 1 cm cuvettes filled with solutions of the investigated molecules in CH_3CN with concentrations between 50 μM and 250 μM : A) $\text{Fe}[(\text{dcp})_2](\text{PF}_6)_2$, 225 μM ; B) $\text{Fe}[(\text{dvpp})_2](\text{PF}_6)_2$, 225 μM ; C) $\text{Fe}[(\text{terpy})_2](\text{PF}_6)_2$, 242 μM ; D) $\text{Fe}[(\text{bpy})_3](\text{PF}_6)_2$, 224 μM ; E) *trans* $[(\text{cyclam})(\text{Fe}^{\text{III}}(\text{N}_3)_2)](\text{PF}_6)$, 106 μM ; F) $\text{Ir}[(\text{ppy})_2(\text{bpy})](\text{PF}_6)$, 50 μM .

These electronic transitions give rise to discrete peaks in the optical absorption spectrum. As an example, the optical absorption spectrum of aqueous $[\text{Fe}(\text{bpy})_3]^{2+}$ is shown in Fig. 2.6. The spectrum exhibits discrete, but broad and thus overlapping absorption bands which have been assigned as in Ref. [65]. Three of the aforementioned types of transitions have been found with optical absorption cross sections on the order of $10^4 - 10^5 (\text{M cm})^{-1}$ (typical values for allowed transitions are on the order of up to $10^5 (\text{M cm})^{-1}$ [66]): MLCT, LMCT and LC. The lowest energy MC transition, which corresponds to the $d-d$ transition $t_{2g} \rightarrow e_g$, is not visible in the spectrum. According to the Laporte selection rule, only transitions between states of different parity are allowed [55], thus the gerade-gerade $d-d$ transition is forbidden. Nevertheless, due to spin-orbit coupling this rule is partially relaxed, giving rise to $d-d$ transitions with low optical cross sections (e.g. for aqueous $[\text{Fe}(\text{CN})_6]^{4-}$ the $d-d$ transitions are visible as a weak shoulder with an absorption coefficient on the order of $10^2 (\text{M cm})^{-1}$ [67]).

The multitude of strong electronic transitions of many transition metal complexes leads to a broad spectrum of bright colors. A picture of solutions of the transition metal complexes investigated in this thesis is shown in Fig. 2.7.

In a potential energy surface (PES) scheme (see e.g. Fig. 2.9), the energies of the distinct electronic states are expressed as a function of the nuclear coordinates. Here, the optical (=electronic) excitation corresponds to a vertical transition (depicted as an upwards pointing arrow), as the optical excitation is required to fulfill the Franck-Condon principle, which states that the nuclear coordinates do not change during the process of an optical (=electronic) excitation [66]. This principle follows from the Born-Oppenheimer approximation, according to which the electronic motion (occurring on $\sim\text{fs}$) is much faster than the nuclear motion ($\sim\text{ps}$).

2.4 Excited State Decay

Upon preparation in an electronically excited state the molecule can undergo different kinds of deactivation mechanisms, which can be grouped into i) intramolecular excited state decay, ii) intramolecular chemical reactions and iii) intermolecular or bimolecular chemical reactions.

Intramolecular Excited State Decay

The intramolecular deactivation processes are summarized in the example Jablonski diagram in Fig. 2.8. The molecule in its singlet S_0 ground state is excited by a photon of energy $h\nu_1$ to its first singlet excited state S_1 (or by a higher photon energy of $h\nu_2$ to its second singlet excited state S_2), eventually with concomitant vibrational excitation. This excitation process is followed by a series of deactivation processes which involve one or more of the following: i) Vibrational relaxation (VR), ii) internal conversion (IC), iii) inter system crossing (ISC) and its inverse process iv) back ISC (BISC, not shown here), iv) non-radiative decay (NR), vi) Fluorescence (F) and vii) Phosphorescence (P). These processes eventually bring the molecule back to its thermalised electronic ground state.

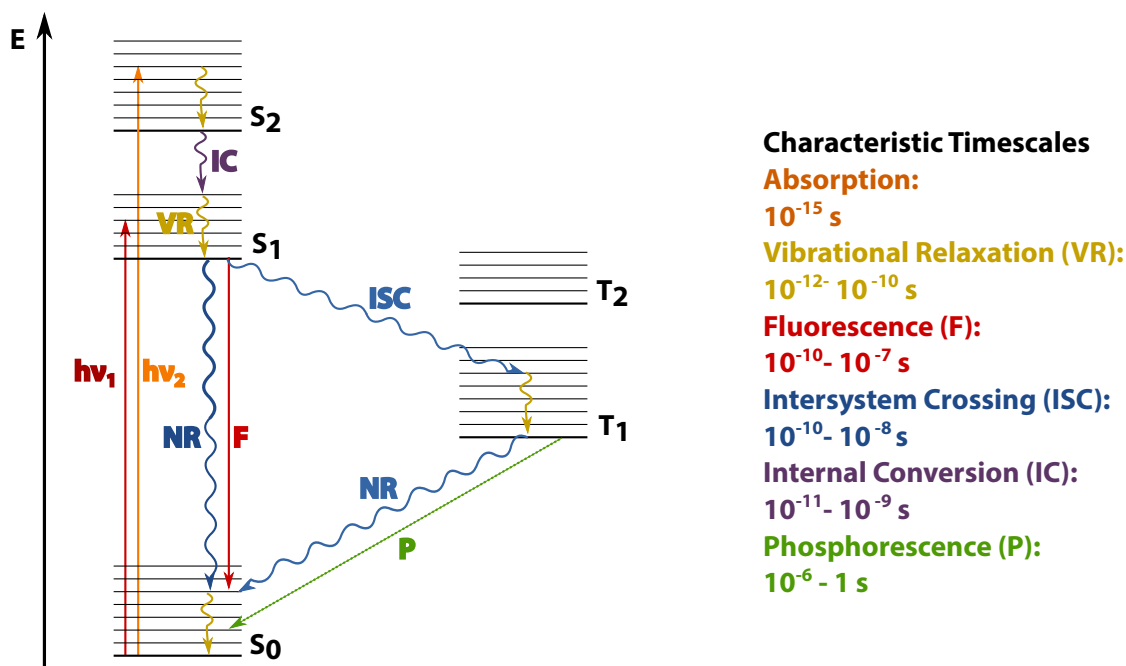


Figure 2.8: Jablonski diagram of a complex with singlet ground state showing photophysical processes of intramolecular excited state decay after optical excitation with $h\nu_1$ or $h\nu_2$: Vibrational relaxation (VR), internal conversion (IC), inter system crossing (ISC), non-radiative decay (NR), fluorescence (F), phosphorescence (P) (Fig. as in [61], timescales from [66]).

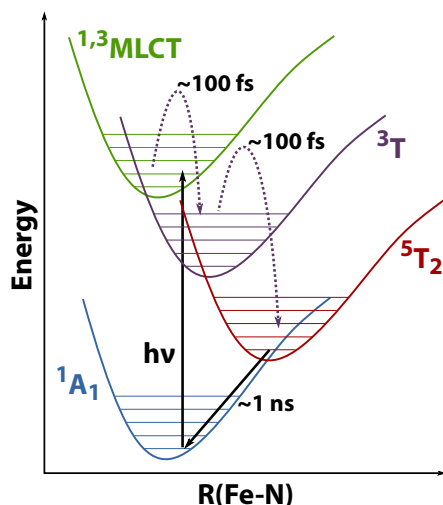


Figure 2.9: Potential energy surfaces involved in the light-induced low spin (LS) to high spin (HS) transition of $[\text{Fe}(\text{bpy})_3]^{2+}$ solvated in H_2O or CH_3CN . Photoexcitation in the MLCT manifold leads to rapid ISC to the triplet MC state (3T) and further to the quintet HS state (5T_2). The back transition to the singlet ground state (1A_1) occurs on a timescale of ~ 1 ns [39].

A good example of TM complexes undergoing several processes of intramolecular excited state decays are the Fe spin transition systems, which include $[\text{Fe}(\text{terpy})_2]^{2+}$ [25], $[\text{Fe}(\text{bpy})_3]^{2+}$ [65], $[\text{Fe}(\text{tren}(\text{py})_3)]^{2+}$ [23] as well as $[\text{Fe}(\text{dcpp})_2]^{2+}$ [52], which will be treated in detail in Chapter 6. In these complexes, excitation from the singlet ground state to the singlet MLCT state is followed by a rapid transfer to a metal centered high spin quintet state, involving multiple ISC via further metal centered (triplet) states [68]. An example of the PES scheme of $[\text{Fe}(\text{bpy})_3]^{2+}$ with the potential surfaces involved in the decay following optical excitation in the MLCT bands is shown in Fig. 2.9.

Furthermore, the Ir photosensitizer $[\text{Ir}(\text{ppy})_2(\text{bpy})]^+$ investigated in Chapter 5 undergoes a large series of deactivation mechanisms. In the experiments shown in this thesis the excitation to a singlet MLCT state is quickly followed by ISC to a triplet MLCT state and in the absence of an electron donor the system returns back to the ground state via a phosphorescent pathway.

Intramolecular Chemical Reactions

Intramolecular chemical reactions involve only the reactant, which does not return to its original ground state. These can be found as competing mechanisms to the above discussed deactivation mechanism back to the parent complex ground state. Amongst these intramolecular chemical reactions we find the processes of ionization (=oxidation), (ligand) dissociation or isomerization.

Examples of such reactions in this thesis are the N_2 as well as the N_3^- dissociation of $\text{trans}[(\text{cyclam})\text{Fe}^{\text{III}}(\text{N}_3)_2]^+$ (see Chapter 7).

Intermolecular/Bimolecular Chemical Reactions

Furthermore, photochemical reactions involving other molecules are possible, such as electron transfer processes from or to a secondary molecule or ligand binding/ligand exchange mechanisms. These processes are often diffusion driven and thus slower than the unimolecular processes.

The $[\text{Ir}(\text{ppy})_2(\text{bpy})]^+$ in the fully functioning photocatalytic system undergoes at least two intermolecular chemical reactions after photoexcitation (see Chapter 5). These are the electron transfer from the sacrificial reductant to the electronically excited IrPS as well as the consecutive electron transfer to the water reduction catalyst.

Another example of such a type of reaction is the binding of a CH_3CN solvent molecule following the optically induced N_3^- dissociation from *trans*[(cyclam) $\text{Fe}^{\text{III}}(\text{N}_3)_2]^+$ (see Chapter 7).

2.5 Numerical Example: Optical Excitation of an Example Molecule

In this section, a numerical example of optical excitation of one of our typical samples will be shown. The aim is to obtain a feeling for typical excited state fractions in the excited volume as well as the required laser pulse energies.

The optical density of a sample of thickness x consisting of solvated molecules with molar absorptivity ϵ (in $\text{M}^{-1} \text{cm}^{-1}$) with concentration c (in $\text{M} = \text{mol/L}$) in a transparent solvent is given by the product

$$OD = -\epsilon cx . \quad (2.2)$$

Assuming no reflection losses, the Beer-Lambert law describes the transmission T_{opt} through a sample of thickness x with optical density OD via

$$T_{\text{opt}} = \frac{N_{\text{Laser}}(x)}{N_{0,\text{Laser}}} = 10^{-OD} . \quad (2.3)$$

Here $N_{0,\text{Laser}}$ is the number of laser photons before the sample and $N_{\text{Laser}}(x)$ the number of laser photons after a sample of thickness x . In this thesis the Beer-Lambert law with a decadic logarithm has been chosen to describe the transmission of optical photons, while for the X-rays its formulation with the natural logarithm is applied, as it is done this way most commonly in the respective fields. One could simply transfer the Beer-Lambert law from decadic to natural logarithm by replacing $T_{\text{opt}} = 10^{-OD} = e^{-\ln(10)OD}$. This allows also to relate OD to the optical absorption cross section σ_{opt} of the molecule, in analogy to the description of the interaction of X-rays with matter: $\sigma_{\text{opt}} = \frac{-\ln(10)OD}{n_{\text{sam}}}$, with $n_{\text{sam}} = cN_A$ being the concentration of molecules in the solution (but now in molecules/ cm^3) and N_A the Avogadro constant. In the regime of linear optical absorption (single photon absorption, neglecting ground state bleach, etc...) and a unitary quantum yield of the

excitation process the excited state fraction is given by ratio of absorbed optical photons and the number of molecules $N_{\text{mol,LF}}$ in the laser excited volume to [69, 70]

$$f = \frac{N_{0,\text{Laser}}(1 - 10^{-OD})}{N_{\text{mol,LF}}} . \quad (2.4)$$

The number of photons in the laser excited volume is given by $N_{\text{mol,LF}} = cN_A A_{LF} d$, with A_{LF} being the laser illuminated area on the sample. For example a 20 mM solution in a 100 μm thick jet illuminated by a round laser spot with diameter 50 μm contains about 2.36×10^{12} molecules. If we assume the sample with molar absorptivity of ~ 8000 $(\text{M cm})^{-1}$, corresponding to $OD = 1.6$, is excited by a 500 nm laser pulse with 0.1 μJ , 2.5×10^{11} photons are absorbed. This would yield an excited state fraction of $f \approx 11$ %.

2.6 Summary and Conclusions

In this chapter, transition metal complexes have been introduced and their photoexcitation and the subsequent deactivation mechanisms have been described. Characterizing the deactivation mechanisms and disentangling the intermediate states in photochemical reactions requires temporal resolutions down to femtoseconds. Nevertheless, understanding the energy-rich (excited) states of transition metal complexes in catalysis is crucial to understand their efficiencies in (photo-) catalytic cycles.

The first class of complexes investigated in this thesis are photosensitizers (or potential candidates in the development of new photosensitizers). To date, several photosensitizers based on $4d$ and $5d$ transition metals exist. For example Ru based systems are being used in DSSC [47] to directly generate electrical energy. Furthermore, Ir based photosensitizer for photocatalytic hydrogen generation by water splitting exist, which will be discussed in great detail in 5. The important characteristic of these systems are long-lived states with charge (electron or hole) separation, allowing for their further use. In Ru- and Ir- systems long-lived MLCT states can serve for this purpose.

Nevertheless, $4d$ and $5d$ transition metals are rare and thus extremely expensive. The goal is to replace these photosensitizers by systems based on cheaper transition metals, e.g. Fe, which is to date very challenging. To understand the difficulty with Fe based systems we need to go back to the simplified Tanabe-Sugano diagram in Fig. 2.3. In this diagram (which in principle only contains the ligand-field states) we have added schematically the MLCT states with a constant offset from the GS. As the Ru- and IrPS possess an extremely large ligand field strength, the ligand-field excited states (5T_2 and also the 3T_1) are found energetically well above the MLCT states. Thus the MLCT states cannot be deactivated by these metal centered states.

This is not the case for Fe complexes: the MLCT bands of (almost) all known low spin Fe complexes are found energetically above the MC states. This is mainly due to the intrinsically low ligand-field strength of Fe. One attempt to remedy this problem is to

tailor new Fe complexes with "stronger" ligands which increases the energy of the MC states, with the ultimate goal to raise their energy to above the MLCT states. Here, just recently first attempts have succeeded, e.g. using ligands such as N-heterocyclic carbenes [71] or a combination of bpy and CN^- [72]. In Chapter 6 we have investigated a candidate towards this new class of low spin Fe(II) complexes.

Apart from photocatalytically relevant complexes we have investigated a model complex for biologically relevant catalytic activity in Chapter 7. Flash photolysis is used to generate an exotic high-valent Fe(V) complex. Such superoxidized species are considered key intermediates in the reactive cycles of the cytochrome P450 class of enzymes, which are in charge e.g. of drug metabolism in mammals [73].

Time-resolved X-ray absorption and emission spectroscopy are ideal tools to investigate the optically induced chemical reactions of these transition metal complexes. The formation of photoproducts as well as reaction intermediates include changes in the electronic states (orbital occupation and spin) as well as the molecular structure of the molecules. In the next chapter we will discuss how, with the help of TR X-ray spectroscopies, all these aforementioned observables can be monitored in real-time.

3 Experimental Methodology - Time-resolved X-ray Spectroscopy

3.1 Interaction of X-rays with Matter

An X-ray photon with energy $E_{\text{x-ray}}$ can interact in several different ways with a sample, of which the most relevant are [74–76]: i) The photo-electric effect with cross section σ_{pe} , where the photon is completely absorbed by a bound electron. ii) Coherent scattering (Rayleigh scattering) with cross section σ_{coh} , where the photon is elastically scattered off the atoms. iii) Incoherent scattering (Compton scattering) with cross section σ_{inc} , where the X-ray energy is partially transferred to a bound electron, leading to ionization. iv) Pair-production, i.e. the generation of a positron-electron pair, with cross section σ_{pb} can occur when the X-ray photon energy exceeds the rest energy $2m_e c^2$ of this positron-electron pair. The total photon cross section σ_{tot} is given by the sum of the cross sections of all interaction mechanisms, $\sigma_{tot} = \sigma_{pe} + \sigma_{coh} + \sigma_{inc} + \sigma_{pb}$. As an example, the X-ray cross sections for iron in the photon energy range from 10^3 eV to 10^{11} eV are plotted in Fig. 3.1. We can distinguish three regimes with distinct dominating interaction mechanisms: up to about 10^5 eV the photoelectric effect, between 10^5 and 10^7 eV inelastic scattering and above 10^7 eV the pair production in the nuclear field.

Together with the density n of particles (atoms), which interact with the photon this yields the total X-ray attenuation coefficient $\mu_{tot} = n\sigma_{tot}$ and the attenuation of the incident X-ray intensity I_0 , when passing through a path length x , is described by the Lambert-Beer-Law [75]

$$I(x) = I_0 e^{-\mu_{tot} x}. \quad (3.1)$$

We limit the further description to the range of photon energies to about 5 to 20 keV, which covers all experimental results described in this thesis. In this regime, the photo-absorption effect is the dominant contribution from light (first row elements, e.g. carbon) to very heavy (e.g. lead) atoms [74]. The probability of the elastic scattering, which is the second strongest interaction mechanism for iron in this energy range, marks a strong angular dependency and is minimal along the polarization vector of the incoming radiation [78]. This can be used to suppress the elastic scattering contribution when measuring the X-ray emission or the X-ray absorption in total fluorescence yield (see later in Sections 3.3.2 and 3.4).

The photo-electric X-ray absorption cross sections ($= \sigma_{pe}$) of both transition metals studied

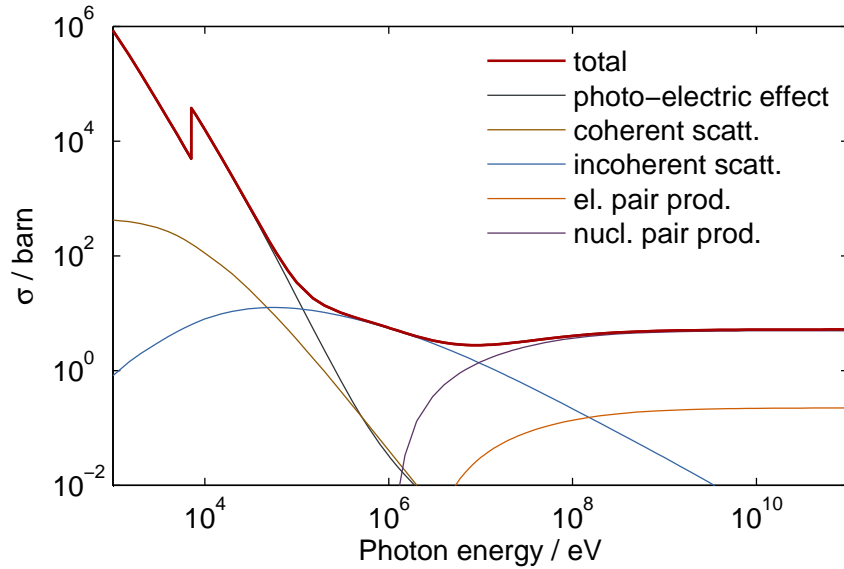


Figure 3.1: Atomic X-ray interaction cross sections of iron for photo-electric effect, coherent and incoherent scattering, pair production as well as the total interaction cross section (data from [77]).

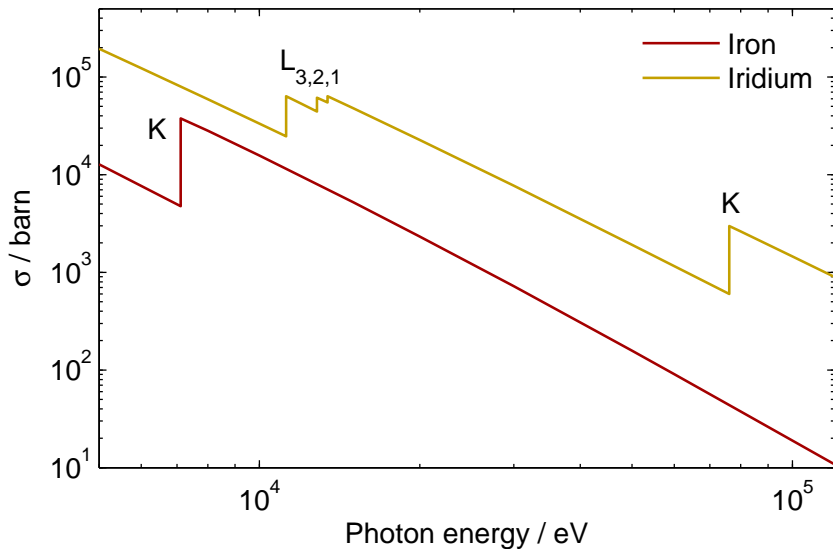


Figure 3.2: X-ray absorption cross sections of iridium (yellow) and iron (red) (data from [77]).

in this thesis, Fe and Ir, are plotted in Fig. 3.2. Both absorption cross sections exhibit a general E^{-3} dependence [75] and furthermore they show sharp edge features at those energies, for which the photon energy exceeds the binding energy of a certain core shell electron. These edges are historically named according to the shell (or main quantum number) from which the ionization occurs, e.g. the K-edge corresponds to ionization

from $1s$ and the L_{3-} , L_{2-} and L_{1-} edges correspond to ionization from $2p_{3/2}$, $2p_{1/2}$ and $2s$, respectively.

At photon energies above the Ir K-edge, i.e. where ionization from all shells of both Ir and Fe contribute, the absorption cross section of Ir is almost 2 orders of magnitude (or to be more precise, a factor of ~ 77) larger than that of Fe. This is caused by the Z^4 dependence of the X-ray absorption cross section [75].

3.2 X-ray Absorption Spectroscopy

In X-ray absorption spectroscopy (XAS) the energy dependent absorption cross sections $\sigma_{tot} \approx \sigma_{pe}$ around the absorption edges are measured and used to obtain structural and electronic information about the local environment around the absorbing atom inside the molecule. Zooming closer into the absorption edge region and analyzing the energy dependent modulations in the XAS, the X-ray absorption fine structure (XAFS) becomes visible. As an example, the Fe K-edge XAS of $[\text{Fe}(\text{terpy})_2]^{2+}$ is shown in Fig. 3.3.

XAS are typically divided into two regimes, which are analyzed and interpreted quite differently. The region around the absorption edge contains the X-ray absorption near edge structure (XANES) and the region far (i.e. at least about 20 - 50 eV) above the absorption edge marks the extended X-ray absorption fine structure (EXAFS). The XANES region furthermore contains the pre-edge region with discrete bound-bound transitions, which will be treated next, before treating the XANES and EXAFS regions above the absorption edge.

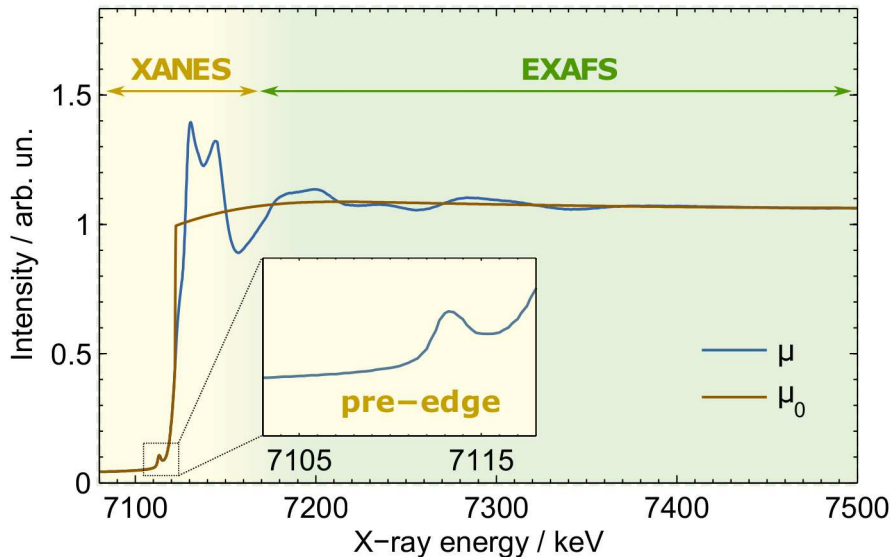


Figure 3.3: X-ray absorption spectrum of $[\text{Fe}(\text{terpy})_2]^{2+}$ containing both X-ray absorption near edge structure (XANES) and extended X-ray absorption fine structure (EXAFS). In the inset, the pre-edge region with one clear pre-edge peak is shown.

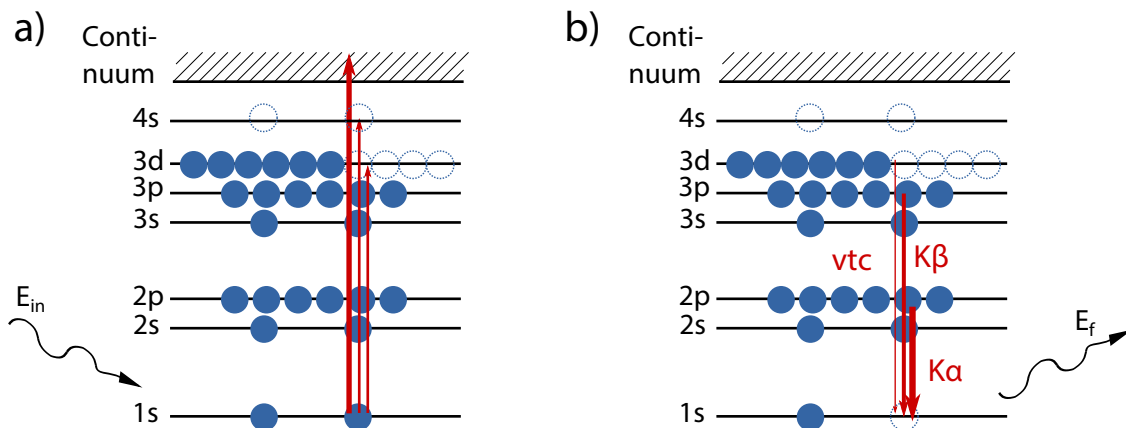


Figure 3.4: Schematic showing the a) X-ray absorption and b) emission process applied to the term scheme of a $3d^6$ electronic configuration of an Fe(II) complex in which the $3d$ orbitals are found below the $4s$ orbitals. The arrow thickness symbolizes the relative oscillator strength for absorption (a) and emission (b).

3.2.1 Pre-edge Peaks to Extract Chemical Information

If the X-ray photon energy $E_{X\text{-ray}}$ matches the difference between the energy $E_{n,j}$ of a core shell (with main quantum number n and total angular momentum j) and the energy $E_{n',j'}$ of a not fully occupied valence orbital,

$$E_{X\text{-ray}} = |E_{n,j}| - |E_{n',j'}| \quad (3.2)$$

a core electron can be promoted to this vacancy. These bound-bound transitions lead to discrete peaks in the pre-edge region of the X-ray absorption spectrum, as can be seen in the inset of Fig. 3.3. The pre-edge peaks are ideally suited to be used to map out the unoccupied molecular orbitals with mainly TM character.

In Fig. 3.4a), the X-ray absorption process containing bound-bound transitions of an Fe(II) system are shown as an example. In the case of $3d$ transition metal complexes, the K-edge XAS pre-edge features mainly consist of $1s \rightarrow 3d$ bound-bound transitions, which are electric dipole forbidden in centrosymmetric systems, i.e. in complexes with octahedral symmetry. They become partially allowed due to $3d$ - $4p$ mixing, when the centrosymmetry is broken [79]. Thus the intensity of the pre-edge peak contains further information about the symmetry of the molecule.

Several systematic studies on the $1s$ pre-edge features of $3d$ transition metal complexes exist, focusing on the $1s \rightarrow 3d$ transition strengths and the energy shift of these, both as a function of the central metal ion ligation and oxidation state. For example, the position of several XANES features of Vanadium oxides revealed a ~ 1 eV shift for the $1s \rightarrow 3d$ pre-edge feature for an oxidation state increase of +1 [80]. The pre-edge peak position has also been found to be sensitive to the Fe oxidation state and has for example been used to determine the Fe(II)/Fe(III) ratio in geological samples [81, 82]. Furthermore, the

relationship between the pre-edge peak position of Fe and the oxidation state has been extended to higher valencies of the Fe up to +VI [83]. More systematic experimental [84] studies, as well as multiplet calculations [79], including also intensity and splitting of the pre-edge features have been used to extend the extractable information content to the coordination/geometry as well as the ligation around the Fe centers.

In the case of $4d$ or $5d$ transition metals the L-edges can be accessible in the hard X-ray domain. For example the L_3 -edges contain $2p_{3/2} \rightarrow 4d$ (or $2p_{3/2} \rightarrow 5d$) bound-bound transitions which are dipole allowed and thus by far more intense than the corresponding transitions starting from the $1s$ shell. This advantage has been used in the case of TR L_3 -edge XAS to determine the electronic structure of solvated $4d$ Ru [85], as well as of $5d$ Re [86], Os [87, 88] and Ir [89] complexes.

3.2.2 X-ray Absorption Near Edge Structure (XANES)

When the binding energy $E_{n,j}$ of a core shell electron matches the incident X-ray energy, $E_{X\text{-ray}} = |E_{n,j}|$, a prompt jump in the X-ray absorption spectrum occurs at the absorption edge. The energetic onset of the absorption edge depends on the oxidation state of the absorbing atom. This can be explained by the $1s$ core-hole shielding: the energy required to remove an electron from the metal center increases as the total oxidation state of the metal center increases [90, 91]. For example a shift of about 1-2 eV between ferrous and ferric $\text{Fe}(\text{CN})_6$ has been found [92, 93]. For Vanadium oxides a positive shift of ~ 2 eV for an oxidation state change of 1 has been determined [80]. Nevertheless, applying the energy of the absorption edge (which could be defined as its onset or the half-rise) to measure the oxidation state can be ambiguous due to other features caused by the coordination geometry determining the edge structure [22, 94] and due to other allowed electronic transitions in the same energy range as the absorption edge [80, 95].

As further single-electron excitations in $3d$ TM complexes, $1s \rightarrow 4s$ and $1s \rightarrow 4p$ transitions have been identified [91]. Shake-down phenomena at energies below the $1s \rightarrow 4p$ transition, consisting of a $1s \rightarrow 4p$ transition combined with strong ligand-to-metal charge transfer, were assigned to give rise to a shoulder in the absorption edge of CuCl_4^{2-} ions [96]. Further features above the $1s \rightarrow 4s$ transition [80] can be due to the very similar shake-up transitions consisting of two-electron excitations [97] and shape resonances, where the photoelectron is temporarily trapped by the shape of the potential [98, 99].

The origin of the XANES features due to the geometric structure of the molecule can be described as follows: If $E_{X\text{-ray}}$ exceeds $|E_{n,j}|$, the absorption of a photon corresponds to a bound-free transition and thus the ionization of the complex. The excess energy of the X-ray photon, after being absorbed by such an electron, is translated into kinetic energy E_{kin} of the photo-electron,

$$E_{kin} = E_{X\text{-ray}} - |E_{n,j}|. \quad (3.3)$$

In other words, a photo-electron wave with a wave number k , defined by 2π times the inverse of its de Broglie wavelength λ [100],

$$\frac{2\pi}{\lambda} = k = \frac{\sqrt{2m_e(E_{X\text{-ray}} - |E_{n,j}|)}}{\hbar} \quad (3.4)$$

$$\approx 0.51232 \text{\AA}^{-1} \sqrt{E_{X\text{-ray}} - |E_{n,j}|} [\text{eV}^{-1/2}], \quad (3.5)$$

is generated at the atom inside the molecule, which absorbs the photon. From here on we set $E = E_{X\text{-ray}}$ and $E_0 = E_{n,j}$. Next, in a simplified picture, this photo-electron wave propagates and scatters from the surrounding atomic potentials, as illustrated in Fig. 3.5, leading to constructive and destructive interference, causing the XAFS modulations in the XAS.

Thus, next to the electronic structure and thus the oxidation state, the edge shape contains information about the geometric structure in the close vicinity of the absorption (e.g. TM, here: Fe) center. Due to the low photoelectron energies with their high scattering cross sections in the XANES regime, multiple scattering events are, next to single scattering events, responsible for the modulations on the XANES spectrum. This should in principle allow to extract bond angles as well as bond lengths from XANES. Overall due to these multiple effects determining the XANES spectra they eventually are the richest in information, but hardest to simulate and interpret in an unambiguous fashion.

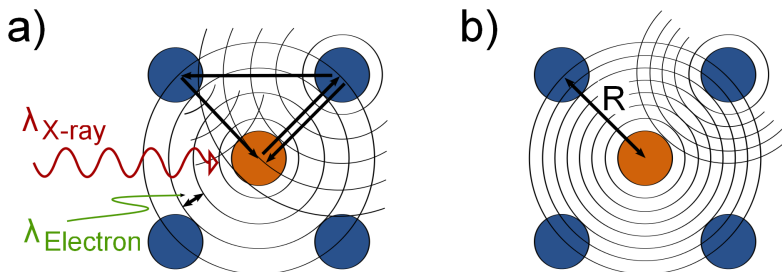


Figure 3.5: Schematic showing the mechanisms of a) multiple and b) single scattering events of the photoelectron generated upon absorption of an X-ray photon at an absorption center. The scattered photoelectron waves interfere constructively or destructively, leading to the X-ray absorption fine structure (reproduced from [16]).

The general concept for the calculation of X-ray absorption spectra is to first determine the electronic structure of the ground state. This ground state electronic structure is then perturbed by an X-ray pulse which liberates a core electron to calculate X-ray absorption spectra. The majority of the results presented in this thesis are taken with 100 ps resolution at Synchrotrons and the electronic structure of the (long lived) excited states can be treated as quasi-static. This approximation might not be valid in case of ultrafast experiments [101].

To calculate bound-bound transitions time-dependent density functional theory (TDDFT) can be used [102, 103], which is implemented in software packages as ORCA [104]. To

model bound-free transitions, a common attempt is to use multiple scattering theory (an excellent review on this can be found in Ref. [105]). Here the X-ray absorption process is described in a single electron picture of the photoelectron released in the core shell. This photoelectron wave is scattered from the potentials of the surrounding atoms. This can be done for example by the finite difference method (FDM), where the photoelectron wavefunction is discretized over an energy grid and iteratively solving the discretized Schrödinger equation until a self-consistent solution is found. In this method, all scattering paths are represented [106]. This method is implemented in the FDMNES (=FDM for Near Edge Structure) code. This code has been used to calculate the XANES spectra of Fe(II) spin transition systems [107], which are similar to the $[\text{Fe}(\text{dcpp})_2]^{2+}$ discussed in Chapter 6. In some cases, e.g. to calculate L-edge spectra of heavier elements, it can be useful to apply higher level theoretical methods such as restricted active space self-consistent field (RASSCF) calculations [108, 109]. This wavefunction based method is currently being used by our collaborators O. Kühn and S. Bokarev to calculate the L_3 -edge spectra of $[\text{Ir}(\text{ppy})_2(\text{bpy})]^+$ presented in Chapter 5. A further alternative approach here is the use of atomic multiplet calculations [110].

3.2.3 Extended X-ray Absorption Fine Structure (EXAFS)

The EXAFS region starting at higher photoelectron energies, i.e. about 20 eV to 50 eV above the absorption edge, allows very precise determination of the bond lengths of the absorption center to its nearest neighbors, e.g. the first and second coordination shells. The EXAFS spectrum is dominated by single scattering events, thus the information content in the EXAFS spectrum is restricted to mainly bond lengths and coordination number, i.e. 1D information. This simplifies the analysis and allows a more quantitative interpretation of the spectra and excellent reviews in Ref. [90, 105] discuss the EXAFS analysis in detail (see also a review on the history of EXAFS [111]). Here, the most essential formalism to understand the EXAFS analysis will be summarized.

In a first step, the XAFS spectrum $\chi(E)$ in energy space is obtained from the measured X-ray absorption coefficient $\mu(E)$ by subtracting the atomic background $\mu_0(E)$ and normalizing the edge jump to 1 by dividing through the step height $\mu_0(E_0)$ [105],

$$\chi(E) = \frac{\mu(E) - \mu_0(E)}{\mu_0(E_0)} \quad (3.6)$$

In the next step the EXAFS spectrum $\chi(E)$ is converted from energy into photo-electron wave vector space by applying Eq. 3.4.

As a simple approximation to calculate EXAFS spectra, a path expansion approach can be used. The distinct scattering paths of the photoelectron wave are calculated and the paths are summed up. Relying on this principle, as an analytical expression describing

this EXAFS pattern, the standard EXAFS formula has been developed [112, 113],

$$\chi(k) = \sum_j S_0^2 N_j \frac{|f_j(k)|}{kR_j^2} \sin(2kR_j + 2\delta_e + \phi) e^{-2R_j/\lambda(k)} e^{-2\sigma_j^2 k^2} . \quad (3.7)$$

Here S_0^2 is an amplitude reduction factor, N_j the degree of degeneracy or the number of equivalent scatterers (=equivalent atomic species at equal bond distance) j , $|f_j(k)|$ the backscattering amplitude, R_j is the half of the effective scattering path length (i.e. the inter-atomic distance), δ_e the central-atom partial-wave phase shift of the final state, $\lambda(k)$ the mean free path of the photoelectron and σ_j the Debye-Waller factor [16]. The effect of the distinct terms of the EXAFS formula are summarized here according to Ref. [105] as follows: The exponential term $e^{-2\sigma_j^2 k^2}$ containing the Debye-Waller factor σ_j^2 describes the uncertainties in the atomic positions, which are for example due to the thermal vibrations. This factor results in a damping of the oscillatory structure of EXAFS at larger k , until typically on the order of $k \approx 10$ the wiggles disappear. The other exponential term $e^{-2R_j/\lambda(k)}$ reflects the decay of the photoelectron wave due to its mean free path and also includes the finite core-hole lifetime. Due to the R dependence of this term, the structural information contained in EXAFS is restricted to the close vicinity (i.e. few coordination shells or few Å) around the absorbing atom. The backscattering amplitude $|f_j(k)|$ describes the dependency of the scattering strength with the scattering atomic species. The factor $\frac{1}{kR_j^2}$ describes the spherical wave propagation of the photoelectron and the factor N_j merely accounts for equal photoelectron scattering paths. The nature of the overall phase shift $2\delta_e + \phi$ will not be discussed here, in practice this phase shift is corrected with an experimental or theoretical reference. The most important factor of all though, is the $\sin(2kR_j)$ factor, which describes the general oscillatory pattern and contains the structural information of EXAFS.

In its original version, the EXAFS equation was developed for single scattering (Fig. 3.5b) paths j , but it is also valid to extend j to sum over multiple-scattering paths (Fig. 3.5a) [105]. The EXAFS spectrum can in addition be Fourier-transformed and analyzed as a pseudo-radial distribution function [112].

The most commonly used software package to calculate EXAFS spectra is FEFF [114]. An EXAFS analysis, relying on FEFF calculations, will be shown in chapter 6 for the example of $[\text{Fe}(\text{dcpp})_2]^{2+}$. There, the four steps of i) the background subtraction and normalization, ii) transformation into k -space, iii) Fourier-transformation into R -space and iv) back-Fourier-transformation into q -space are displayed in Fig. 6.8.

3.3 X-ray Absorption Spectroscopy Measurement Techniques

In this section, the experimental considerations to measure XAS will be discussed: XAS in the hard X-ray domain is typically measured in transmission or in total fluorescence yield (TFY) mode (in the soft X-ray regime, where the X-ray fluorescence efficiencies are low, often the (Auger) electron yield is measured). In transmission mode, the X-ray transmission through the sample is measured and the Lambert-Beer-Law is used to extract the X-ray absorption coefficient. In TFY mode, the total X-ray fluorescence yield, which originates from the decay of the core excited states (i.e. the filling of a core hole with an electron from a higher lying shell), is measured. Under certain circumstances, which will be discussed later, the TFY is directly proportional to the X-ray absorption coefficient. A comparison of transmission and fluorescence measurements for time-resolved XAS will be presented here. The ultimate goal is to estimate the achievable signal-to-noise ratio (S/N) for our typical sample conditions and determine the optimum measurement technique to be applied. The derivations follow the descriptions in Refs. [65, 115, 116].

3.3.1 Transmission Measurement of X-ray Absorption Spectra

In this subsection an analytical formula for the X-ray absorption cross section measured in transmission mode is derived for a simplified pump-probe experiment, where the solvated molecules can be either in ground (GS) or excited state (ES). This represents the simplest case of a reaction $\text{GS} \rightarrow \text{ES}$, without involving any intermediate states or further distinct photoproducts. The case with multiple excited states can be derived accordingly to the here presented case.

The probability that an X-ray photon of energy E will be absorbed within a path length dx is given by $\mu_{\text{tot}}(E)dx$, where $\mu_{\text{tot}}(E)$ is the total X-ray absorption coefficient of the sample. If the initial intensity of X-rays is I_0 , the X-ray intensity $I(E, x)$ after passing through a thickness x of the sample is given by

$$I(E, x) = I_0(E)e^{-\mu_{\text{tot}}(E)x} . \quad (3.8)$$

The X-ray absorption cross section can be determined by measuring the transmitted intensity I_1 through the sample (see Fig. 3.6). The total X-ray absorption coefficient of the sample is then obtained to

$$\mu_{\text{tot}}(E) = \frac{1}{d} \ln \left(\frac{I_0(E)}{I_1(E)} \right) . \quad (3.9)$$

In the case of a sample consisting of solvated transition metal (TM) centered molecules the total X-ray absorption coefficient can be described as the sum of the absorption coefficient of the TM center of the solvated molecules μ_{sam} together with the X-ray absorption coefficient μ_{bckg} of all other atoms in the solution (thus including solvent molecules, impurities,

counterions and ligands) via,

$$\mu_{\text{tot}}(E) = \mu_{\text{sam}}(E) + \mu_{\text{bckg}}(E) . \quad (3.10)$$

Assuming a time-resolved experiment in which a fraction f of the solvated molecules is excited to an excited state, $\mu_{\text{sam}}(E)$ consists of a sum of the absorption coefficients $\mu_{\text{sam,GS}}(E)$ and $\mu_{\text{sam,ES}}(E)$ of the sample in its ground and excited state, respectively, weighted with the excited state fraction,

$$\mu_{\text{sam}}(E) = (1 - f)\mu_{\text{sam,GS}}(E) + f\mu_{\text{sam,ES}}(E) . \quad (3.11)$$

Furthermore, the total X-ray absorption coefficient can also be expressed as a function of densities and X-ray absorption cross sections of all involved molecules to [70]

$$\mu_{\text{tot}}(E) = n_{\text{sol}}\sigma_{\text{sol}}(E) + (1 - f)n_{\text{sam}}\sigma_{\text{GS}}(E) + fn_{\text{sam}}\sigma_{\text{ES}}(E) + n_{\text{rest}}\sigma_{\text{rest}}(E) . \quad (3.12)$$

Here n_{sol} , n_{sam} and n_{rest} are the concentrations of solvent molecules, the solvated sample molecules (both in GS and ES) as well as of all other molecules (counterions, ligands, impurities, etc...) in the solution, $\sigma_{\text{sol}}(E)$, $\sigma_{\text{GS}}(E)$, $\sigma_{\text{ES}}(E)$, $\sigma_{\text{rest}}(E)$, are the X-ray absorption cross sections of the solvent molecules, of the sample molecules in GS and ES as well as of all other molecules. The total X-ray absorption cross section of the sample measured in transmission mode is then

$$(1 - f)\sigma_{\text{GS}} + f\sigma_{\text{ES}} = \frac{1}{n_{\text{sam}}} \left[\frac{1}{d} \ln \left(\frac{I_0(E)}{I_1(E)} \right) - \mu_{\text{bckg}}(E) \right] . \quad (3.13)$$

To extract an absolute measurement of σ_{GS} from a transmission measurement requires a measurement of $\mu_{\text{bckg}}(E)$ alone, contrary to the TFY measurement (which will be seen later in Section 3.3.2). Since $\mu_{\text{bckg}}(E)$ is only slowly varying with E one can assume it being constant and subtract it as a baseline defined by the value of the X-ray absorption coefficient before the absorption edge of the spectrum.

Assuming the only source of uncertainty being the Poissonian shot noise of I_0 allows to calculate the absolute statistical error as well as relative error of a static measurement ($f=0$) to

$$\Delta\sigma(E) = \frac{1}{n_{\text{sam}}d} \sqrt{\frac{1}{I_1(E)}} \quad \text{and} \quad (3.14)$$

$$\frac{\sigma}{\Delta\sigma} = \sqrt{I_1(E)} \left[\ln \left(\frac{I_0(E)}{I_1(E)} \right) - d\mu_{\text{bckg}}(E) \right] . \quad (3.15)$$

The S/N of a time-resolved measurement ($f \neq 0$) of XAS in transmission mode will be treated later in Section 3.3.3.

3.3.2 Total Fluorescence Yield Measurement of X-ray Absorption Spectra

In this subsection a similar formula for the X-ray absorption cross section measured in TFY mode is derived.

The experimental setup for a TFY measurement of XAS is shown schematically in Fig. 3.6. A sample of thickness d' which is turned to an angle of θ with respect to the X-ray propagation direction is considered, leading to an effective X-ray path length of $d = d'/\sin(\theta)$ through the sample. In this thesis transition metal centered molecules in (organic) solutions are studied using hard X-radiation. We restrict the following description to K -edge absorption spectroscopy of $3d$ transition metal complexes. Thus only the X-ray absorption with subsequent generation of K -shell vacancies leads to fluorescence in the "hard" X-ray regime ($K\alpha$, $K\beta$, vtc, discussed later in Section 3.4), which is measured. The probability of an X-ray photon to be absorbed by the sample molecules within a pathlength dx is $\mu_{\text{sam}}(E)dx$. Of the absorbed X-ray photons, a fraction of ϵ_{tot} , the total fluorescence efficiency, leads to hard X-ray fluorescence, while the $(1 - \epsilon_{\text{tot}})$ of the core-excited states decay via an Auger process. A detector situated at an angle of ϕ with respect to sample (see Fig. 3.6) is used to measure the fluorescence photons with energy E_f . Thus the photons need to travel through an additional path length of $(\sin(\phi)/\sin(\theta))x$ through the sample to the detector, leading to an attenuation of $\exp(-\mu_{\text{tot}}(E_f)(\sin(\theta)/\sin(\phi))x)$. Furthermore, the detector covers a solid angle of Ω and the detector efficiency at E_f is given by $\phi_{\text{det}}(E_f)$. Thus the fluorescence measured by the detector is given by the integral [115]

$$\begin{aligned}
 I_{\text{TFY}}(E) &= \int_0^d I_0(E) e^{-\mu_{\text{tot}}(E)x} \epsilon_{\text{tot}} e^{-\mu_{\text{tot}}(E_f) \frac{\sin(\theta)}{\sin(\phi)} x} \mu_{\text{sam}}(E) \Omega \phi_{\text{det}}(E_f) dx \\
 &= I_0(E) \epsilon_{\text{tot}} \mu_{\text{sam}}(E) \Omega \phi_{\text{det}}(E_f) \frac{(1 - e^{-(\mu_{\text{tot}}(E) + \mu_{\text{tot}}(E_f) \frac{\sin(\theta)}{\sin(\phi)})d})}{\mu_{\text{tot}}(E) + \mu_{\text{tot}}(E_f) \frac{\sin(\theta)}{\sin(\phi)}} \quad (3.16)
 \end{aligned}$$

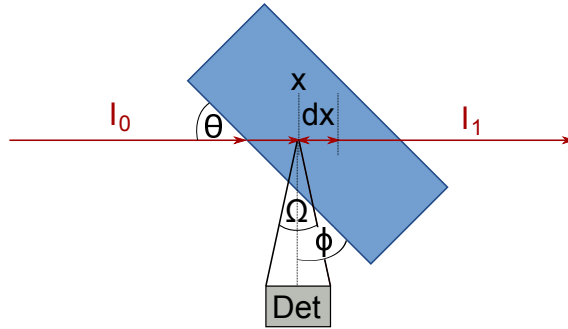


Figure 3.6: Schematic showing the total fluorescence yield measurement. A sample (blue), e.g. a liquid jet, is turned to an angle of θ with respect to the X-ray propagation direction and the TFY is measured with a detector (Det) situated at an angle of ϕ in respect to the sample surface normal and covering a solid angle Ω .

With this expression it is possible to use the measurements of $I_0(E)$ and $I_{\text{TFY}}(E)$ to obtain a measurement of the X-ray absorption coefficient of the sample. By measuring the TFY in both ground and excited state and using Eq. 3.12 one can extract the X-ray absorption cross section of the solvated molecules, if the absorption cross sections of all other molecules (solvent, counterions, etc...) and the total fluorescence efficiency ϵ_{tot} are known. It is worth mentioning that the measurement of absolute quantities also requires, next to an exact knowledge of the TFY geometry (e.g. solid angle) and the TFY detector efficiency, a well absolute calibrated I_0 detector.

We would like to further simplify Eq. 3.16: Typically the sample is turned to 45° and the TFY detector to 90° with respect to the X-ray propagation direction, resulting in $\sin(\phi)/\sin(\theta) = 1$. If the absorption length of the total sample is much longer than the sample thickness, i.e. $(\mu_{\text{tot}}(E) + \mu_{\text{tot}}(E_f))d \ll 1$ (for our samples this is typically the case) we can expand the exponential term $e^{-(\mu_{\text{tot}}(E) + \mu_{\text{tot}}(E_f))d} \approx 1 - (\mu_{\text{tot}}(E) + \mu_{\text{tot}}(E_f))d$. which can be used to further simplify Eq. 3.16 to

$$I_{\text{TFY}}(E) \approx I_0(E)\epsilon_{\text{tot}}\mu_{\text{sam}}(E)\Omega\phi_{\text{det}}(E_f)d. \quad (3.17)$$

When the sample thickness increases or the sample becomes more concentrated a large fraction of the X-rays can be absorbed in the sample, i.e. in the case $(\mu_{\text{tot}}(E) + \mu_{\text{tot}}(E_f))d \gg 1$ the exponential term in Eq. 3.16 can be neglected and we can rewrite it to

$$I_{\text{TFY}}(E) \approx \frac{I_0(E)\epsilon_{\text{tot}}\mu_{\text{sam}}(E)\Omega\phi_{\text{det}}(E_f)}{\mu_{\text{tot}}(E) + \mu_{\text{tot}}(E_f)\frac{\sin(\theta)}{\sin(\phi)}}. \quad (3.18)$$

As we are mainly concerned with relatively thin and dilute samples we restrict our further considerations to Eq. 3.17 and use Eq. 3.12 to obtain a general expression for the X-ray absorption cross section of the sample, the quantity which we intend to measure, via

$$(1 - f)\sigma_{\text{GS}}(E) + f\sigma_{\text{ES}}(E) = \frac{I_{\text{TFY}}(E)}{I_0(E)\epsilon_{\text{tot}}\phi_{\text{det}}(E_f)n_{\text{sam}}\Omega d}. \quad (3.19)$$

Assuming the only source of uncertainty being the shot noise of I_{TFY} we can calculate the absolute statistical error of an X-ray absorption cross section σ to obtain the relative error $\frac{\sigma}{\Delta\sigma}$ for the static ($f=0$) case via

$$\Delta\sigma(E) = \sigma\sqrt{\frac{1}{I_{\text{TFY}}(E)}} \quad \text{and} \quad \frac{\sigma(E)}{\Delta\sigma(E)} = \sqrt{I_{\text{TFY}}(E)}. \quad (3.20)$$

Thus the error of the measurement exclusively scales with square root of the TFY count rate. The S/N of a time-resolved measurement ($f \neq 0$) of XAS measured in TFY will be treated in the following section.

3.3.3 Signal-to-Noise of Transient X-ray Absorption Spectra

Depending on if the TFY XAS measurement is done with ($f > 0$) or without ($f=0$) laser excitation we can define the measured X-ray absorption cross sections to

$$\sigma_{\text{OFF}}(E) = \sigma_{\text{GS}}(E) \quad \text{and} \quad \sigma_{\text{ON}}(E) = (1 - f)\sigma_{\text{GS}}(E) + f\sigma_{\text{ES}}(E), \quad (3.21)$$

and the transient X-ray absorption spectrum to

$$\sigma_{\text{trans}} = \sigma_{\text{ES}} - \sigma_{\text{GS}} = \frac{1}{f}(\sigma_{\text{ON}} - \sigma_{\text{OFF}}). \quad (3.22)$$

If f is known, one can reconstruct the ES X-ray absorption cross section via

$$\sigma_{\text{ES}} = \sigma_{\text{OFF}} + \frac{1}{f}(\sigma_{\text{ON}} - \sigma_{\text{OFF}}). \quad (3.23)$$

In the next step a general expression of the S/N which can be achieved in a measurement of σ_{trans} is derived for the two described measurement techniques, transmission and fluorescence XAS.

To calculate the statistical errors an equal total number of accumulated incident X-ray photons I_0 for both ground (OFF) state ($I_{\text{TFY,OFF}}(E)$ and $I_{1,\text{OFF}}(E)$) and laser excited (ON) ($I_{\text{TFY,ON}}(E)$ and $I_{1,\text{ON}}(E)$) measurements is assumed. This can experimentally be realized by setting the pump laser repetition rate to half the X-ray probe repetition rate and probing alternating ground and excited state of the sample. In practise, this is not always the case and the ground state is often measured with higher statistical accuracy, due to lower laser repetition rates.

Using Eqs. 3.21 and 3.22 as well as Gaussian error propagation and assuming a shot-noise limited measurement the transient X-ray absorption cross section $\sigma_{\text{trans,TFY}}(E)$ with statistical error $\Delta\sigma_{\text{trans,TFY}}(E)$ is obtained,

$$\sigma_{\text{trans,TFY}}(E) = \frac{(I_{\text{TFY}}(E) - I_{\text{TFY,OFF}}(E))}{fI_0(E)\epsilon_{\text{tot}}\phi_{\text{det}}(E_f)n_{\text{sam}}\Omega d} \quad \text{and} \quad (3.24)$$

$$\Delta\sigma_{\text{trans,TFY}}(E) = \frac{\sqrt{I_{\text{TFY,ON}}(E) + I_{\text{TFY,OFF}}(E)}}{fI_0(E)\epsilon_{\text{tot}}\phi_{\text{det}}(E_f)n_{\text{sam}}\Omega d}. \quad (3.25)$$

Taking the quotient of these and simplifying leads to the S/N ratio of the TFY measurement

$$S/N_{\text{TFY}} = \frac{\sigma_{\text{trans,TFY}}(E)}{\Delta\sigma_{\text{trans,TFY}}(E)} = \frac{\sqrt{I_0 n_{\text{sam}} \sqrt{\epsilon_{\text{tot}} \Omega \phi_{\text{det}}} df (\sigma_{\text{ES}} - \sigma_{\text{GS}})}}{\sqrt{f (\sigma_{\text{ES}} + \sigma_{\text{GS}})}} \quad (3.26)$$

Analogously we derive $\sigma_{\text{trans,tr}}(E)$ and $\Delta\sigma_{\text{trans,tr}}(E)$ for a measurement in transmission mode,

$$\sigma_{\text{trans,tr}}(E) = \frac{1}{fn_{\text{sam}}d} \ln \left(\frac{I_{1,\text{OFF}}(E)}{I_{1,\text{ON}}(E)} \right) \quad \text{and} \quad (3.27)$$

$$\Delta\sigma_{\text{trans,tr}}(E) = \frac{1}{fn_{\text{sam}}d} \sqrt{\frac{1}{I_{1,\text{ON}}(E)} + \frac{1}{I_{1,\text{OFF}}(E)}}. \quad (3.28)$$

And the S/N for a transmission measurement is given by

$$S/N_{\text{tr}} = \frac{\sigma_{\text{trans,tr}}(E)}{\Delta\sigma_{\text{trans,tr}}(E)} \quad (3.29)$$

$$= \frac{\sqrt{I_0}n_{\text{sam}}d(f(\sigma_{\text{ES}} - \sigma_{\text{GS}}))}{\sqrt{\exp(\mu_{\text{bckg}}d)[\exp(((1-f)\sigma_{\text{GS}} + f\sigma_{\text{ES}})n_{\text{sam}}d) + \exp(\sigma_{\text{GS}}n_{\text{sam}}d)]}}. \quad (3.30)$$

As expected, the S/N in both cases has a $\sqrt{I_0}$ dependence, but while in the case of the transmission measurement the S/N scales with n_{sam} , in the case of the TFY it scales with $\sqrt{n_{\text{sam}}}$. Thus we expect the TFY measurement to be advantageous for measurements on dilute samples, while the transmission measurement is rather beneficial in the case of higher concentrated samples.

Numerical Example

We have used the above derived equations for the S/N of TFY and transmission measurements to estimate a number of required accumulated photons to achieve a S/N = 1 as well as to achieve S/N = 10 in a TR XAS measurement as a function of the solute concentration. To do so, we have assumed a sample consisting of an Fe complex solvated in H₂O in a 100 μm thick layer of liquid, i.e. a liquid jet. The difference in the absorption cross sections $\sigma_{\text{ON}} - \sigma_{\text{OFF}}$ is assumed to be 10 % of the K-edge jump and is found above the absorption edge. This is a typical situation for the systems discussed in this thesis.

In the estimation of the transmission measurement we have assumed $\sigma_{\text{rest}} = 0$, i.e. the X-ray absorption of the ligands, the counterions, etc., have been neglected. This assumption is valid for two reasons: Due to their low concentration which is comparable to the one of the solute and due to their low X-ray absorption cross section (Z^4 dependence) they only contribute marginally to the total absorption of the sample. Furthermore, they do not have any absorption edges around the Fe K-edge and can be seen as a very weak constant background. The concentration of the solvent H₂O in the solution has been assumed to be constant and was set to 55.6 M, the concentration of pure H₂O. This approximation can be made, as the solute concentrations in this calculation are below 1 M and thus affect the solvent concentration only slightly. In the calculation for the TFY measurement the total fluorescence yield was set to the $K\alpha$ fluorescence yield of Fe, $\epsilon_{\text{tot}} = 0.32$ [76], which accounts for ~ 90 % of the X-ray fluorescence of Fe [76]. Furthermore, we assumed a

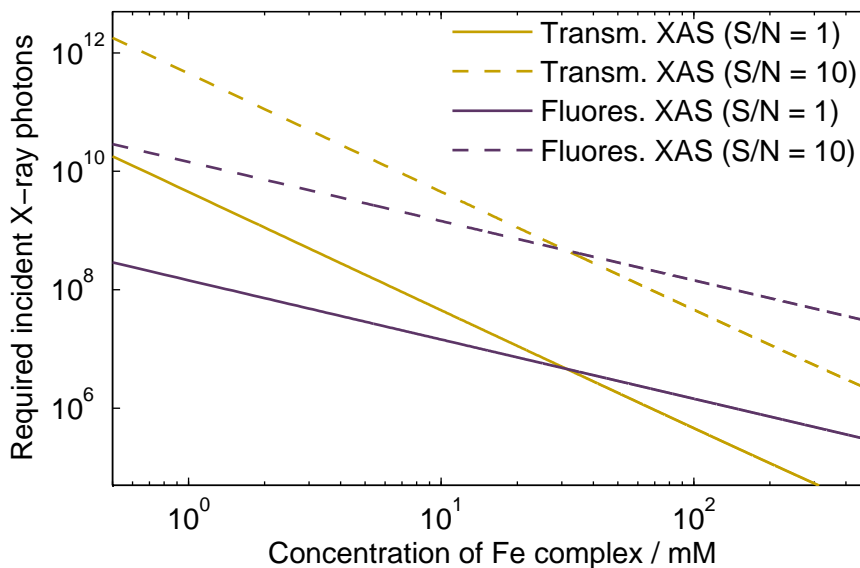


Figure 3.7: Estimate of required accumulated incident X-ray photons to achieve S/N of 1 or 10 for a transient signal above the absorption edge with a signal strength corresponding to 10 % of the edge jump of an Fe complex in aqueous solution. The values for a transmission and fluorescence yield measurement as a function of the sample concentration in a 100 μm thick liquid jet are compared (see text for more details).

covered solid angle of $\Omega = 0.25$ sr (or 2% out of 4π) and a unitary detector efficiency (detector efficiencies can be as high as 95% at 6 keV in the case of a commercially available APD detector head [117] commonly used by us). The X-ray absorption cross sections are taken from [77]. A calculation of the required incident X-ray photons to achieve S/N of 1 respectively 10 for a single energy point of a transient XAS measurements of Fe complexes of concentrations from 0.5 mM to 500 mM in transmission and total fluorescence yield mode can be found in Fig. 3.7. The plot shows that at concentrations below 30 mM the measurements in TFY are expected to deliver better S/N, while for higher concentrations the transmission measurement is advantageous. This justifies the choice of TFY detection for the measurements presented in this thesis, as most samples consisted of 10-20 mM solutions. Furthermore, this plot shows that S/N of 10 for a 10 mM sample (a typical combination of concentration and S/N required to obtain interpretable data) can be achieved with as little as about 10^9 incident X-ray photons, which corresponds to an acquisition time of 1 ms at an X-ray source delivering 10^{12} photons/s.

3.4 X-ray Emission Spectroscopy of Transition Metal Complexes

The core hole, which is generated in the X-ray absorption process, is rapidly filled with an electron from a higher lying shell. The excess energy of the transition can either be passed on to another bound electron which leaves its shell, this process is called Auger decay. Alternatively, the excess energy is emitted in form of a fluorescent photon, which is termed X-ray emission. In this work we make use of the X-ray emission by measuring the X-ray fluorescent photons energetically resolved in X-ray emission spectroscopy (XES). XES is ideally suited as a complementary technique to XAS, as in XAS the empty orbitals and in XES the occupied orbitals of an atom or molecule are probed. In Fig. 3.4b), a term scheme showing the X-ray emission of an Fe(II) system following a K-edge absorption is shown as an example.

In this section, the $K\alpha$, $K\beta$ and vtc XES of 3d TM complexes (Fe) and the $L\alpha$ XES of 5d TM (Ir) complexes will be discussed.

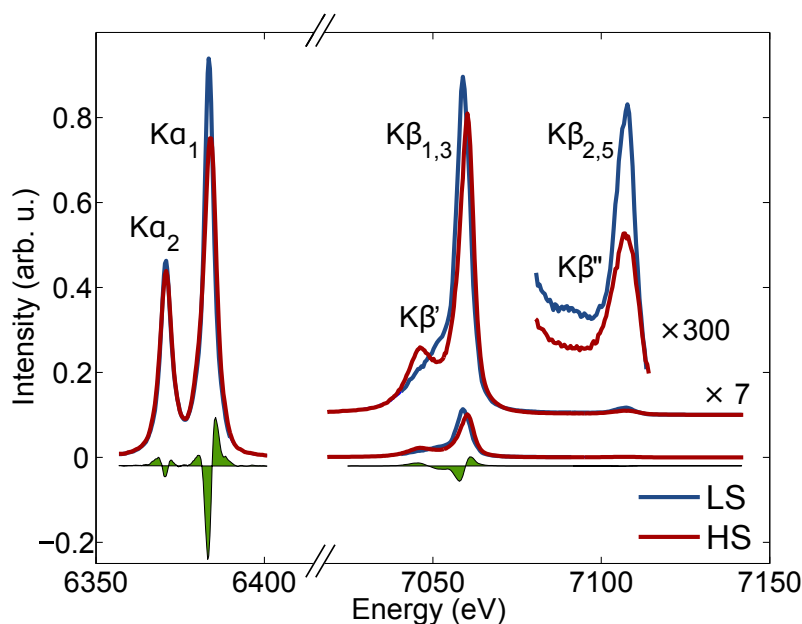


Figure 3.8: X-ray emission spectrum of S=0 (LS) and S=2 (HS) Fe complexes (Figure from G. Vankó) [118].

3.4.1 3d Transition Metal Complexes - $K\alpha$ X-ray Emission Spectroscopy

The $K\alpha$ XES resulting from the $2p \rightarrow 1s$ transition is the strongest of the K-shell fluorescence lines. The $K\alpha$ XES is split into two main lines by spin-orbit coupling, the $K\alpha_1$ from the $2p_{3/2} \rightarrow 1s$ transition and the $K\alpha_2$ from the $2p_{1/2} \rightarrow 1s$ transition. The $K\alpha_1$ is about twice as intense as the $K\alpha_2$ XES, which can be easily understood to be due to the two-fold degeneracy of the $2p_{3/2}$ shell compared to the non-degenerate $2p_{1/2}$ shell.

The $K\alpha$ XES of 3d TMs is mainly dependent on the spin state of the 3d center [118, 119].

As can be seen in Fig. 3.8 the $K\alpha_1$ line is red shifted and broadened for the $S=2$ high spin (HS) complex compared to the $S=0$ low spin (LS) complex. In this work we use the $K\alpha_1$ line as a spin sensitive probe, but instead of the peak position we analyze the full-width half-maximum (FWHM) line width which due to the (2p,3d) exchange interaction [119] scales linearly with the TM spin state [118].

3.4.2 3d Transition Metal Complexes - $K\beta$ X-ray Emission Spectroscopy

The $K\beta$ emission results from the $3p \rightarrow 1s$ transition and is in the case of 3d TM complexes up to about one order of magnitude weaker than the $K\alpha$ emission.

For 3d TM complexes, similar to the $K\alpha$ XES, the lineshape of the $K\beta$ XES mainly depends on the spin state of the TM center. This can be seen in Fig. 3.9, where $K\beta$ XES of static Fe reference samples with singlet, doublet, triplet, quartet and quintet spin multiplicity are plotted. Next to the main $K\beta_{1,3}$ peak a weak, so-called satellite peak, $K\beta'$, is visible in the spectra with non-zero spin momentum of the Fe. This feature is due to the (3p,3d) exchange interaction [118–120]. In addition to the appearance of the $K\beta'$, the splitting between $K\beta'$ and $K\beta_{1,3}$ increases with increasing spin state, i.e. the $K\beta_{1,3}$ shifts to larger energies. Although the $K\beta$ XES is by almost one order of magnitude weaker than the $K\alpha$, it seems to be even better suited to determine the spin state of the TM centers of complexes, as spectra not only shift or change their intensity, but also show new distinct features when the spin states changes from LS to HS.

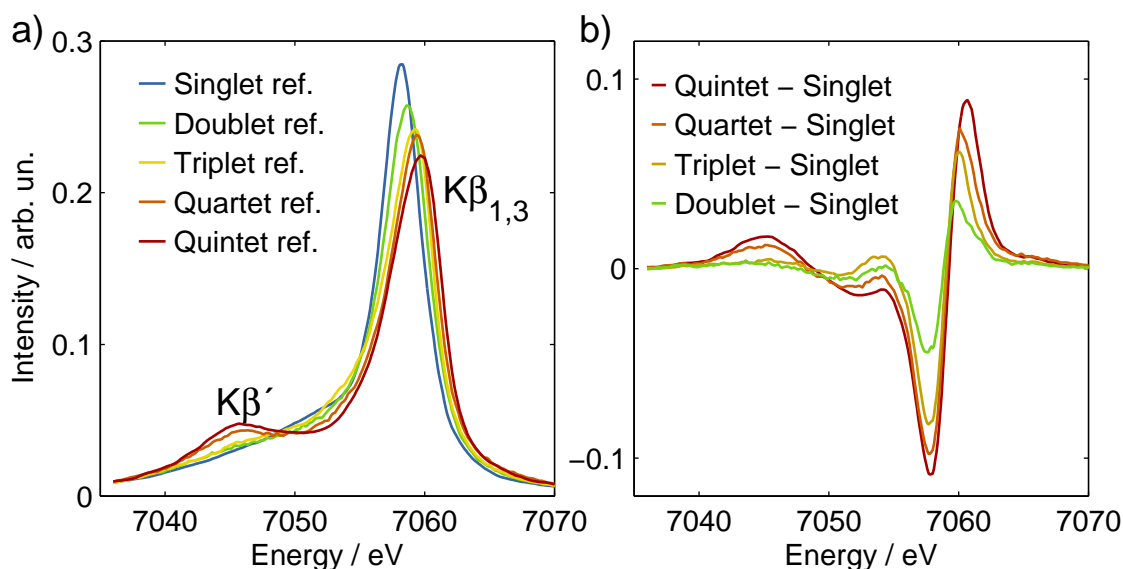


Figure 3.9: a) Iron $K\beta$ XES of singlet, doublet, triplet, quartet and quintet references and b) quintet-singlet, quartet-singlet, triplet-singlet and doublet-singlet differences of $K\beta$ XES (all data taken from [39]).

3.4.3 3d Transition Metal Complexes - Valence-to-Core X-ray Emission Spectroscopy

The vtc XES resulting from the $3d \rightarrow 1s$ transition is the weakest K-shell emission line and is split into the lines $K\beta''$ and $K\beta_{2,5}$. In the case of Fe centered complexes, the vtc line is about 500 times weaker than the $K\alpha$ line (Fig. 3.8). While the difference in the vtc between the LS and HS Fe(II) seems to be merely a decrease in intensity, vtc XES of TM complexes has been shown to be quite ligand sensitive [121, 122] in a sense that vtc XES allows determining the ligation state in a complex. Depending upon the atomic species in the first coordination shell around the TM center the vtc XES line may mark distinct spectral features. Example measurements have shown that the Cr $K\beta''$ line contains distinct peaks at different energies depending on ligation of C, N or O [123]. Another study of Fe $K\beta_{2,5}$ line for different Fe-carbonyl and Fe-hydrocarbon complexes revealed not only distinct features for the Fe-hydrocarbon and Fe-CO bond but was also able to distinguish different types of Fe-carbonyl complexes [124]. Thus while the $K\alpha$ and $K\beta$ main lines are mainly restricted to determining the spin state, vtc XES can be used to determine ligation state and thus complement the structural information from XAS.

3.4.4 5d Transition Metal Complexes - $L\alpha$ X-ray Emission Spectroscopy

The main fluorescence decay channel of 5d transition metals, after creation of a $2p_{3/2}$ hole (L_3 -edge absorption), is the $L\alpha$ XES, which corresponds to the $3d \rightarrow 2p_{3/2}$ transition. Due to spin-orbit coupling the $3d$ orbitals split into $3d_{3/2}$ and $3d_{5/2}$, which results in a splitting of the $L\alpha$ line into $L\alpha_1$ for $3d_{5/2} \rightarrow 2p_{3/2}$ and $L\alpha_2$ for $3d_{3/2} \rightarrow 2p_{3/2}$. To the best of our knowledge, $L\alpha$ XES of 5d TM complexes has to date not been applied as a chemically sensitive probe.

3.4.5 Time-resolved X-ray Emission Spectroscopy

In TR XES, the XE intensity of the sample I_{ON} with and I_{OFF} without laser excitation is measured. The difference corresponds then, analogously to the measurement of TR XAS, to the transient difference I_{trans} of the intensities I_{ES} and I_{GS} of the XES lines of the sample in its excited and ground state, respectively, weighted by the excited state fraction f ,

$$I_{\text{trans}} = I_{\text{ES}} - I_{\text{GS}} = \frac{1}{f}(I_{\text{ON}} - I_{\text{OFF}}). \quad (3.31)$$

As $I_{\text{GS}} = I_{\text{OFF}}$, the equation above can be used to determine the XES lineshape of the excited state, if f is known, or vice versa.

Similar to XAS, $K\alpha$ and $K\beta$ XES have been implemented in a TR fashion at both synchrotrons [26, 27] and XFEL sources [39]. It has been shown to be extremely helpful as a complementary tool to determine the spin state of molecules and/or the fraction of excited state of the molecule [25, 28, 40] or to show the integrity of a sample [125]. Just recently, TR XES experiments have been extended to vtc XES [126].

3.5 X-ray Emission Measurement Techniques

X-ray emission in the hard X-ray regime (here 5 keV - 10 keV) can be measured with high (~ 1 eV) resolution by energetically dispersing the X-ray fluorescence using the Bragg reflection of perfect crystals. Bragg's law describes the angle θ of the m -th order of the reflection of a photon with wavelength λ by a crystal with lattice spacing d [75],

$$m\lambda = 2d \sin(\theta). \quad (3.32)$$

A series of example combinations of X-ray emission lines and possible crystal reflections is shown in Table 3.1.

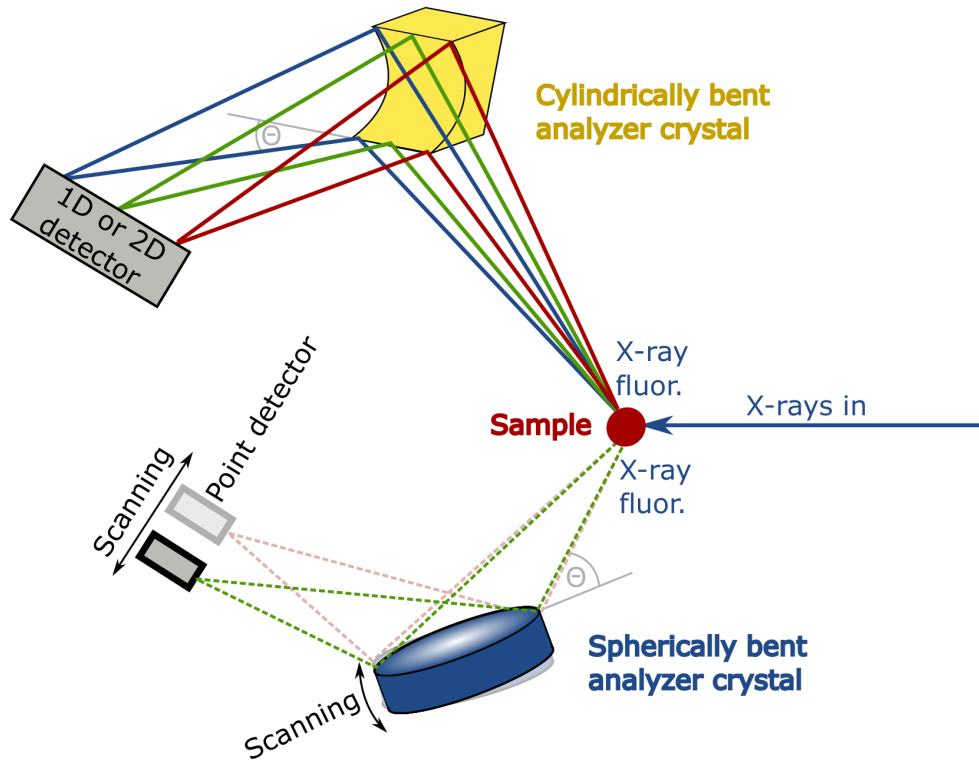


Figure 3.10: Comparison between dispersive X-ray emission spectrometer with cylindrically bent analyzer crystal (von Hamos geometry) and scanning X-ray emission spectrometer with spherically bent analyzer crystal (Johann or Johansson geometry) [121].

The X-ray emission spectra in this thesis have been measured with two different X-ray emission spectrometer geometries both applying Bragg reflection of crystals to energetically disperse the X-ray fluorescence of the sample: i) dispersive von Hamos [127] spectrometers and ii) scanning high-resolution spectrometers in Johann [128] or Johansson [129] geometry. In Fig. 3.10 a comparison between the two geometries is shown.

In the dispersive von Hamos geometry a cylindrically bent analyzer crystal is used to focus

the dispersed X-ray photons in the plane perpendicular to the dispersive axis of the spectrometer, leading to a re-imaging of a line spectrum via a 2f-2f geometry onto a position sensitive detector. This setup allows recording the full spectrum without any scanning of motors. To increase the resolution of such a spectrometer, the crystals can be segmented instead of bent, which results in an increased resolution allowing for smaller bending radii and thus more compact spectrometers [130]. To increase the solid angle, multi-crystal solutions have been implemented [131].

In the scanning geometry, spherically bent analyzer [128] crystals which can be additionally ground [129] are used to focus the energetically dispersed emission spectra onto a 0D detector. As in this geometry, the Bragg condition is only fulfilled for one single wavelength, the Bragg angle of the analyzer crystal as well as the 0D detector have to be moved from energy point to energy point in order to collect full emission spectra.

Table 3.1: List of X-ray emission line / analyzer crystal reflection combinations used in this thesis. The values of the lattice spacings d for the different crystal reflections are taken from Ref. [132].

XES line	X-ray energy	X-ray wavelength λ	Crystal reflection	Lattice spacing d	Bragg angle θ
Fe $K\alpha_2$	6390 eV	1.940 Å	Ge(440)	1.00020 Å	75.51°
Fe $K\alpha_1$	6404 eV	1.936 Å	Ge(440)	1.00020 Å	75.42°
Fe $K\beta$	7058 eV	1.757 Å	Si(531)	0.9183 Å	73.08°
Fe vtc	7110 eV	1.744 Å	Si(531)	0.9183 Å	71.76°
Fe $K\beta$	7058 eV	1.757 Å	Ge(440)	1.00020 Å	61.42°
Fe vtc	7110 eV	1.744 Å	Ge(440)	1.00020 Å	60.66°
Fe $K\beta$	7058 eV	1.757 Å	Si(220)	1.92013 Å	27.22°
Fe vtc	7110 eV	1.744 Å	Si(220)	1.92013 Å	27.01°
Ir $L\alpha_2$	9100 eV	1.362 Å	Ge(800)	0.70725 Å	74.35°
Ir $L\alpha_1$	9175 eV	1.351 Å	Ge(800)	0.70725 Å	72.81°

3.6 Advanced X-ray Spectroscopies: RXES, HERFD

In this chapter we will discuss more advanced X-ray spectroscopies, namely resonant X-ray emission (RXES) and high-energy resolution fluorescence detection (HERFD) XAS. These techniques combine aspects of XAS and XES.

3.6.1 Resonant X-ray Emission Spectroscopy

In resonant X-ray emission spectroscopy (RXES), often referred to as inelastic X-ray scattering (RIXS), the emitted fluorescence and (in)elastically scattered X-rays are measured energy resolved while scanning the incident X-ray energy. This results in 2D intensity maps. The $2p_{1/2} - 5d$ and $2p_{3/2} - 5d$ RXES plane containing the L_3 -edge absorption spectrum and the resonant $L\alpha$ emission spectrum of $[\text{Ir}(\text{ppy})_2(\text{bpy})]\text{PF}_6$ powder can be found in Fig. 3.11. We refrain from explaining RXES in detail and refer the reader to journals [119, 120, 133] or a more detailed description about resonant X-ray emission/scattering processes [134]. Here we only use the RXES plane to visualize the high-energy resolution fluorescence detection XAS technique.

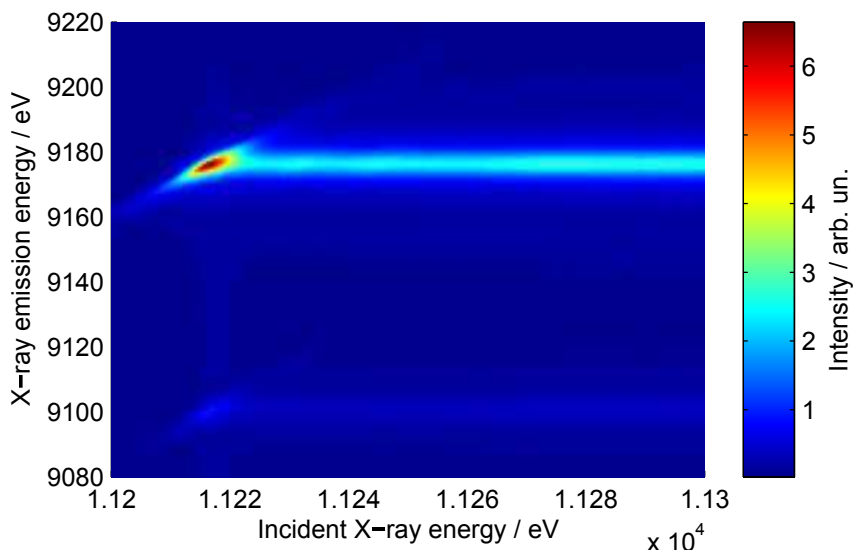


Figure 3.11: RXES plane of $[\text{Ir}(\text{ppy})_2(\text{bpy})]\text{PF}_6$ powder. The spectrum suffers from self-absorption due to the thickness of the powder sample, this only affects (=decreases) the peak intensities but still helps to understand the general shape of the $2p_{1/2} - 5d$ and $2p_{3/2} - 5d$ RXES plane of $[\text{Ir}(\text{ppy})_2(\text{bpy})]\text{PF}_6$.

3.6.2 High-Energy Resolution Fluorescence Detection XAS

In high-energy resolution fluorescence detection (HERFD) XAS, XANES and EXAFS spectra are measured by scanning the incident X-ray energy and measuring the absorbed

intensity with an X-ray emission spectrometer and fixing the detected energy to a selected value, i.e. the maximum intensity of an X-ray emission line. In the RXES plane shown in Fig. 3.11 this corresponds to a horizontal line-out. Hämäläinen *et al.* have shown in [135] that this can facilitate measuring X-ray absorption spectra with a resolution better than the core-hole lifetime broadening. The technique has been used to (at least partially) remove the rather large lifetime broadening in 5d TM L-edges of Au [136] or Pt [137, 138].

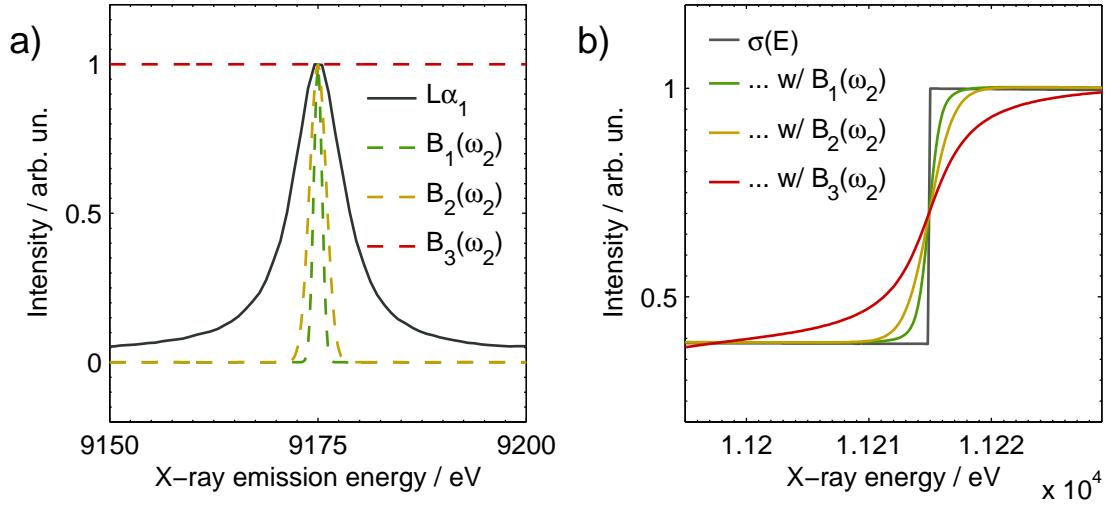


Figure 3.12: a) Ir $L\alpha_1$ XES line (grey solid line), Gaussian shaped analyzer bandwidth functions $B(\omega_2)$ with 1.18 eV FWHM (green dashed line) and 2.35 eV FWHM (yellow dashed line) representing X-ray emission spectrometers with the respective energy resolution to measure HERFD XAS and for comparison constant $B(\omega_2) = 1$ representing a conventional TFY measurement. b) Literature [77] absorption cross section of Ir (grey solid line) and calculated measured X-ray fluorescence intensity at the Ir L_3 edge according (Eq. 3.33) with the analyzer bandwidth examples from a).

The essence to understand HERFD XAS will be presented as in [135]. First, we assume that the bandwidth of the incident X-ray energy is much smaller than the lifetime broadenings Γ_L and Γ_M of the of the L- and M- shells, and can thus be neglected. The fluorescence ω_2 is detected with an energy resolving detector (e.g. an X-ray emission spectrometer) with bandwidth $B(\omega_2)$ while scanning the incident X-ray energy ω_1 over the absorption edge. The X-ray absorption cross section measured in HERFD is given by [135]

$$\begin{aligned} \sigma(\omega_1) = & \left(\frac{\Gamma_{L,R}}{\Gamma_L} \right) \int_0^\infty d(\hbar\omega_2) \int_0^\infty d\epsilon B(\omega_2) \left(\frac{\omega_2}{\omega_1} \right) \\ & \times \frac{(E_M - E_L + \hbar\omega_1 - \hbar\omega_2)}{E_M - E_L} \frac{\Gamma_L/2\pi}{(\hbar\omega_1 + E_L - \epsilon)^2 + \Gamma_L^2/4} \\ & \times \frac{\Gamma_M/2\pi}{(\hbar\omega_1 + E_M - \hbar\omega_2 - \epsilon)^2 + \Gamma_M^2/4} \sigma_L(-E_L + \epsilon). \end{aligned} \quad (3.33)$$

Here ϵ is the photoelectron kinetic energy, E_L and E_M the L- and M- shell binding energies and $\sigma(-E_L + \epsilon)$ the X-ray absorption cross section of the L-shell.

In Fig. 3.12a) the $L\alpha$ XES of Ir, together with three different bandwidth functions $B(\omega_2)$, is shown: Two Gaussian shaped bandwidths $B_1(\omega_2)$ and $B_2(\omega_2)$ with 1.18 eV FWHM and 2.35 eV FWHM are used to simulate the X-ray emission spectrometer with the respective resolution and, for comparison, a constant $B_3(\omega_2) = 1$ is used to mimic a TFY measurement with a core-hole lifetime broadening of 5.25 eV. These lineshapes have been used to simulate the expected broadening of a sharp absorption edge, i.e. a step function. The result can be found in Fig. 3.12b).

3.7 X-ray Sources: From Synchrotrons to XFELs

Time-resolved hard X-ray spectroscopy poses a set of key requirements to the X-ray probe sources: i) The X-rays have to be pulsed and the pulse duration of the X-rays (as well as that of the pump laser) limits the accessible timescales of the investigated photophysical and photochemical reactions. In general, the timescales we are interested in are defined by the relevant chemical reaction timescale and start in the femtosecond regime and extend to beyond nano- and microseconds. A detailed description of the photochemical and photophysical processes with their respective timescales can be found in chapter 2. ii) The photon flux has to be large enough to obtain sufficient S/N. For this, the number of accumulated incident X-ray photons (as a function of the sample concentration) for the example of solvated iron complexes has been estimated in Section 3.3.3. iii) Measuring XAS in TFY mode or applying advanced X-ray spectroscopies such as HERFD XAS or RXES in the hard X-ray regime requires a monochromatic X-ray source with tunable X-ray energies larger than the electron binding energies of the X-ray absorption edges of interest. The energy resolution should be at least on the order of the core-hole lifetime broadenings of these X-ray absorption edges, i.e. in the case of the 3d TM K-edges typically ~ 1 eV [139].

When we evaluate these key requirements for the two types of sources used in this thesis they differ (to date) mainly in the X-ray pulse duration and thus the accessible timescales: ~ 100 ps at Synchrotrons and ~ 100 fs at XFELs. Here, the two types of sources will be introduced in brief.

3.7.1 Synchrotrons

Synchrotrons [140] consist of storage rings filled with bunches of electrons (or positrons) which are kept at constant energies on the order of GeVs. X-rays are generated, when the electrons are deflected (=accelerated) in magnetic fields, and three main types of magnetic structures acting as X-ray sources exist: Bending magnets, wigglers and undulators. Here we focus on undulators, for a general description of all three types of sources and their properties see e.g. [78].

Undulators are (typically 1-5 m long) arrays of periodically poled magnetic structures,

which force electrons passing through them onto a zigzag trajectory. The relativistic electrons on this trajectory emit radiation in a confined cone with opening angle $1/(\gamma\sqrt{N_u})$, where γ is the Lorentz factor and N_u the number of periods of the undulator [78]. The emission of radiation occurs at many different points along this trajectory, but only the radiation with the wavelength fulfilling the resonance condition [141, 142]

$$\lambda_n = \frac{\lambda_u}{2n\gamma^2} \left(1 + \frac{K^2}{2} \right), \quad \text{with} \quad K = \frac{eB_u\lambda_u}{2\pi m_e c}, \quad (3.34)$$

interferes constructively. Here $n = 1, 2, 3, \dots$ is the harmonic order, λ_u the undulator period, K the undulator parameter, e and m_e the charge and mass of an electron, B_u the peak magnetic field amplitude of the undulator and c the speed of light. Thus the spectrum of the undulator radiation consists of narrow lines of harmonics n and the bandwidth of each harmonic is given by $\Delta\lambda/\lambda = 1/(nN_u)$ [78]. The typical number of undulator periods is on the order of 100, resulting in a bandwidth $\Delta\lambda/\lambda \approx 10^{-2}$. The relativistic correction factor $2\gamma^2$ consists of a factor γ due to the longitudinal Lorentz contraction of the undulator in the electron reference frame [143] and a factor of 2γ due to the longitudinal Doppler effect of the emitted wave seen in the laboratory reference frame [143]. Thus these relativistic effects allow an undulator with a period on the order of 1 mm to produce photons in the hard X-ray regime (i.e. with wavelengths $< \text{nm}$) and it becomes clear that producing hard X-rays requires electrons at high (relativistic) energy.

As the bunched electrons passing through the undulator do not possess a fixed phase relation (or in other words: as they are randomly distributed within the electron bunch [141]), the total emitted power P_e of the radiation adds up incoherently, thus the total power scales linearly with the number of electrons in the bunch: $P_{e,i} \propto N_e$ [142]. All interference terms between two different electrons cancel out due to the random phase relation of electrons.

However, this allows us to compare the different Synchrotrons, i.e. the photon flux they can deliver, via the total number of electrons passing through their undulators. We have compiled Table 3.2 comparing a selection of the large Synchrotrons in terms of the useful number of electrons (i.e. the useful flux) for TR experiments, which is given by the number of electrons in each bunch multiplied by the repetition rate of the useful X-ray bunches¹ (as already been published in [33]). The table ranks PETRA III, APS, ESRF and Soleil (in its 8-bunch mode operation) well above the other synchrotrons. We refrained from including more exotic patterns permitting higher time resolution, e.g., low alpha mode at BESSY-II and ANKA [144, 145] the use of X-ray streak cameras, and sliced femtosecond X-rays generated at ALS [146], BESSY-II [147], and SLS [34], since these deliver X-ray fluxes orders of magnitude lower than considered in the present work with MHz repetition rates.

¹Useful here means we can synchronize an optical pump laser to this repetition rate and the repetition rate is smaller than the inverse of the risetime of the detector, e.g. an APD for TFY XAS measurements

The total X-ray flux available at the sample position of each individual beamline is further affected by additional parameters, such as the utilized undulator or the transmission through different optical components of the beamline (e.g. mirrors, monochromators, lenses, windows, diagnostic tools). Monochromatic (~ 1 eV resolution) X-ray beams with photon fluxes $\sim 10^7$ photons/pulse can be generated at large Synchrotrons such as PETRA III or APS [33]. Few synchrotrons offer beamlines with polychromatic X-ray pulses (in a so-called pink beam mode) exceeding 10^{10} photons/pulse but a lower (1 kHz) repetition rate, e.g. beamline ID09 at the ESRF [148] or BioCARS at the APS [149].

Another limitation of Synchrotrons, next to the lack of a fixed phase relation of the electrons emitting X-rays, are the relatively long electron bunches on the order 100 ps, which lead to ~ 100 ps long X-ray pulses, restricting the temporal resolution in time resolved experiments to this duration.

A large number of Synchrotrons are available worldwide, for a comprehensive overview see e.g. Ref. [150].

3.7.2 X-ray Free Electron Lasers (XFELs)

In X-ray free electron lasers (XFELs), electrons are also accelerated to relativistic energies ($> \text{GeV}$) in linear accelerators. Instead of being stored (as in Synchrotrons) the electrons are used only once to generate X-rays in very long undulators and are dumped afterwards. The length of the undulators is typically $\sim 100\text{-}200$ m, thus about 100-fold longer than those implemented at Synchrotrons. The number of FELs routinely delivering hard X-radiation for user experiments is still limited to 2; LCLS [43, 159] and SACLA [157, 160]. Nevertheless, several new hard XFELs are in the process of being completed and starting operation soon, these are: SwissFEL [161], PAL XFEL [162] and European XFEL [141]. XFELs, as a next (4th) generation of Synchrotron radiation source, allow for a laser-like X-ray generation via self-amplified spontaneous emission (SASE), which will be phenomenologically explained here (following Refs. [141, 142, 163, 164]).

As has been mentioned in the previous section, a fixed phase relation between the electrons emitting X-rays is required for the electrons to collectively and thus coherently radiate at the undulator resonance wavelength in Equation 3.34. To fulfill this requirement, the electrons have to be "microbunched" in bunches separated by λ_u [142]. Externally modulating the electron filling pattern within a bunch appears difficult, but luckily this happens by itself as follows: When the electrons enter the undulator they start to wiggle in the periodically poled magnetic field which leads to first (=spontaneous) emission of radiation, with the electric field vector pointing along the undulator axis. This electric field has a small component in the direction of the electron movement (on the zigzag curve), which accelerates the electrons if they are in the first half-cycle in front of the maximum of the electric peak amplitude, and decelerates those electrons in the half-cycle after the maximum of the field amplitude [141]. Thus all electrons are accelerated towards the minimum of the field amplitude, where the microbunches are formed. During the process of the microbunching,

Table 3.2: Upper panel: overview of the electron bunch filling patterns at selected synchrotrons together with their corresponding single bunch charges. The product of the X-ray repetition rate f_{SR} and bunch charge Q gives a measure of the useful flux for time-resolved measurements with a laser system matching that repetition rate. For comparison the last row contains the results for a 1 kHz laser system. This table has been published in Ref. [33].

Lower panel: Repetition rates and bunch charges for the three XFELs, LCLS, SACLA and European XFEL. Here, the useful flux product has been omitted, as due the SASE process, the number of electrons are not proportional to the generated number of X-ray photons.

Synchrotron/filling pattern	Repetition rate f_{SR}	Stored charge Q per bunch $/10^{10}e^-$	$f_{SR} \times Q$ (\sim useful flux) $/10^{16}e^-/s$
PETRA III /40 bunch [151]	5.204 MHz	12	62.4
PETRA III /60 bunch [151]	7.8 MHz	8	62.4
APS /24-bunch [152]	6.5 MHz	9.8	63.7
APS /hybrid [152]	0.272 MHz	37	10.1
ESRF /4-bunch [153]	1.42 MHz	17.6	25.0
ESRF /16-bunch [153]	5.68 MHz	9.9	56.2
ESRF /hybrid [153]	0.355 MHz	7.0	2.5
Soleil /8-bunch [154]	6.776 MHz	7.36	49.9
Soleil /hybrid [154]	0.847 MHz	3.68	3.1
ALS /2-bunch [155]	3.05 MHz	7.1	21.3
ALS /hybrid[155]	1.52 MHz	2.4	3.6
KEK	0.794 MHz	3.9	3.1
SLS/hybrid [30, 156]	1.04 MHz	1.2	1.2
SLS/kHz [30, 156]	1 kHz	1.2	0.0012
<hr/> XFEL <hr/>			
LCLS [43]	120 Hz	0.6 ^a	
SACLA [157]	30 Hz ^b	0.12-0.18	
European XFEL [158]	10 Hz/4.5 MHz ^c	0.6	

^adesign value

^bforeseen to be increased to 60 Hz

^cThe bunch pattern at European XFEL consists of bursts with 2700 X-ray pulses with a repetition rate of 4.5 MHz within the bunch. The bunch repetition rate is 10 Hz.

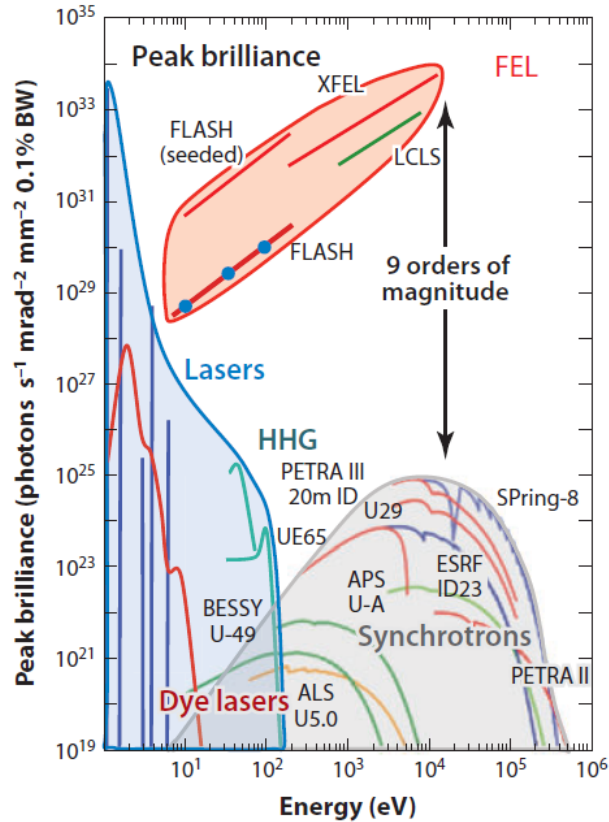


Figure 3.13: Peak brilliance of FELs compared to synchrotrons and lasers (Figure taken with permission from [165], copyright © 2012, Annual Reviews).

while the electron bunch travels along the undulator, the power increases exponentially. Once saturation is reached and all electrons are microbunched, they all radiate coherently leading to a total irradiated power of X-rays which scales with $P_{e,c} \propto N_e^2$ [142, 164].

For comparison, we have added the LCLS, SACLA and European XFEL to Table 3.2, neglecting the parameter of the useful flux, as the linear relationship between between total number of useful electrons with the capability to generate X-rays is only valid for spontaneous undulator radiation and not for the SASE process. Although the electron bunch charges of XFELs are up to two orders of magnitude smaller than those of synchrotrons, they are capable of producing two orders of magnitude larger photon fluxes of $> 10^{12}$ per pulse [141, 165].

High electron peak currents are required to facilitate the interaction between the electrons and the field they irradiated, which after all leads to the microbunching. These high peak currents are achieved by compressing the electron bunches in magnetic chicanes to ~ 100 fs. [141] The additional advantage of the short electron bunches are the short X-ray pulses they generate, with pulse durations < 100 fs.

A well established characteristic to compare synchrotron radiation sources is the peak brilliance defined as

$$\text{peak brilliance} = \frac{\text{number of photons}}{\text{source size} \times \text{beam divergence} \times 0.1\% \text{ band width} \times \text{pulse duration}}$$

A plot comparing the peak brilliance of Synchrotrons, XFELs (and also optical lasers), is shown in Fig. 3.13. XFELs deliver X-ray pulses with peak brilliances 9 orders of magnitude higher than those of synchrotrons. Optical lasers have already been able to reach comparable peak brilliances, but at photon energies in the single eV range, thus several orders of magnitude below X-rays.

Comparing synchrotrons and XFELs we find that the advantages of synchrotrons are the high pulse-to-pulse spectral and intensity stability of the X-rays, while the pulse-to-pulse fluctuations of XFELs are extremely large, requiring at least single pulse I_0 normalization. Even single pulse spectral monitoring would be beneficial. Furthermore, the regenerative use of electrons in a synchrotron storage ring allows for large numbers of simultaneously operating beamlines in a single storage ring facility, making it a "cheaper" X-ray source compared to XFELs. The key advances of XFELs over synchrotrons are the three orders of magnitude shorter pulse duration and the \sim two orders of magnitude larger number of available photons per pulse.

The third main difference in the photon beam characteristics, which we do not exploit for our class of experiments, but should also be mentioned here, is the coherence of XFEL radiation.

3.8 Experimental Setups for Combined Time-resolved X-ray Absorption and Emission Spectroscopy and X-ray Diffuse Scattering

First attempts to combine different X-ray spectroscopies with scattering in a single experimental setup have been made in our group and setups at both synchrotrons [25, 28] and XFELs [40, 41] have been developed. One of the aims of this thesis was to continue establishing experimental setups in which XAS, XES and XDS are measured quasi simultaneously in a single setup. The advantage of such setups are numerous: The information obtained from different techniques can be used in a complementary way and facilitate an unambiguous analysis and interpretation of the data. Furthermore, obtaining simultaneously as much information as possible is important especially at XFELs, where beamtime is extremely scarce and expensive. Last but not least, combining all three techniques allows to map out the time-resolved inter-molecular changes in structure, spin- and electronic state via XAS and XES as well as the intramolecular interaction such as the changes in the solvation environment of the molecule via XDS. Although the data presented in this thesis consists mainly of XAS and XES, the concept of combining all these techniques will

be presented here. The three experimental setups, at PETRA III/P01, at APS/7ID-D and at SACLA, which have been used for the experimental work presented in this thesis, are described in detail.

3.8.1 Experimental Setup

In Fig. 3.14 the setup for combined TR XAS, XES and XDS is shown. A laser system excites the sample in a free flowing liquid jet, which contains the sample typically consisting of a solution of molecules. The X-rays generated in undulators or bending magnets (all beamlines used for the experiments in this thesis used undulators) enter the setup from the right and are monochromatized, here by a double crystal monochromator (DCM). The X-rays are focused and the incident X-ray intensity I_0 is measured before the X-rays impinge on the sample.

A 0D detector, such as a Si PIN diode, an APD or a scintillator in combination with a photomultiplier tube, is used to measure the XAS in TFY. The liquid jet is usually turned to $\sim 45^\circ$ with respect to the X-ray beam, which facilitates measuring the fluorescence from the jet at an angle of $\sim 90^\circ$. Additionally, this is used to suppress the contribution from elastic scattering, which is minimal along the X-ray polarization direction. An analyzer crystal is employed to energetically disperse the X-ray fluorescence in order to measure XES. Furthermore, a 2D detector can be used to collect the XDS patterns in forward direction.

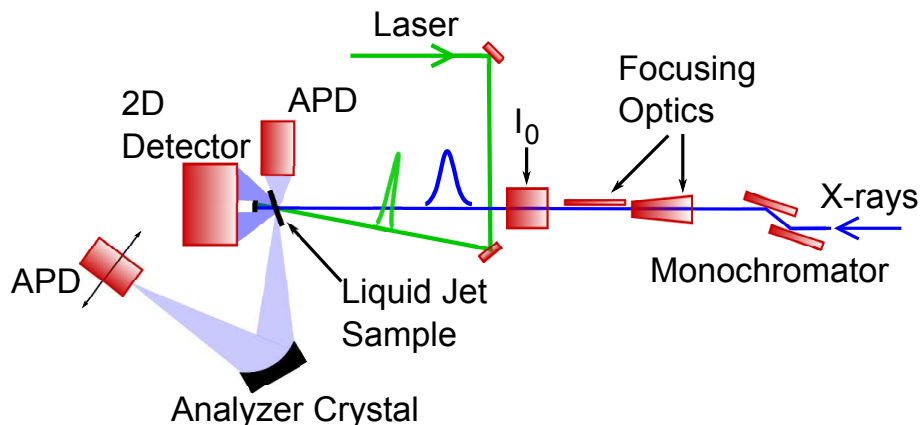


Figure 3.14: Experimental setup for combined TR XAS, XES and XDS. See text for details.

3.8.2 Synchrotrons: Beamline 7ID-D at the Advanced Photon Source

The experimental setup at the Advanced Photon Source, which has been used for the experiments presented in this thesis, is described in detail in [32] and has been applied in several experiments [25, 27–29, 126]. Here the setup will be described in brief following

the descriptions in these references.

For all measurements the 24 bunch mode of the APS with an X-ray repetition rate of 6.52 MHz, corresponding to 153 ns inter bunch spacing, and a storage ring current of 102 mA has been used. The photon flux at the Fe K-edge (7112 eV) yields typically $\sim 10^{12}$ photons/s. The X-rays are monochromatized using a diamond(111) DCM to 5×10^{-5} (almost three-fold better than a Si(111) monochromator). The X-rays are further focused to a spot size $\ll 10 \mu\text{m}$ using KB mirrors.

A MHz laser system (Duetto from time-bandwidth products) is used as the optical pump source, delivering laser pulses at an adjustable repetition rate between 54 kHz and 6.5 MHz. Often the laser repetition rate is set to a repetition rate which allows to make use of all of the 24 bunches as the probe of the laser excited sample at a certain point in time. In other words, the repetition rate is set to "run around the storage ring" with the laser excitation. To clarify this let's consider the following example: If the repetition rate of the laser is set to 1.3 MHz it takes 5 round-trips of the synchrotron until each single electron bunch has been matched with a laser excitation. The consequence of this is that not only a subset of the 24 bunches is used for the laser ON measurements (as it would be when setting the repetition rate to e.g 3.26 MHz). This synchronization scheme allows for using a slow I_0 detector and the measurement does not suffer from uneven distribution of electrons into the bunches (i.e. during top up).

The fundamental laser wavelength of 1064 nm can be frequency doubled, tripled and quadrupled to obtain 532 nm, 355 nm and 266 nm, respectively. The laser pulse duration is ~ 10 ps (FWHM) thus about an order of magnitude smaller than the X-ray pulse durations at the APS in 24 bunch mode of ~ 70 ps.

X-ray absorption is measured in TFY mode, which is ideal for dilute (Fe) samples with concentrations of below 30 mM (see section 3.3.3), and both scintillation detectors as well as APDs are available. The data acquisition scheme relies on constant fraction discriminators (CFDs) which discriminate the single photon events coming from the detector to a logic signals. These logic signals are sent to a counter, limiting the detection to a single photon per X-ray pulse. In practice, to prevent pile-up effects, the average count rate has to be kept below ~ 0.2 photons/pulse. A more detailed comparison of single photon and multi photon detection schemes is discussed in chapter 4.

To measure the XES presented in this thesis, both von Hamos dispersive and Johann scanning spectrometers have been used. The von Hamos spectrometers consist of cylindrically bent analyzer crystals with 0.25 m radius and typical crystal sizes of 10 cm, which dispersed the spectra onto a gated Pilatus 100k detector [166]. The Johann spectrometers consisted of 1 m radius spherically bent analyzer crystals with typical crystal diameters of 10 cm.

Additionally, a 2D detector is available and can be set up to collect XDS [28].

3.8.3 Synchrotrons: Dynamics Beamline P01 at PETRA III

Within the scope of this thesis, we have developed a setup to measure TR XAS at beamline P01 of PETRA III. The setup is optimized to fully exploit the high photon flux of 7×10^{13} photons/s available at the P01 beamline as well as the high repetition rate of PETRA III in 40 and 60 bunch modes of 5.2 MHz and 7.8 MHz, respectively. This setup consists of two key components: a synchronized (and repetition rate tunable) MHz laser system and a multi-photon counting data acquisition scheme with single photon sensitivity. The setup is described in detail in 4. Recently, a 16-crystal von Hamos dispersive XES spectrometer with 0.5 m radius, similar to the one in [131], has been added to the setup.

3.8.4 X-ray Free Electron Lasers: SACLA

For experiments with improved temporal resolution (<1 ps), the SPring-8 Angstrom Compact free-electron Laser (SACLA) in Japan has been used. Earlier studies at SACLA have applied a dispersive transmission XAS setup to study solvated Fe centered complexes [38, 167] as well as combined XDS and XES studies on a solvated Ru-Co electron donor-acceptor complex [40]. Nevertheless, the full setup combining all three techniques, XAS, XES and XDS, has been developed by us in 2014 and 2015 and applied to studies on ZnO, $\text{Fe}(\text{CN})_6$ as well as on the here presented *trans*[(cyclam) $\text{Fe}^{\text{III}}(\text{N}_3)_2$] $^+$. For a detailed description of the SACLA facility Refs. [157, 160] are available, here the experimental setup as used for collecting the experimental data of this thesis is briefly described with all relevant parameters.

SACLA is capable to produce X-ray pulses with a total energy of ~ 0.5 mJ and a bandwidth of ~ 0.5 %. At 7.1 keV this corresponds to a flux of $\sim 4 \times 10^{11}$ photons/pulse and a bandwidth of 35 eV. For XES and XDS experiments usually the pink beam with the full 0.5 % bandwidth and 0.5 mJ X-ray pulse energy is used to benefit from the high total flux per pulse in the full spectrum. For XAS experiments a four-bounce channel cut Si(111) monochromator has been applied to monochromatize the X-rays to a level of $\sim 1.4 \times 10^{-4}$, which reduces the X-ray flux on the sample by almost two orders of magnitude. Although SACLA is in principle designed to operate at a repetition rate of 60 Hz, during the experiments described in this thesis SACLA has been operated only at 30 Hz. The X-ray beam can be micro-focused to achieve <10 μm spotsizes at the sample position.

A Ti:Sa system with fundamental wavelength of 800 nm is used as an optical pump laser. To produce light with wavelengths in the visible or UV, this 800 nm can be frequency doubled or tripled. Alternatively, an optical parametric amplifier (OPA) [168] can be used to generate other wavelengths in the IR which are subsequently frequency doubled, tripled or quadrupled to obtain excitation wavelengths tunable over a large part of the optical and near-UV spectral range. In the experiments described in this thesis, the wavelength 266 nm and 355 nm are used to excite the sample. 266 nm radiation is obtained from third harmonic generation of the fundamental 800 nm. To generate 355 nm light, the 800

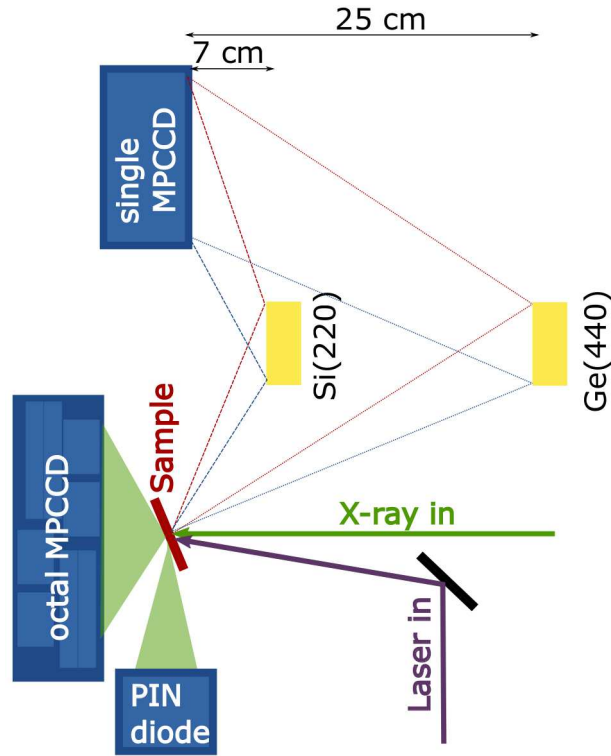


Figure 3.15: Experimental setup at SACLA. See text for details.

nm are converted to 1420 nm in the OPA and the 1420 nm are subsequently frequency-quadrupled to 355 nm.

The setup which we have implemented is shown in Fig. 3.15 and is very similar to our aforementioned setups at the synchrotrons PETRA III and APS. The sample consisted of a solution pumped through a 100 μm thick sapphire nozzles. X-ray absorption is measured in TFY using Si PIN diodes. To measure XES, we have implemented von Hamos spectrometers with 0.07 m and 0.25 m radii. The energetically dispersed XE spectra are measured with single tile MPCCD detectors (i.e. with one detector tile of 1024×512 pixels with $50 \times 50 \mu\text{m}^2$ pixels size [169]). Furthermore, octal (8 tiles) MPCCD detectors are used to collect diffuse scattering patterns in forward direction.

4 Time-resolved X-ray Absorption Spectroscopy at PETRA III

In this chapter the implementation of a setup for time-resolved X-ray absorption spectroscopy at the P01 beamline of PETRA III is presented. The setup combines a synchronized MHz fiber amplifier laser system with a multi-MHz data acquisition scheme capable of detecting multi-photon events in a single X-ray pulse. This system is optimized to fully exploit both the high-repetition rate and the high photon flux per pulse of PETRA III in 40- and 60-bunch modes. Thus it permits recording time-resolved X-ray absorption spectra with quasi static signal quality. This chapter has already been published in Ref. [33] and has only been slightly modified from the original publication.

4.1 Introduction

Time-resolved (TR) XRD [146, 148, 170–172], XDS [173] and XAS [19, 25, 69, 85, 156] experiments have been quite successful on solvated chromophores in liquids by using free-flowing flat sheets (with typical thicknesses in the 0.1-0.5 mm range) intersected by the X-ray probe beam (with typically 0.1-0.3 mm X-ray beam diameters). Optical lasers providing sufficient pulse energies to excite a significant fraction of reactant molecules (typical concentrations in the 0.01-0.1 M range), over a typical sample volume governed by the X-ray probe beam size (on the order of nL), required laser pulse energies right below the milli-Joule range [16], e.g. as routinely delivered by amplified titanium-sapphire (Ti:Sa) laser systems at 1-10 kHz repetition rates. Synchrotrons generate X-ray pulses at much higher repetition rates (on the order of several MHz, see Table 3.2), causing a mismatch of more than 3 orders of magnitude in repetition rate between laser excitation and X-ray probe sources. In such a kHz pump-probe scheme one needs to secure synchronization between the laser and X-ray sources [30], but also establish appropriate gating schemes to record those few selected X-ray pulses, and both mechanical [148] and electronic [30, 156] solutions have been realized at 1 kHz repetition rate. The recorded X-ray data thus suffers dramatically in signal quality, as compared to steady-state X-ray studies using the full (or thousand-fold larger) X-ray flux available, and this penalty results in excessive collection times (on the order of several hours) needed for moderate signal-to-noise ratios (S/N) [26, 156]. In a pioneering early attempt Stern *et al.* used a 272 kHz Ti:Sa laser system synchronized to the APS storage ring to drive solid-amorphous phase transitions in Ge samples, which were probed via extended X-ray absorption fine structure spectroscopy

(EXAFS) with sub-nanosecond time resolution [174]. Their laser system delivered 4 μJ at 800 nm, which was sufficient to excite the solid Ge film. For chemical dynamics applications, one would need to reduce the illuminated spot size to well below 50 μm diameter and increase the fundamental laser pulse energy to higher values, since for most photochemical reactions the optical pump wavelength lies in the UV-VIS range, which can be generated with nonlinear optical crystals at selected wavelengths with 10-50 % efficiency from the IR fundamental.

With the advent of ultrafast high repetition rate amplified laser systems, which deliver rather high pulse intensities in the IR (typically on the order of 10-30 μJ , and currently reaching 100-200 μJ) at variable (and adjustable) repetition rates throughout the 0.1-25 MHz range, the repetition rate mismatch to SR sources is largely overcome [31, 175–177]. Now the X-ray signal quality increases by much more than an order of magnitude for otherwise equal data collection times. Such MHz optical laser pump - X-ray probe experiments can now deliver S/N values matching those of conventional static X-ray experiments. For TR experiments this leads to an unprecedented sensitivity in revealing accurate excited state geometrical structures [25]. Furthermore, these high repetition rates now allow extending the TR methodology into more flux-hungry techniques, such as TR non-resonant XES [26], resonant XES (resonant inelastic X-ray scattering, RIXS) [27], and possibly even towards TR X-ray Raman spectroscopy [178–183].

At MHz repetition rates one can still record the laser-excited and dark sample in rapid alternating sequence, but such a scheme requires appropriate electronic gating and recording schemes for the X-ray signal (as mechanical solutions do not exist). Fast MHz gating, recording, and sorted averaging is laboratory standard for low signal content, i.e., for single photon counting (SPC) methods. This is done using, e.g. scintillators or APDs in combination with gated constant fraction discriminators (CFD) to measure for example X-ray absorption spectroscopy [25, 32]. The successful use of SPC techniques limits the useful pulse intensity on the detector to well below one photon per X-ray pulse in order to prevent pile-up artefacts due to multiphoton events, which are counted as single photons. To exploit not only high repetition rates, but equally the large single X-ray pulse intensity available at third generation synchrotrons, we have developed a TR XAS setup at PETRA III, which permits recording X-ray intensities with suitable dynamic range using a Si-based APD, which is capable to measure intensities from well below single photons up to in principle several thousand photons per pulse (or more) [26, 30, 156]. This setup can thus be also applied at intense XFEL sources, and European XFEL will have similar repetition rates (albeit with much higher single pulse intensities) [158] as we experience today at SR sources, which underlines the need for dynamic range at MHz repetition rates.

4.2 Experimental Approach for Implementing MHz Pump-Probe Experiments in the Hard X-ray Domain at P01 Beamline of PETRA III

Time-resolved (pump-probe) measurements at synchrotron radiation sources benefit enormously, when the repetition rate of the laser system matches that of the delivered X-ray pulses. However, in practice, there are limits to how much the optical laser repetition rate can be increased, either due to the time scale of the investigated reaction, or due to conditions resulting in repeatedly striking the same sample volume, before it has been moved out of the probe volume. In the following we describe the implementation of the required instrumentation at beamline P01 at PETRA III for repetition rates from 0.13 MHz (single bunch round trip frequency) up to 7.8 MHz available in 60 bunch mode. Our data acquisition (DAQ) scheme was also applied at beamline P11 of PETRA III at 0.13 MHz probe repetition rates for experiments using a 65 kHz laser system [184], but could also operate reliably at even higher repetition rates towards the inverse pulse width of typical electrical photodiode signals (ca. 30 MHz).

4.2.1 The PETRA III SR Source for Pump-Probe Studies

The PETRA III electron storage ring has a circumference of 2304 m, its RF-accelerating cavities operate at ca. 500 MHz, generating 3840 of the so called buckets with 2 ns separation, which can each support stable storage of electron charges. In practice, only 40, 60, or 960 buckets are filled with electrons yielding bunch separations of 192 ns, 128 ns and 8 ns, respectively. The total current of the ring is kept constant at 100.5 mA within $\pm 0.5\%$ via relatively frequent (every 1-2 min) injections of electrons, in the so-called top-up operation mode. For the TR (pump-probe) measurements described in this work, only 40- and 60-bunch modes are used. In 60-bunch mode, where the X-ray pulse-repetition rate is 7.8 MHz, every other (= every second) X-ray pulse records the laser-excited sample, when the laser is tuned to half of its repetition rate. The high stability of the X-ray flux allows for accurate comparison (normalization) of the recorded intensities for the dark and laser-illuminated sample.

One issue about top-up operation of the synchrotron concerns fluctuating X-ray intensities on the sample during the injection process itself, which lasts for a few seconds. These top-up-induced fluctuations occur on a slow time scale (much slower than 1 kHz), so rapid recording of alternate intensities is not at all hampered, and transient signals (= normalized laser-on and laser-off X-ray signals) do not detect the injection process (apart from subtly larger error bars, more details below in section 4.3.4). However, each of the 60 stored electron bunches is not equally refilled in a controlled fashion, and this leads therefore to small step-wise changes in the recorded transient signal, when e.g.,

the top-up mode preferentially filled into some of e.g. the even buckets. We have previously circumvented this (though weak) issue by synchronizing the laser to a repetition rate, which is not an integer of the single bunch frequency of the storage ring (e.g., every 5th pulse at APS in 24-bunch mode) [25], which eliminates this artefact conveniently, since the laser-excited and laser-off X-ray signals are equally generated and averaged over every single pulse inside the storage ring. Another way to eliminate this artefact is to simply use a gated IO detector for single shot intensity normalization, which have been applied in this work.

4.2.2 The Dynamics Beamline P01

The experiments were performed at the Dynamics beamline, P01, of PETRA III at DESY in Hamburg [185]. This beamline is dedicated to nuclear resonant scattering measurements in experimental hutch 1 (EH1) [186], to inelastic X-ray scattering (IXS) in EH2 [187], and towards laser-driven melting of geologically relevant samples (e.g. silicate melts with a cw/ns heating laser) [182]. EH2 has recently upgraded its capabilities to permit laser-driven pump-probe experiments on solvated samples together with our adjustable 0.1-10 MHz femtosecond laser system, the latter having already passed its proof-of-principle test at ESRF [25]. The present work concerns experiments at 7.8 MHz repetition rate, thus to the best of our knowledge at the highest repetition rate ever applied for TR XAS measurements at any SR source worldwide.

A schematic of the beamline setup used in these experiments is shown in Fig. 4.1. X-ray pulses are created when electron bunches pass through two 5 m long undulators. The X-ray pulses are monochromatized to $\Delta E/E=1.4 \times 10^{-4}$ with a liquid N₂ cooled Si(111) fixed-exit double crystal monochromator (DCM). Beryllium lenses after the monochromator are used to pre-focus the beam to match the acceptance of the Kirkpatrick-Baez (KB) mirrors, which subsequently focus the beam on the sample to a size of about $15 \times 30 \mu\text{m}^2$ (V×H). The total number of monochromatic photons at the sample position is on the order of 10^{13} per second.

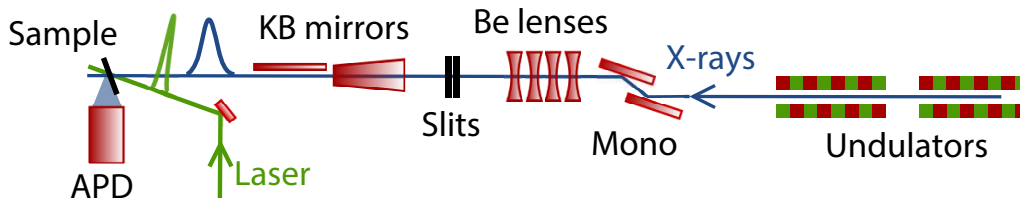


Figure 4.1: Sketch of the dynamics beamline P01 of PETRA III consisting of 2 x 5m long undulators to generate X-rays, a Si(111) double crystal monochromator, a stack of Beryllium prefocusing lenses followed by slits and KB mirrors for micro-focusing.

4.2.3 The Liquid Jet Flat Sheet Target

The experimental setup described here has been developed with the aim to investigate photoexcited solvated molecular systems, and extends our previously implemented setups [30, 156] into the MHz repetition rate range, similar to developments at other synchrotron radiation sources [31, 32]. It is based on using flat sheet liquid jets generated through rectangular shaped nozzles (Victor Kyburz AG) with selected thicknesses in the 0.1 to 0.3 mm range (and widths of about 6-8 mm). Fig. 4.2 shows a picture of the liquid jet produced by the sapphire nozzle.

We generally use the 0.1 mm thick nozzle flowing the liquid downwards at an adjustable speed in the range of 0.5 to 30 m/s with either a (specially coated, thus chemically resistant) gear pump or with a (slower) peristaltic pump with Teflon-tubing. Stable flat sheets were obtained with both pumps, but using the micro annular gear pump (mzr-11508X1, HNP Mikrosysteme) proved to operate reliably with various solvents covering a fairly broad range of viscosities. The thin film jet is usually rotated around the vertical axis to about 45° with respect to the X-ray beam direction. This permits to record XAS in TFY mode with its detector placed sideways from the sample (and/or to disperse the sideways emitted X-ray fluorescence with a secondary crystal-based bent crystal arrangement to record the X-ray emission spectra [28]).



Figure 4.2: The sapphire nozzle produces a liquid flat sheet jet of 100 μm thickness over a width of about 6 mm. The sheet flows downwards at an adjustable speed in the range of 0.5 m/s to 30 m/s (in this photo: ~ 5 m/s).

4.2.4 Multi-MHz Fiber Amplifier Laser System

The high repetition rate laser consists of a bulk oscillator (t-Pulse, Amplitude Systemes) [188], synchronized and locked to the RF of the storage ring, which seeds a high energy fiber amplifier (Tangerine 20W, Amplitude Systemes). The Yb:KYW bulk oscillator generates

a stable train of 200 fs mode-locked pulses at 62.5 MHz with an average power of 1.5 W. The laser cavity contains a set of actuators that are used to precisely lock the frequency of the laser cavity to the PETRA III RF frequency and reduce the timing jitter to less than one picosecond (the synchronization scheme is described in section 4.2.7). A small fraction of the average power is coupled into a single-mode polarization-conserving fiber and seeds the high-power fiber amplifier. Using chirped pulse amplification together with a state-of-the-art single-mode rod-type fiber (which mitigates the accumulation of non-linearities during propagation and amplification in the core of the fiber amplifier), a maximum pulse energy of 60 μJ (and 300 fs pulse width) are produced at 400 kHz. The repetition rate of the output pulses can be changed from below 400 kHz to 15.6 MHz via an acousto-optical modulator (AOM) based pulse picker situated upstream in the amplifier chain. The output power and all spatial beam parameters remain constant at all selectable repetition rates ensuring the production of 300 fs / 6 μJ pulses at 3.9 MHz and maintaining the pointing stability. The laser wavelength of 1030 nm can be converted to 515 nm, 343.3 nm and 257.5 nm by second- (SH), third- (TH) and fourth-harmonic (FH) generation crystals, respectively. The optical laser beam is then guided to and focused on the liquid jet, the losses from the amplifier output to the sample position can reach 50 %. The beam size at the position of the jet is on the order of $50 \times 50 \mu\text{m}^2$, thus slightly larger than the X-ray spot size of $15 \times 30 \mu\text{m}^2$. The conversion efficiencies which we obtained amount to $\sim 36\%$, $\sim 9.6\%$ and $\sim 4.6\%$, at 400 kHz repetition rate this leads to maximum pulse energies at the sample position of $\sim 30 \mu\text{J}$, $\sim 11 \mu\text{J}$, $\sim 2.9 \mu\text{J}$ and $\sim 1.4 \mu\text{J}$ for fundamental, SH, TH and FH, respectively. For example at 257.5 nm we can adjust the excitation intensities with this system (using a half-waveplate and a polarizer) up to $240 \text{ GW}/\text{cm}^2$.

4.2.5 Spatial and Temporal Overlap of X-ray and Laser Beams

The X-ray and laser beams are overlapped in a near-collinear geometry. The angle between both beams is as small as possible (5° - 20° , depending on setup, here we used $\sim 10^\circ$), to ensure a long longitudinal range with good overlap. Both beams are spatially overlapped using tungsten pinholes with different diameters between 25 μm and 100 μm . To achieve temporal overlap, a fast photodiode (Opto Diode Corp., Model AXUVHS5) with a 700 ps rise-time on a fast oscilloscope (LeCroy WaveRunner 640Zi with 4 GHz analog bandwidth and 20 GS/s acquisition) are used to record traces of laser and X-ray pulses. The half-rise position of each pulse and thus their time separation can be determined with an accuracy of around 100 ps. Eventually, the actual pump-probe signal is used to determine time zero accurately. Adjusting the time delay between both laser and X-ray pulses is described below in section 4.2.5.

4.2.6 X-Ray Fluorescence Detection Strategy

The total X-ray fluorescence yield (TFY) from the liquid jet is detected with an APD [189] system, consisting of an APD head combined with a fast preamplifier (APD0008, FMB Oxford) and a control/power supply unit (ACE BOX, FMB Oxford). The APD head ($10 \times 10 \text{ mm}^2$ active surface area) is placed about 20 mm away from the sample perpendicular to the X-ray propagation direction (or along the linear polarization axis of the X-ray beam), to minimize the detection of elastic scattering from the solvent. In this geometry the detector covers a solid angle of 0.25 sr (or 2 % of 4π). A second APD system can be used to measure the TFY of a lower Z material, e.g. a Mn foil (in case of Fe-containing samples), located downstream from the sample position. Although located behind the actual liquid sample, we exploit this device as a reliable indicator of the incident intensity (I_0), especially concerning the frequent intensity fluctuations due to top-up injections: The X-rays impinging on the sample (here: 20 mM of aqueous $[\text{Fe}(\text{bpy})_3]^{2+}$) penetrate through the entire length of the sample of about 0.14 mm (corresponding to the 0.1 mm thick jet rotated to 45°), and this results in an attenuation by 18 % due to the solvent alone (which is very constant at all energies used around the Fe K edge). The solute contributes to 0.1 % below and to 0.6 % above the Fe K edge (with an excited state fraction $f = 0$ for the stationary sample) and the X-ray transmission through the liquid flat sheet jet T_{jet} is given by the ratio of intensity before and after the sample via [16]

$$T_{\text{jet}} = \frac{I_1}{I_0} = \exp(-n_{\text{sol}}\sigma_{\text{sol}}d) \exp(-n_{\text{sam}}\sigma_{\text{rest}}d) \dots \quad (4.1)$$

$$\times \exp(-(1-f)n_{\text{sam}}\sigma_{\text{GS}}d) \exp(-fn_{\text{sam}}\sigma_{\text{ES}}d) \quad (4.2)$$

Here n_{sol} and n_{sam} are the solvent and sample concentrations (in particles/ mm^3), respectively, σ_{sol} , σ_{GS} , σ_{ES} and σ_{rest} are the X-ray (thus energy-dependent) absorption cross sections of the solvent and solute molecules in their ground (GS) and excited states (ES) and rest of all other elements within the solute molecule (including counterions), respectively. The laser power (given in number of laser photons per pulse $N_{ph,0}$) enters via the photoexcitation yield of the excited solute molecules via $f = f(n_{\text{sam}}, N_{ph,0}, \sigma_{\text{opt}})$, with σ_{opt} being the optical absorption cross section of the solute molecule at the selected laser wavelength (for the current estimate of sample transmission we use $f = 0$, but we include it later for the analysis of the TR signals), the incident X-ray intensity is I_0 . Thus the X-ray transmission through the sample to the second foil is 81.9 % below and 81.4 % above the Fe K-edge, and the difference between both transmission values is thus 0.7 %, which would only become distinguishable (within Poisson statistics), if the collected intensity is $\gg 10^4$ (we typically collect $\sim 10^8$ photons/s).

Finally, in this setup we record an X-ray fluorescence signal, e.g., from the Mn foil downstream of the sample, of

$$I_{Mn} = I_0 \times T_{\text{jet}} \times (1 - T_{Mn}) \times \epsilon_{Mn} \times \Sigma_{\text{det}} \times \phi_{\text{det},Mn}, \quad (4.3)$$

thus correcting the incident intensity I_0 for the transmission T_{jet} through the liquid sample, the absorption $(1 - T_{Mn})$ in the Mn foil, the X-ray emission quantum yield ϵ_{Mn} , the covered X-ray emission solid angle Σ_{det} to the detector and the detector efficiency $\phi_{(\text{det}, Mn)}$. This yields a fluorescence count rate of >50 photons under our experimental conditions with an incident flux of 10^{13} photons/s (corresponding to about 10^6 photons/pulse incident on the liquid sample). The fluorescence count rate I_{Mn} is adjusted to at least the count rate of the X-ray fluorescence signal I_{TFY} from the sample itself to ensure that normalization (to remove top up injection artefacts) does not spoil the overall error of this measurement. When measuring with less than 10^4 photons/pulse the small variation of T_{jet} (below/above the edge) does not change the count rate for I_{Mn} significantly, and can thus even serve for (rough) single shot normalization for the incident intensity I_0 . Of course, when collecting several millions of shots this deviation becomes measurable (see section 4.3.4 later), but the goal here is to normalize to the top up injection process on a shot-by-shot basis, which increase certain X-ray pulses by up to a few percent (and averages over all bunches within a round trip) to the limiting set value of 1 % top up injection).

The actual setup aims to measure TR XAS of photoexcited samples in the hard X-ray regime in TFY mode. This is done by scanning the incident X-ray energy with the primary DCM and recording the TFY with the sideways placed APD (Fig. 4.3). The number of total fluorescence photons I_{TFY} is given by the number I_{abs} of absorbed X-ray photons by the solute alone, by the total fluorescence yield ϵ_{total} , the covered solid angle Σ_{APD} and detection efficiency $\phi_{(\text{det}, I1)}$ of the APD as scaling factors via [116]

$$I_{TFY} = I_{\text{abs}} \times \epsilon_{\text{total}} \times \Sigma_{APD} \times \phi_{(\text{det}, I1)} \quad (4.4)$$

$$\text{with } I_{\text{abs}} = I_0(1 - T_{\text{jet}}) \frac{(1 - f)n_{\text{sam}}\sigma_{GS} + fn_{\text{sam}}\sigma_{ES}}{n_{\text{sol}}\sigma_{\text{sol}} + n_{\text{sam}}\sigma_{\text{rest}} + (1 - f)n_{\text{sam}}\sigma_{GS} + fn_{\text{sam}}\sigma_{ES}}. \quad (4.5)$$

To roughly estimate the fluorescence signal per X-ray pulse of a 20 mM Fe compound in aqueous solution in a 100 μm jet tilted to 45° we assume an incident X-ray flux of 10^6 photons/pulse at photon energies just above the Fe K-edge. About 5000 photons are absorbed at the Fe K-edge (thus 0.5 % of the incident ones, which can emit K radiation), which results together with the total fluorescence efficiency of Fe $\epsilon_{\text{total}} \approx \epsilon_{K\alpha} + K\beta \approx 36\%$ [76], the 0.25 sr covered by the APD and the $\sim 95\%$ detector efficiency of the APD at 6 keV [117] to an expected flux of about 35 photons/pulse.

In the case of relatively thin samples ($n_{\text{sol}}\sigma_{\text{sol}} + n_{\text{sam}}\sigma_{\text{rest}} + (1 - f)n_{\text{sam}}\sigma_{GS} + fn_{\text{sam}}\sigma_{ES} \ll 1$) the exponential term in Eq. 4.1 can be simplified and we can approximate $I_{\text{abs}} \approx I_0 dn_{\text{sam}} [(1 - f)\sigma_{GS} + f\sigma_{ES}]$ [116]. Using this, we can provide an estimate for the expected pump-probe transient signal $S = I_{(\text{TFY}, \text{ON})} - I_{(\text{TFY}, \text{OFF})} = I_{(\text{TFY})}(f) - I_{(\text{TFY})}(f = 0)$, which is given by the normalized difference of the total fluorescence yield $I_{(\text{TFY}, \text{ON})}$ with and $I_{(\text{TFY}, \text{OFF})}$ without laser excitation to

$$S = f \times (\sigma_{ES} - \sigma_{GS}) \times n_{\text{sam}} \times d \times I_0 \times \epsilon_{\text{total}} \times \Sigma_{APD} \times \phi_{(\text{det}, I1)}. \quad (4.6)$$

For the above-mentioned case the excitation yield f is typically 10 %, while the X-ray absorption cross sections for the ground and excited species typically differ by less than 100 % (in the XANES region, compared to the K edge jump), thus we obtain for the transient X-ray fluorescence signal a value of 3.5 photons/pulse (on the static 35 photons/pulse), or 10 %. When the expected pump-probe signal becomes smaller (e.g., in the EXAFS region or due to smaller differences in f), it is therefore paramount to increase the statistics significantly, which the presented experimental DAQ scheme, in combination with a MHz laser system, provides.

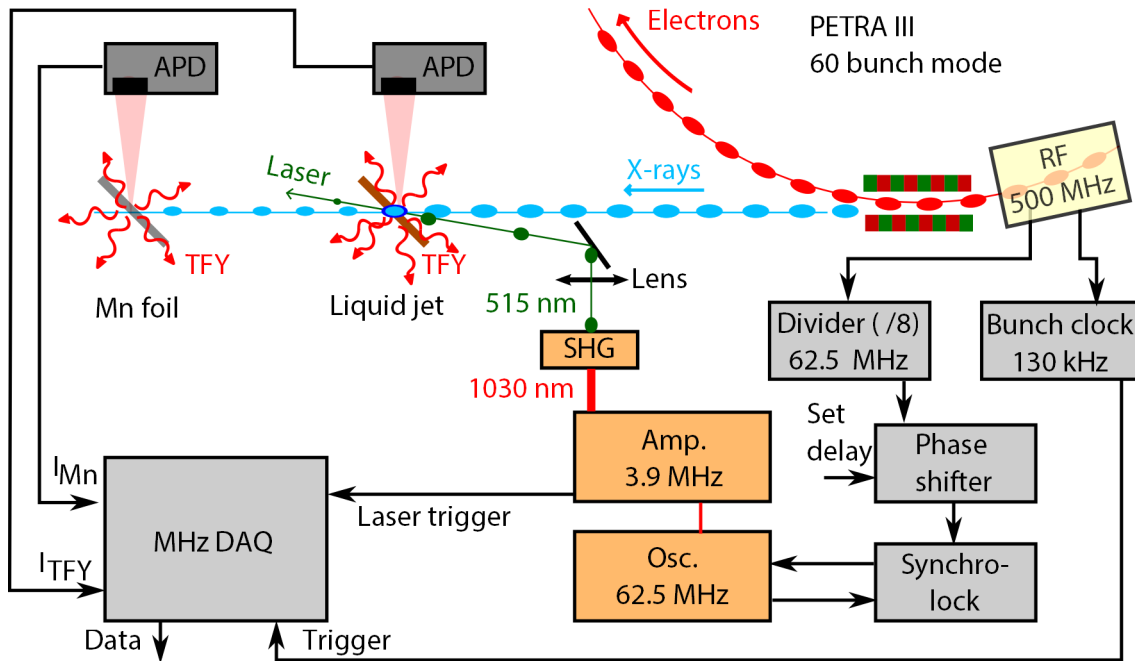


Figure 4.3: Sketch of the experimental setup at the dynamics beamline P01 of PETRA III (here: in 60 bunch mode delivering X-ray pulses at 7.8 MHz), including a fiber amplifier laser system synchronized to the RF frequency of the storage ring and our MHz DAQ system capable of digitizing and integrating the APD detector signal traces.

4.2.7 Synchronization and Data Acquisition Strategy at MHz repetition Rates

The laser system is synchronized to the storage ring in the following way (Fig 4.3): The RF signal from the storage ring (a 500 MHz sinusoidal) is converted into a 62.5 MHz trigger signal by a frequency divider (1/8). This trigger is sent over a phase shifter module before it enters a frequency mixer unit, where it is combined with the 62.5 MHz signal from the laser oscillator to derive and actively correct for any phase variations. These phase variations between both signals cause a variation of the relative timing between the laser and X-ray pulses, and are minimized in the synchronization lock unit to maintain a reliable (constant) timing between laser and X-ray pulses. This is realized with a timing jitter

much better than the laser-X-ray instrument response function which mainly consists of the X-ray pulse width of ca. 100 ps [190] (see, e.g., later Fig. 4.10). In order to change the relative timing between laser and X-ray pulses the frequency-divided (1/8) RF signal is phase-shifted using an electronic phase shifter unit, so that the signal entering the synchronization lock unit leads to an adjustment of the laser oscillator frequency (via moving one of the end mirrors in the laser cavity), so that the output laser pulses exit at a slightly shifted time, until the desired time delay has been reached. Therefore, the phase shifter unit acts as a tool to control the relative laser-X-ray time delay. This is done by coarse and fine adjustment of the optical path length in the oscillator by translating one mirror with a servo motor and the second one with a piezo actuator. A proportional-integral-derivative (PID) controller in the synchronization lock unit is used to online correct timing jitter by controlling the piezo of the one mirror. With the 62.5 MHz of the RF-signal, we calculate that a phase shift of 1° results in a time shift of the laser pulses of 44.44 ps with respect to the X-ray pulses. The phase shifter unit is connected to the data acquisition PC in order to monitor and control the time delay while acquiring data during a scan.

The X-ray TFY signal generates APD signal traces that are fed into the DAQ system (a micro TCA based solution with high speed digitizers, SP Devices). Each digitizer consists of four 12 bit analog-to-digital converter (ADC) accompanied with a Field Programmable Gate Array (FPGA, Xilinx Virtex 6) for online data processing. In its standard configuration, this ADC is able to digitize the traces of our APD detectors at a sampling rate of 2 GS/s. Alternatively, it is also possible to configure the digitizer in the so-called two-channel interleaved mode to increase the sampling rate to 4 GS/s per channel (which reduces the number of available channels to 2 per ADC). The digitizer is synchronized to a sub-harmonic of the accelerating RF to ensure stable phase relations. In addition a time-to-digital converter (TDC) firmware core has been implemented in the FPGA for precise measurement of the rising edge of the provided trigger relative to the sampling clock. The TDC implementation allows for an accuracy of about 42 ps RMS. A similar approach reported on a quadrant APD together with a commercially available ADC at an 8-fold lower sampling rate (and no TDC implementation) to measure multi-photon events at MHz repetition rates [191]. Our large sampling rate has proven to be beneficial in order to extract precise integrated signal intensities. As the maximum peak-to-peak input signal to our ADC is limited to 800 mV, the APD signal must be attenuated accordingly when signal intensities exceed this limit.

The trigger and gating scheme for DAQ with the XFEL MHz DAQ is depicted in Fig. 4.4 and works as follows: The entire detection system is triggered by the so called Bunch-clock, a device which generates trigger pulses either at the repetition rate of the X-ray pulses or at the round trip frequency of a single bunch from the 500 MHz RF signal. In our scheme, the round trip frequency of about 130 kHz is used to trigger the data acquisition, even if the laser operates at higher repetition rates, i.e. 20-fold (40 bunch) or 30-fold (60 bunch). The APD traces are sampled and processed for the duration of

the following 40 or 60 X-ray pulses (following each trigger signal at 130 kHz), depending on the bunch mode of the experiment. The sampled traces can be displayed online to select regions of interest for i) the background signal before the pulse, and ii) the X-ray pulse, respectively. An example of such a sampled single APD trace can be found in Fig. 4.5a). The following parameters are defined during operation and are applied to the system employing an integration algorithm: The starting point and total number of sampling points i) of the background/baseline and ii) of the APD signal trace (see Fig. 4.5a)). The FPGA-based algorithm calculates the sum of the pulse and background samples and scales the background sum to be correctly removed from the pulse sum resulting in the single shot detection signal I_{TFY} . A second trigger, derived from a photodiode within the MHz laser amplifier, is used to distinguish between traces i) right after laser excitation and ii) those without prior laser excitation; these are rapidly sorted into $I_{\text{TFY,ON}}$ and $I_{\text{TFY,OFF}}$ for pumped and un-pumped signals, respectively. Additionally, some parameters are calculated online as e.g. mean values of $I_{\text{TFY,ON}}$ and $I_{\text{TFY,OFF}}$ and their respective standard deviations. In the current state of the MHz DAQ we are able to acquire, integrate, baseline correct and average up $\sim 6 \times 10^6$ pulses/s in real time (neglecting $\sim 10\%$ dead time due to communication between beamline control PC and e.g., the X-ray monochromator motor controls, or the phase shifter mirror controls).

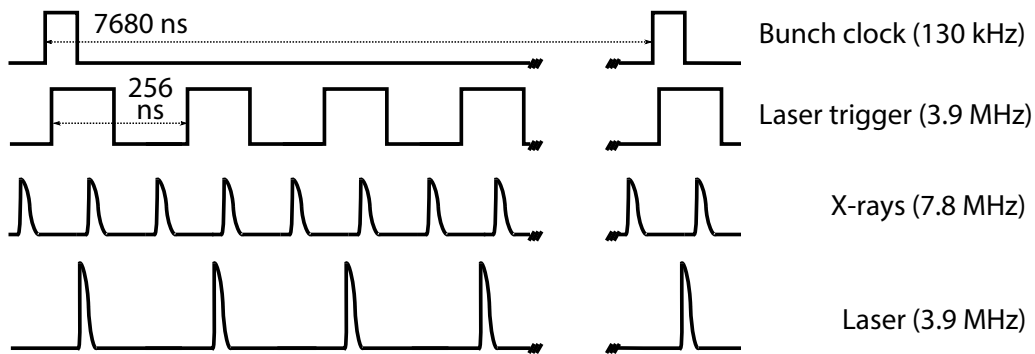


Figure 4.4: Example of the trigger and gating scheme of the MHz DAQ in 60 bunch mode of PETRA III, where the laser repetition rate is set to 3.9 MHz. In our experiments we mainly used 60 bunch mode, but 40 bunch mode is equally useful (for details see text).

4.3 Results: Signal Statistics and Time-resolved XAS Measurements

In this section, first results obtained with the above described setup are shown. These include tests of the linearity of the detector/DAQ system combination, a characterization of the detector signal statistics and benchmark TR XAS measurements of transition metal complexes with extremely high signal quality.

4.3.1 Detector Signal Statistics

To test the detector/DAQ combination we have measured the TFY from a 300 μm liquid jet containing a 50 mM aqueous solution of $\text{K}_4[\text{Fe}(\text{CN})_6]$. The total fluorescence from the iron atom consists of mainly $K\alpha$ X-ray photons around 6.40 keV and the weaker $K\beta$ emission at 7.05 keV (the ratio of fluorescence yield is $K\alpha/K\beta \approx 150/17$, so 90 % of the fluorescence mainly contains $K\alpha$ photons [76], the remaining valence-to-core emission we disregard here, since it is 500-fold times weaker than the $K\alpha$ emission [118]). We have varied the APD bias voltage from 200 V up to 350 V (right below its break-down voltage) to adjust the internal APD gain, depending on the recorded X-ray flux. For calibration purposes the upstream beamline slits have been gradually closed to attenuate the incident X-ray intensity, and the incident flux on sample was monitored with a PIN diode measuring scattered X-rays from a Kapton window downstream of the high-vacuum KB focusing mirror system (and before the sample). The recorded sample fluorescence signal for a collection of 10^5 shots with attenuated beam reveals the expected Poisson statistics for an average single pulse intensity of about 5 photons/pulse (Fig. 4.5) Being mainly of statistical nature, the signals follow a Poisson distribution,

$$P(\lambda, k) = \frac{\lambda^k \exp(-\lambda)}{k!}. \quad (4.7)$$

Hereby k corresponds to the number of photons detected in a single pulse with λ being the mean value of photons detected after a large (towards infinite) number of acquired pulses; in our case λ corresponds to the total fluorescence yield I_{TFY} extracted via Equation 4.7 after, e.g., 10^5 acquired pulses (as shown later in section 4.3.2).

In case of few photons only striking on the detector the discrete peaks representing one, two, three, etc photon events are well separated (up to ~ 10 per pulse). This already allows for a very precise calibration from the integrated signal voltage to absolute number of photons. The broadening of each peak is due to effects in the amplification process in the APD itself including avalanche gain noise and preamplifier noise, next to electronic noise, which can be best seen in the zero photon event (Fig. 4.5b)). To separate the signals belonging to each integer number of photons, a sum of Gaussian peaks has been fitted to the measured pulse height distribution (Fig. 4.5b)), and the area of each single Gaussian is proportional to the number of events for this chosen number of photons. These Gaussian areas are then normalized to a total area of 1, and a fit to a Poisson distribution (Equation 4.7) delivers the precise single pulse intensity of $I_{\text{TFY}} = 4.85$ (Fig. 4.5c)). For larger single photon intensities (thus at higher incident flux), the Poisson distribution curve (blue trace in Fig. 4.5c)) merges into a Gaussian distribution, and this already (via Equation 4.7) for single pulse intensities around/above ten. In the case of a Gaussian distribution, where a clear separation of the discrete peaks is no longer present, the mean number of photons can still be precisely determined: For a shot-noise limited measurement the standard deviation of measured average signal becomes $\sigma_P = \sqrt{\lambda}$ and we can relate

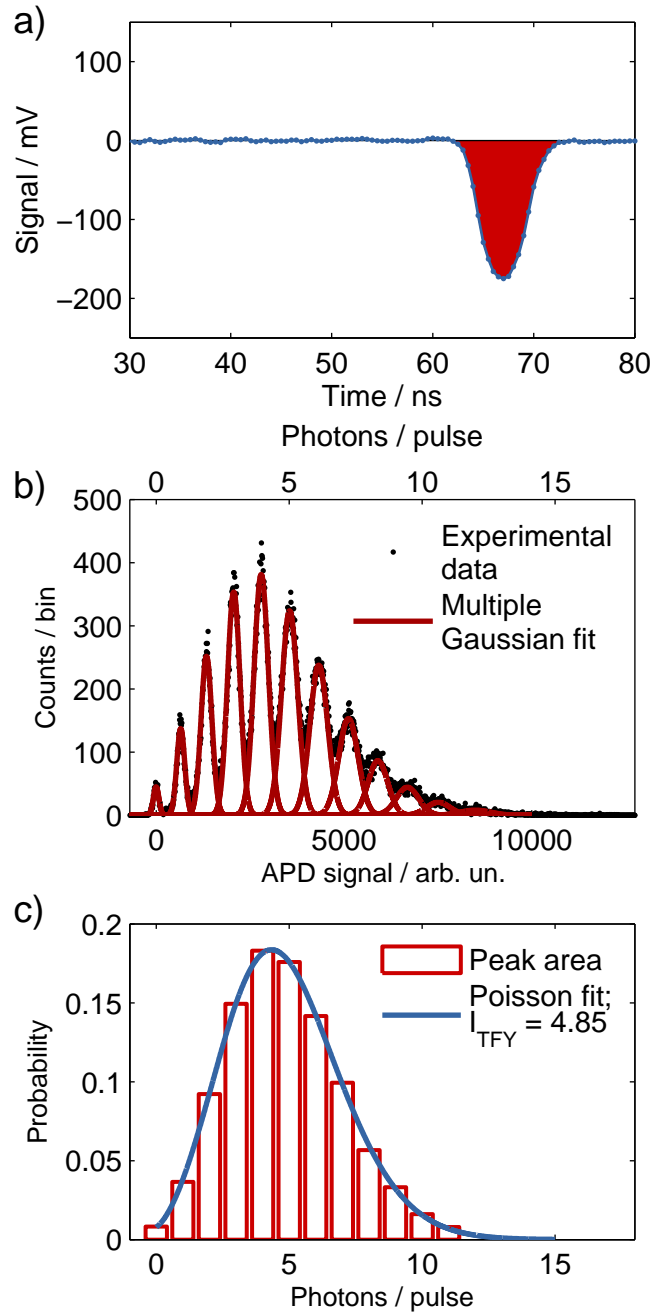


Figure 4.5: a) A single X-ray induced APD signal trace sampled with 2 GS/s. These are then processed to determine the baseline and the integrated signal area (indicated), delivering a measure of the X-ray intensity of the corresponding pulse. Here ~ 100 samples are used to extract the background and ~ 70 for the signal, delivering 10 fold more precise values than the standard deviation of ~ 1.4 mV of the baseline signal. b) Measured pulse-height distribution of the integrated APD signal traces for 10^5 single shots. The bottom ordinate denotes the raw signal amplitude per pulse, and the upper ordinate identifies the number of photons/pulse. A sum of 12 Gaussians, each corresponding to integer photon numbers between 0 and 11 has been fitted. The integrated areas of each Gaussian, shown in c), follow a Poisson distribution delivering a mean value of 4.85 photons per X-ray pulse in this measurement.

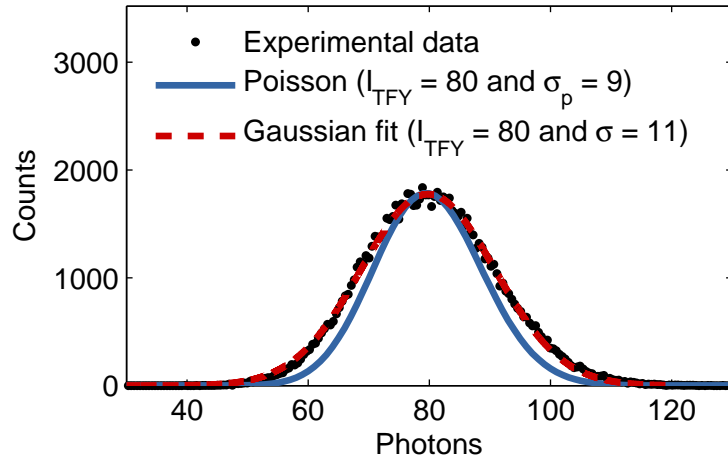


Figure 4.6: Pulse height distribution of the integrated APD single pulse intensity for 10^5 X-ray pulses (black dots). A mean flux of 80 photons per pulse is derived, when scaling the measured signal to the values as derived in Fig. 4.5. A Poisson function with $I_{\text{TFY}} = 80$ (blue solid line) and Gaussian fit to the data with $\sigma = 11$ (red dashed line) are shown for comparison

I_{TFY} with its experimentally determined standard deviation via [30]

$$\lambda = \left(\frac{\lambda}{\sigma_P} \right)^2 \geq \left(\frac{I_{\text{TFY}}}{\sigma} \right)^2 \quad (4.8)$$

In case of a purely shot-noise broadened distribution (neglecting all electronic noise), the greater-equal sign becomes an equal sign. An example of a pulse-height distribution of the detector signal with a mean signal corresponding to $I_{\text{TFY}}=80$ photons (recorded at a bias voltage of 350 V, and scaled using the extracted single photon correlation as seen in Fig. 4.5 and Fig. 4.7) is shown in Fig. 4.6, thus already scaled to the calibrated number of recorded photons/pulse. The corresponding Poisson distribution with $\sigma_P = \sqrt{80} \approx 9$ next to a Gaussian fit yielding $\sigma=11$ is shown, the latter indicating a roughly 20 % additional contribution to the shot noise. This increase in the standard deviation of the experimental data is due to several reasons which, amongst others, are: i) The broadening of each single discrete photon peak as described above, ii) in top-up mode not all 40/60 bunches are equally refilled at once, which effectively leads to charge fluctuations in individual electron bunches, which are larger than the 1 % top up limit of the total (= bunch-averaged) storage ring current. In summary, the result in Fig. 4.6 shows that we have a nearly shot-noise limited detection scheme operational, where only less than 20 % of the noise is accountable by electronic (and other systematic) noise contributions.

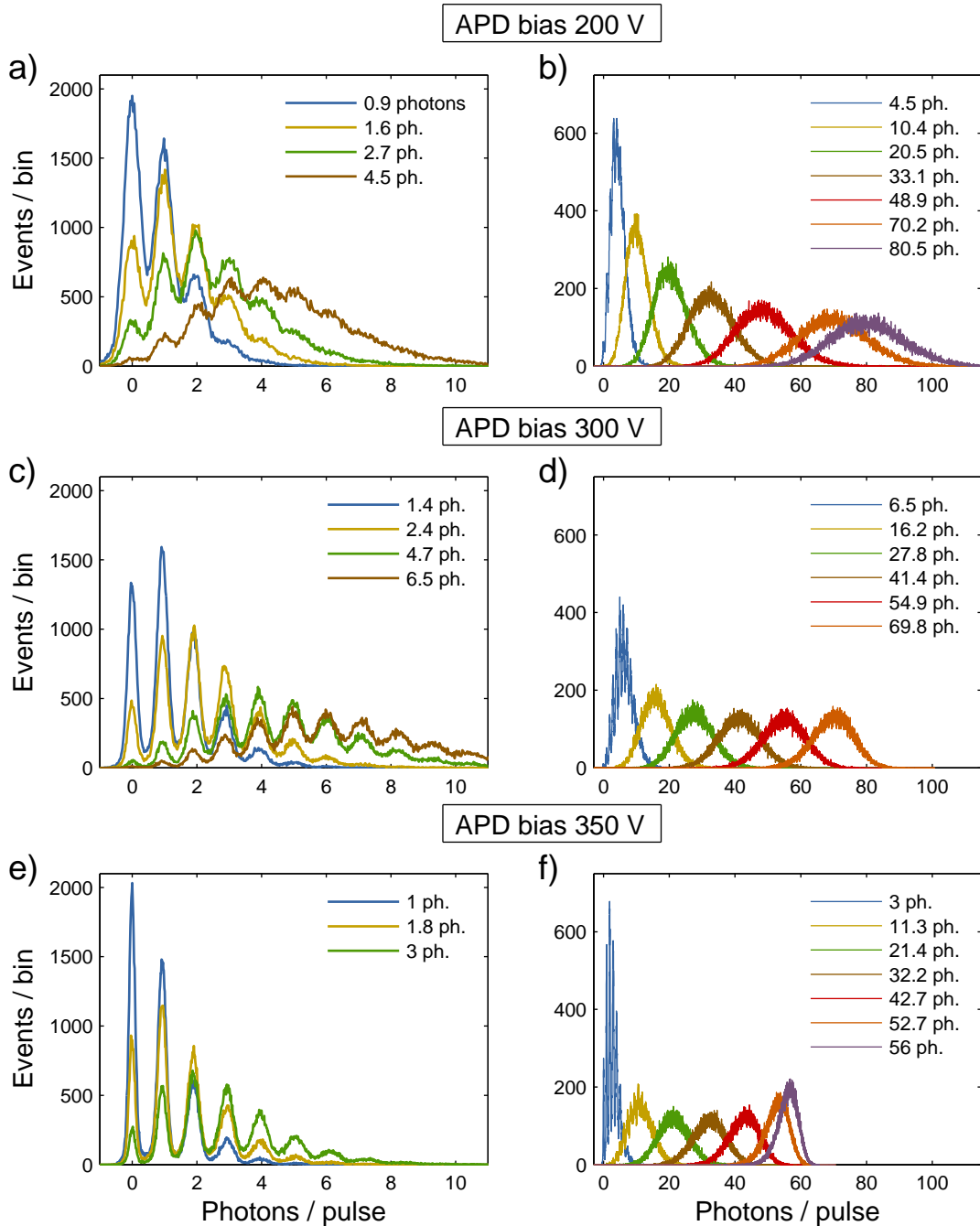


Figure 4.7: Integrated detector signal for a collection of single measurements (or pulse height distributions) for 200 V bias and low (a) and high (b) photon flux, 300 V bias with low (c) and high (d) photon flux, 350 V bias with low (e) and high (f) photon flux. The strong preamplifier gain amplifies the signal to its limiting value leading to the asymmetric pulse shape near 60 photons in (f) (see also Fig. 4.8).

4.3.2 Linearity of APD and Dynamic Range

To assess the linear detector response over the entire dynamic range, we analyzed in detail the pulse height distributions of each integrated APD pulse (Fig. 4.6): In the low flux cases shown in Fig. 4.7 a), c) and e), the detector response is rather linear, independent of the bias voltage on the APD. In the high flux distributions (Fig. 4.7 b), d) and f)), the distributions clearly indicate a non-linear behaviour (slowly merging to saturation) at the larger bias voltages of 300 and 350 V. Qualitatively this is due to a saturation of the integrated pre-amplifier within the APD head. In order to quantify the linear

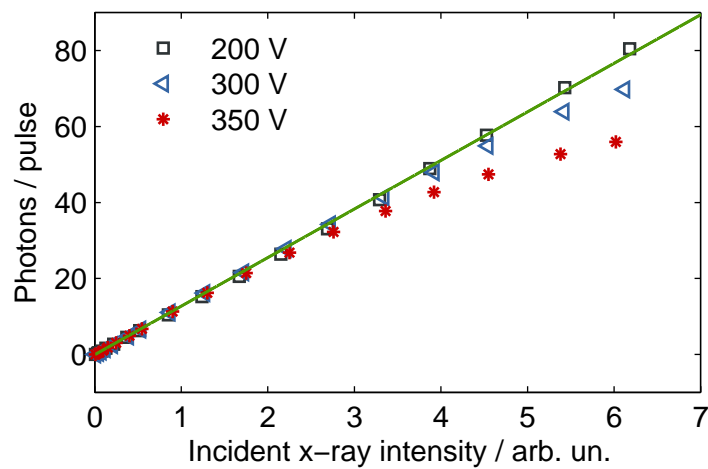


Figure 4.8: Mean APD signal as a function of incident X-ray intensity for 200 V, 300 V and 350 V APD bias voltages, derived from the histograms in Fig. 4.7. The APD signal is given in units of Fe fluorescence photons, which constitute of mainly K photons of 6.4 keV. At the highest bias of 350 V the APD response is linear up to a mean signal of 20 photons, at 300 V bias up to 40 photons and at 200 V bias of beyond 80 photons.

response regime of the APD as a function of the bias voltage, the mean APD signal as a function of incident X-ray intensity is plotted in Fig. 4.8. At the highest bias of 350 V the APD response is linear up to a mean signal of 20 photons, at 300 V bias further up to 40 photons and at 200 V bias up to at least 80 photons. In addition, these measurements also verify the linear response of the entire system up to these limits. Thus our setup is able to operate at total fluorescence yield count rates of up to 100 photons/pulse with single photon sensitivity or $\gg 10^8$ photons/s when applied at PETRA III in 60 bunch mode. This also shows the dynamic range increase of two to three orders of magnitude compared to single photon counting methods, where the count rates are limited to $\ll 1$ photon/pulse.

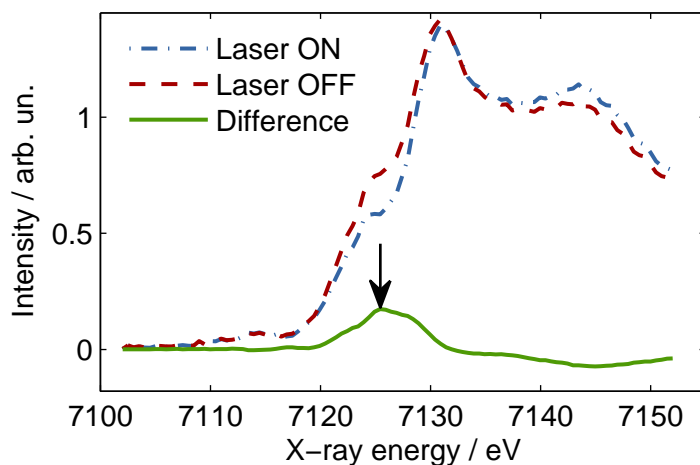


Figure 4.9: Time-resolved XANES scan without (blue dashed curve) and 100 ps after (red dashed curve) laser excitation of photoexcited $[\text{Fe}(\text{bpy})_3]^{2+}/\text{CH}_3\text{CN}$ together with its transient absorption signal (green curve).

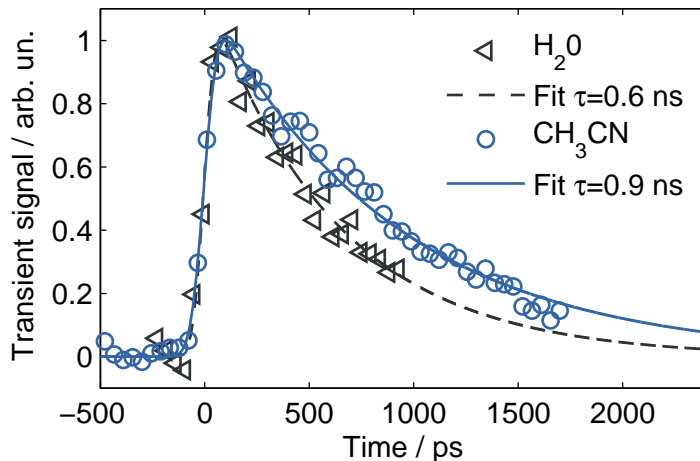


Figure 4.10: Time delay scan of the transient signal of $[\text{Fe}(\text{bpy})_3]^{2+}$ in H_2O (black triangles) and CH_3CN (blue circles) at 7125 eV (arrow in Fig. 4.9), together with a fit of a Gaussian error function convoluted with a single exponential decay. The decay times of 0.6 ns in H_2O (dotted black line) and 0.9 ns in CH_3CN (solid blue line) agree with the literature data. The rise time of 0.1 ns is almost equivalent to the pulse duration of the X-rays. The relatively low S/N of ~ 20 is due to the fact that these spectra were recorded with relatively poor laser/X-ray overlap conditions (after these initial time-delay scans we usually optimize overlap conditions to achieve S/N values as shown e.g. in Fig. 4.9).

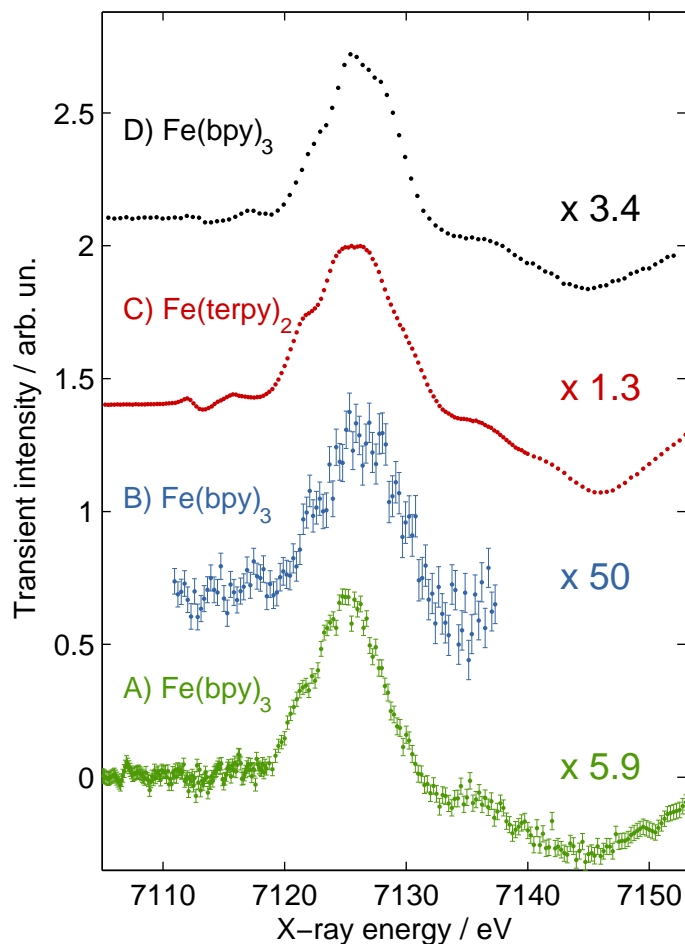


Figure 4.11: Comparison of different normalized transient XANES spectra. A) shows the result using a 1 kHz laser system with a total collection time of about 10 hours [24]. B) displays the result with the current DAQ scheme, but averaging only 2×10^5 X-ray pulses per data point, C) is a measurement of the similar $[\text{Fe}(\text{terpy})_2]^{2+}$ measured with a Single Photon Counting DAQ scheme [25], and D) displays our recent measurement on $[\text{Fe}(\text{bpy})_3]^{2+}$ using $\sim 5 \times 10^6$ pulses per data point (or only ~ 1 s per data point).

4.3.3 High Signal Quality for Measuring a Spin Transition Process: Solvated $[\text{Fe}(\text{bpy})_3]^{2+}$

As a benchmark experiment to compare the present DAQ scheme with previously reported TR-XAS measurements, we have chosen aqueous iron(II)-tris(2,2)-bipyridine ($[\text{Fe}(\text{bpy})_3]^{2+}$) which has been readily studied using both low- and high-repetition optical laser pump / X-ray probe setups both at synchrotrons and XFELs [22, 24, 34, 192, 193]. Upon laser excitation with 515 nm light the system is excited from a low-spin (LS) ground state to a Metal-to-Ligand Charge Transfer (MLCT) excited state and subsequently relaxes (on a 100 fs time scale) to a high-spin (HS) quintet state [194]. This LS to HS spin transition is accompanied by an Fe-N bond elongation of ~ 0.2 Å, giving rise to a fairly strong transient XANES signal. The HS state relaxes back to the LS ground state with a solvent-dependent lifetime, e.g. with 0.6 ns in H_2O [193] and 0.96 ns in CH_3CN [52]. The changes in structure and spin states result in a change of the X-ray absorption spectrum and have been analyzed via EXAFS [24] and XANES [193]. We show TR XANES data during two different measurement campaigns: earlier results have been limited in signal quality due to software constraints, so only the raw digitized APD signal traces were recorded (Fig. 4.5a)) and post-processed but more severely - the number of acquired pulses per data point was constrained to only a few tens of thousands (albeit the laser operated at MHz repetition rates). After soft- and hardware improvements our latest results not only reproduce the earlier data quality (when taking the dramatically different statistics into account) but facilitated nearly real-time data acquisition and pre-processing at 7.8 MHz (60 bunch mode), which includes i) baseline correction and integration of all signal traces, and ii) averaging over several samples to deliver an average signal value I_{TFY} together with its standard deviation σ .

Fig. 4.9 shows the TR XANES of $[\text{Fe}(\text{bpy})_3]^{2+}$ dissolved in CH_3CN , thus the ground state (= laser-off), ~ 100 ps after photoexcitation (=laser-on) and the resulting transient signal (=difference). The average laser power measured at the sample position was ~ 2 W at 1.3 MHz repetition rate (thus a pulse energy of ~ 1.5 μJ), and the laser spot size $\sim 50 \times 50$ μm^2 (slightly larger than the X-ray spot size of $\sim 15 \times 30$ μm^2). The X-ray probe energy was scanned over a range of 50 eV in 0.5 eV steps (to cover the XANES region) with the collection time set to 1 sec per data point. The excited state fraction was determined by the amplitude of the transient signal (relative to the absorption edge jump) to ~ 28 %.

The kinetics of the transient signal at its maximum value (7125 eV, or vertical arrow in Fig. 4.9) have been recorded via time-delay scans (in steps of 44.44 ps) for both solvents (Fig. 4.10). A convolution of a Gaussian error function with a single exponential decay has been fitted to the measured values, yielding a decay time of 0.6 ns in H_2O and 0.9 ns in CH_3CN , both agreeing well with published values [52, 193]. A slight lifetime shortening for CH_3CN (0.9 versus 0.96 ns) can be attributed to the higher temperature of the laser-heated solvent in this MHz pump-probe experiment. The rise time of 0.1 ns corresponds to the X-ray pulse duration (the laser pulse width of 0.3 ps does not contribute here) and

no significant broadening of the rise time due to possible additional timing jitter between laser and X-ray pulses is present.

In order to judge the performance of the current MHz scheme we compare the transient XANES spectra with different setups using kHz and MHz laser systems, with integrated detection scheme and SPC schemes (Fig. 4.11). With a 1 kHz laser system and gated integrator scheme [193] an appreciable S/N is achieved only after long measurement times (about 10 hours in total, Fig. 4.11A). With the present MHz DAQ scheme we already achieved with limited pulses (2×10^5 , Fig. 4.11B), or only 26 ms collection time per data point, only a roughly two-fold worse S/N ratio, which underscores the high potential of the current DAQ scheme. Fig. 4.11C shows the state-of-the-art for SPC at 1.3 MHz pump-probe rate (thus after 35 s collection time per data point) [25], which is topped by our recent integrated detection scheme (of aqueous $[\text{Fe}(\text{bpy})_3]^{2+}$, Fig. 4.11D), recorded in 1 s per data point. The multiplication factors in Fig. 4.11 reflect the achieved excited state population, which is only governed by the exciting laser source and the X-ray/laser focusing conditions, thus it does not depend on the utilized DAQ scheme. The $2.5 \times$ larger factor for the present study versus the SPC experiment at APS reflects the smaller focusing conditions at APS (which excite accordingly $2.5 \times$ more molecules), and is fully in line with our shot-noise analysis presented earlier (section 4.3.1). In order to compare these different experiments we have analyzed the achieved signal-to-noise ratio (S/N). In this regard we define the experimental S/N of the transient XANES spectrum (in Fig. 4.11) as the ratio $S/N_{\text{exp}} = (S/\sigma_S)$ of the transient absorption signal S and its standard error σ_S at the energy, where the transient XANES exhibits its maximum (absolute) value S_{max} , e.g. in the case of $[\text{Fe}(\text{bpy})_3]^{2+}$ at 7125 eV (the maximum transient value in Fig. 4.11, or the vertical arrow in Fig. 4.9). We thus corrected each experiment for its different laser excitation condition, since these do not influence the capacity of the utilized DAQ scheme, but merely reflects the varying focusing (and thus laser fluence) conditions of the exciting laser source (together with the achievable X-ray focus). The normalized conditions together with the relevant experimental parameters for each experimental scheme are summarized in Table 4.1. Interestingly, this comparison equally confirms that all these different DAQ schemes deliver very much similar S/N ratios (when normalizing their values to the expected ones, see Table 4.1): The $[\text{Fe}(\text{terpy})_2]^{2+}$ transient spectrum represents the current state-of-the-art S/N in TR XAS, and the comparison with our MHz measurement of $[\text{Fe}(\text{bpy})_3]^{2+}$ in CH_3CN (Fig. 4.11D) shows that we have achieved a comparable signal quality, however, with 35 times less collection time per data point, agreeing with our expectations: SPC techniques (Fig. 4.11C) limit the detected flux to about 0.1 photons/pulse (to avoid pile-up artifacts), while we detected about 5 photons/pulse (Fig. 4.11D), and together with the different excitation yields in both measurements we get nearly identical results, thus with better signal quality (in less time) with the current MHz DAQ scheme. Summarizing this collection in Table 4.1, in the last line we scaled the S/N_{exp} to comparable values of transient signal S_{max} (thus correcting out the different excitation yields and maximum

transient signal) together with the different data collection times. This allows comparing the different DAQ schemes: The 1 kHz experiment shows the lowest S/N_{scaled} with the MHz SPC method delivering ~ 10 larger S/N_{scaled} , while the current MHz DAQ scheme delivered the largest S/N_{scaled} under otherwise comparable experimental conditions. The up to ~ 30 fold increase from the MHz SPC experiment to the here presented MHz DAQ scheme clearly reflects the ~ 1000 fold increase in counted photons/pulse, leading to an increase of $\sqrt{1000}$ in S/N. We can also compare our representative single scan XANES transient of $[\text{Fe}(\text{bpy})_3]^{2+}$ in Fig. 4.9 with a S/N of 350 to the representative single XANES transient scan of the same molecule in [31] with a S/N of 45. Our measurement presented here yields a factor $350/45 \approx 7.8$ better S/N which agrees nicely with the expected improvement of $\sqrt{62.4/1.2} \approx 7.2$ from the ratio 62.4/1.2 of useful flux between both sources (see Table 4.1). Furthermore, the dynamic range of an APD can in principle be boosted from ~ 100 to several thousands (10^3) photons per pulse, as was demonstrated in the kHz experiment at SLS and ALS [30] measuring transient XAS signals in transmission mode, which provides ample room for even further improvement.

4.3.4 TR XANES of Weakly Excited Aqueous $[\text{Co}(\text{CN})_6]^{3+}$

We further applied the implemented DAQ scheme to aqueous hexacyanocobaltate(III) ($[\text{Co}(\text{CN})_6]^{3+}$). This sample exhibits two ligand field absorption bands around 260 and 310 nm [195], and light excitation into these bands is followed by an intersystem crossing to a ligand field excited triplet state with a near-unit quantum yield [196]. This triplet state has a lifetime of about 2.6 ns and decays back to the ground state (with a quantum yield of 0.69) or undergoes $(\text{CN})^-$ ligand detachment (with a yield of 0.31), and is promptly followed by association of a solvent water molecule. [197] This system serves ideally as a challenging benchmark experiment as its molar absorptivity at 257.5 nm is only about 130 (M cm)^{-1} , thus about 45 times smaller than that for $[\text{Fe}(\text{bpy})_3]^{2+}$ in H_2O at 515 nm. The present $[\text{Co}(\text{CN})_6]^{3+}$ thus represents a sample with very low excitation yields. The details of the photocycle of this molecule will not be addressed in this publication; we will only use this sample to demonstrate the capabilities to measure small TR transient signals in fairly short data acquisition times.

We have measured TR XANES of a 100 mM aqueous solution of $[\text{Co}(\text{CN})_6]^{3+}$ after photoexcitation with 257.5 nm light (the 4th harmonic of our laser system) operating at 1.95 MHz, and probing in 40 bunch mode of PETRA III at 7.8 MHz. The XANES spectrum measured with an acquisition time of 2 s per energy point shows a very weak transient signal of about 1/1000 of the K-edge-jump itself, but the S/N is already ~ 10 (Fig. 4.12a)). We have also compiled the relevant experimental parameters in Table 4.1, which show that the signal quality is very close to our expectations. Concerning the strategy to record all pulses at 7.8 MHz while the laser-on X-ray pulses arrive at 1.95 MHz (or for every 4th X-ray pulse), this is nicely apparent from the statistically derived error bars for the groups of laser-on and laser-off data: the laser-on error bars are indeed $\sqrt{3}$ times larger than the

Table 4.1: Experimental laser excitation and X-ray probing parameters of the transient XANES shown in Fig. 4.11 and Fig. 4.12a): To compare the achievable S/N with different DAQ schemes and laser excitation conditions the scaled experimental S/N_{scaled} is calculated by normalization of the experimental S/N_{exp} to S/N_{scaled} for identical conditions (here $S_{\text{max}} = 10\%$ of the respective K-edge jump and $t_{\text{acq}} = 1\text{s}$).

Sample	[Fe(bpy) ₃] ²⁺ in H ₂ O [22, 24, 30]	[Fe(bpy) ₃] ²⁺ in H ₂ O (this work)	[Fe(terpy) ₂] ²⁺ in H ₂ O [25]	[Fe(bpy) ₃] ²⁺ in H ₂ O (this work)	[Co(CN) ₆] ³⁺ in H ₂ O (this work)
Beamline	Micro- XAS@SLS	P01 @ PETRA III	7ID-D @ APS	P01 @ PETRA III	P01 @ PETRA III
Concentration	25 mM	20 mM	13 mM	20 mM	100 mM
Laser excitation wavelength	400 nm	515 nm	532 nm	515 nm	257.5 nm
Laser pulse energy	~200 μJ	~2 μJ	~2 μJ	~1.5 μJ	<1 μJ
Laser spot size (μm^2 V×H)	~300x300	~150x120	<100x100	~50x50	~50x50
Laser repetition rate	1 kHz	3.9 MHz	1.3 MHz	1.3 MHz	1.95 MHz
Excited state fraction f	17 %	2 %	76 %	28 %	
X-Ray repetition rate	2 kHz	7.8 MHz	6.5 MHz	5.2 MHz	7.8 MHz
X-ray spot size / μm^2 (V×H)	100×260	500×100	~ 8x7	~ 15×30	~ 15×30
Max trans. norm. to edge jump (S_{max})	10 %	1.2 %	46 %	17 %	0.1 %
Acquisition time per energy point t_{acq} / s	~100	0.026	35	~1	2
Detected X-ray photons/pulse	~1	~50	<0.1	~5	~100
Calculated S/N_{theo} at S_{max}	28	18	750	450	15
Observed S/N_{exp} at S_{max}	23	9	550	350	10
S/N_{scaled}^a ($t_{\text{acq}}=1\text{s}$; $S_{\text{max}}=10\%$)	2.3	465	20	206	710 ^b

^anormalization via $S/N_{\text{scaled}} = S/N_{\text{exp}}/(S_{\text{max}}\sqrt{t_{\text{acq}}})$

^bNote that this value is for DAQ capability comparison reasons only, since its experimental realization would require much larger UV pulse energies (which in return would open the door to nonlinear excitations and thus change the experiment drastically). However, with regular laser intensities in the deeper UV range (not reasonably possible with the current laser system), where the sample exhibits a larger optical cross section, this S/N could be realized, in principle

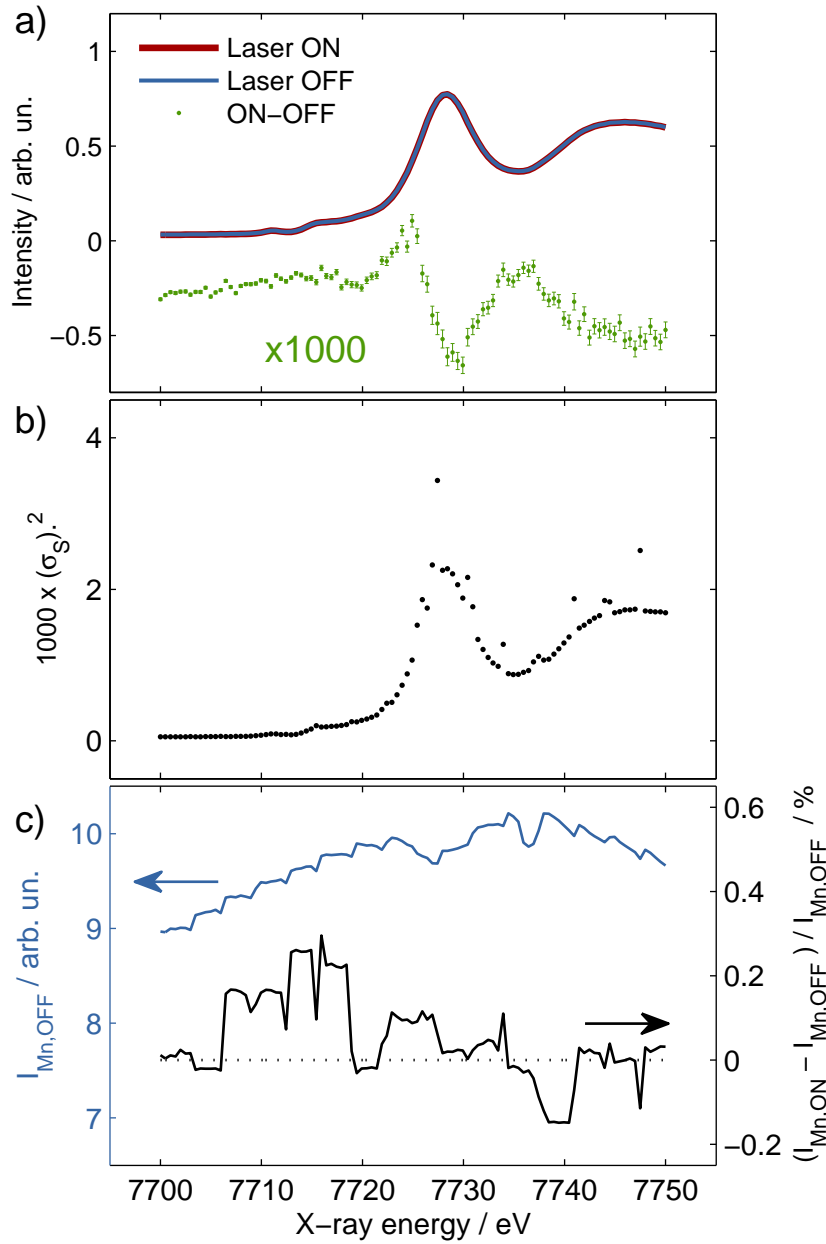


Figure 4.12: a) XANES of $[\text{Co}(\text{CN})_6]^{3+}$ after 257.5 nm excitation, b) squared error bars of transient difference and c) I_{Mn} measurement which is used as an I_0 measurement as well as the normalized difference between I_{Mn} for laser ON and OFF which shows the unbalanced top up of electron bunches corresponding to laser ON and laser OFF.

laser-off error bars. Equally important is to inspect the error bars on the transient data (difference between laser-on and laser-off data), derived from the on-board fast averaging process: the value of the error bars in the transient of Fig. 4.12a) are squared and plotted in Fig. 4.12b) for each energy point. It resembles very much the ground state spectrum, which is indeed expected for a shot-noise limited detection method. But one also observes occasional deviations (outliers) with larger values. These are due to the top-up operation mode of PETRA III, which are easily identified for this scan in Fig. 4.12c): The blue curve shows the measured fluorescence intensity from the Mn foil downstream of the sample, which we used for correcting the abrupt intensity changes in our measurement. Every time an injection occurs, the intensity into the beamline fluctuates for a few seconds. These fluctuations lead in return to worse statistics in the MHz DAQ averaging, which nicely explains the increased error bar sizes. Two examples are marked in red circles in Fig. 4.12, but actually every single injection delivers such increased error bar sizes, equally supporting the soundness of the implemented averaging scheme. It also helps understand better the issues when filling a few bunches among the 40/60 stored bunches: some electron bunches are preferentially filled, and since we record the laser-on and laser-off data on alternating thus different bunches, there is some probability that the groups of even or odd bunches are slightly preferentially filled. Fig. 4.12c) shows this, when we divide the measured intensity on the laser-on bunches by those being used for the laser-off signal (and in absence of any laser-induced effect). The intensity on each subgroup changes by up to 0.2 % following each injection. This is substantially higher than the 0.1 % transient difference signal which we desire to measure, but normalization takes care of these fluctuations.

4.4 Summary and Outlook

We have implemented a setup for TR XAS at the dynamics beamline P01 of PETRA III with two key components, which improve the data collection efficiency by a total of up to six orders of magnitude. The first one is a MHz fiber amplifier laser system with a 24 W average output power and an adjustable repetition rate from 400 kHz to 15.6 MHz synchronized to the RF frequency of the PETRA III storage ring. Compared to a traditional kHz Titanium-Sapphire laser system this allows for a thousand fold faster acquisition of laser excited XAS data in TFY mode. The second element is a MHz DAQ system developed at European XFEL, which acts similar to a gated integrator, but operates - in principle - up to the full RF of PETRA III (500 MHz). Here we recorded X-ray spectra by averaging typically $\sim 10^7$ shots at 7.8 MHz, which were pre-sorted according to laser-on and laser-off conditions. The APD signal traces were sampled with 2 GS/s (and 12 bit) over the APD pulse trace and the integration algorithm delivered a reliable measure of each integrated single pulse intensity. We have confirmed the linear operation of the entire DAQ scheme

and furthermore characterized in detail the linear working regimes of the APD as a function of the bias voltage. These measurements exploit the increased dynamic range of this setup compared to standard single photon counting techniques by about three orders of magnitude; overall, we can achieve total fluorescence yield count rates up to 100 photons/pulse or $\gg 10^8$ photons/s at PETRAIII in 60 bunch mode. Currently the limitation to measure even higher photon numbers ($\gg 100$ photons/pulse) with our commercially pre-amplified APD is related to its fixed large pre-amplifier gain and will be eliminated in the near-term by implementing a switchable gain preamplifier. At even higher photon fluxes (exceeding 104 photons/pulse) the APD without pre-amplifier should be able to reliably operate, and we also use the internal APD gain (driven by the bias voltage) to fine tune the output trace to the desired voltage level on the ADC input. This will enable the setup to be used at powerful X-ray free electron lasers, such as the European X-ray Free Electron laser, which delivers even larger X-ray intensities (10^{12} ph/pulse) at 4.5 MHz, thus conveniently within the specs of the current setup. Last but not least we have measured TR XANES spectra with quasi static S/N of Fe-based spin transition systems next to a weakly (UV light) absorbing Co complex. Comparing the measurements of the MHz DAQ to those of a SPC DAQ scheme shows that we can effectively decrease acquisition times by a factor 500 or acquire accordingly better TR signals at equivalent acquisition times, which is quantitatively fully in line with the corresponding reduced SPC intensity. One next step will be to make use of the significant decrease in acquisition time, e.g. for measuring TR XAS of samples undergoing non-reversible dynamical changes. The increase in S/N ratio will allow measuring TR XAS with very small changes thus improving the sensitivity to even smaller light-induced electronic and structural changes. Furthermore, we will be able to measure transients with very small excited state fractions, allowing for decreased laser excitation energies, thus performing tickle-and-probe experiments under the same laser excitation conditions used in laser-only pump-probe experiments. Just recently, this setup has been complemented by a multicrystal dispersive von Hamos X-ray emission spectrometer similar to a previously published one [131], which utilizes the MHz pump-probe scheme to collect high quality TR X-ray emission spectra as in [26, 27].

In the Appendix A a user's guide to the data acquisition system at P01 beamline at PETRA III can be found.

5 Iridium Photosensitizer for Solar Hydrogen Generation

This chapter describes the study of an iridium-based photosensitizer for solar hydrogen generation via time-resolved X-ray spectroscopies. The study focuses on the changes in the electronic structure of the photosensitizer in acetonitrile solution and the measurements are extended to the study of the photosensitizer as part of the fully functioning homogeneous catalytic system. In the first section, the photocatalytic system is briefly introduced, in the second section the experimental results are shown and in the third section these results are analyzed and discussed in detail before the chapter ends with final conclusions and an outlook towards possible future research projects.

5.1 Introduction – $[\text{Ir}(\text{ppy})_2(\text{bpy})]^+$

The photocatalytic system for solar hydrogen generation, which is investigated in this work, consists of a homogeneous solution of a sacrificial reductant (SR), a photosensitizer (PS) and a water reduction catalyst (WRC). A schematic showing the reaction cycle is depicted in Fig. 5.1. The specific system studied here employs the iridium-based photosensitizer (IrPS) $[\text{Ir}(\text{ppy})_2(\text{bpy})](\text{PF}_6)$ [48] shown in Fig. 5.2, where bpy = bipyridine and ppy = phenylpyridine. Furthermore, triethylamine (=TEA= $\text{N}(\text{CH}_2\text{CH}_3)_3$) is used as a SR and $\text{Fe}_3(\text{CO})_{12}$ as the WRC¹ [49]. The function of this system is described in [49, 199–202] by a four-step process: The IrPS absorbs a photon and is excited to an electronically excited state IrPS* (step I). The IrPS* is subsequently reduced by an electron transfer (ET) process from the TEA to IrPS⁻ (step II) and the IrPS⁻ further transfers the electron to the WRC (step III). The WRC then reduces a proton of a water molecule to hydrogen (step IV). This thesis focuses on the photocycle of the IrPS, i.e. processes I-III.

A UV-vis absorption spectrum of $[\text{Ir}[(\text{ppy})_2(\text{bpy})](\text{PF}_6)]$ in CH_3CN is shown in Fig. 5.3 and spectral peaks were assigned to electronic transitions in [205] as follows: The relatively weak bands around 330 to 500 nm consist of ³MLCT and LC transitions, the shoulder at around 300 nm contains two ¹MLCT transitions. The dominating peak at around 260 nm contains further LC ($\pi(\text{bpy}) \rightarrow \pi^*(\text{bpy})$ and $\pi(\text{ppy}) \rightarrow \pi^*(\text{ppy})$) transitions as well as transitions to the strong and medium CT states.

¹Actually, $\text{Fe}_3(\text{CO})_{12}$ is only the precursor of the WRC. It decomposes into different iron-carbonyls in the solution, and the radicals $[\text{HFe}_3(\text{CO})_{11}]^-$ and $[\text{HFe}(\text{CO})_4]^-$ have been identified as major catalytic species [198]. For simplicity in this thesis, we call the precursor $\text{Fe}_3(\text{CO})_{12}$ the WRC.

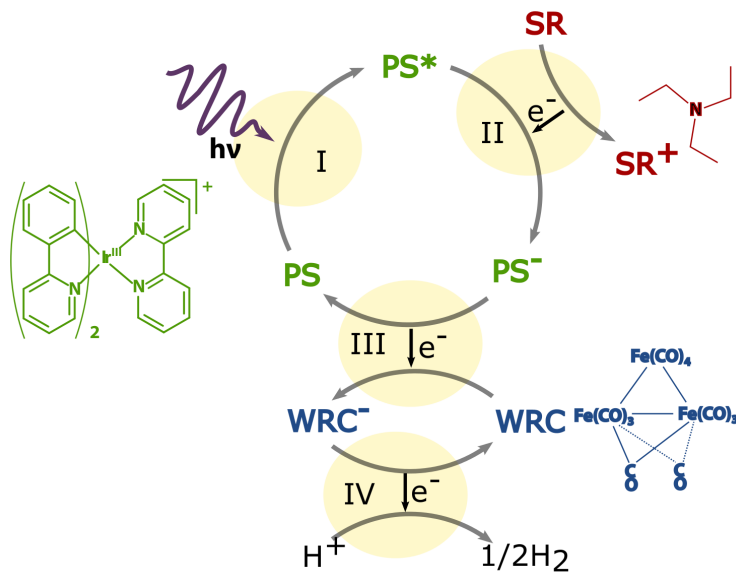


Figure 5.1: Reaction cycle of a photocatalytic system consisting of a homogeneous solution of a sacrificial reductant (SR), a photosensitizer (PS) and a water reduction catalyst (WRC) for solar hydrogen generation [49, 199–202]. The system discussed here consists of the PS $[\text{Ir}(\text{ppy})_2(\text{bpy})]^+$, triethylamine (TEA) as the SR and $\text{Fe}_3(\text{CO})_{12}$ as the WRC.

The photocatalytic reaction in Fig. 5.1 is initiated by excitation in the MLCT bands, thus in the near UV regime around 350 nm, and the photophysical and -chemical processes of the IrPS as occurring in the photocatalytic reaction upon excitation in the $^1\text{MLCT}$ band are shown in detail in Fig. 5.4. The excitation of the molecule occurs within the Franck-Condon regime from the singlet $^1\text{A}_1$ ground state to one of the singlet MLCT states labeled S_m and is followed by rapid relaxation via internal conversion (IC) and intersystem crossing (ISC) into the lowest lying triplet MLCT state labeled T_1 . In the long lived charge separated T_1 state the IrPS can be reduced to the doublet D_0 state by an ET from the SR and the excess electron of the IrPS^- in the D_0 state can be further passed on to the WRC. A competing mechanism to the reduction is a radiative or non-radiative deactivation of the T_1 back into the ground state of the IrPS. The photoluminescence lifetimes of the T_1 state in tetrahydrofuran (THF) solution in absence of a SR as well as with the TEA as a SR present as a co-solvent in a THF/TEA mixture with a 5/1 volume ratio have been determined to 370 ns and 13 ns, respectively [201].

The goals of the experiments reported on here were to first find an X-ray spectroscopic signature of the excited states of the PS and later to use this signature to monitor the previously described steps in the photocycle, i.e. processes I-III of Fig. 5.1, during the photocatalytic activity. Prior to the actual experiments we evaluate the expected changes in structure, spin and electronic states of the IrPS within the photocycle as in Fig. 5.4. In contrast to the Fe-based spin transition systems (see Chapter 6), almost no structural changes are expected. This can be seen in Tab. 5.1, in which the bond lengths of the first

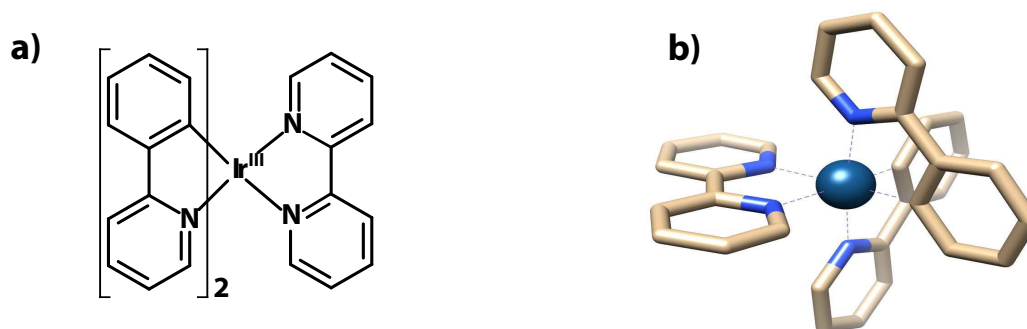


Figure 5.2: a) Two dimensional representation of the $[\text{Ir}(\text{ppy})_2(\text{bpy})]^+$ with the two ppy ligands on the left of the Ir^{III} center and the bpy ligand on the right side. Figure has been plotted with MarvinSketch [203]. b) 3D view of the approximately octahedral structure of $[\text{Ir}(\text{ppy})_2(\text{bpy})]^+$. Figure has been plotted with Chimera [204].

Table 5.1: First coordination shell bond lengths from density functional theory (DFT) calculations of $\text{Ir}(\text{ppy})_2(\text{bpy})^+$ in the singlet ground state S_0 , in the energetically lowest singlet excited state S_1 , in the lowest lying triplet excited state T_1 and in the reduced doublet state D_0 . The calculations have been performed by O. Kühn, S. Bokarev *et al.* [201, 205, 206].

Electronic state	$R(\text{Ir}-\text{N}_{\text{bpy}})$	$R(\text{Ir}-\text{N}_{\text{ppy}})$	$R(\text{Ir}-\text{C}_{\text{ppy}})$
S_0	2.164 Å	2.058 Å	2.012 Å
S_1	2.164 Å	2.056 Å	1.992 Å
T_1	2.163 Å	2.057 Å	1.986 Å
D_0	2.149 Å	2.050 Å	2.014 Å

coordination shell around Ir of the S_0 ground state as well as of three relevant excited states, the energetically lowest lying singlet and triplet MLCT states (S_1 and T_1) and of the reduced D_0 doublet state, are summarized. The strongest structural changes, though small compared to those of Fe-based spin transition systems (see Chapter 6), can be found in the $\text{Ir}-\text{C}_{\text{ppy}}$ bond, which is contracted by about 0.02 Å in the MLCT states. The spin state of the Ir center changes only by 1/2: In the S_0 GS as well as in the reduced D_0 state the electronic configuration of the Ir center is $5d^6$, while in the S_n and T_n MLCT states the configuration is $5d^5$. As discussed in Section 3.4, core-to-core XES can be used to determine the local metal center spin state in $3d$ TM based complexes, thus we have tested if $L\alpha$ XES can be used accordingly to determine the changes in the spin state of the Ir center here. Finally the strongest time-resolved changes are expected to be of electronical nature and we can use L-edge XANES at 11215 eV (L_3) and 12824 eV (L_2) to map out the unoccupied orbitals of the IrPS. The L_3 and L_2 edges correspond to ionization from the the $2p$ orbitals with the additional advantage that the $2p \rightarrow 5d$ bound-bound transitions are dipole allowed and thus expected to be very strong.

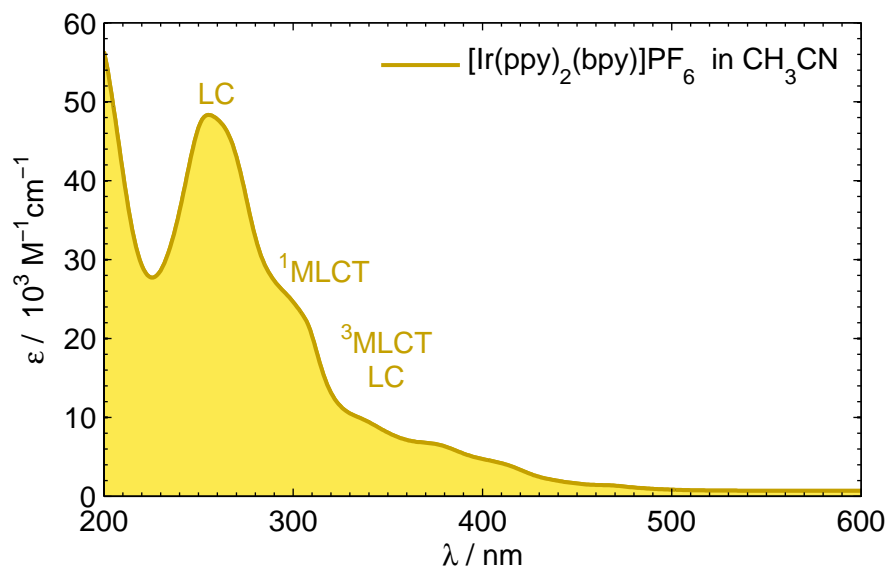


Figure 5.3: UV-vis absorption spectrum of $\text{Ir}[(\text{ppy})_2(\text{bpy})](\text{PF}_6)$ in CH_3CN . The relatively weak bands around 330 to 500 nm consist of $^3\text{MLCT}$ and LC transitions, the shoulder at around 300 nm contains two $^1\text{MLCT}$ transitions. The dominating peak at around 260 nm contains further LC transitions and the transitions to the strong and medium CT states [205].

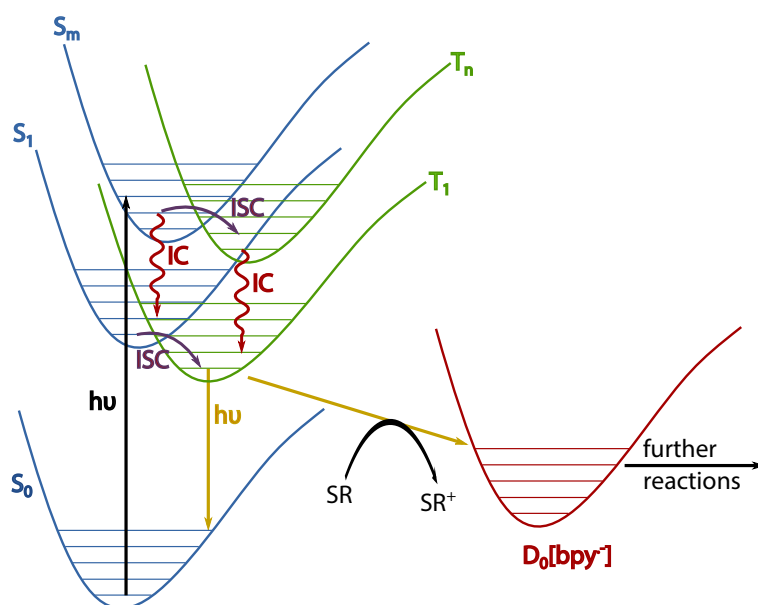


Figure 5.4: Potential energy surface scheme of the relevant potentials as well as the photophysical and -chemical reactions of the $\text{Ir}[(\text{ppy})_2(\text{bpy})]^+$ acting in the photocatalytic system described in Fig. 5.1. (Figure reproduced from [202]).

5.2 Results - Picosecond-resolved X-ray Spectroscopy

5.2.1 Experimental Conditions

Time-resolved X-ray absorption spectra of $[\text{Ir}(\text{ppy})_2(\text{bpy})]^+$ have been measured at beam-line 7ID-D at the APS both in total fluorescence yield (TFY) as well as in high energy resolution fluorescence detection (HERFD) mode. A detailed description of the experimental setup can be found in section 3.8.2. Here, only the X-ray and laser parameters which have been applied in this experiment are briefly summarized.

The APS was used in 24 bunch mode, delivering X-ray pulses at a repetition rate of 6.52 MHz. The X-ray flux at 11.25 keV was 4×10^{11} ph/s after the KB mirrors which focused the the X-rays to a spotsize of $4 \times 5 \mu\text{m}^2$ (V×H) on the sample. As an optical pump source, the third harmonic of the laser system with a wavelength of 355 nm, where the molar absorptivity of $[\text{Ir}(\text{ppy})_2(\text{bpy})]^+$ is $\epsilon=7525$ (M cm) $^{-1}$, has been used. The laser repetition rate was set to 931 kHz, the 7th sub-harmonic of the X-ray repetition rate, thus the spacing between consecutive laser pulses was $\sim 1.07 \mu\text{s}$. The 6th X-ray pulse after the optical excitation, i.e. the one just before the following optical excitation, has been used as a laser OFF pulse. The six X-ray pulses between laser pulses between laser ON and laser OFF measurement correspond to 917 ns, thus about 2.5 times the 370 ns ground state recovery time of the IrPS measured in THF, which allows for an almost complete ground state recovery. The laser was focused to $21 \times 13 \mu\text{m}^2$ (V×H) on the sample. During the L₃-edge XANES scans the laser power was set to 132 mW corresponding to a pulse energy of ~ 142 nJ, thus a laser fluence of 66 mJ/cm² and a laser peak intensity of 6.6 GW/cm². During the L₃-edge EXAFS as well as during the L₂-edge XANES scans the laser power was set to 227 mW corresponding to a pulse energy of 244 nJ, a laser fluence of 114 mJ/cm² and a laser peak intensity of 11 GW/cm².

We have investigated the following three samples:

- **Sample 1:** $[\text{Ir}(\text{ppy})_2(\text{bpy})]\text{PF}_6$ solution in CH_3CN with a concentration of 15 mM and a total volume of 25 mL. The optical density of this sample in a 100 μm thick jet turned to 45° is 1.6.
- **Sample 2:** $[\text{Ir}(\text{ppy})_2(\text{bpy})]\text{PF}_6$ in a $\text{CH}_3\text{CN}/\text{TEA}$ mixture with a concentration of 15 mM and a total volume of 25 mL. The $\text{TEA}/\text{CH}_3\text{CN}$ ratio was about 1:4 in volume. The concentration of $[\text{Ir}(\text{ppy})_2(\text{bpy})]^+$ is equivalent to the one in sample 1 and thus the OD is also 1.6.
- **Sample 3:** $[\text{Ir}(\text{ppy})_2(\text{bpy})]\text{PF}_6$ and $\text{Fe}_3(\text{CO})_{12}$ in a $\text{CH}_3\text{CN}/\text{TEA}$ mixture. The $\text{TEA}/\text{CH}_3\text{CN}$ ratio was about 1:5 in volume and the total volume of the sample was 30 mL. The $[\text{Ir}(\text{ppy})_2(\text{bpy})]^+$ concentration was with 12.5 mM slightly lower, leading to an OD of 1.33. The $\text{Fe}_3(\text{CO})_{12}$ concentration was 9 mM.

The $[\text{Ir}(\text{ppy})_2(\text{bpy})]\text{PF}_6$ has been synthesized by our collaborators in Rostock (Stefan Lochbrunner, Nils Rockstroh, Oliver Kühn, Sergey Bokarev, Henrik Junge and Matthias Beller). The TEA and $\text{Fe}_3(\text{CO})_{12}$ are commercially available and have been bought from Sigma Aldrich.

Due to the fairly small sample volumes we had to compensate the evaporation of CH_3CN by frequent injections of pure CH_3CN to the sample, e.g. once per hour a few (< 5) mL. The TFY XAS spectra were measured with a scintillator placed at an angle of 90° with respect to the X-ray propagation direction. Static $L\alpha$ XES have been measured with a 25 cm von Hamos spectrometer using the Ge(800) reflection of a Germanium crystal and a Pilatus 100k detector. The HERFD XAS spectra were measured with a 1 m Johann spectrometer using also the Ge(800) reflection and fixing the Bragg angle to the maximum of the $L\alpha$ XES line, i.e. to 9175 eV.

5.2.2 Static $L\alpha$ X-ray Emission Spectroscopy

The static $L\alpha$ X-ray Emission Spectra (XES) of powder samples of $\text{Ir}^{\text{III}}[(\text{ppy})_2(\text{bpy})](\text{PF}_6)$, $\text{Ir}^{\text{IV}}\text{O}_2$ and $\text{Sr}_2\text{FeIr}^{\text{V}}\text{O}_6$ have been measured. In Fig. 5.5 the spectra over a range from 9070 eV to 9195 eV are shown, consisting of two discrete XES lines, $L\alpha_2$ at 9100 eV and $L\alpha_1$ at 9175 eV [76]. The emission lines appear structureless and no clear differences between the three spectra are visible. As the three spectra correspond to Ir in different chemical environments and of three different oxidation states, namely +III ($\text{Ir}^{\text{III}}[(\text{ppy})_2(\text{bpy})](\text{PF}_6)$), +IV (in $\text{Ir}^{\text{IV}}\text{O}_2$) and +V (in $\text{Sr}_2\text{FeIr}^{\text{V}}\text{O}_6$), the $L\alpha$ XES does not (within our sensitivity) show a dependency on oxidation or ligation state.

5.2.3 Time-resolved L_3 -Edge X-ray Absorption Spectroscopy

Total Fluorescence Yield XANES

The L_3 -edge XANES spectra, corresponding to the ionization from the $2p_{3/2}$ shell, of $[\text{Ir}(\text{ppy})_2(\text{bpy})]^+$ in CH_3CN have been measured in TFY over a range from 11190 eV to 11250 eV. The spectra corresponding to the laser excited ensemble, the ground state, the reconstructed excited state as well as the transient difference are plotted in Fig. 5.6a). The spectral features are very broad due to the 5.25 eV (FWHM) corehole lifetime width of the Ir L_3 -edge [139]. The ground state spectrum shows two main features which are labeled B and C. The laser excited ensemble shows a slight blue shift of the features B and C as well as an increase of the intensity in the low energy tail of B. The excited state fraction of the laser excited ensemble is found to be 12% (how the excited fraction is determined will be explained later in section 5.3.2), which allowed reconstructing the excited state spectrum using Eq. 3.22. Here the shifts of features B and C are even more pronounced and an additional feature, labeled A, is found at the low energy edge of feature B. In the laser excited ensemble, A was only visible as a slight intensity increase in the low energy tail of B. The transient difference spectrum shows as the main characteristic

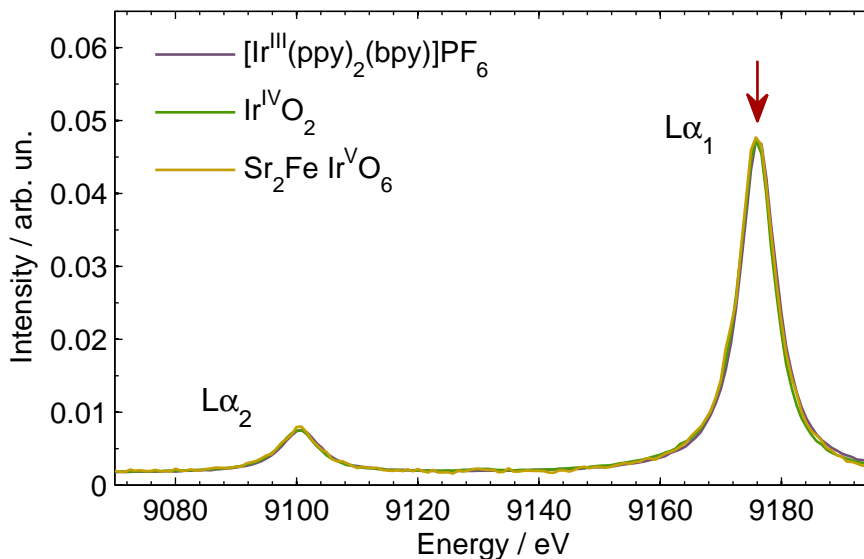


Figure 5.5: Static $L\alpha$ X-ray emission spectra of powder samples of $[\text{Ir}^{\text{III}}(\text{ppy})_2(\text{bpy})](\text{PF}_6)$ (red), $\text{Ir}^{\text{IV}}\text{O}_2$ (green) and $\text{Sr}_2\text{FeIr}^{\text{V}}\text{O}_6$ (orange). The red arrow at 9175 eV marks the position at which the HERFD spectra are measured.

an "up-down-up" feature, which is the result of the additional transition A ("up") and the shift of the strongest feature B ("down-up").

We can use the simplified orbital diagram in Fig. 5.11 to tentatively assign B to the transitions to the $5d(e_g)$ orbitals and A to the transitions to the $5d(t_{2g})$. In the GS with $5d^6$ configuration the $5d(t_{2g})$ orbital is completely filled, thus A appears only in the ES which has, due to the $5d^5$ configuration, a vacancy in the $5d(t_{2g})$ orbitals.

We are currently working with Sergey Bokarev, Oliver Kühn *et al.* on calculations of the X-ray absorption spectra in the dipole approximation at the first principles restricted active space self-consistent field (RASSCF) level and LS-coupling perturbative scheme for the spin-orbit coupling [108, 109]. These high level wavefunction based calculations allow us to tentatively assign the transition above the B feature, i.e. the C feature, to shake-up transition. These shake-up transitions consist of two electron transitions: a $2p_{3/2} \rightarrow e_g$ transition plus a $t_{2g} \rightarrow \pi^*(\text{bpy})$ transition [207].

High Energy Resolution XANES

The HERFD L_3 -edge XANES spectra of $[\text{Ir}(\text{ppy})_2(\text{bpy})]^+$ in CH_3CN have been measured simultaneously to the TFY spectra and are shown in Fig. 5.6b), again for the laser excited ensemble, the ground state, the reconstructed excited state as well as the transient difference. As the TFY and HERFD spectra are measured simultaneously, the excited state fraction here is also 12 %. The spectral features of the HERFD XAS are the same

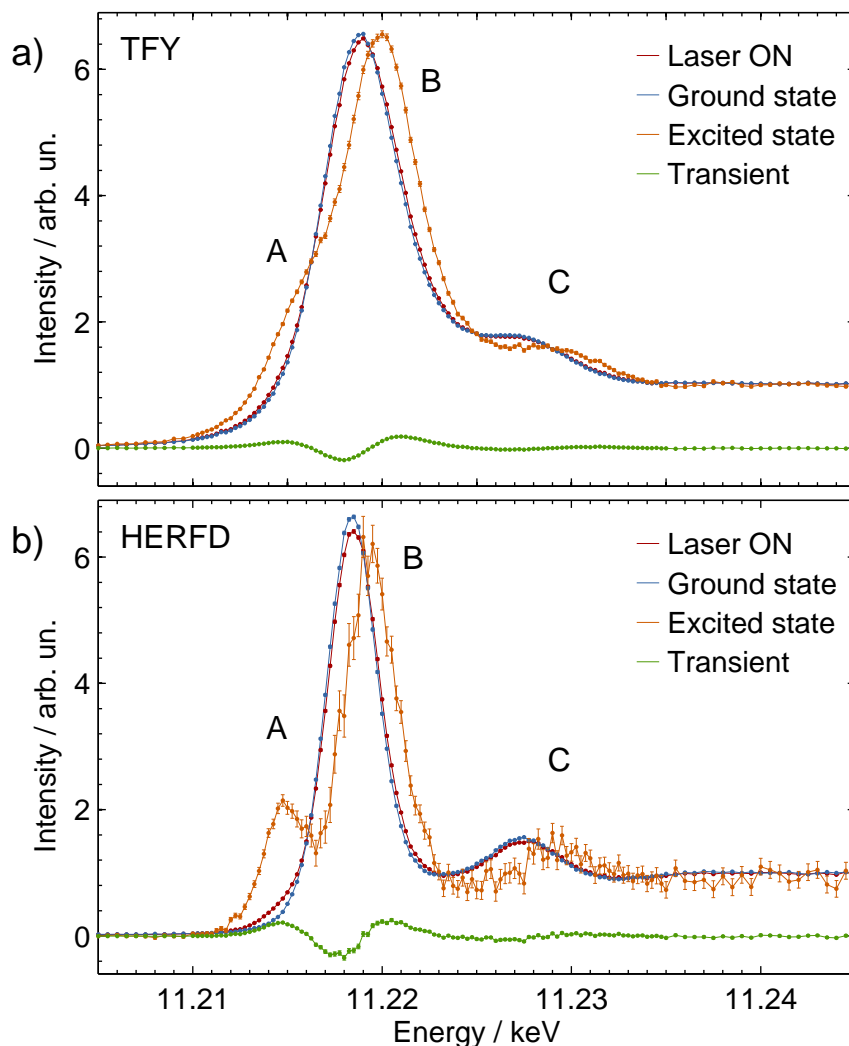


Figure 5.6: L₃-edge XANES measured in a) TFY and b) HERFD of the laser excited ensemble (red), the ground state (blue), the reconstructed excited state (orange) and the transient difference (green) of $[\text{Ir}(\text{ppy})_2(\text{bpy})]^+$ in CH_3CN .

ones as in the TFY case, but thanks to the HERFD measurement technique, the features are by far sharper, allowing also a clear distinction between the peaks A, B and C.

Total Fluorescence Yield EXAFS

A single EXAFS scan of the L₃-edge over a range up to ~ 150 eV above the L₃ absorption edge has been measured, the resulting spectra are shown in Fig. 5.7. The laser pulse energy was with 244 nJ a factor 1.72 larger than the 142 nJ during the XANES scans, which would lead to an excited state fraction of 21 %. We have determined the excited state fraction independently by scaling the transient in the XANES region of the EXAFS scan to the one of the XANES scan in Fig. 5.6. The required scaling factor to match the

transient intensities is 1.7, thus in excellent agreement with the ratio of pulse energies. This is a clear signature of a purely linear optical excitation. In addition to spectral signatures A, B and C, an additional feature D at ~ 50 eV above the L_3 absorption edge can be seen, which also exhibits a blue shift upon laser excitation.

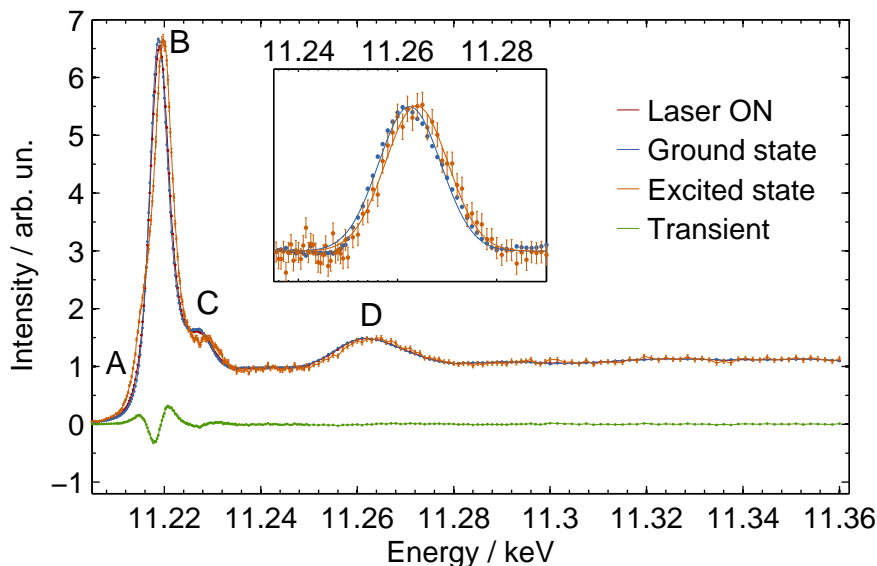


Figure 5.7: L_3 -edge EXAFS measured in TFY of the laser excited ensemble (red), the ground state (blue), the reconstructed excited state (orange) and the transient difference (green) of $[\text{Ir}(\text{ppy})_2(\text{bpy})]^+$ in CH_3CN . An additional feature D at about 50 eV above the absorption edge is visible. In the inset, a fit of a Voigt profile to D in the ground and excited state is shown.

5.2.4 Time-resolved L_2 -Edge Total Fluorescence Yield XANES

The L_2 -edge XANES spectra, corresponding to the ionization from the $2p_{1/2}$ shell, have been measured and are shown in Fig. 5.8a). The laser excited spectrum has been acquired at the same laser excitation conditions as the L_3 -edge EXAFS, thus the laser pulse energy of 244 nJ results also here in an excited state fraction of 21 %.

The L_2 corehole lifetime width of 5.69 eV (FWHM) [139] is slightly larger than of the L_3 -edge. The ground state spectrum shows, analogously to the L_3 -edge, two main features B' and C'. Upon laser excitation, these features shift to higher energies, but contrary to the L_3 -edge, no clear feature A' at lower energies appears. In Fig. 5.8b) the L_2 -edge transient is compared to the one of the L_3 -edge. The transient of the L_2 edge has an "down-up" characteristic due to the shift of B', a clear signature of a feature A' is missing. Only the reconstructed excited state spectrum marks a shoulder in the low energy tail of B', which could be due to A'.

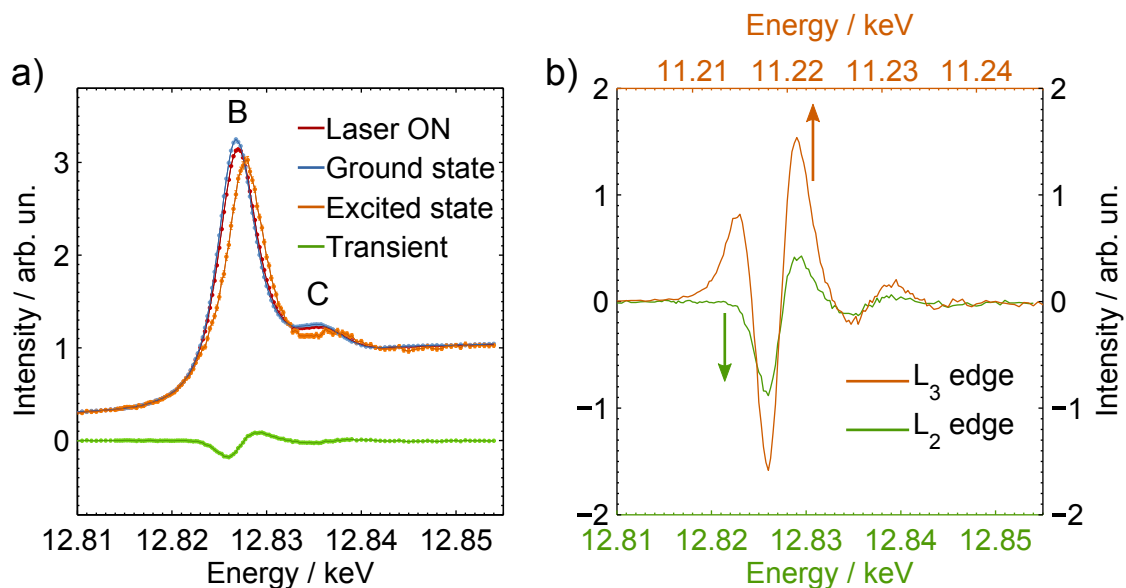


Figure 5.8: a) TFY L₂-edge XANES of the laser excited ensemble (red), the reconstructed excited state (orange), the ground state (blue) and the transient difference (green) of [Ir(ppy)₂(bpy)]⁺ in CH₃CN. In b), a comparison between this L₂-edge transient (green) to the L₃-edge transient (orange) is shown, the transients are normalized to the respective edge jump and scaled to 100 % excited state fraction.

5.2.5 Time-resolved XAS of Fully Functioning Photocatalytic System

L₃-edge XANES - Total Fluorescence Yield

We have measured the TR L₃-edge XANES in TFY of the IrPS also in a CH₃CN/TEA mixture as well as in a CH₃CN/TEA/ Fe₃(CO)₁₂ mixture. The static L₃-XANES spectra and the scaled transient differences \sim 100 ps after photoexcitation are shown in Fig. 5.9 a) and b), respectively. Both the ground state and the transient spectra have been scaled to match their respective relative intensities in order to facilitate a comparison between the individual spectra.

Neither the static nor the transient spectra show any qualitative difference. From the static result we conclude that the addition of TEA and/or Fe₃(CO)₁₂ does not (significantly) change the electronic or geometric structure of the IrPS. Furthermore, from the 100 ps transients we can conclude that the energetically lowest lying excited state, in which the IrPS has predominantly arrived 100 ps after photoexcitation, is the same for all three samples.

Time Delay Scans

Time delay scans at 11.2215 keV (where the transient XANES exhibits its maximum) have been performed to measure the lifetime of the excited state of the IrPS. The scans of the

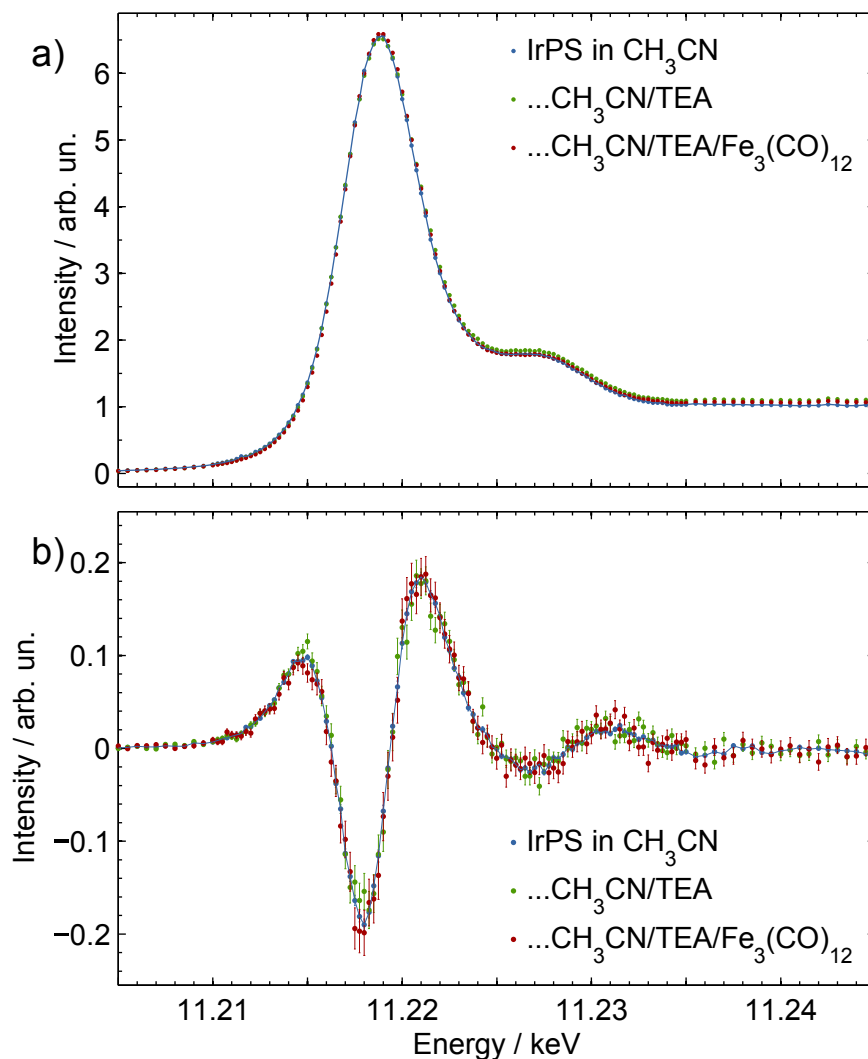


Figure 5.9: Comparison of XANES of $[\text{Ir}(\text{ppy})_2(\text{bpy})]^+$ in CH_3CN (blue), as well as in $\text{CH}_3\text{CN}/\text{TEA}$ (green) and in $\text{CH}_3\text{CN}/\text{TEA}/\text{Fe}_3(\text{CO})_{12}$ (red) mixtures, respectively. In a) the ground state spectra and in b) the transient differences are shown. The static spectra and the transient differences are arbitrarily scaled in intensity to simplify comparison.

IrPS in CH_3CN , in the $\text{CH}_3\text{CN}/\text{TEA}$ mixture as well as in the $\text{CH}_3\text{CN}/\text{TEA}/\text{Fe}_3(\text{CO})_{12}$ mixture are shown in Fig. 5.10. A fit² of a convolution of a Gaussian-broadened step function with a mono-exponential decay yielded the respective lifetimes of the excited state of the IrPs in these three samples to (39.6 ± 2.8) ns, (5.0 ± 0.6) ns and (6.7 ± 0.7) ns. As the delay scans are taken at the rising edge of the B-feature, which shifts proportionally to the change in oxidation state [208], we directly probe the oxidation state of the Ir center. This allows us to interpret the measurements the following way: The 39.7 ns

²The time delay scan fits in this thesis have been performed with the *lsqcurvefit* function in Matlab. The given error is the 95 % confidence interval which is calculated with the *nlparci* function.

measured for sample 1, the IrPS in CH_3CN alone, correspond to the (radiative or non-radiative) relaxation from the T_1 state back to the S_0 ground state with a rate constant of $k_{S1} = 2.52 \times 10^7 \text{ s}^{-1}$. The 5.0 ns, thus a rate constant $k_{S2} = 2.0 \times 10^8 \text{ s}^{-1}$, measured for sample 2 (IrPS in $\text{CH}_3\text{CN}/\text{TEA}$ mixture) corresponds to the decay of the T_1 excited state via two distinct pathways, the relaxation back to the ground state and the reduction to the D_0 state via ET from the TEA to the IrPS*. The 6.7 ns which we have measured for the case of the third sample (IrPS in $\text{CH}_3\text{CN}/\text{TEA}/\text{Fe}_3(\text{CO})_{12}$ mixture) corresponds to the same deactivation mechanisms as in the case of sample 2. The slightly longer lifetime found here is merely caused by the 1.25 times lower TEA concentration, leading to a roughly 1.25 times lower rate of the diffusion driven and thus concentration dependent quenching of the t_{2g} vacancy via the ET.

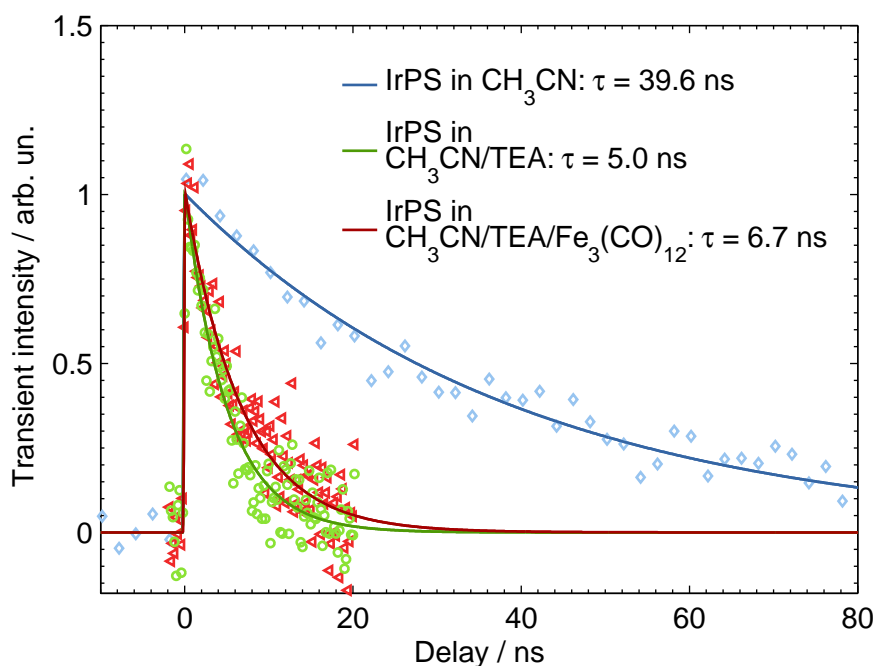


Figure 5.10: Time delay scan of $[\text{Ir}(\text{ppy})_2(\text{bpy})]^+$ in CH_3CN (blue), as well as in $\text{CH}_3\text{CN}/\text{TEA}$ (green) and $\text{CH}_3\text{CN}/\text{TEA}/\text{Fe}_3(\text{CO})_{12}$ (red) mixtures. A fit of an exponential decay resulted in excited state lifetimes of (39.6 ± 2.8) ns, (5.0 ± 0.6) ns and (6.7 ± 0.7) ns for the three samples, respectively.

5.3 Analysis and Discussion

5.3.1 XANES Analysis

To determine the energies of the bound-bound transitions and of the absorption edge more precisely, we have reconstructed the L_3 -edge spectra using a superposition of Voigt³ profiles for the discrete bound-bound transitions and an arctangent broadened step function for the absorption edge. This analysis is done in full analogy to the one of TR L_3 -edge spectra of $\text{Ru}(\text{bpy})_3$ published in [21, 209] and of $\text{Ir}(\text{ppy})_3$ in [184].

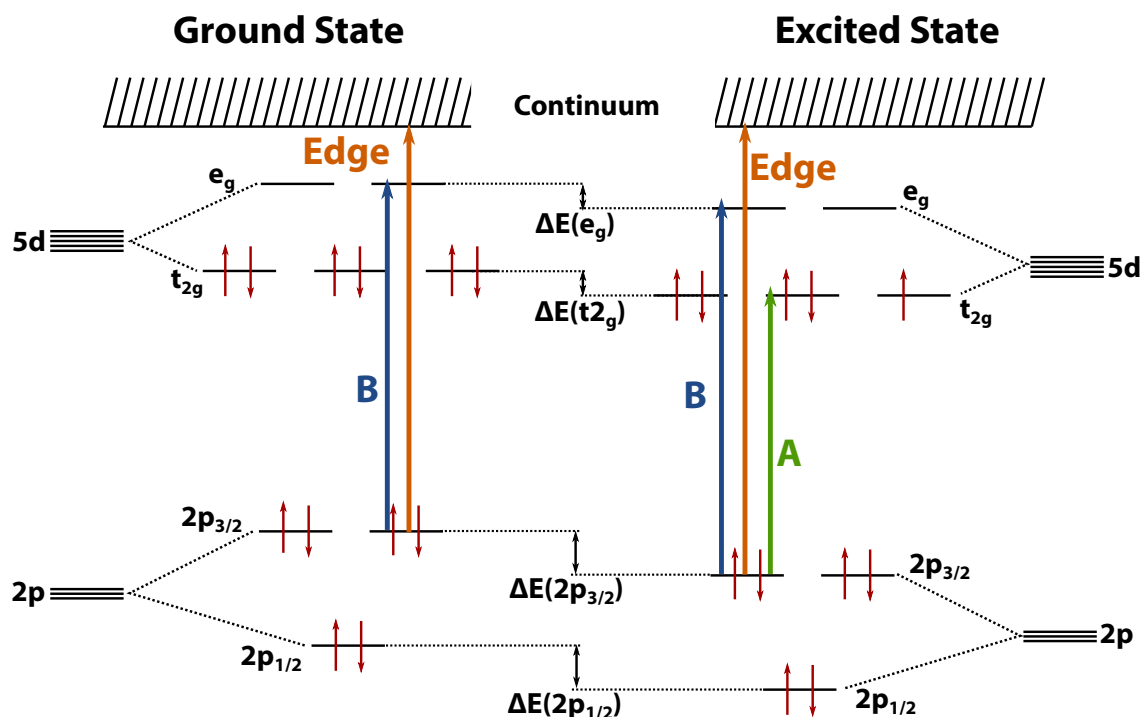


Figure 5.11: Diagram showing the $2p$ and $5d$ Ir orbitals. The $5d$ orbitals are mainly split by the ligand field, the spin-orbit coupling leads to a much smaller splitting of the $5d$ orbitals (<1 eV), which is neglected here. The $2p$ orbitals are split by 75 eV due to the spin-orbit coupling. The transitions of the L_3 -edge involve the orbitals $2p_{3/2}$ and $5d(t_{2g})$ and $5d(e_g)$, they are shown together with the edge as arrows labeled A, B and Edge, respectively. The L_2 -edge XANES contains the corresponding transitions starting from the $2p_{1/2}$ sub-shell (not shown with arrows).

First we have reconstructed the HERFD L_3 -edge XANES spectra. For the GS spectrum, two discrete transitions B and C were required, see Fig. 5.12a). For the ES spectrum in Fig. 5.12c), an additional transition A was needed. The width of the discrete peaks

³A Voigt distribution is a convolution of a Gaussian distribution $G(E) = C_1 \exp(-(E_0 - E)^2/(2\sigma))$ and Lorentzian distribution $L(E) = C_2 \Gamma / ((E_0 - E)^2 + (\Gamma/2)^2)$. Typically $L(E)$ accounts for the core-hole lifetime broadening Γ (FWHM) and $G(E)$ for the experimental resolution $2\sqrt{2 \ln 2} \sigma$ (FWHM), given e.g. by the monochromator. The constants C_1 and C_2 describe the amplitudes of the distributions and E_0 the energy, where they exhibit their maximum.

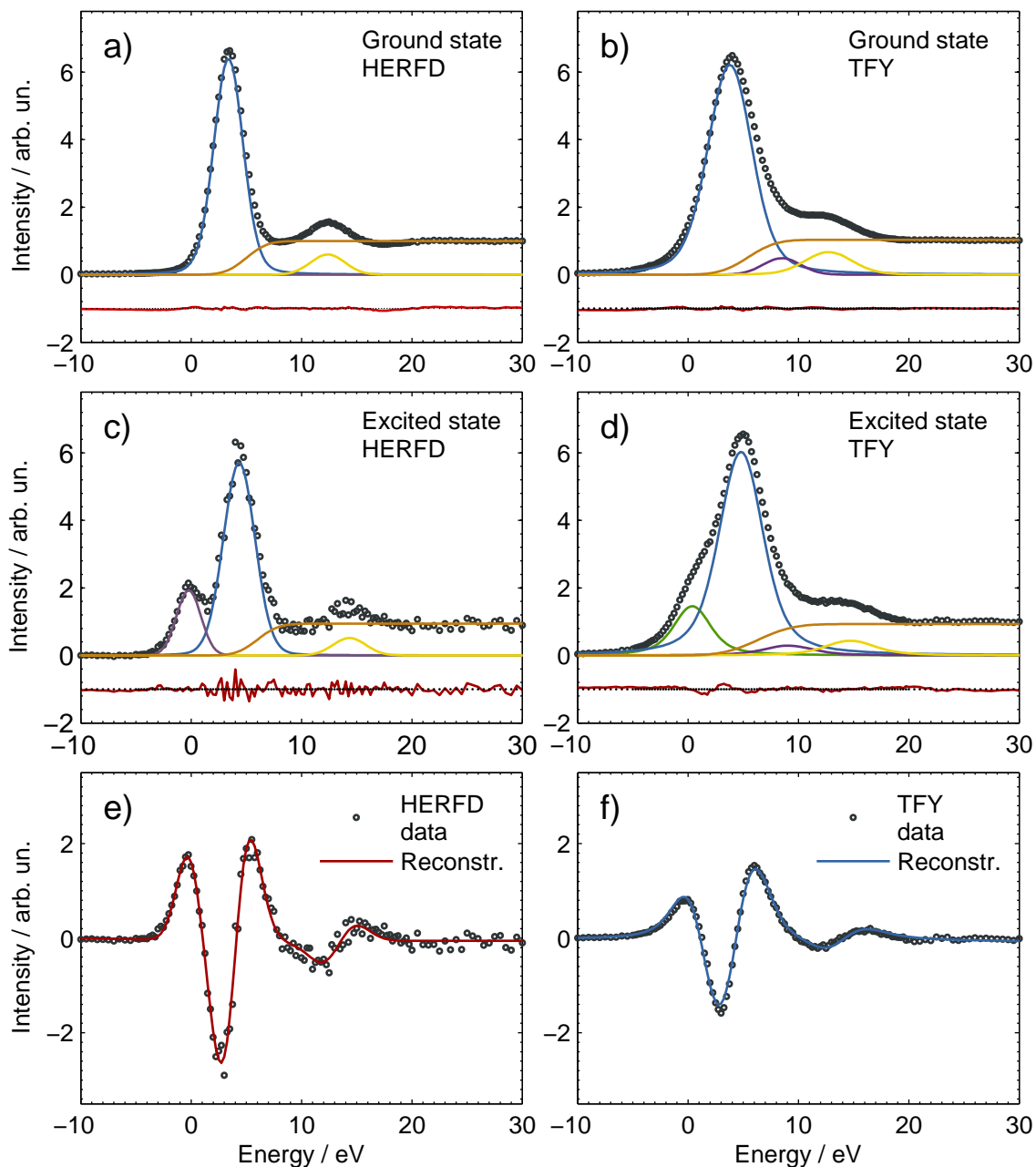


Figure 5.12: Reconstructed XANES spectra together with measured data of $[\text{Ir}(\text{ppy})_2(\text{bpy})]^+$ in CH_3CN in its GS in a) HERFD and in b) TFY as well as of the ES in c) HERFD and d) TFY. In e) and f) the measured as well as reconstructed transients in HERFD and TFY, respectively, are shown. The x-axis is given relative to the $2p_{3/2}$ ionization energy of 11215 eV.

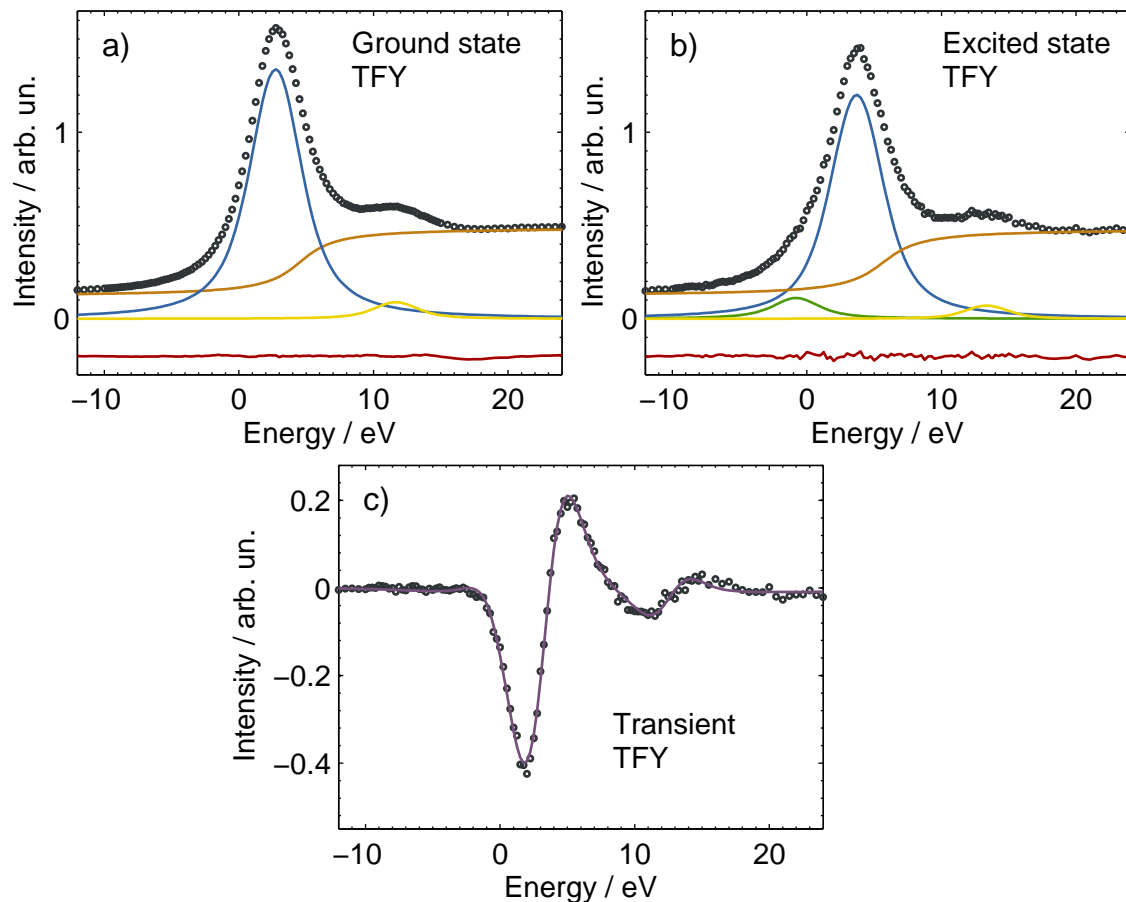


Figure 5.13: Reconstructed L_2 -edge XANES spectra measured in TFY together with measured data of $[\text{Ir}(\text{ppy})_2(\text{bpy})]^+$ in CH_3CN , a) in its GS, b) in the ES and c) the measured as well as reconstructed transients. The x-axis is given relative to the $2p_{1/2}$ ionization energy of 12824 eV.

as well as the width of the arctangent are on the order of 3.0-3.5 eV (FWHM) for all transitions. In [210] the expected broadening of the L_3 -edge HERFD measured via $L\alpha$ XES of Pt and Pb have been calculated to 3.2 eV and 3.4 eV, respectively. Thus the here observed resolution is within the expectations from literature. The energies of the transitions found in these fits are summarized in Table 5.2. The residues (plotted as red solid line offset from zero), consists of merely statistical noise. Using these transitions we were able reconstructed the transient spectrum shown in Fig. 5.12e), which is in excellent agreement with the experimental data.

In the next step we have analyzed the TFY L_3 -edge XANES spectra. Here we have fixed the energy positions obtained in the analysis of the HERFD spectra and only optimized the broadening and area of each of the transitions. The positions are fixed to within ± 0.05 eV for features B, C and the edge and to ± 0.2 eV in case of feature A, to account for uncertainties in the determination of the exact positions from the HERFD spectra.

Table 5.2: Energy positions of L₃-edge and L₂-edge XANES features obtained from their respective reconstructions with Voigt profiles and arctangent broadened edges. All energies are given in eV, in the case of the L₃-edge features relative to the 2p_{3/2} ionization energy of 11215 eV and for the L₂-edge features relative to the 2p_{1/2} ionization energy of 12814 eV. The fits were performed in Matlab using the *lsqcurvefit* function and the error bars correspond to the 95 % confidence interval which is calculated with the *nlparci* function.

	A	B	B ₂	edge	C	D
L ₃ GS		3.8 ±0.1	9.0±1.0	5.4±1.6	12.8±0.3	47.4±0.3
L ₃ ES	0.2 ±0.2	4.8 ±0.3	9.5	6.4±8.8	14.7±0.4	49±0.4
L ₃ ΔE		+1.0±0.4	+1.1	+1.0	+1.9±0.5	+1.6±0.5
L ₂ GS		2.7±0.1		4.5±1.1	11.7±0.1	
L ₂ ES	-0.8±0.4	3.7±0.2		5.7±3.3	13.4±0.3	
L ₂ ΔE		+1.2±0.3		+1.2±3.5	+1.7±0.4	

Here we noticed, that one additional, although fairly weak, transition between B and C is required to reconstruct the spectra. This transition is labeled B₂ and its energy has also been added to Table 5.2. The reconstructions of the TFY L₃-edge XANES spectra in GS, ES and of the transient difference are shown in Fig. 5.12 b), d) and f), respectively. The optimized widths of the arctangent as well as of the bound-bound transitions are on the order of 5 eV (FWHM), which is in excellent agreement with the tabulated 2p_{3/2} core-hole lifetime-width of 5.25 eV for Ir [139]. For pure lifetime-broadening, one would expect the line-shape to have mainly Lorentzian character. Nevertheless, we have observed that the broadening has a large Gaussian contribution, rather than a Lorentzian one. This is illustrated in the Appendix B and the origin of this remains to date unsolved.

The fact that one additional transition is required to reconstruct the TFY spectrum than the HERFD spectrum is not completely surprising. The intensity of features such as shake-up transitions may be reduced in HERFD XAS [210], this possible mismatch has been explained in even greater detail in [211, 212].

The L₂-edge XANES spectra measured in total fluorescence yield have been analyzed in full analogy to the L₃-edge XANES spectra. We were able to reconstruct the GS spectrum using two discrete transitions B' and C', see Fig. 5.13a). To reconstruct the ES spectrum in Fig. 5.13b), additionally a very weak feature A' was required. The energies obtained from the L₂-edge fit are summarized in the lower panel of Table 5.2.

The A' feature has been discussed in detail in Refs. [21, 209] for the case of 4d⁶ TM complex Ru(bpy)₃ which is compared to the perfectly octahedral Ru(NH₃)₆. In the L₂-edge of the 4d⁵ TM complex Ru(NH₃)₆, the A' feature is completely missing [213], as in perfect octahedral symmetry this transition is dipole forbidden. Due to a trigonal distortion this transition becomes also partially allowed in the excited MLCT state of

$\text{Ru}(\text{bpy})_3$ with a $4d^5$ TM center.

In the same table we have also summarized the relative shifts of the energies of the different features between ground and excited states. As obtained from the L_3 -edge XANES, feature B and the absorption edge shift by ~ 1 eV. This shift is also present in the L_2 -edge XANES and reflects merely the change in oxidation state of +1 between ground and excited state of the $[\text{Ir}(\text{ppy})_2(\text{bpy})]^+$. The magnitude of the shift is in line with literature: In [208], XANES spectra of a series of Ir complexes with Ir in oxidation states +II to +IV are presented and an average shift of the white line peak (here: feature B) of around 1.3 eV per increase of 1 in oxidation number has been found.

As can be seen in Fig. 5.11 we can estimate the ligand field splitting in the ES as the difference of the energies of transitions B and A, which results in $10Dq = (4.6 \pm 0.4)$ eV. This ligand field splitting is larger than the ~ 3.8 eV found for $\text{Ru}(\text{bpy})_3$ [21], which is due to the larger ligand field strength exerted by Ir (a $5d$ TM) than by Ru (a $4d$ TM). It is roughly identical to the 4.4 eV one found for $\text{Os}(\text{terpy})_2$ [88], which could be understood by the similar ligand field strengths of terpy, bpy and ppy⁻ and the fact that Ir and Os are direct neighbors in the periodic table. For $\text{Ir}(\text{ppy})_3$ nevertheless, the ligand field splitting of ~ 6.4 eV [89] appears by far larger, which could be explained by the stronger ligand field of the ppy⁻ ligand.

The fits of both L_3 -edge and L_2 -edge summarized in Table 5.2 both deliver very large errors on the edge position, thus without prior knowledge we are not able to precisely determine the ionization potential of the $[\text{Ir}(\text{ppy})_2(\text{bpy})]^+$.

The detailed XANES analysis shows further the improvement in resolving the spectral features by about 1.5-2.0 eV with the help of the HERFD method. Comparing the HERFD spectra with the TFY spectra, an additional remark has to be made: all spectral features in the HERFD spectra were shifted by 0.4 eV compared to the TFY spectra. This shift is caused by a slight offset of the Ge(800) analyzer crystal from the peak intensity of the $L\alpha_1$ line during the HERFD measurement. This artifact becomes clear when considering the RXES plane (see Fig. 3.11) and taking a lineout along a fixed emission energy. Depending on the exact choice of the X-ray emission energy at which the lineout is taken, the onset of the HERFD XANES spectrum (and with this the other XANES features as well) may shift. This has already been discussed in [210]. The absolute energies summarized in Table 5.2 correspond to the TFY energies, as they reflect the "real positions" of the features.

5.3.2 Determination of Excited State Fraction

The excited state fraction of the L_3 edge XANES measurements has been determined using an ionic approximation similar to [21, 89, 209], which can briefly be summarized as follows: In the excited MLCT state the t_{2g} orbitals are occupied with five electrons, thus yielding one vacancy and the e_g orbitals are empty with a total of four vacancies. In the ground state, the t_{2g} orbitals are fully occupied by six electrons. As the transition probability scales with the density of final states in an ionic approximation [89, 209] we can assume that the transition probability to the $5d$ orbitals in the excited state is 25 % larger than in the ground state. In other words, the transition B in the excited state should be four times more intense than the transition A.

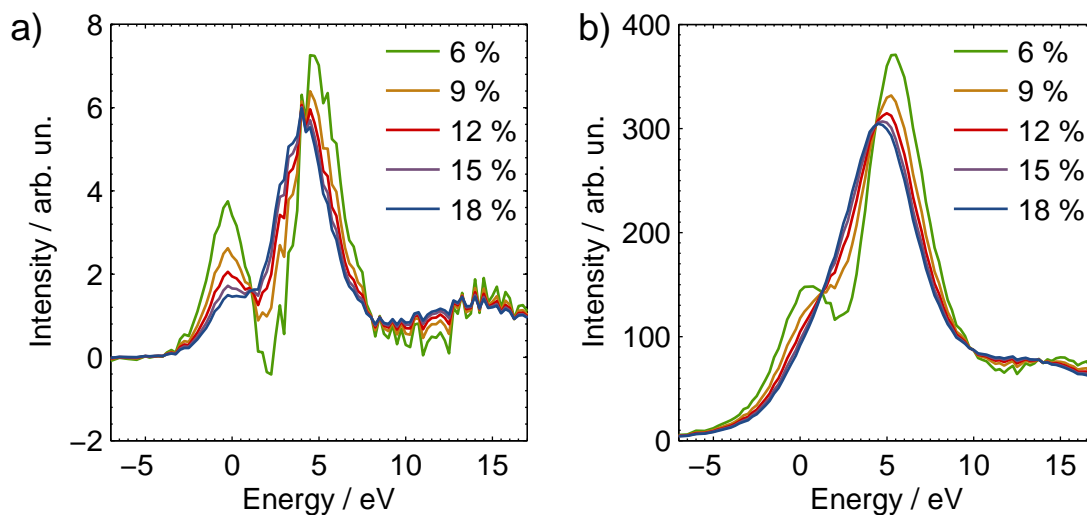


Figure 5.14: Reconstructed ES spectrum of $[\text{Ir}(\text{ppy})_2(\text{bpy})]^+$ in CH_3CN for a series of anticipated excited state fractions between $f = 6\%$ and $f = 18\%$ for XAS measured in a) HERFD and b) TFY. The x-axis is given relative to the $2p_{3/2}$ ionization energy of 11215 eV.

Following this line of argumentation, we can relate the areas $A_{B,GS}$, $A_{A,ES}$ and $A_{B,ES}$ underneath the peaks B in GS and A and B in ES, respectively, via

$$A_{B,GS} = A_{B,ES} = 4 \times A_{A,ES} . \quad (5.1)$$

To determine the excited state fraction f of our experiment, we have reconstructed the L_3 -edge ES spectrum for different anticipated excited state fractions and deconvoluted in each case the XANES spectrum as in Fig. 5.12. A selection of reconstructed ES spectra for $f = 6\%$, 9% , 12% , 15% and 18% is shown in Fig. 5.14a) and b) for the HERFD and TFY measurement, respectively. From this reconstruction we can determine the peak areas $A_{B,GS}$, $A_{A,ES}$ and $A_{B,ES}$ for each anticipated f . In Fig. 5.15a) the ratios $A_{B,ES}/A_{A,ES}$ and $A_{B,GS}/A_{A,ES}$ as a function of f are shown. We find $A_{B,ES}/A_{A,ES} \approx A_{B,GS}/A_{A,ES} \approx 4$

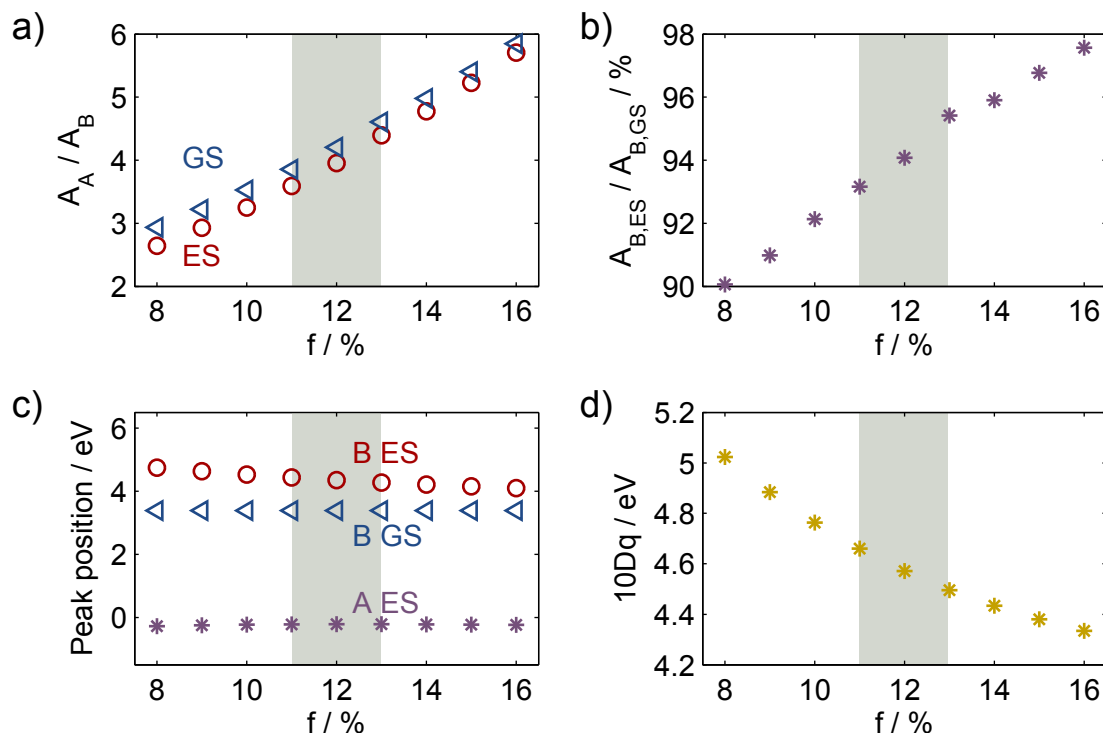


Figure 5.15: a) Plot of ratio of areas $A_B/A_{A,ES}$ underneath the peaks B and A, for B in GS and ES, respectively, as a function of the anticipated excited state fraction f . This determines the correct excited state fraction to $f = 12\% \pm 1\%$, as here $A_{A,ES}/A_{B,ES} \approx 4$. For a discussion of b) to d) see text.

for $f = 12\% \pm 1\%$. Thus the excited state fraction is $12\% \pm 1\%$.

In Fig. 5.15, further quantities as a function of f are plotted and are briefly discussed here: The ratio of the $A_{B,ES}/A_{B,GS}$ (b) shows a $\sim 5\%$ decrease in intensity of transition B in the ES. In (c) the peak position of B in the GS as well as those of A and B in the ES are plotted. Here in the ES feature B shows the strongest dependency on the anticipated excited state fraction. The dependency of the ligand field splitting $10Dq$ on f plotted in (d) and results in an estimate of ± 0.2 eV for the error of $10Dq$ due to the uncertainty in f of $\pm 1\%$. This error in $10Dq$ is negligible compared to the ± 0.4 eV due to the uncertainties in the positions of A and B.

5.3.3 Electron Transfer Rates from TEA to IrPS*

In this subsection we aim to determine the ET rate using the excited state decay times from the fit in Fig. 5.10, following the method described in [201], where the ET rate for $[\text{Ir}(\text{ppy})_2(\text{bpy})]^+$ in THF has been estimated analogously.

The decay rate k_{S1} of sample 1, i.e. of the IrPS in CH_3CN alone, corresponds to the ground state recovery rate via (non)radiative decay of the triplet excited state. The decay rate k_{S2} of sample 2, i.e. of the IrPS in CH_3CN together with TEA, corresponds to the lifetime of the triplet excited state when it is additionally deactivated via ET from the TEA to the IrPS* and subsequent reduction to IrPS⁻. Thus k_{S2} consists of the sum of the ET rate k_{ET} and the ground state recovery rate k_{S1} and we can calculate the ET rate k_{ET} via

$$k_{ET} = k_{S2} - k_{S1} = 1.76 \times 10^8 \text{ s}^{-1}. \quad (5.2)$$

In the next step we calculate an expected ET rate in the case that every encounter, i.e. every collision, of IrPS* with a TEA molecule leads to an ET process. To start, we first calculate the diffusion rate constant k_D for the IrPS and TEA in CH_3CN using [66, 201]

$$k_D = 4\pi N_A R_C D \quad \text{with} \quad D = \frac{k_B T}{6\pi\eta} \left(\frac{1}{R_{TEA}} + \frac{1}{R_{IrPS}} \right). \quad (5.3)$$

Here R_C is the distance of closest approach of the two molecules, D the mutual diffusion constant and η the viscosity of the solvent (here CH_3CN). R_C can be approximated by the sum $R_C = R_{TEA} + R_{IrPS}$ of the gyration radii $R_{TEA} = 2.5 \text{ \AA}$ and $R_{IrPS} = 4.2 \text{ \AA}$ of TEA and the IrPS, respectively. Using for the viscosity of CH_3CN $\eta_{\text{CH}_3\text{CN}} = 3.43 \times 10^{-4} \text{ kg (ms)}^{-1}$ at 298 K from [214] and the temperature $T = 298 \text{ K}$ we obtain

$$k_D = 2.06 \times 10^{10} (\text{M s})^{-1}. \quad (5.4)$$

This is $\sim 40\%$ larger than the $1.5 \times 10^{10} (\text{M s})^{-1}$ found in [201] in THF, which is due to the higher viscosity of THF of $\eta_{\text{THF}} = 4.8 \times 10^{-4} \text{ kg (ms)}^{-1}$ [214].

The concentration of c_{TEA} TEA in the sample mixtures is given by

$$c_{\text{TEA}} = \frac{F_{\text{TEA}} \times \rho_{\text{TEA}}}{M_{\text{TEA}}}, \quad (5.5)$$

where F_{TEA} is the fraction (in volume) of TEA in the sample, and ρ_{TEA} and M_{TEA} , the density and molecular mass of TEA, respectively. Using $F_{\text{TEA}} = 0.2$ of TEA in sample 2, $M_{\text{TEA}} = 101.19 \text{ g/mol}$ [215] and $\rho_{\text{TEA}} = 0.728 \text{ g/cm}^3$ [216] we obtain a concentration of $c_{\text{TEA}} = 1.44 \text{ M}$ in sample 2. The expected ET rate is then

$$k_{\text{ET,exp}} = k_D \times c_{\text{TEA}} = 3.0 \times 10^{10} \text{ s}^{-1}, \quad (5.6)$$

and thus about 170-fold larger than the measured value. In other words, only every 170th encounter of an excited IrPS* with a TEA molecule leads to an ET.

5.4 Summary

We have applied TR X-ray spectroscopies to investigate an IrPS for solar hydrogen generation. While the Ir $L\alpha$ XES has turned out to be not chemically sensitive, we were able to quantify the electronic structural changes of the IrPS as they occur during the photocatalytic cycle by mapping out the (metal centered) unoccupied orbitals of the IrPS in its GS and its ES using (L_2 -edge and mainly) L_3 -edge XANES. The features in the TFY spectra are extremely broadened due to the >5 eV core-hole lifetime broadening and applying HERFD XANES improved the resolution by ~ 1.5 - 2.0 eV down to ~ 3.0 - 3.5 eV. The improved resolution of the XANES features allowed for an accurate analysis of their energies and a decomposition of the edge into its main transitions. The GS XANES yielded one main bound-bound transition corresponding to the dipole allowed $2p \rightarrow 5d(e_g)$ transition. The appearance of an additional feature in the excited state has been assigned to the transition to a vacancy in the $5d(t_{2g})$ orbitals, which are fully occupied in the GS. The energy difference of these two transitions corresponds approximately to the ligand field splitting, which is found to be $10Dq = (4.6 \pm 0.4)$ eV.

We have further investigated the IrPS in the fully functioning photocatalytic system and were able to directly observe the ET process from TEA to the IrPS via a quenching of the triplet MLCT ES and a reduction of the ES lifetime of the IrPS by a factor of about 8. More specifically, we can monitor the arrival of the additional electron from the TEA in the t_{2g} orbital. The ET rate from TEA has been calculated and compared to a collision rate of TEA with the IrPS*, showing that only every 170th encounter leads to an ET process.

In a next step it would be desirable to also apply TR XAS and XES to the the WRC ($\text{Fe}_3(\text{CO})_{12}$) to monitor the last step (IV) of the reaction cycle in Fig 5.1.

6 Towards an Iron-based Photosensitizer

In this chapter the characterization of structure and spin of the excited state of $[\text{Fe}(\text{dcp})_2]^{2+}$ will be presented. $[\text{Fe}(\text{dcp})_2]^{2+}$ is considered a candidate towards a new class of Fe(II) centered low spin ground state complexes with increased ligand field strength, possibly towards the triplet-quintet crossing point [52, 217]. In this context, $[\text{Fe}(\text{dcp})_2]^{2+}$ will be compared to a series of conventional low spin Fe(II) complexes which undergo light-induced LS-HS transitions.

6.1 Introduction - $[\text{Fe}(\text{dcp})_2]^{2+}$

The complex $[\text{Fe}(\text{dcp})_2]^{2+}$ has been introduced in [52] and here its main characteristics are summarized in the context of the well established $[\text{Fe}(\text{bpy})_3]^{2+}$ and $[\text{Fe}(\text{terpy})_2]^{2+}$ as in the aforementioned reference. Here, the ligand abbreviations stand for di(carboxypyridyl)pyridine (dcp), terpyridine (terpy) and bipyridine (bpy).

The structure of $[\text{Fe}(\text{dcp})_2]^{2+}$ is depicted schematically in Fig. 6.1. Similar to $[\text{Fe}(\text{terpy})_2]^{2+}$, the complex consists of an Fe(II) center with two tridentate polypyridyl dcp ligands. The first coordination shell consists of six nitrogen atoms around iron, these can be grouped into two axial nitrogen atoms ($= N_{ax}$) along the symmetry axis of the molecule and four equatorial nitrogen atoms ($= N_{eq}$) in the plane normal to the symmetry axis. The second coordination shell consists of twelve carbon atoms which are further split into three groups of each four, C_{ax} , C_{eq1} and C_{eq2} (Fig. 6.1a)). The symmetry of the complex in its ground state is almost perfectly octahedral (see Fig. 6.1b)), with cis and trans

Table 6.1: Bond lengths of the atoms in the first and second coordination shell of $[\text{Fe}(\text{dcp})_2]^{2+}$ grouped as shown in Fig. 6.1. The table contains the results for the 1A_1 ground state and the two possible excited states 3T_1 and 5T_2 from density functional theory (DFT) calculation (by Elena Jakubikowa), and for comparison, the first coordination shell bond lengths from single-crystal X-ray structure determination (from [52]) are shown.

	$R(\text{Fe}-N_{ax})$	$R(\text{Fe}-N_{eq})$	$R(\text{Fe}-C_{ax})$	$R(\text{Fe}-C_{eq1})$	$R(\text{Fe}-C_{eq2})$
1A_1	1.999 Å	2.020 Å	2.931 Å	2.947	2.944 Å
3T_1	1.981 Å	2.143 Å	2.915 Å	3.024 Å	3.059 Å
5T_2	2.158 Å	2.170 Å	3.073 Å	3.084 Å	3.059 Å
1A_1 (via X-rays)	1.974 Å ± 0.002 Å	1.985 Å-1.989 Å ± 0.002 Å			

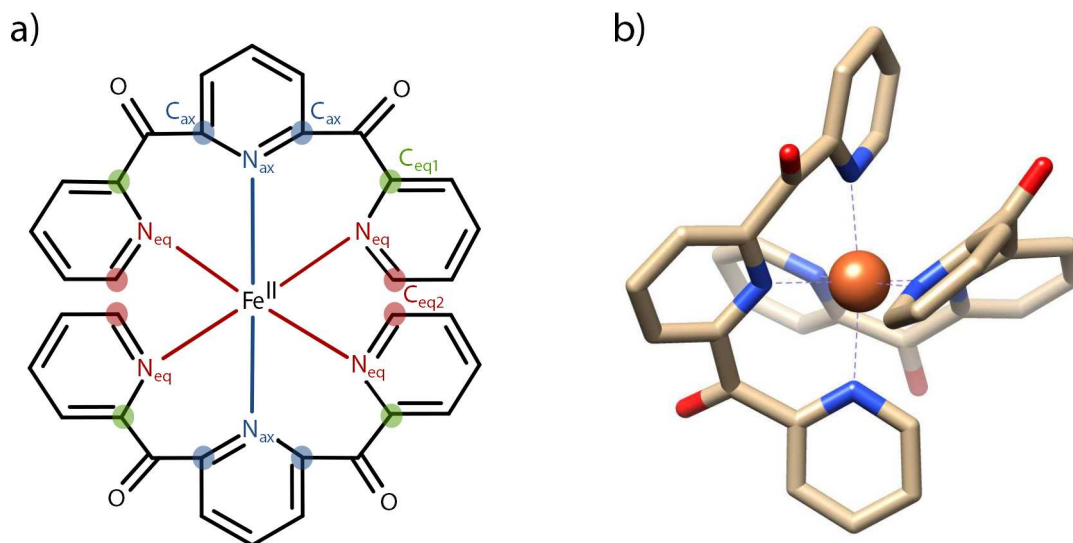


Figure 6.1: a) Structure of $[\text{Fe}(\text{dcp})_2]^{2+}$ in 2D. The nitrogen atoms in the first coordination shell can be separated in axial (blue) and equatorial (red) ones, the carbon in the second coordination shell can be grouped into axial ones (C_{ax}) as well as into those linked to the carbonyl group (C_{eq1}) and those at the outer end of the dcp ligand (C_{eq2}). This figure has been plotted with MarvinSketch [203]. b) 3D structure of $[\text{Fe}(\text{dcp})_2]^{2+}$ with the propeller like twisted arrangement of the two dcp ligands around Fe. This figure has been plotted with Chimera [204]

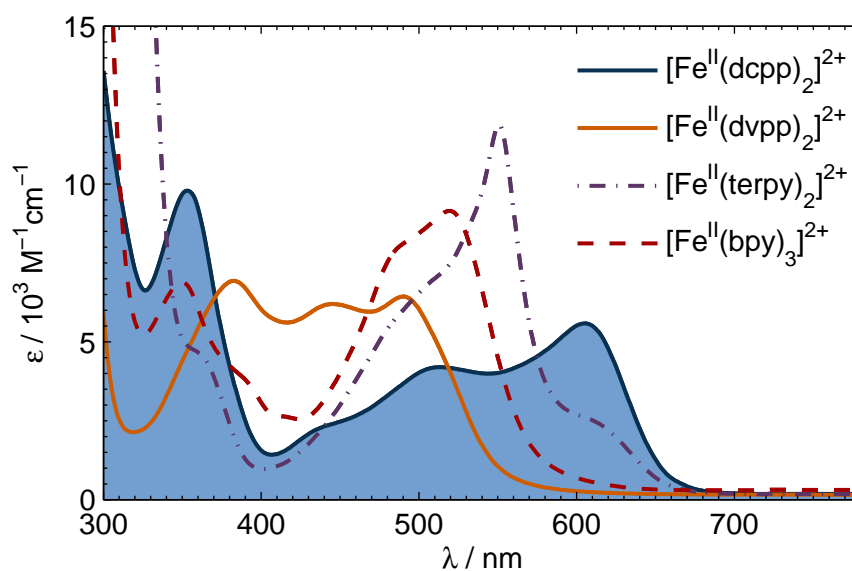


Figure 6.2: UV-vis absorption spectra of Fe-based spin transition systems $\text{Fe}[(\text{dcp})_2](\text{PF}_6)_2$ (blue solid line), $\text{Fe}[(\text{dvpp})_2](\text{PF}_6)_2$ (orange solid line), $\text{Fe}[(\text{terpy})_2](\text{PF}_6)_2$ (purple dashed line) and $\text{Fe}[(\text{bpy})_3](\text{PF}_6)_2$ (red dashed line) solvated in CH_3CN .

bond angles of $90.35^\circ \pm 0.55^\circ$ and $178.35^\circ \pm 0.70^\circ$, respectively, in contrast to $[\text{Fe}(\text{bpy})_3]^{2+}$ (79.8° - 100.5° and 161.0° - 178.7°) and $[\text{Fe}(\text{terpy})_2]^{2+}$ (81.8° - 94.3° and 174.6°) [52]. Table 6.1 summarizes the bond distances of the iron center to the atoms in the first and second coordination shells. The Fe-N bond lengths in the $^1\text{A}_1$ singlet ground state of around 2.00 Å are comparable to those of most Fe-based spin transition systems in their $^1\text{A}_1$ ground states.

The UV-vis absorption spectrum of $[\text{Fe}(\text{dcpp})_2]^{2+}$ in CH_3CN (see Fig. 6.2) exhibits MLCT bands between 400 nm and 650 nm, similar to the other LS Fe(II) complexes. Optical excitation in these bands results in a transition to its energetically lowest lying excited state, for polypyridyl low spin Fe(II) complexes this transition has been found to take <1 ps [39, 218, 219]. According to the Tanabe-Sugano diagram (see Fig. 2.3) this lowest lying excited state is, with the exception of a few cases [71, 220–222], the $^5\text{T}_2$ quintet high spin (HS) state. From there the complex relaxes back to the ground state. The ground state recovery time of $[\text{Fe}(\text{dcpp})_2]^{2+}$ in CH_3CN has been measured to be $0.28 \text{ ns} \pm 0.01 \text{ ns}$ [52], while in CH_3CN the $[\text{Fe}(\text{bpy})_3]^{2+}$ HS-LS transition takes 0.96 ns and for $[\text{Fe}(\text{terpy})_2]^{2+}$ 5.35 ns [52]. In the Marcus' theory [223] treatment of the HS-LS transition as an electron transfer process, $[\text{Fe}(\text{bpy})_3]^{2+}$ is expected to be very close to the barrier-less case [224], which should make it the fastest possible HS-LS ground state recovery. According to Jamula et al. [52], the dcpp ligand is expected to result in a stronger ligand field than the bpy ligand, thus destabilizing the $^5\text{T}_2$ state, eventually leading to an increase in the barrier and thus a longer HS lifetime. To explain this mismatch, Jamula et al. [52] have proposed, next to other explanations, that this could be due to the fact that $^5\text{T}_2$ is destabilized compared to the $^3\text{T}_1$ state, resulting in the $^3\text{T}_1$ being the energetically lowest lying excited state.

The two possible excited states $^3\text{T}_1$ and $^5\text{T}_2$ are expected to possess very distinct geometric structures. The first and second coordination shell bond lengths of the structural models of these two possible excited states as well as those of the $^1\text{A}_1$ ground state, as anticipated from density functional theory (DFT) calculations, are summarized in Tab. 6.1. Compared to the ground state the occupation of the anti-bonding e_g orbitals with one electron in the $^3\text{T}_1$ leads to an average Fe-N bond elongation of 0.08 Å. In the case of the $^5\text{T}_2$ this elongation is twice as large, i.e. 0.16 Å, due to the double occupation of the e_g orbitals. Furthermore, the bond elongation in the $^3\text{T}_1$ is restricted to the equatorial bonds, while in the $^5\text{T}_2$ all bonds are elongated by about the same amount.

The goal of the experiments presented here were to characterize the longest lived excited state of $[\text{Fe}(\text{dcpp})_2]^{2+}$ and to proof or falsify the hypothesis that the ligand field strength is sufficiently increased to destabilize the quintet MC state in respect to the triplet MC so far that the triplet MC state becomes energetically lower than the quintet state. In case of a falsification of this hypothesis the aim is to find an alternative explication for the unprecedentedly short lifetime of a MC quintet state for optically induced Fe(II) spin transition.

Here the TR XAS and XES of $[\text{Fe}(\text{dcpp})_2]^{2+}$ in CH_3CN measured at the APS, including

a detailed interpretation of the measurements leading to the determination of the spin state and structure of the energetically lowest lying excited state of $[\text{Fe}(\text{dcpp})_2]^{2+}$, will be presented.

6.2 Picosecond-resolved X-ray Spectroscopies of $[\text{Fe}(\text{dcpp})_2]^{2+}$

The light-induced LS-HS transitions of Fe-centered systems in solution has been extensively studied with TR XAS. These samples have actually been used in the development of the technique and the early studies on $[\text{Fe}(\text{bpy})_3]^{2+}$ in H_2O [22, 24, 65] and on $[\text{Fe}(\text{tren}(\text{py})_3)]^{2+}$ in CH_3CN [23] represent one of the first applications of picosecond-resolved XANES and EXAFS. With later studies on $[\text{Fe}(\text{terpy})_2]^{2+}$ in H_2O [25] and in CH_3CN [225, 226] the S/N of TR XAS measurements has now reached the level of those of state-of-the-art static measurements, thus reaching the next level in sensitivity to light induced structural changes as TR EXAFS is now able to distinguish two distinct reaction coordinates, i.e. between Fe-ligand bond elongations in equatorial and axial direction in quasi octahedral complexes. These studies have been later extended by TR XES (and the samples were actually used to develop and test the technique): the spin of the energetically lowest lying states of $[\text{Fe}(\text{bpy})_3]^{2+}$ [26–28] and of $[\text{Fe}(\text{terpy})_2]^{2+}$ [25] as well as the spin of a short (< 100 fs) lived reaction intermediate in the LS-HS transition of $[\text{Fe}(\text{bpy})_3]^{2+}$ [39] was measured. Here we apply combined TR XAS and XES to determine both ES spin and structure of $[\text{Fe}(\text{dcpp})_2]^{2+}$. The TR XAS and XES of $[\text{Fe}(\text{dcpp})_2]^{2+}$ solvated in CH_3CN measured at the beamline 7ID-D of the APS will be shown here.

6.2.1 Experimental Conditions

The experimental setup has been described in [32] and used for similar studies of the spin-transition systems $[\text{Fe}(\text{bpy})_3]^{2+}$ [28] and $[\text{Fe}(\text{terpy})_2]^{2+}$ [25]. The experimental parameters applied in this experiment are as follows.

The $[\text{Fe}(\text{dcpp})_2](\text{PF}_6)_2$ has been synthesized in the group of Jim McCusker at Michigan State University. A 12 mM solution of $[\text{Fe}(\text{dcpp})_2]^{2+}$ in CH_3CN , which was flown through a 100 μm thick sapphire nozzle creating a flat sheet jet, tilted to $\sim 45^\circ$ with respect to the X-ray beam direction. Due to the small sample quantity available, a peristaltic pump has been used to reduce the required sample volume to ~ 20 mL. Special care was taken to minimize evaporation of CH_3CN during the experiment. The measures consisted of i) fully enclosing the sample environment and ii) cooling the sample reservoir by placing it in a chilled water container. Furthermore, a second remote-controlled pump has been set up to refill the sample with neat solvent, allowing occasional (about once per hour) injections of small quantities (on the order of 1 mL) without entering the experimental hutch (and thus interfering with the data acquisition).

APS has been used in 24 bunch mode, which delivered X-ray pulses at a repetition rate of 6.5 MHz. 532 nm laser light resulting from second harmonic generation of the optical

pump laser has been used to excite the sample. The optical laser repetition rate was set to 1.3 MHz (1/5 of the 24 bunch repetition rate). The laser power of 1.5 W results in a pulse energy of 1.15 μ J. TR XAS and XES were measured at a delay of \sim 50 ps.

The X-ray absorption spectra were measured in total fluorescence yield (TFY) mode using a scintillator placed at 90° with respect to the X-ray beam. The visible photons produced in the scintillator were finally detected with a photo-multiplier tube. X-ray signals were measured for all incoming pulses at 6.5 MHz and sorted in laser ON and laser OFF. Thus the ratio of 4/1 of unpumped and pumped signals leads to a two-fold better statistical error in the laser OFF spectrum.

The TR XAS and XES spectra were measured quasi simultaneously, meaning the full setup for TR XAS and XES has been built at once and to change from XAS acquisition to XES acquisition only the incident X-ray energy has been changed from resonant excitation (around the absorption edge at \sim 7125 eV) to non-resonant excitation (far above the absorption edge, \sim 7600 eV), leaving the whole setup untouched. This was done to ensure identical excitation conditions and thus an identical excited state fraction.

To measure the TR XES, two different emission spectrometers have been used. The $K\alpha_1$ XES spectra have been measured with a Johann X-ray emission spectrometer [128] using a spherically bend 10 cm diameter Ge(440) crystal (1 m bend curvature). The energetically dispersed photons detected with a scintillator in combination with a photo-multiplier tube. The $K\beta$ XES were measured (in a later experimental campaign) using a 25 cm von Hamos spectrometer exploiting a Si(531) monochromatizing crystal. To ensure an identical excited state fraction in the $K\beta$ XES, XAS has been measured quasi simultaneously and the laser power has been adjusted such that the transient XAS strength (i.e. the transient intensity relative to the K-edge jump) at its maximum (i.e. at \sim 7123 eV) was equivalent to the transient intensity of the earlier measurements at the same X-ray energy.

6.2.2 K-edge X-ray Absorption Spectroscopy

XANES and EXAFS Scans

The K -edge X-ray absorption spectrum in the ground state (= without laser excitation), the spectrum 50 ps after 532 nm excitation, the transient difference and the reconstructed excited state spectrum over a range from 7080 to 7600 eV containing both XANES and EXAFS region are shown in Fig. 6.3. Furthermore, a zoom into the XANES region is presented and the different features in this region are labeled in full analogy with the labeling in Ref. [22] for the very similar features observed for the photoexcited $[\text{Fe}(\text{bpy})_3]^{2+}$ in H_2O . These features are: A) the pre-edge peaks belonging mainly to the $1s \rightarrow 3d$ transitions, B) a shoulder at about the half rise of the K -edge, C) and D) the white line features and E) the first EXAFS oscillation. The error bars have been omitted, as they are not visible on the scale of the plot. Nevertheless it is worth mentioning that in the laser

ON spectrum they are indeed twice as large as in the laser OFF spectrum, as expected for the 4-fold number of pulses used to measure laser OFF than laser ON.

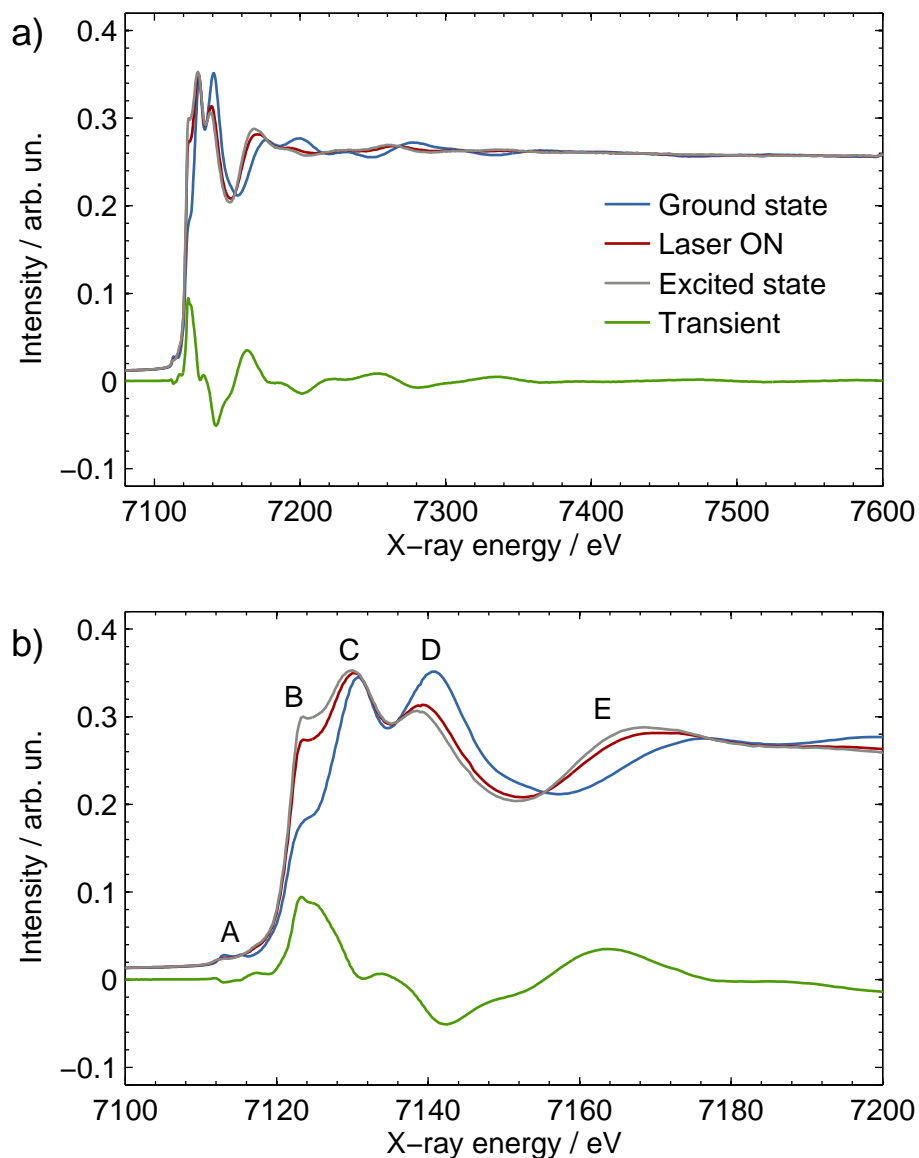


Figure 6.3: a) XAFS spectra of $[\text{Fe}(\text{dcpp})_2]^{2+}$ in CH_3CN in ground state (blue), 50 ps after laser excitation (red), the transient difference (green) and of the reconstructed excited state (grey). In b) a zoom into the XANES region of the spectrum is shown. The different features are labeled A-E, in full analogy to the labeling of the features of $[\text{Fe}(\text{bpy})_3]^{2+}$ in [22].

Time Delay Scans

The lifetime of the excited state has been measured by performing a time delay scan on the B-feature from -200 ps to 800 ps in 10 ps steps, see Fig. 6.4. A fit consisting of a convolution of a Gaussian error function with an exponential decay yields a risetime of (77 ± 3) ps (FWHM) and a decay of $\tau_{\text{dcpp}} = (272 \pm 4)$ ps, which is in excellent agreement with the lifetime of 280 ps reported in Ref. [52].

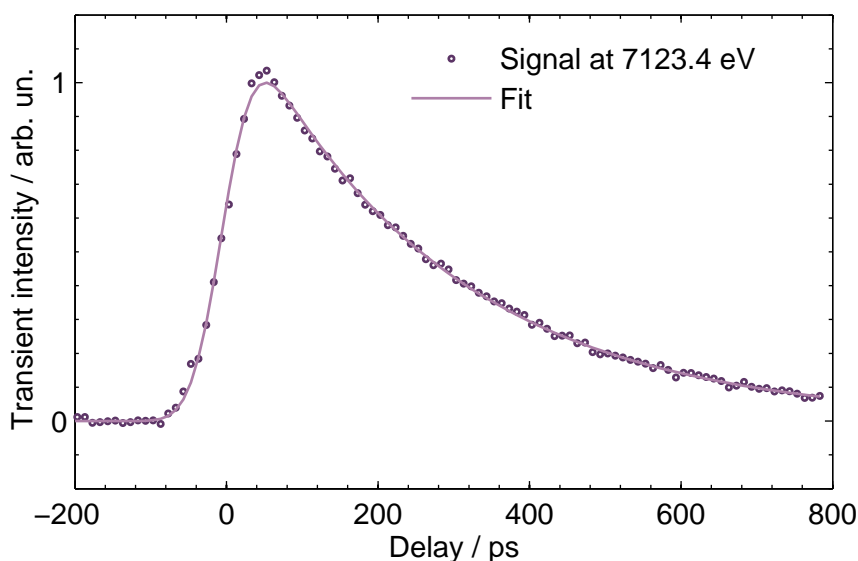


Figure 6.4: Time delay scan (solid points) at 7123.4 eV corresponding to feature B in Fig. 6.3 and a fit (solid line) of a Gaussian rise of (77 ± 3) ps convoluted with an exponential decay with (272 ± 4) ps. The measured decay time is in good agreement with the 280 ps lifetime of the lowest lying excited state of $[\text{Fe}(\text{dcpp})_2]^{2+}$ in CH_3CN found in [52]. The error bars are too small to be visible on the scale plotted here.

6.2.3 X-ray Emission Spectroscopy

TR XES were measured to determine the spin multiplicity of the energetically lowest lying excited state of $[\text{Fe}(\text{dcpp})_2]^{2+}$ but were also exploited to determine the excited state fraction of the laser excited ensemble. This is done in analogy to the cases of the thermally induced LS-HS transition of Fe complexes [118] as well as of ultrafast optically induced spin state changes of $[\text{Fe}(\text{bpy})_3]^{2+}$ [27]. We have measured the TR $K\alpha_1$ and TR $K\beta$ XES, which will be presented in the following subsections.

$K\alpha$ XES

The $K\alpha_1$ XES spectra of the ground state (=laser OFF), the laser excited ensemble (=laser ON) and their respective difference (=transient) are shown in Fig. 6.5. We have also measured the $K\alpha_1$ XES of solid (powder) reference samples with quartet ($S=3/2$) and quintet

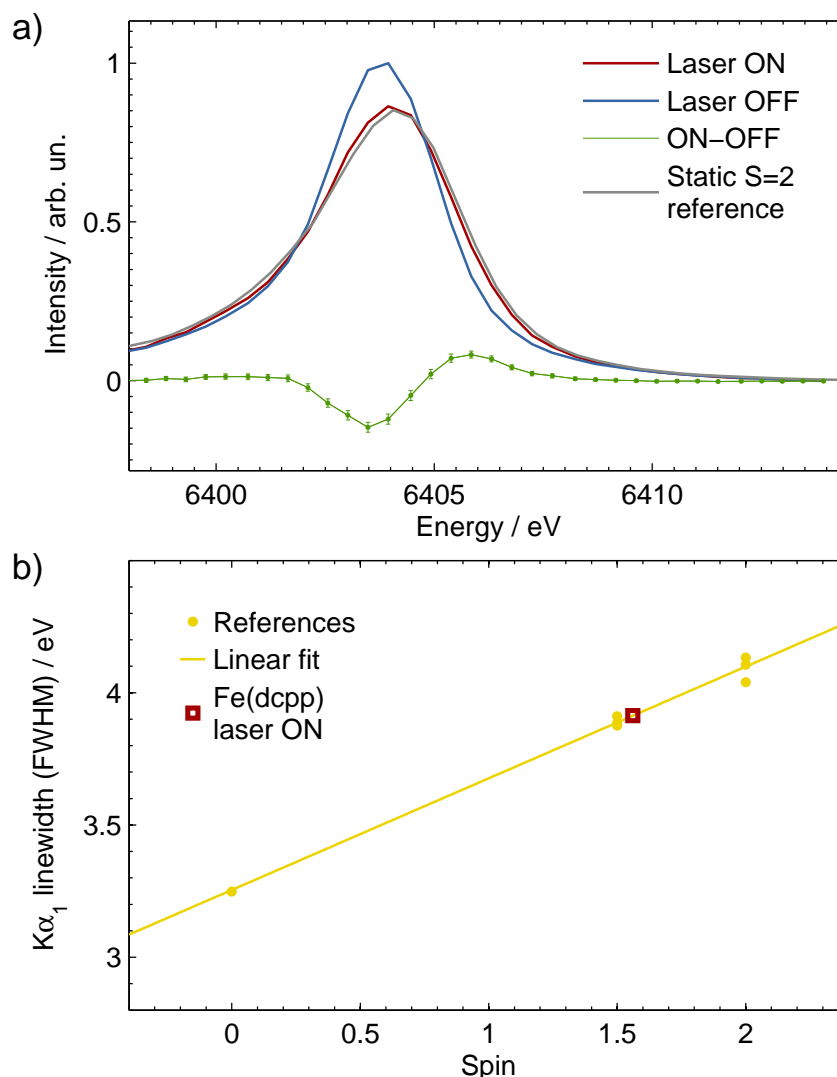


Figure 6.5: a) $K\alpha_1$ XES of $[\text{Fe}(\text{dcpp})_2]^{2+}$ in CH_3CN in ground state with $S=0$ (blue), 50 ps after photoexcitation at 532 nm (red) and transient difference (green) as well as $S=2$ reference (black). b) $K\alpha_1$ linewidths of $S=0$, $S=3/2$ as well as $S=2$ reference complexes as a function of spin-state of Fe center (yellow dots) and linear fit (yellow line). The linewidth of the laser excited spectrum from a) (red open square) corresponds to an average spin state of $\bar{S}_{\text{dcpp,LOn}} = 1.56$.

($S=2$) spin multiplicities. The spectrum of a $S=2$ reference is plotted in Fig. 6.5 as well. The dispersive plane of the XES spectrometer which has been used in the measurements presented here is the horizontal plane and thus also contains the X-ray beam direction. Thus the absolute energy calibration of the spectrometer depends critically on the source (= the liquid jet or the powder sample) position along the X-ray beam. When we inserted the powder samples we were only able to reproduce the source position along the X-ray beam direction to about 1-2 mm. This slight offset does not affect the resolution of the

spectrometer, but causes an offset on the order of up to 1-2 eV in the absolute energy calibration. This calibration has only been done ones for the whole set of measurements, including the TR XES of the liquid samples and all powder reference samples. For comparison we have shifted the spectra of the powder references arbitrarily in the plot. Most importantly, the analysis of the line shapes and line widths is not affected by this energy shift, as it depends only on the resolution of the spectrometer. To further facilitate a comparison of the spectra we have removed the background which is at least partially due to scattered light. We have assumed a constant background and used the value of the measured spectra at the high energy wings (i.e. at 6415 eV) for subtraction. Furthermore, the areas of all spectra have been normalized.

Compared to the ground state XES line shape, the laser excited ensemble exhibits a broadening, a decrease in peak height and a slight shift to higher energies. The XES line shape of the S=2 reference is even broader and has an even lower maximum intensity at the peak. Overall, the laser excited spectrum resembles very well the S=2 reference, which already points towards the energetically lowest lying excited state of the $[\text{Fe}(\text{dcpp})_2]^{2+}$ being a S=2 state.

K β XES

The advantage of K β over K α XES is that the HS spectra show, next to a broadening and a shift, an additional feature whose intensity depends on the spin state.

The sample concentration of 10 mM used here was slightly lower than during the K α_1 (and EXAFS) measurements. The laser power was about 2.5 W at a repetition rate of 0.931 MHz, corresponding to a pulse energy of 2.7 μJ . The pulse energy has been set such that the maximum transient XANES signal (at the B feature) matches the transient signal of the XANES measurements in sections 6.2 and 6.2.3, to ensure an identical excited state fraction. The larger pulse energy required to match the transient is most probably due to a larger laser spot size. Furthermore, the delay was set to 50 ps. The measured spectra, shown in Fig. 6.6a), correspond to the one with (red) and without (blue) laser excitation, as well as to the transient difference (green). The spectrum of a singlet (S=0) reference compound from Ref. [39] is plotted for comparison (blue dotted line), it resembles very well the GS spectrum of $[\text{Fe}(\text{dcpp})_2]^{2+}$. The reference spectra are shifted by 0.3 eV, which is in the range of a typical calibration error of the spectrometers. The S=0 reference spectrum is further used to scale our measured spectra to the reference spectra. Due to the large pixel size of the Pilatus 100k detector and the relatively short focal length of the analyzer crystal in the von Hamos spectrometer the energy spacing between two energy points is ~ 0.6 eV.

We have compared the measured transient difference XES of $[\text{Fe}(\text{dcpp})_2]^{2+}$ to the quintet-singlet and triplet-singlet differences of reference spectra (from [39], see Fig. 3.9 b)), the transient difference is plotted together with the reference differences scaled to the

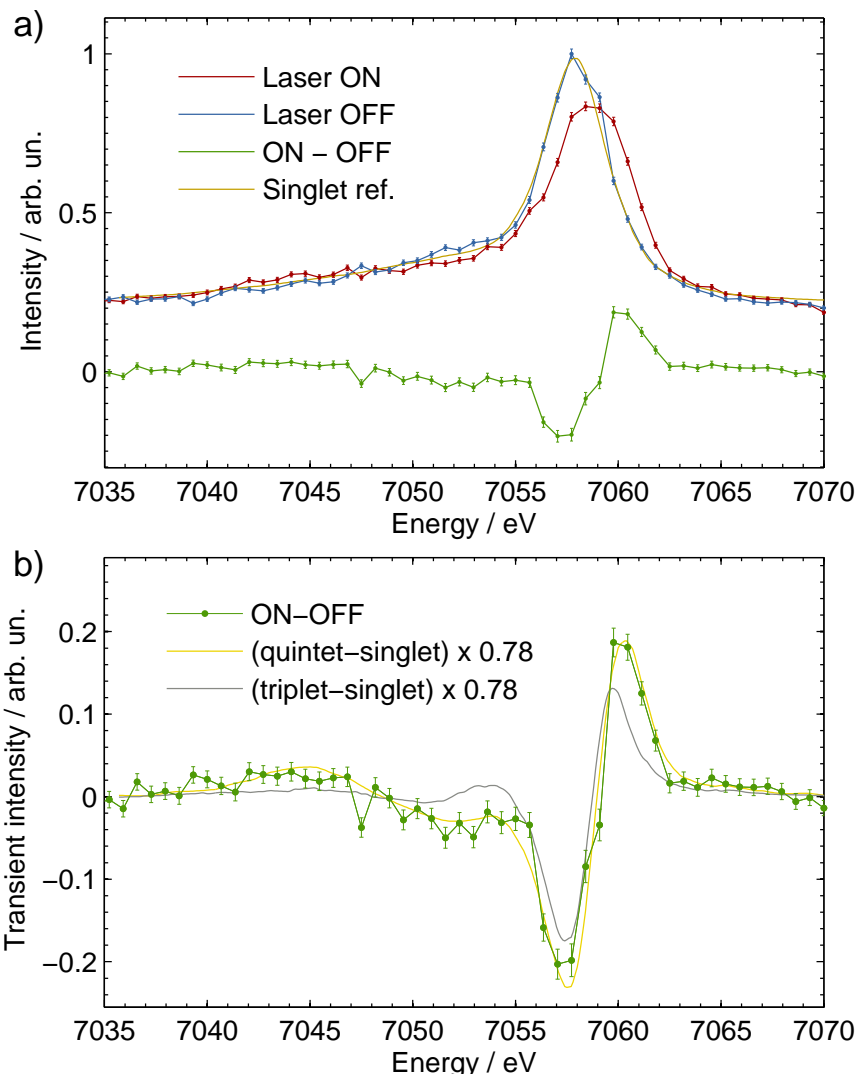


Figure 6.6: a) $\text{K}\beta$ XES of $[\text{Fe}(\text{dcpp})_2]^{2+}$ in CH_3CN in ground state with $S=0$ (blue solid line), after photoexcitation at 532 nm (red solid line) and transient difference (green line and points), the $S=0$ reference from [39] (yellow line) is plotted for comparison. b) transient difference as in a) (green points) together with reference transients for quintet-singlet (yellow) and triplet-singlet (grey) transition, both scaled by 78 % (references from [39]).

78 % excited state fraction of $[\text{Fe}(\text{dcpp})_2]^{2+}$ determined in section 6.2.3. The quintet-singlet reference difference matches the measured transient almost perfectly in intensity. Furthermore, the measured transient of $[\text{Fe}(\text{dcpp})_2]^{2+}$ shows the expected spectral feature of a quintet-singlet transient, i.e. the shoulder at 7045 eV, while the positive feature at 7055 eV which is expected for a triplet-singlet difference is clearly missing. This independently verifies the excited state of $[\text{Fe}(\text{dcpp})_2]^{2+}$ being of quintet spin multiplicity.

6.3 Analysis and Discussion

6.3.1 Analysis of X-ray Emission Spectra

To further refine the spin state of the laser excited ensemble, which consists of a superposition of GS and the ES, we have analyzed the line width of the $K\alpha$ XES spectra. In Ref. [119] the $K\alpha_1$ line width has been shown to be linearly dependent on the number of unpaired $3d$ electrons, thus the spin state of $3d$ transition metals and a line width analysis of the $K\alpha_1$ line to determine the spin state in molecular spin transition systems has been suggested in Ref. [118]. This has been applied here to determine the average spin state of the photo-excited ensemble of solvated $[\text{Fe}(\text{dcpp})_2]^{2+}$, containing molecules in both ground and excited state. The $K\alpha_1$ full-width half-maximum (FWHM) line-width of the ground state ($S=0$) of $[\text{Fe}(\text{dcpp})_2]^{2+}$ as well as those of the HS references are plotted in 6.5b) (yellow points). A linear regression (yellow line) shows the proportionality between spin state and $K\alpha_1$ line width. The line-width of the laser excited ensemble can be found at $\bar{S} = 1.56$.

The average spin \bar{S}_{LON} of the laser excited ensemble is a superposition of the GS and ES spin state, S_{GS} and S_{ES} , respectively, weighted with the excited state fraction f ,

$$\bar{S}_{\text{LON}} = (1 - f) S_{\text{GS}} + f S_{\text{ES}} . \quad (6.1)$$

As the oxidation state of the Fe center of $[\text{Fe}(\text{dcpp})_2]^{2+}$ does not change, we can assume that the pure excited state can only have either singlet, triplet or quintet spin multiplicity. As the excited ensemble has an average spin of $\bar{S}_{\text{LON}} = 1.56$ and assuming that we have only a single excited state species present we can conclude that the spin of the lowest lying excited state must be

$$S_{\text{ES}} = 2 \quad (6.2)$$

with an excited state fraction of

$$f = 78\% . \quad (6.3)$$

This result relies strongly on the assumption that we have only a single excited state species. Of course, an average spin of $\bar{S} = 1.56$ could also stem from a superposition of quintet and triplet excited state. Possible scenarios could allow for a triplet contribution up to 44 % triplet, with a quintet contribution as low as 56 % and no ground state in the laser excited ensemble (although experience tells us that it is very unlikely to excite 100 % of the molecules in the volume probed by the X-rays).

To analyze the $K\beta$ XES spectra we have calculated the reduced χ_r^2 , which is the χ^2 divided by the degrees of freedom given by the number of data points N minus the number of fit parameters n_{fit} minus 1. χ^2 is the sum of the squared deviations of a model transient M_i from the measured transient S_i with standard deviation ΔS_i at each X-ray emission

energy E_i [227],

$$\chi_r^2 = \frac{\chi^2}{N - n_{\text{fit}} - 1} \quad \text{with} \quad \chi^2 = \sum_{i=1}^N \left(\frac{S_i - M_i}{\Delta S_i} \right)^2. \quad (6.4)$$

The model transient consists of a sum of the triplet T_i and quintet Q_i reference transients (as from Fig. 3.9b)), weighted with a triplet (f_T) and quintet (f_Q) state fraction, respectively, $M_i = f_T T_i + f_Q Q_i$. Fig. 6.7 shows a 2D map of the χ_r^2 calculated for each f_T and f_Q between 0 % and 100 % (although a total excited state fraction $f_T + f_Q > 100$ % is physically impossible). The minimum is achieved with $f_T = 0$ % and $f_Q = 72$ % (meaning the other 28 % of the excited ensemble are still in ground state). The area in which the χ^2 increase by up to ~ 6 , or the χ_r^2 by 12 %, compared to its minimum value gives a 95 % confidence interval for this optimization [227]. This confidence interval, which is the dark innermost area in Fig. 6.7, allows for a possible triplet contribution up to $f_T < 24$ % and a quintet contributions $f_Q > 57$ % and $f_T < 78$ %.

This measurement proves our assignment of the energetically lowest lying excited state of $[\text{Fe}(\text{dcpp})_2]^{2+}$ to have a quintet spin multiplicity and helps to exclude the presence of a second excited state species with a different spin state. Last but not least it also roughly verifies the excited state fraction of 78 % which has been found as a result of the $\text{K}\alpha$ XES analysis.

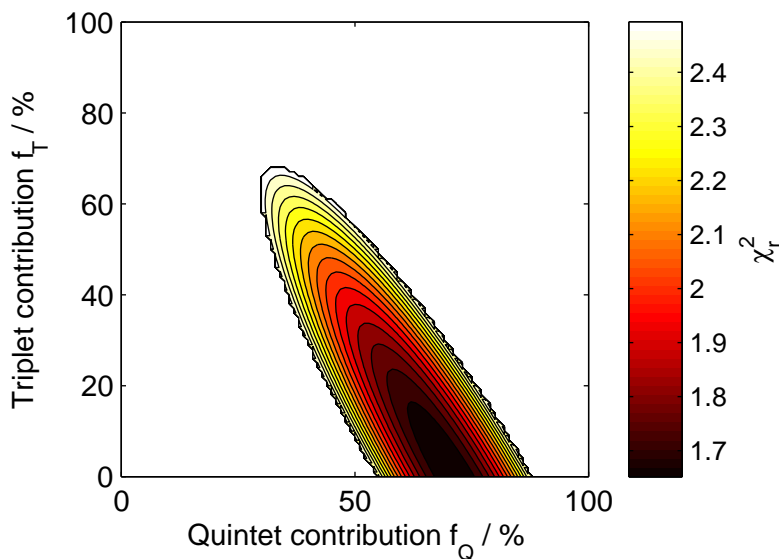


Figure 6.7: χ_r^2 values of transient $\text{K}\beta$ XES fit as a function of triplet-singlet and quintet-singlet references transient contributions. The minimum is observed at 0% triplet and 72% quintet, thus confirming a pure $\text{LS} \rightarrow \text{HS}$ transition. The two innermost dark areas corresponds to the 95 % confidence interval.

6.3.2 EXAFS analysis

The analysis of the measured EXAFS presented in this section includes the following steps: i) Normalization and background removal, ii) modeling of EXAFS scattering paths, iii) fit of the ground state EXAFS and iv) fit of the excited state EXAFS. The measurements were taken in the same experimental campaign and the EXAFS measurements on $[\text{Fe}(\text{terpy})_2]^{2+}$ and the analysis is done in full analogy to the analysis on the $[\text{Fe}(\text{terpy})_2]^{2+}$ measurements [25].

Normalization, Background Removal and Conversion of EXAFS Spectra into k - and R - Space using Athena

As a first step of the EXAFS analysis the spectra presented in Fig. 6.3 have to be background subtracted and normalized. This is done using the ATHENA 0.9.21 software which is part of the Ifeffit software package [228]. The description of the background removal and normalization follows the lines of Refs. [65, 228, 229]. The whole procedure for the ground state spectrum of $[\text{Fe}(\text{dcpp})_2]^{2+}$ is summarized in Fig 6.8.

After normalization to the incident X-ray flux (I_0), the experimental X-ray absorption spectrum $\mu(E)$ measured in TFY is imported in ATHENA. The background function $\mu_{bg}(E)$ is determined with the AUTOBK algorithm. The edge position E_0 is set to the first inflection point of the edge, i.e. the first large maximum of its derivative. The pre- and post-edge regions are approximated by polynomials and the difference of the extrapolated polynomials at E_0 delivers the edge step $\mu_{bg}(E_0)$. Using these, the background subtraction can be done via

$$\chi(E) = \frac{\mu(E) - \mu_{bg}(E)}{\mu_{bg}(E_0)}. \quad (6.5)$$

$\mu(E)$, $\mu_{bg}(E)$ as well as the post and pre-edge polynomials can be found in Fig. 6.8a). The next step is to convert the EXAFS spectrum $\chi(E)$ from energy into (photo-electron wave vector) k -space by applying the E - k relation

$$k = \frac{\sqrt{2m_e(E - E_0)}}{\hbar} \approx 0.51232 \text{\AA}^{-1} \sqrt{E - E_0} [\text{eV}^{-1/2}]. \quad (6.6)$$

Here E is the X-ray energy and E_0 the binding energy of the electron in the respective shell. The spectrum can additionally be weighted by k , k^2 , k^3 or an arbitrary exponential of k to enhance the feature in the range of larger k . The k^2 weighted EXAFS spectrum $\chi(k)$ can be seen in Fig 6.8b). This spectrum can be truncated by application of a window function (in this example from $k = 2.5$ to 10.5 , with $dk = 0.2$ broad edges) and subsequently Fourier transformed into R -space, giving the pseudo-radial distribution function in Fig. 6.8c). The back transform into k space, which we refer to now as q space, after further truncation (with a similar window function as in k -space) in R space can be found in Fig. 6.8d).

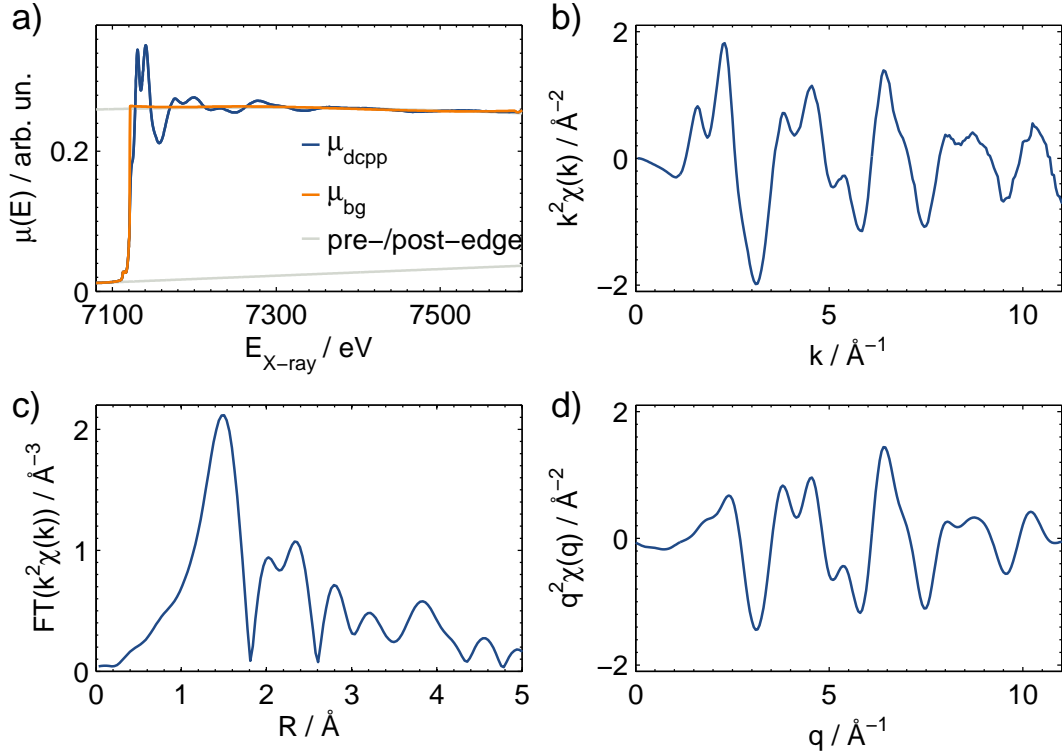


Figure 6.8: Ground state XAS spectrum of $[\text{Fe}(\text{dcpp})_2]^{2+}$ a) in E -space, b) in k -space, c) in Fourier-transform R -space and d) in back-Fourier-transformed q -space (d). See text for details.

General EXAFS fitting procedure for GS and ES

Once the background subtracted and normalized EXAFS spectrum in k - and R -space is obtained it can be used to refine the bond lengths R_j of the absorption center (here Fe) to the different next neighbor atoms. This done by modeling the EXAFS spectrum and refining the structure in order to fit the model to the measured data.

As discussed in Section 3.2.3, the EXAFS spectrum in k space is described by the EXAFS formula [112, 113]

$$\chi(k) = \sum_j S_0^2 N_j \frac{|f_j(k)|}{k R_j^2} \sin(2kR_j + 2\delta_e + \phi) e^{-2R_j/\lambda(k)} e^{-2\sigma_j^2 k^2}, \quad (6.7)$$

where S_0^2 is an amplitude reduction factor, N_j the degree of degeneracy or the number of equivalent scatterers j , $|f_j(k)|$ the backscattering amplitude, R_j is the half of effective scattering path length, i.e. the interatomic distance, δ_e the central-atom partial-wave phase shift of the final state, $\lambda(k)$ the mean free path of the photoelectron and σ_j^2 the Debye-Waller factor [16].

First the EXAFS spectra are simulated using FEFF8 [114], an example FEFF input file

can be found in Appendix D. Then the simulated spectra are fitted to the experimental data in Fourier transform R -space using Artemis (also part of the Iffeffit toolbox) [228].

The photoelectron scattering paths are imported from the FEFF8 calculation. Here we have limited the paths to those with a backscattering amplitude $> 5\%$ and a path lengths $< 5 \text{ \AA}$. The fit has been performed in R -space with k^2 -weighted EXAFS spectra. In k -space the spectrum has been truncated with a "Hanning"-type window in the range from $k = 2.5 \text{ \AA}$ to $k = 10.5 \text{ \AA}$ with 0.2 \AA wide edges. The fitting range in R -space has been set to 1.0 \AA to 3.6 \AA and another "Hanning"-type window of this range, with 0.2 \AA wide edges, has been used to back-Fourier-transform the spectrum to q -space. The options to also fit a background (slowly varying with energy) as well as to phase-correct the spectra in R -space have not been used.

For the whole fit procedures for both the GS and ES we have defined the following set of 10 fit parameters: An amplitude reduction factor S_0^2 , an energy shift ΔE_0 , bond lengths changes of the bonds in the first (nitrogen) and second (carbon) coordination shell grouped into axial and equatorial direction, $\Delta R(Fe-N_{ax})$, $\Delta R(Fe-N_{eq})$, $\Delta R(Fe-C_{ax})$, $\Delta R(Fe-C_{eq})$, one Debye-Waller factor for all nitrogens, one for all first shell carbons and one for all longer photoelectron scattering paths (including also multiple scattering paths), respectively, σ_N^2 , σ_C^2 and σ_{rest}^2 as well as a small correction to the path length of all other scattering paths ΔR_{rest} . Although we cannot obtain any structural information from the longer scattering paths beyond the second (=carbon) shell, the fit especially in the k -space improves remarkably by including these longer scattering paths.

Ground State EXAFS Fit

As an initial guess for the structure, the DFT calculation of the 1A_1 state in Table 6.1 is used and the EXAFS scattering paths have been simulated in FEFF8 using these coordinates.

In the GS fit, only 8 of the above mentioned 10 parameters have been optimized. To decrease the parameter space we have set $\Delta R(Fe-N_{ax}) = R(Fe-N_{eq})$ and $\Delta R(Fe-C_{ax}) = \Delta R(Fe-C_{eq})$. The result of the fit in k , R and q space is shown in Fig. 6.9. The non-structural parameters obtained from the GS EXAFS fit as well as the corrections to the initial guess from the DFT calculation are summarized in Table 6.2.

We would like to evaluate the non-structural parameters in comparison to the results of the TR EXAFS analysis of the similar iron spin transition systems $[Fe(terpy)_2]^{2+}$ in H_2O published in [25] and in CH_3CN in [225, 226] as well as to the one of $[Fe(bpy)_3]^{2+}$ in H_2O from [65]. The obtained amplitude reduction factor S_0^2 of 0.80 ± 0.07 is in excellent agreement with the ones of $[Fe(terpy)_2]^{2+}/H_2O$ (0.78 ± 0.04) and $[Fe(bpy)_3]^{2+}/H_2O$ (0.75 ± 0.20) but lower although still within the errors of the one of $[Fe(terpy)_2]^{2+}/CH_3CN$ (0.97 ± 0.10). The same holds for the Debye-Waller factor of the 1st shell nitrogen σ_N^2 which is found to be $0.0022 \pm 0.001 \text{ \AA}^2$, also in very good agreement with the values found for $[Fe(terpy)_2]^{2+}$ (both around 0.003) but smaller than the one of $[Fe(bpy)_3]^{2+}/H_2O$ ($0.006 \pm 0.001 \text{ \AA}^2$). The

Debye-Waller factor of the 2nd shell carbon σ_C^2 is found to be $0.0046 \pm 0.0014 \text{ \AA}^2$, thus larger than σ_N^2 and also in agreement with the one of $[\text{Fe}(\text{terpy})_2]^{2+}/\text{CH}_3\text{CN}$ ($0.004 \pm 0.003 \text{ \AA}^2$). The increase compared to σ_N^2 is reasonable as the carbons are only indirectly linked to the Fe via the nitrogen, leading to a larger uncertainty in the Fe-C distance. The Debye-Waller factor of all longer paths is with $\sigma_{rest}^2 = 0.009 \pm 0.003 \text{ \AA}^2$ about twice as big as σ_N^2 and σ_C^2 which is very likely as the longer scattering paths are dominated by contributions from multiple (double) scattering paths. For multiple scattering paths the Debye-Waller factors of the single scattering events add up.

The corrections to the structure which the fit delivered are $\Delta r_{N_{ax}} = \Delta r_{N_{eq}} = -0.038 \pm 0.006 \text{ \AA}$, $\Delta R(\text{Fe-N}_{ax}) = R(\text{Fe-N}_{eq}) = -0.023 \pm 0.012 \text{ \AA}$ and $\Delta R_{rest} = -0.044 \pm 0.018 \text{ \AA}$. These are only small corrections to the initial ground state DFT structure.

The Fe-N and Fe-C bond lengths which we obtain after correcting the initial guesses from the DFT structures by the corrections from the EXAFS analysis are summarized in Table 6.3. Thus the fit reproduces the structure obtained from DFT as well as the structure obtained from X-ray crystallography.

Excited State EXAFS Fit

Table 6.2: Upper panel: Non-structural parameters obtained from the EXAFS fit of $[\text{Fe}(\text{dcp})_2]^{2+}$. In the ground state fit, all parameters are optimized, while in the excited state fit, all except for E_0 are locked to the values obtained from the ground state. Lower panel: Difference between the bond lengths obtained from the EXAFS fit and those from the initially guessed structure obtained from the DFT calculation (see Table 6.1). In the table all energies are given in eV, distances in \AA , Debye-Waller factors in \AA^2 . The given error estimates are directly obtained during the fit in Artemis.

	S_0^2	ΔE_0	σ_N^2	σ_C^2	σ_{rest}^2	χ^2
GS	0.80 ± 0.07	-7.07 ± 0.54	0.0022 ± 0.001	0.0046 ± 0.0014	0.009 ± 0.003	387
ES	0.80	-6.37 ± 0.86	0.0022	0.0046	0.009	332

	$\Delta R(\text{Fe-N}_{ax})$	$\Delta R(\text{Fe-N}_{eq})$	$\Delta R(\text{Fe-C}_{ax})$	$\Delta R(\text{Fe-C}_{eq})$	ΔR_{rest}
GS	-0.038 ± 0.006	$=\Delta R(\text{Fe-N}_{ax})$	-0.023 ± 0.012	$=\Delta R(\text{Fe-C}_{ax})$	-0.044 ± 0.018
ES	-0.109 ± 0.016	$+0.038 \pm 0.011$	-0.101 ± 0.038	0.014 ± 0.020	$+0.014 \pm 0.020$

The EXAFS scattering paths have been simulated in FEFF8 using the DFT coordinates of the $^5\text{T}_2$ state. The excited state EXAFS fit has been done by setting the non-structural parameters S_0^2 , σ_N^2 , σ_C^2 and σ_{rest}^2 to those obtained from the GS fit, leaving only the bond-lengths $\Delta R(\text{Fe-N}_{ax})$, $\Delta R(\text{Fe-N}_{eq})$, $\Delta R(\text{Fe-C}_{ax})$, $\Delta R(\text{Fe-C}_{eq})$ and ΔR_{rest} as well as the energy shift ΔE_0 as open fit parameters to be determined. The EXAFS fit has been performed with the exact same settings (same range in R - and k -, same k^2 weighting, no background fitted) as the GS fit. The fit result in k -, R - and q -space is plotted in Fig.

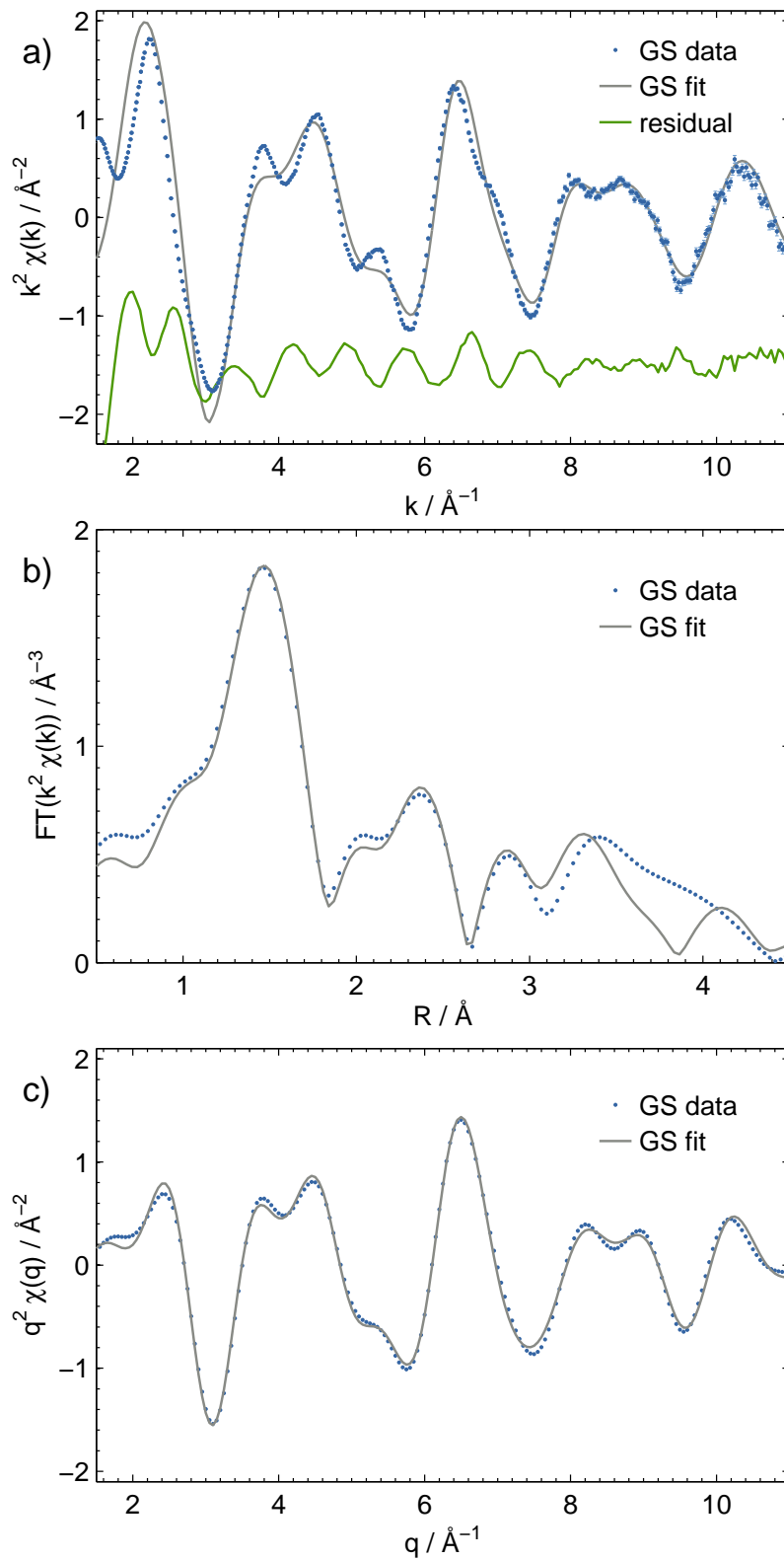


Figure 6.9: Ground state EXAFS of $[\text{Fe}(\text{dcp})_2]^{2+}$ in CH_3CN . a) In k -space, b) in Fourier-transform R -space and c) in back transformed q -space. The experimental data (blue points) and fit (solid grey line) deviate only by high frequency contributions, see residual (green line) in a).

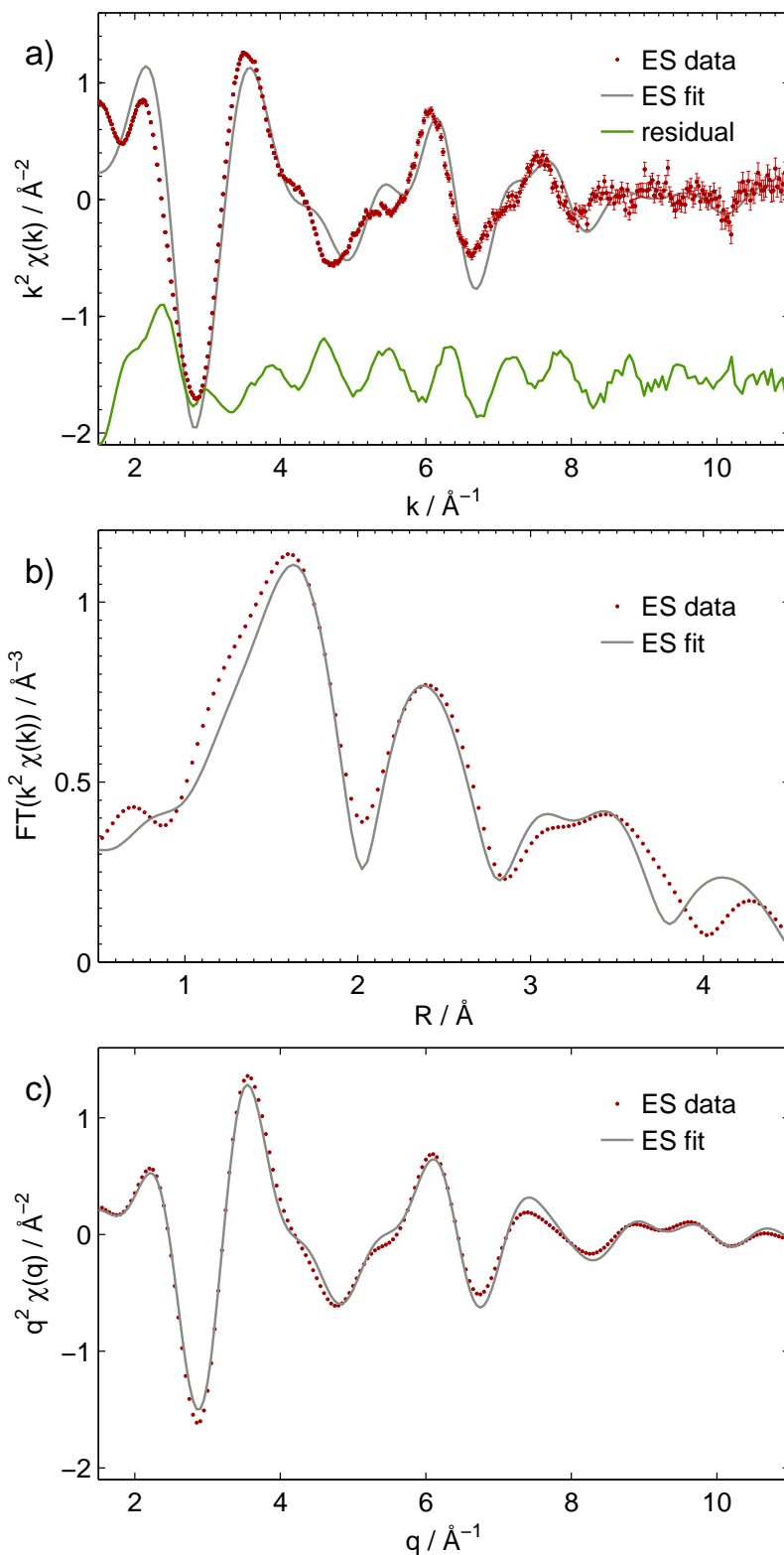


Figure 6.10: Excited state EXAFS of $[\text{Fe}(\text{dcp})_2]^{2+}$ in CH_3CN . a) In k -space, b) in Fourier-transform R -space and c) in back transformed q -space. The experimental data (red points) and fit (solid grey line) deviate only by high frequency contributions, see residual (green line) in a).

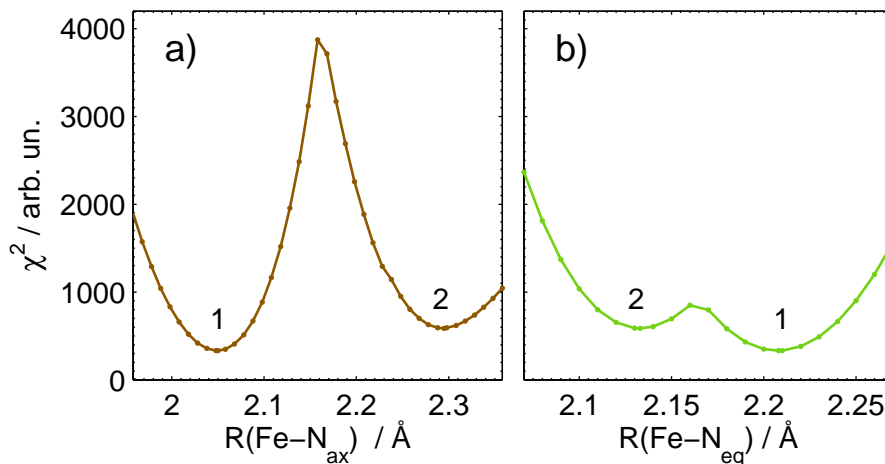


Figure 6.11: χ^2 as a function of a) $R(Fe-N_{ax})$ and b) $R(Fe-N_{eq})$. Two minima are visible: The absolute minimum (marked with 1 in both plots) corresponds to the EXAFS excited state fit result in section 6.3.2 with contracted axial Fe-N bonds compared to the equatorial ones, the second local minimum (marked 2) corresponds to a structure in which the axial Fe-N bonds are elongated compared to the equatorial ones.

6.10 and the resulting parameters are summarized in Table 6.2.

The resulting $\Delta E_0 = (-6.37 \pm 0.86)$ eV is slightly smaller than the one found in the GS and results in a relative shift of the GS to the ES of $\Delta E_{0,ES} - \Delta E_{0,GS} = (+0.7 \pm 1.1)$ eV, which is in line with the shifts found for $[Fe(terpy_2)]^{2+}$ of $(+1.8 \pm 0.9)$ eV in [25] and $(+1.9 \pm 0.4)$ eV in [226].

The bond-lengths deviate strongly from the initially guessed DFT structures, a comparison between the initial guess for the 5T_2 state can be found in Table 6.2. The $Fe-N_{ax}$ bond length is found to be (0.109 ± 0.016) Å shorter and the $Fe-N_{eq}$ bond is found to be $(+0.038 \pm 0.011)$ Å longer than the one of the DFT 5T_2 structure. Furthermore, we find that the deviations of the Fe-C bonds in axial and equatorial direction agree within the error bars with the deviations of the Fe-N bonds, i.e. $\Delta R(Fe-N_{ax}) \approx \Delta R(Fe-C_{ax})$ and $\Delta R(Fe-N_{eq}) \approx \Delta R(Fe-C_{eq})$. This is also expected, as the C-N bonds within the pyridine rings are very rigid, thus the carbon in axial and equatorial direction should follow the respective nitrogen to which they are directly bound. The fit value for all other bond lengths, which can be seen as an average correction of all longer scattering paths, is almost negligible with $\Delta R_{rest} = (+0.014 \pm 0.020)$ Å. The bond lengths from the initially guessed DFT structures are corrected by these corrections and the EXAFS refined first and second coordination shell bond distance are summarized in Table 6.3.

The here presented minimum of the excited state EXAFS fit is the absolute minimum, but at least another local minimum exists. In the second local minimum found in the analysis, the axial bonds are elongated compared to the equatorial ones. To visualize the second local minimum, we have plotted χ^2 as a function of $R(Fe-N_{ax})$ in Fig. 6.11 a) and as a function of $R(Fe-N_{eq})$ in Fig. 6.11 b).

6.3.3 Discussion of EXAFS Refined Structures and Comparison to Simulation

We have used the Fe-N and Fe-C bond lengths of the DFT structures from Table 6.1 and corrected them using the EXAFS fit results for both GS and ES (lower panel in Table 6.2). In Table 6.3 these final results are summarized. While the GS EXAFS fit confirmed the almost perfect octahedral structure of $[\text{Fe}(\text{dcpp})_2]^{2+}$ in its $^1\text{A}_1$ GS, this octahedral structure is not preserved in the ES, in contrast to the DFT calculations. The pyridine rings in axial directions only move ~ 0.09 Å away from the Fe, while those in equatorial direction move ~ 0.23 Å away, leading to a strongly Jahn-Teller distorted structure where the difference between of bond lengths between axial and equatorial direction is ~ 0.16 Å.

Table 6.3: Experimentally determined first and second coordination shell bond lengths of $[\text{Fe}(\text{dcpp})_2]^{2+}$ in its ground state, its excited state, and their respective difference. All bond lengths are given in Å.

	$R(\text{Fe}-N_{ax})$	$R(\text{Fe}-N_{eq})$	$R(\text{Fe}-C_{ax})$	$R(\text{Fe}-N_{eq1})$	$R(\text{Fe}-N_{eq2})$
Ground state	1.961 ± 0.006	1.982 ± 0.006	2.908 ± 0.012	2.924 ± 0.012	2.921 ± 0.012
Excited state	2.049 ± 0.016	2.208 ± 0.011	2.972 ± 0.038	3.098 ± 0.020	3.073 ± 0.020
Difference ES - GS	+0.089 ± 0.018	+0.226 ± 0.013	+0.064 ± 0.040	+0.174 ± 0.024	+0.152 ± 0.024

6.3.4 Excited State Lifetime

To find an alternative explanation for the unusually short (280 ps in CH_3CN) lifetime of the excited state of $[\text{Fe}(\text{dcpp})_2]^{2+}$ we aimed to find an alternative potential energy surface (PES) scheme of the $^1\text{A}_1$ and $^2\text{T}_2$ states of $[\text{Fe}(\text{dcpp})_2]^{2+}$ and $[\text{Fe}(\text{bpy})_3]^{2+}$, which would explain the 0.28 ps ground state recovery time of $[\text{Fe}(\text{dcpp})_2]^{2+}$ in CH_3CN , which is three-fold shorter than the 0.96 ns of $[\text{Fe}(\text{bpy})_3]^{2+}$ in CH_3CN .

According to Marcus theory the rate of an electron transfer process is given by [64, 223]

$$k_{ET} = \nu_N \kappa_{el} \exp\left(-\frac{\Delta G^\ddagger}{RT}\right) \quad \text{with} \quad \Delta G^\ddagger = \frac{\lambda}{4} \left(1 + \frac{\Delta G^0}{\lambda}\right). \quad (6.8)$$

Here ν_N is the average nuclear frequency factor, κ_{el} the electronic transmission coefficient, ΔG^\ddagger the activation energy (i.e. the "barrier"), ΔG^0 the standard free energy change of the reaction and λ the nuclear reorganizational energy [64]. If we assume that ν_N and κ_{el} are equivalent for $[\text{Fe}(\text{bpy})_3]^{2+}$ and $[\text{Fe}(\text{dcpp})_2]^{2+}$ the rate of the electron transfer only differs by the different activation energies, which depends on the ligand field strength. Using these assumptions, the by a factor 3 times shorter lifetime of the excited state of

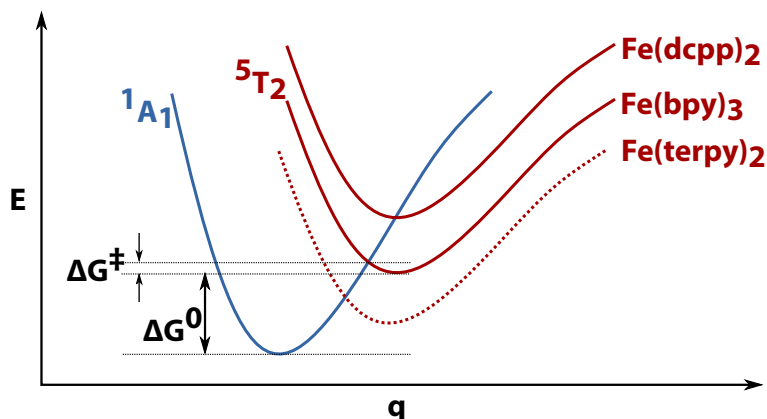


Figure 6.12: Qualitative comparison of the ordering of 1A_1 and 5T_2 potential energy surfaces as a possible explanation of the 2T_2 excited state lifetimes of $[\text{Fe}(\text{terpy})_2]^{2+}$ ($\tau=5.4$ ns), $[\text{Fe}(\text{bpy})_3]^{2+}$ ($\tau=0.96$ ns) and $[\text{Fe}(\text{dcpp})_2]^{2+}$ ($\tau=0.28$ ns).

$[\text{Fe}(\text{dcpp})_2]^{2+}$ compared to $[\text{Fe}(\text{bpy})_3]^{2+}$ could be explained by the following scenario: The PES of the 1A_1 and 5T_2 states of $[\text{Fe}(\text{dcpp})_2]^{2+}$ cross without barrier, $\Delta G^\ddagger \approx 0$ eV, while for $[\text{Fe}(\text{bpy})_3]^{2+}$ the barrier is $\Delta G^\ddagger \approx 30$ meV (i.e. on the order of thermal energies at room temperature, thus still very small). For room temperature ($T \approx 300$ K) the exponential factor in Equation 6.8 for $[\text{Fe}(\text{bpy})_3]^{2+}$ is then

$$\exp(-30 \text{ meV}/RT) \approx 1/3 \quad (6.9)$$

while this factor for $[\text{Fe}(\text{dcpp})_2]^{2+}$ is

$$\exp(0 \text{ meV}/RT) \approx 1. \quad (6.10)$$

The ratio of the two exponential factors corresponds than to the ratio of ET rates k_{bpy} of $[\text{Fe}(\text{bpy})_3]^{2+}$ and k_{dcpp} of $[\text{Fe}(\text{dcpp})_2]^{2+}$,

$$\frac{k_{\text{bpy}}}{k_{\text{dcpp}}} \approx \frac{\exp(-30 \text{ meV}/RT)}{\exp(0 \text{ meV}/RT)} \approx 1/3. \quad (6.11)$$

Thus this would explain the factor 3 difference in excited state lifetimes. The potential energy surfaces for this scenario are shown in Fig. 6.12. Here the PES of $[\text{Fe}(\text{terpy})_2]^{2+}$ has been added to this scheme, following the description in [52].

These estimates concerning the barrier of $[\text{Fe}(\text{dcpp})_2]^{2+}$ and $[\text{Fe}(\text{bpy})_3]^{2+}$ have just recently been confirmed in the group of J. McCusker via temperature dependent optical transient absorption spectroscopy [230].

6.3.5 Comparison to $[\text{Fe}(\text{terpy})_2]^{2+}$

In the next step we would like to compare the EXAFS spectra as well as their respective fits of $[\text{Fe}(\text{dcpp})_2]^{2+}$ to the ones of $[\text{Fe}(\text{terpy})_2]^{2+}$ from [25].

In Fig. 6.13a) the EXAFS spectra of both systems in GS is shown. Both spectra differ strongly from each other, especially at larger photoelectron energies, i.e. larger k , the oscillations of $[\text{Fe}(\text{terpy})_2]^{2+}$ are damped more than those of $[\text{Fe}(\text{dcpp})_2]^{2+}$. This could be attributed to the fact that in the GS $[\text{Fe}(\text{dcpp})_2]^{2+}$ is almost perfectly octahedral, while $[\text{Fe}(\text{terpy})_2]^{2+}$ is Jahn-Teller distorted in the ground state (with $R(\text{Fe}-N_{ax}) \approx 1.87 \text{ \AA}$ and $R(\text{Fe}-N_{eq}) \approx 1.97 \text{ \AA}$ [25]). This mismatch of bond lengths in axial and equatorial Fe-N bond lengths leads to different photo-electron scattering paths which in the EXAFS spectrum at larger k are of opposite phase. This results in an effective damping of the oscillatory pattern of the GS EXAFS spectrum of $[\text{Fe}(\text{terpy})_2]^{2+}$.

In Fig. 6.13b), the transient EXAFS spectra are shown, which are very similar in both shape as well as in amplitude (none of the transients has been scaled). This reflects the fact that the Laser ON spectra contain about the same excited state fraction in both cases, 78 % for $[\text{Fe}(\text{dcpp})_2]^{2+}$ and 76 % for $[\text{Fe}(\text{terpy})_2]^{2+}$. Furthermore, it shows that the structural changes, which both samples exhibit upon laser excitation, are comparable, i.e. an Fe-ligand bond elongation of $\sim 0.2 \text{ \AA}$.

In Fig. 6.13c) the reconstructed ES spectra of both samples are shown. Both spectra are almost identical, which is expected, as the excited state structure of $[\text{Fe}(\text{terpy})_2]^{2+}$ (with $R(\text{Fe}-N_{ax}) \approx 2.04 \text{ \AA}$ and $R(\text{Fe}-N_{eq}) \approx 2.19 \text{ \AA}$ [25]) is very similar to the excited state structure of $[\text{Fe}(\text{dcpp})_2]^{2+}$.

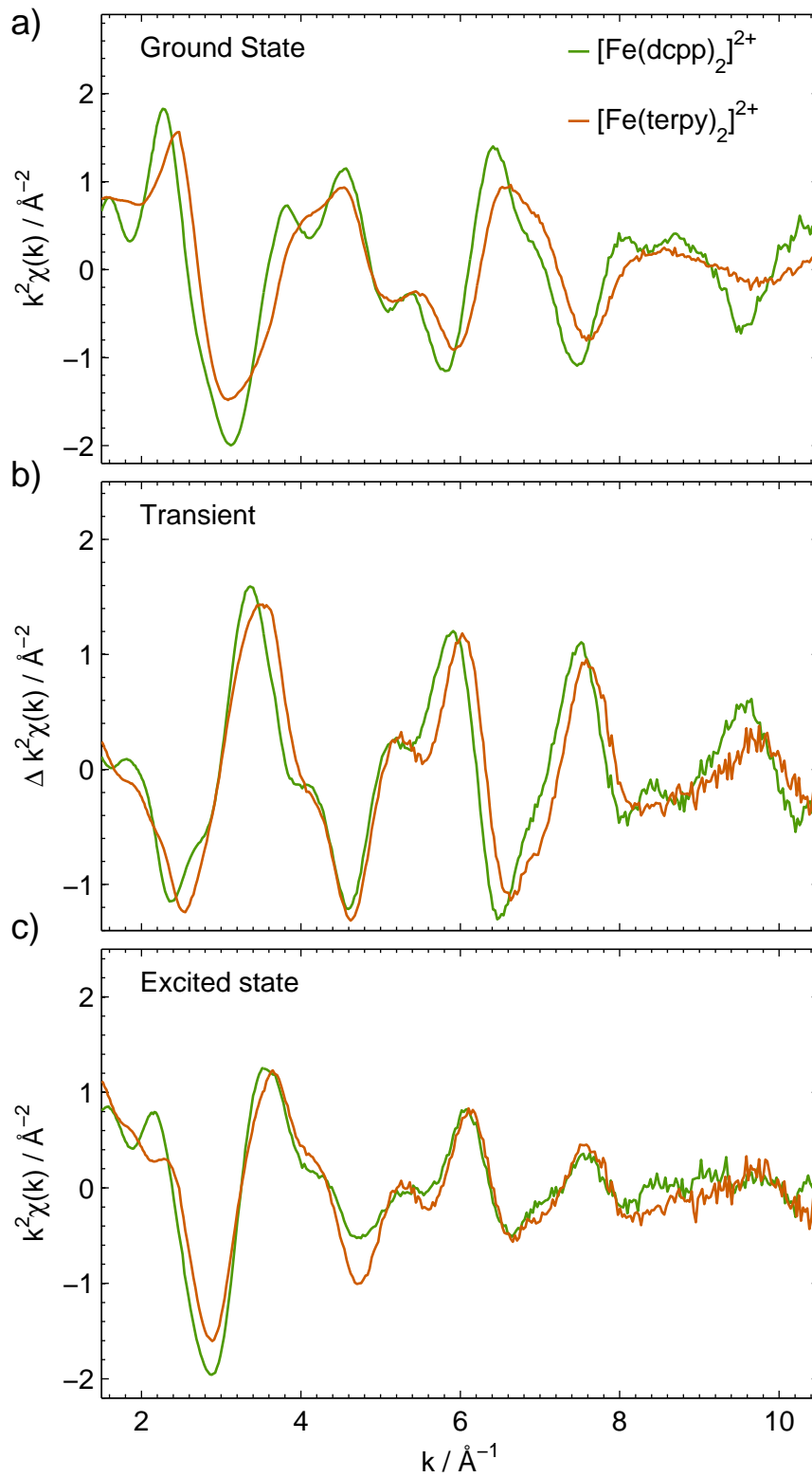


Figure 6.13: Comparison of EXAFS spectra of $[\text{Fe}(\text{dcpp})_2]^{2+}$ (green) and $[\text{Fe}(\text{terpy})_2]^{2+}$ (purple) of a) GS, b) transient and c) ES.

6.4 Summary

In this chapter we have used TR X-ray absorption and emission spectroscopy to characterize the ES of $[\text{Fe}(\text{dcpp})_2]^{2+}$. The key results are:

- Using $K\alpha$ and $K\beta$ XES we showed that the spin state of $[\text{Fe}(\text{dcpp})_2]^{2+}$ in its excited state is >1.5 and with $f=78\%$ becomes $S=2$. This confirms the 5T_2 and excludes the 3T_1 state as possible final product, this means that we can determine unambiguously the energetically lowest lying excited state of $[\text{Fe}(\text{dcpp})_2]^{2+}$ to be the 5T_2 .
- EXAFS has been applied to determine the geometric structural changes of the first and second coordination shells of $[\text{Fe}(\text{dcpp})_2]^{2+}$ (in CH_3CN) following 532 nm excitation. The average expansion of the Fe-N bonds of 0.16 Å agrees very well with the typical bond elongation observed in LS→HS transitions of Fe(II) complexes [62].
- The EXAFS analysis confirmed the almost perfectly octahedral ground state structure. But the excited state EXAFS fit suggests that the excited state is strongly Jahn-Teller distorted, very similar to the ES of $[\text{Fe}(\text{terpy})_2]^{2+}$, this result is further backed up by comparing the ES EXAFS spectra of $[\text{Fe}(\text{dcpp})_2]^{2+}$ and $[\text{Fe}(\text{terpy})_2]^{2+}$, which are found to be almost identical.
- A possible explanation of the extremely short excited state lifetime of 280 ps (a factor three shorter than the 0.9 ns of $[\text{Fe}(\text{bpy})_3]^{2+}$) is that $[\text{Fe}(\text{dcpp})_2]^{2+}$ has no activation barrier between the PES of the GS and ES, while the barrier for $[\text{Fe}(\text{bpy})_3]^{2+}$ is rather about 30 meV. This would, according to Marcus theory, explain the three-fold longer lifetime of the ES of $[\text{Fe}(\text{bpy})_3]^{2+}$ compared to $[\text{Fe}(\text{dcpp})_2]^{2+}$.

In a next step, we will analyze the EXAFS spectrum of $[\text{Fe}(\text{dvpp})_2]^{2+}$, where dvpp is di(vinylpyridyl)pyridine. $[\text{Fe}(\text{dvpp})_2]^{2+}$ is an isostructural complex to $[\text{Fe}(\text{dcpp})_2]^{2+}$ and their comparison will improve the understanding of their optically induced structural changes.

7 Direct Observation of Ultrafast High-valent Iron Formation

This chapter presents the investigation of the photophysical and photochemical processes leading to a high-valent iron complex, where the iron center is in the exotic oxidation state +V. This high-valent Fe complex is formed via flash-photolysis from its precursor *trans*[(cyclam)Fe^{III}(N₃)₂]⁺ in CH₃CN solution. Picosecond-resolved XAS is used to determine the spectral fingerprints of the Fe(V) complex as well as of a second photoproduct which is formed in a competing reaction channel. The ultrafast formation of both photoproducts is observed in real-time using femtosecond XAS and XES.

7.1 Introduction – *trans*[(cyclam)Fe^{III}(N₃)₂]⁺

High-valent Fe complexes are complexes with the metal Fe center in the unusual high oxidation states +IV, +V and +VI. High valent oxo-Fe complexes [231, 232] with a terminal oxygen ligand, as well as high-valent nitrido-Fe species [83, 233–238] with a terminal nitrogen ligand are known. Such high-valent Fe complexes are extremely reactive and play a major role in biochemical catalytic activity. The most prominent example for a high-valent iron-oxo species is the active site of the cytochrome P450 family, which acts in many enzymatic catalytic cycles in charge e.g. of drug metabolism [73, 239, 240]. Due to their tremendous reactivity, these high-valent Fe complexes are short-lived and difficult to detect within the natural catalytic cycles and at biological conditions (room temperature, in solution, etc.) [241]. Thus the early evidences of superoxidized species with Fe(V) and Fe(VI) were restricted to cryogenically cooled samples [83, 232–235]. Recently, two different high-valent Fe(V)-nitrido species in solution phase at room temperature have been investigated in the group of Peter Vöhringer. Here the high-valent Fe complexes were generated from their precursors [(cyclam-acetato)Fe^{III}(N₃)⁺ and *trans*[(cyclam)Fe^{III}(N₃)₂]⁺ via flash photolysis and subsequently detected using IR spectroscopy [53, 236, 237, 242].

Here we focus on the photophysics of *trans*[(cyclam)Fe^{III}(N₃)₂]⁺ (complex **1**) in CH₃CN. A UV-vis absorption spectrum of the reactant (**1**), i.e. the ground state molecule, is shown in Fig. 7.1. The reactions following the absorption of a photon in the absorption bands in the UV and vis spectral range have been studied extensively on ps to ns timescales. Torres-Alacan *et al.* have employed TR Fourier-transform IR (FTIR) spectroscopy to show the formation of the octahedral Fe(V) complex at room temperature in solution phase [53].

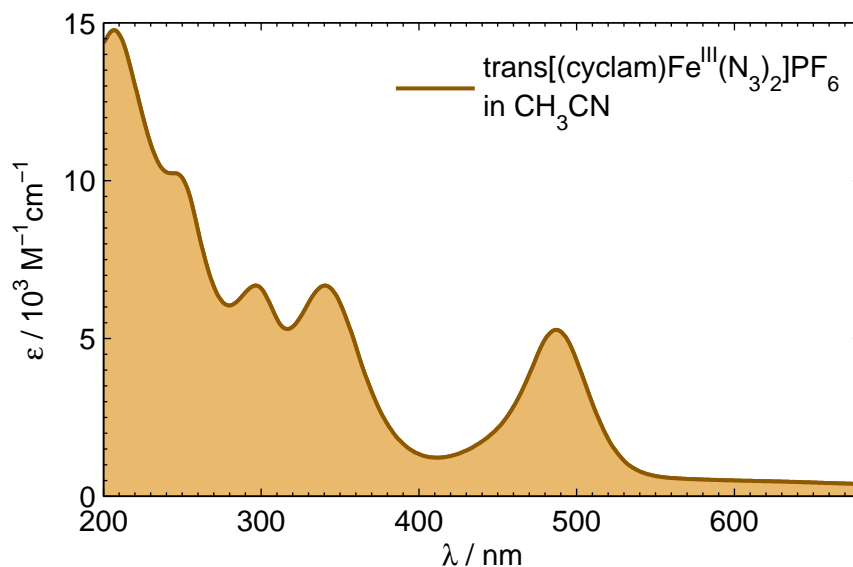


Figure 7.1: UV-vis absorption spectrum of $trans[(cyclam)Fe^{III}(N_3)_2]^+$ in CH_3CN .

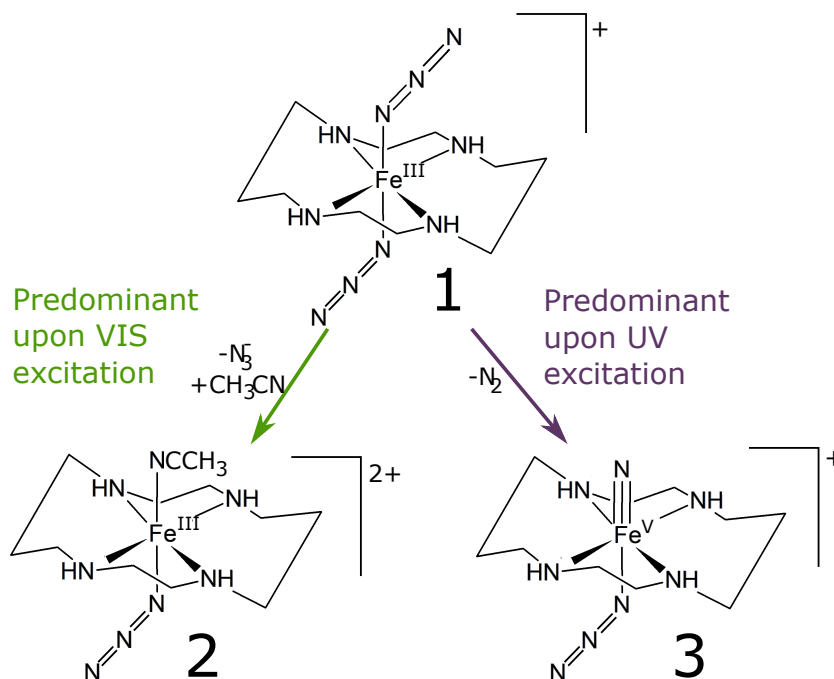


Figure 7.2: Schematic showing the two most relevant reaction pathways of $trans[(cyclam)Fe^{III}(N_3)_2]^+$ in CH_3CN as described in [53]. UV excitation predominantly leads to dissociation of an N_2 from the azide (N_3^-) ligand and subsequent formation of the Fe(V) centered complex **3**. Upon excitation closer to the visible regime the prevalent reaction is the abstraction of a complete azide ligand which is quickly followed by the association of a solvent molecule and formation of complex **2**.

With their findings they have established the wavelength dependent photochemical reaction scheme of the parent complex **1** depicted in Fig. 7.2, where the most prominent two reaction pathways have been characterized as follows: i) Photoexcitation of **1** in the visible to near-UV spectral range mainly leads to the dissociation of an azide ($=\text{N}_3^-$) ligand. An intermediate complex **2_{int}** (not shown in the simplified reaction scheme) is formed, with an open Fe coordination site. This coordination site is rapidly filled, presumably with a solvent CH_3CN molecule, forming complex **2**. The recombination of complex **1** is found to occur on a timescale of 200 μs . The quantum yield of the formation of **2** after excitation at 355 nm has been determined to 70 %. ii) Photoexcitation of **1** in the UV regime, i.e. around 266 nm, predominantly leads to dissociation of a dinitrogen molecule from one of the two azide ligands. Consecutively, the remaining terminal N^- forms a triple bond with the Fe center, leading to the formation of complex **3**, with the iron center formally oxidized to +V. The lifetime of **3** was found to be 350 μs at their experimental conditions and the quantum yield of the formation of **3** upon excitation at 266 nm has been quantified to roughly 80 %.

The most intriguing reaction is certainly the formation of **3** and femtosecond mid-IR spectroscopy has been used to determine the ultrafast processes of the high-valent iron formation [242]. Here the photoexcitation of **1** to an electronically excited state has been found to result in the formation of **3** via the following two distinct reaction pathways: In parts, the high-valent complex **3** is promptly formed via direct dissociation of a dinitrogen. Furthermore, internal conversion to the highly vibrationally excited electronic ground state (termed "hot ground state") is possible. From there, vibrational energy relaxation (VER) and thus cooling back to the parent complex **1** can occur with a time constant of 7.5 ps. In competition to the VER, barrier crossing with dinitrogen dissociation has been found, leading to a "dynamic build-up" of **3** with a time constant of 10 ps.

In all the above described experiments in solution phase at room temperature the high-valent Fe complexes have been detected indirectly via a change in the asymmetric stretching vibration of the remaining azide ligand in the mid-IR regime. The aim of the TR X-ray experiments on *trans*[(cyclam)Fe^{III}(N₃)₂]⁺ in CH_3CN described in this chapter is to directly probe the electronic and spin state configuration of the iron center during the photochemical reactions described in Fig. 7.2. The ultimate goal is to site-selectively probe the Fe center to proof the existence of the high-valent Fe(V) at room temperature in solution phase and to determine the ultrafast processes of its light induced formation. Furthermore, disentangling the different reaction pathways on sub-ps to ns timescales will allow gaining further insight into ligand exchange reactions via the reaction pathway of the complete azide detachment and subsequent solvent binding, which occurs in competition to the high-valent Fe formation.

The experimental results presented in this chapter can be separated in two parts. The first one contains the 100-ps-resolved results obtained at Synchrotrons, which are used to show the existence of the high-valent Fe(V) complex as well as to determine the X-ray

absorption fingerprints of the parent complex **1** and both photoproducts **2** and **3**. In the second part of the experimental results, the sub-ps-resolved measurements obtained at the SACLA XFEL in Japan are shown, which were used to measure in real time the formation of both complexes **2** and **3**. In the end of the chapter these experimental results are discussed and compared to the TR optical results.

7.2 Results I - Picosecond-resolved X-ray Spectroscopy

Initially we have measured TR XAS of *trans*[(cyclam)Fe^{III}(N₃)₂]⁺ in CH₃CN at the APS after photoexcitation at three different laser wavelengths, 532 nm, 355 nm and 266 nm. Later, selected XANES measurements following 343 nm and 257 nm excitation have been repeated with increased S/N using the newly developed setup at P01 beamline of PETRA III (see Chapter 4). The results of both measurement campaigns are presented here.

7.2.1 APS XAS Measurements

The experimental setup at beamline 7ID-D of the APS is described in detail in Section 3.8.2. Here, only the parameters specific to this experiment are summarized.

Table 7.1: Experimental conditions of the XAS measurements at the APS. The 266 nm and 532 nm measurements were taken in November/December 2015 and the 355 nm measurements in March 2015.

Wavelength	266 nm	355 nm	532 nm
X-ray spot size / μm^2 (V×H, FWHM)	<10×10	<10×10	4×5
X-ray repetition rate / MHz	6.52	6.52	6.52
X-ray flux / photons/s	1.5×10^{12}	1.5×10^{12}	1.5×10^{12}
Laser spot size / μm^2 (V×H, FWHM)	~30 ×40	~35 ×20	~10 ×10
Laser repetition rate / kHz	133	133	210
Laser power / mW	345	182	501
Laser pulse duration / ps	10	10	10
Laser pulse energy / μJ	2.59	1.36	2.38
Laser fluence / J/cm^2	~0.27	~0.25	~3.0
Laser intensity / GW/cm^2	~27	~25	~300

The *trans*[(cyclam)Fe^{III}(N₃)₂] complex has been synthesized in the group of Peter Vöhringer from the University of Bonn. The samples consisted of about 25 mL solutions of *trans*[(cyclam)Fe^{III}(N₃)₂]⁺ in CH₃CN with a concentration of 10 mM. To guarantee fresh solutions without long-lived photoproducts, the sample solutions were exchanged every 1-2 hours. The pump laser and X-ray probe parameters applied during the experiments at all three wavelengths are summarized in Table 7.1. At all three wavelengths, both laser and X-ray spot sizes were kept extremely small at diameters of around 10 μm . This allowed to

excite the sample at relatively high optical laser repetition rates of about 100 kHz - 280 kHz rates while ensuring a completely replenished sample before every optical excitation. The laser pulse energies at all three wavelengths were optimized on the order of 1 μ J and were sufficient to excite a large fraction of the molecules in the sample volume but still small enough to restrict the excitation process to a linear regime.

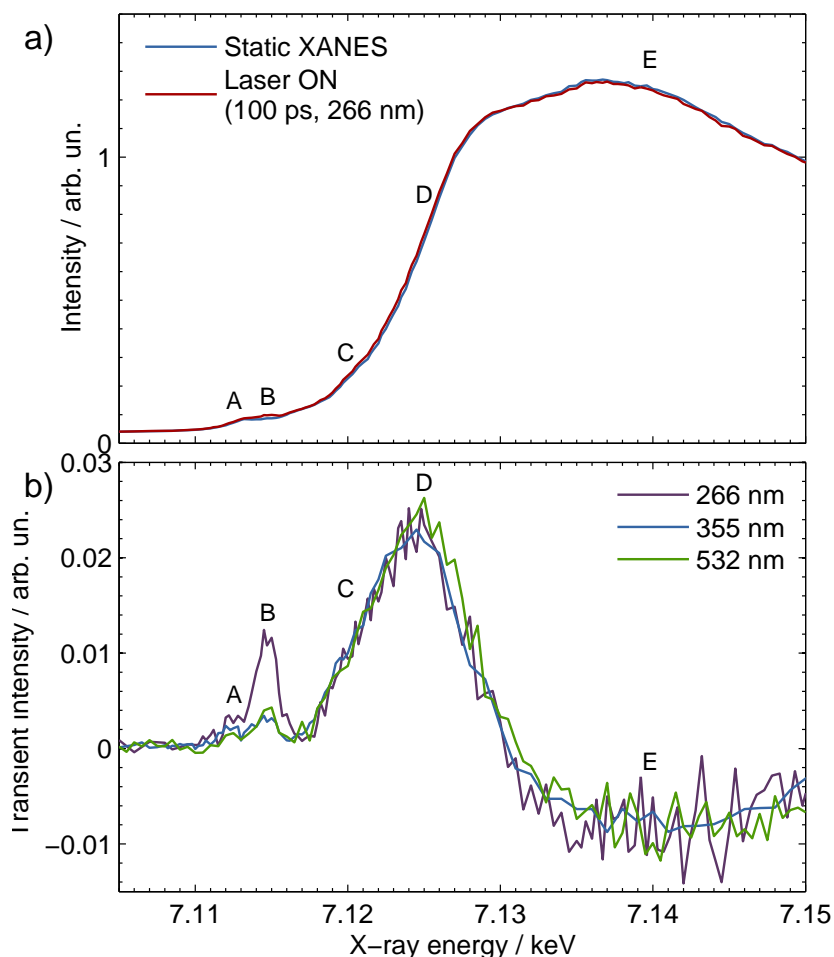


Figure 7.3: a) XANES of $trans[(cyclam)Fe^{III}(N_3)_2]^+$ of static ground state (blue) and 100 ps after 266 nm excitation (red). b) Transient XANES spectra 100 ps after photoexcitation at 266 nm (violet), 355 nm (blue) and 532 nm (green).

The XANES spectra in the static case, as well as the transient spectra 100 ps after photoexcitation at 532 nm, 355 nm and 266 nm, can be found in Fig. 7.3. We observe different features in the XANES which we label A-E: A first pre-edge peak at ~ 7112.5 eV (A), a second pre-edge peak (B) at ~ 7115 eV, the low-energy tail of the rising absorption edge at around 7120 eV (C), the half-rise of the absorption edge at around 7124 eV (D) and the region behind the white line (E). All these features except for B are already present in the ground state spectrum.

Features A and B correspond to the $1s \rightarrow 3d$ transitions, as discussed in detail in Chapter 3.2.1. Although they are dipole forbidden in octahedral symmetry, they can become partially allowed due to a distortion from the octahedral symmetry. Furthermore, their energy position is strongly dependent on the oxidation state. The structure on the rising edge and above the edge, which comprises features C, D and E, could be caused merely by the geometric structure of the molecule but also by a multitude of electronic transitions.

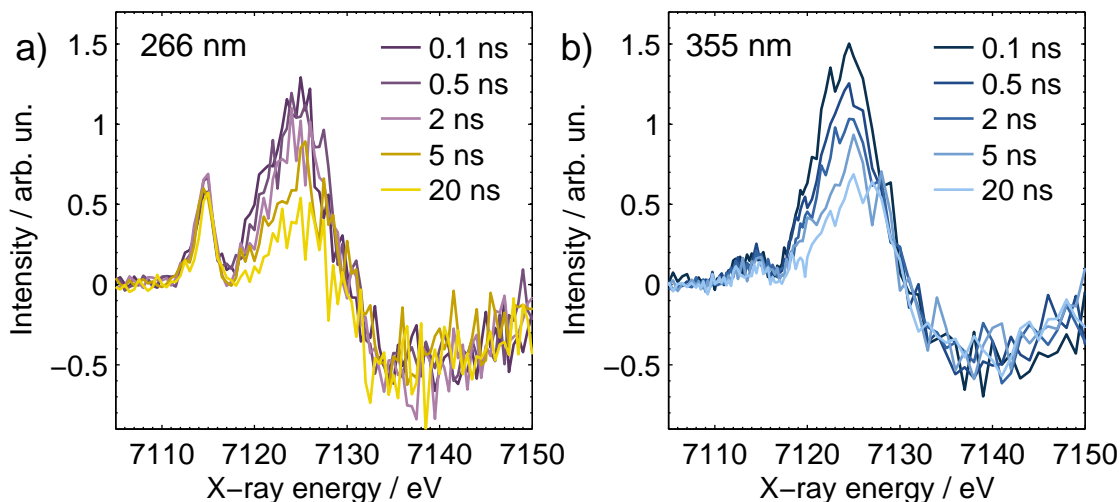


Figure 7.4: a) Transient XANES of $trans[(cyclam)Fe^{III}(N_3)_2]^+$ in CH_3CN 100 ps, 500 ps, 2 ns, 5 ns and 20 ns after photoexcitation with 266 nm. b) The analogous transients after 355 nm photoexcitation.

The transient difference spectra, 100 ps after photoexcitation, at all three laser wavelengths are very similar, as they show the same features: An increase of the intensity of the first pre-edge peak A, the appearance of the second pre-edge peak B and an edge shift, which manifests itself as an increase of the intensities around the features C and D, as well as a decrease of the intensity in the region around E. The fact that the same transient features are present at all three wavelengths indicates that both reaction pathways are present at the three applied pump wavelengths, though with distinct (wavelength dependent) quantum yields. Furthermore, the 532 nm and 355 nm transients appear identical, which is also expected, as the branching of the two reaction pathways at these wavelengths is similar [53]. Thus from here on we have restricted our excitation wavelengths to 355 nm and 266 nm.

Next to the transient spectra 100 ps after photoexcitation, we have measured further transient spectra at longer delays up to 20 ns (see Fig. 7.4). The 266 nm spectrum exhibits the same spectral features as the transients following 355 nm and 532 nm excitation. Almost all spectral features appear with the same transient intensity, except for the exceptionally strong second pre-edge peak (feature B). The increased intensity of the pre-edge peak hints towards a complex which is strongly distorted from octahedral and the unusually

high energy of the $1s \rightarrow 3d$ pre-edge peak hints towards an Fe complex of a high oxidation state (see Chapter 3.2). This allows us already at this point to tentatively assign B to the high-valent Fe complex **3**.

Furthermore, we have taken time delay scans at the features B, C and D after photoexcitation at 266 nm and 355 nm, see Fig. 7.5. All six time delay scans consist of a relatively short lived (few ns) and a long lived ($\gg 50$ ns) component. Thus we have fitted a kinetic model to these delay scans, which consists of a superposition of two components, one which grows in within the temporal resolution of 100 ps and decays exponentially and one which grows in within the same 100 ps and stays constant.

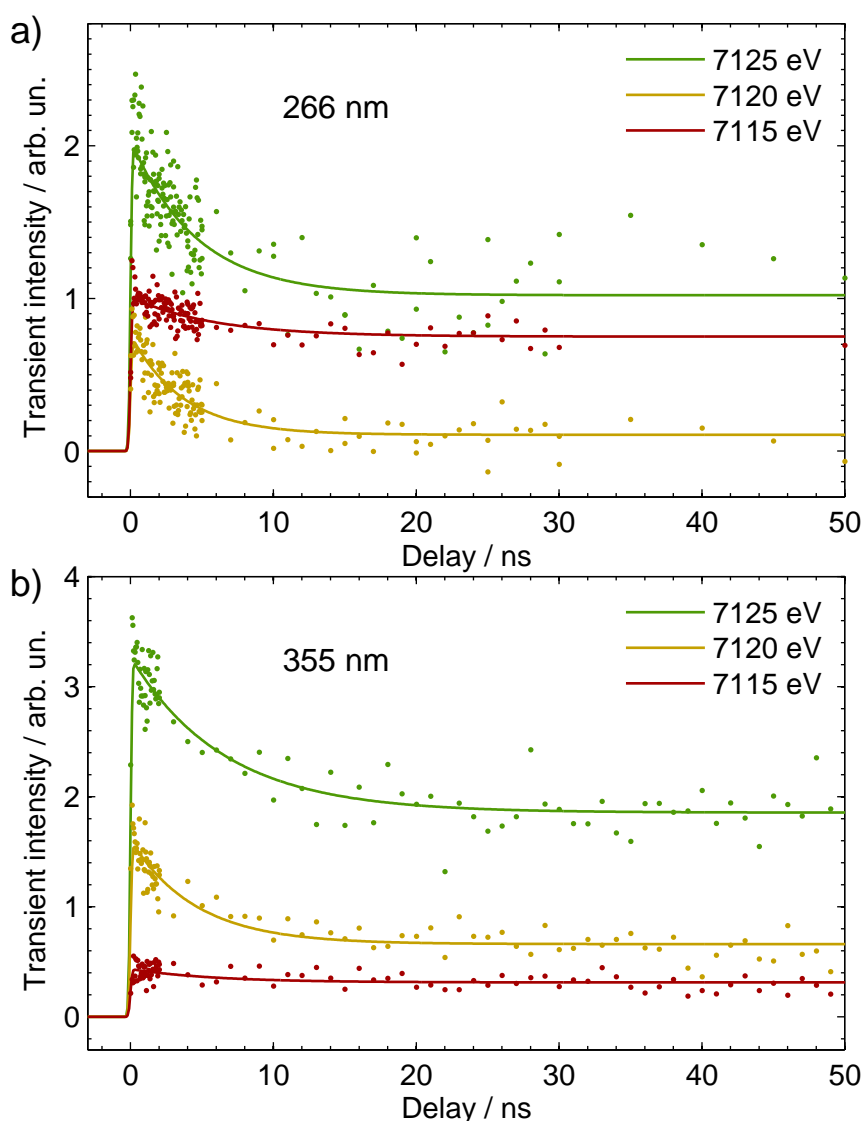


Figure 7.5: Time delay scans of the transient XANES intensity of $trans[(cyclam)Fe^{III}(N_3)_2]^+$ in CH_3CN at 7115 eV (feature B), 7120 eV (feature C) and 7125 eV (feature D) after photoexcitation with a) 266 nm and b) 355 nm.

The fit results (see Table 7.2) can be summarized as follows: The kinetics of the intensities I_B of feature B and I_D of feature D are similar at both wavelengths. I_B decreases only marginally by 25 % whereas I_D decreases by 50 %. A clear difference between the kinetics at both wavelengths can be found in I_C , which decreases by more than 80 % after 266 nm excitation and only by 60 % in the case of the 355 nm excitation. The decay times for all features are found to be roughly identical, $\tau_B \approx \tau_C \approx \tau_D \approx 5$ ns.

Table 7.2: Transient intensities $I_B(t)$, $I_C(t)$ and $I_D(t)$ as well as the decay times τ_B , τ_C and τ_D of the XANES features B, C, and D, respectively. The results are obtained from the fits of the time delay scans in Fig. 7.5. The 95 % confidence intervals are given in brackets for the obtained decay times.

	τ_B	$I_B(0)$	$I_B(\infty)$	τ_C	$I_C(0)$	$I_C(\infty)$	τ_D	$I_D(0)$	$I_D(\infty)$
266 nm	5.8 (1.6;10.1)	1010	750	3.7 (2.9;4.4)	746	107	4.6 (3.4;5.8)	2040	1020
355 nm	5.8 ^a	434	312	4.8 (3.1;6.0)	1606	660	6.6 (4.3;8.8)	3271	1855

^aFixed to the value obtained from the 266 nm fit. The B-feature is too weak at 355 nm excitation to give a meaningful result.

7.2.2 PETRA III XAS Measurements

We have also measured TR XANES spectra of *trans*[(cyclam)Fe^{III}(N₃)₂]⁺ in CH₃CN at the P01 beamline of PETRA III. The experimental setup, which has been developed in order to optimally benefit from the high photon flux at PETRA III, is described in Chapter 4. The aim of repeating the XANES measurements was to improve the S/N using this newly developed setup in order to better resolve the spectral features discussed in the previous section.

As the experimental setup is described in great detail in Chapter 4, we only discuss the specific experimental parameters here. For a summary of the experimental laser and X-ray conditions see Table 7.3. The fundamental wavelength of the Tangerine laser system is 1030 nm (instead of the 1064 nm fundamental of the Duetto laser system at the APS). Here we have used the TH of 343 nm and the FH of 257 nm to optically excite *trans*[(cyclam)Fe^{III}(N₃)₂]⁺ in CH₃CN, nevertheless the by few nm shifted wavelengths are not expected to lead to different photochemical processes (see UV-vis spectrum in Fig. 7.1). The laser spot sizes were again optimized to assure a completely replenished sample (i.e. via tight focusing on the sample position). The laser pulse energies are slightly smaller than during the APS experiments, but due to the shorter laser pulses on the order of 300 fs (instead of 10 ps) the laser intensities are increased.

Table 7.3: Experimental conditions of the XAS measurements at P01 beamline of PETRA III. These measurements were taken in April 2016.

Wavelength	257 nm	343 nm
X-ray spot size / μm^2 (V×H)	7×9	7×9
X-ray repetition rate / MHz	5.2	5.2
X-ray flux / photons/s	10 ¹³	10 ¹³
Laser spot size / μm^2 (V×H, FWHM)	24×19	40×30
Laser repetition rate / kHz	130	130
Laser power / mW	95	120
Laser pulse energy / nJ	730	930
Laser pulse duration / fs	~300	~300
Laser fluence / mJ/cm ²	~200	~99
Laser Intensity /GW/cm ²	~680	~330

The static XANES spectrum and the one 100 ps after photoexcitation at 257 nm are shown in Fig. 7.6 a). The transient differences 100 ps and 10 ns after photoexcitation at 343 nm are plotted in Fig. 7.6b), the transient differences 100 ps, 10 ns and 20 ns after photoexcitation at 257 nm in Fig. 7.6c).

The transients exhibit the same features as those measured at the APS (Fig. 7.3). Due to the multi-photon counting capability of the PETRA III setup, the S/N is significantly increased. For example the S/N at the maximum of the transient (i.e. at an incident

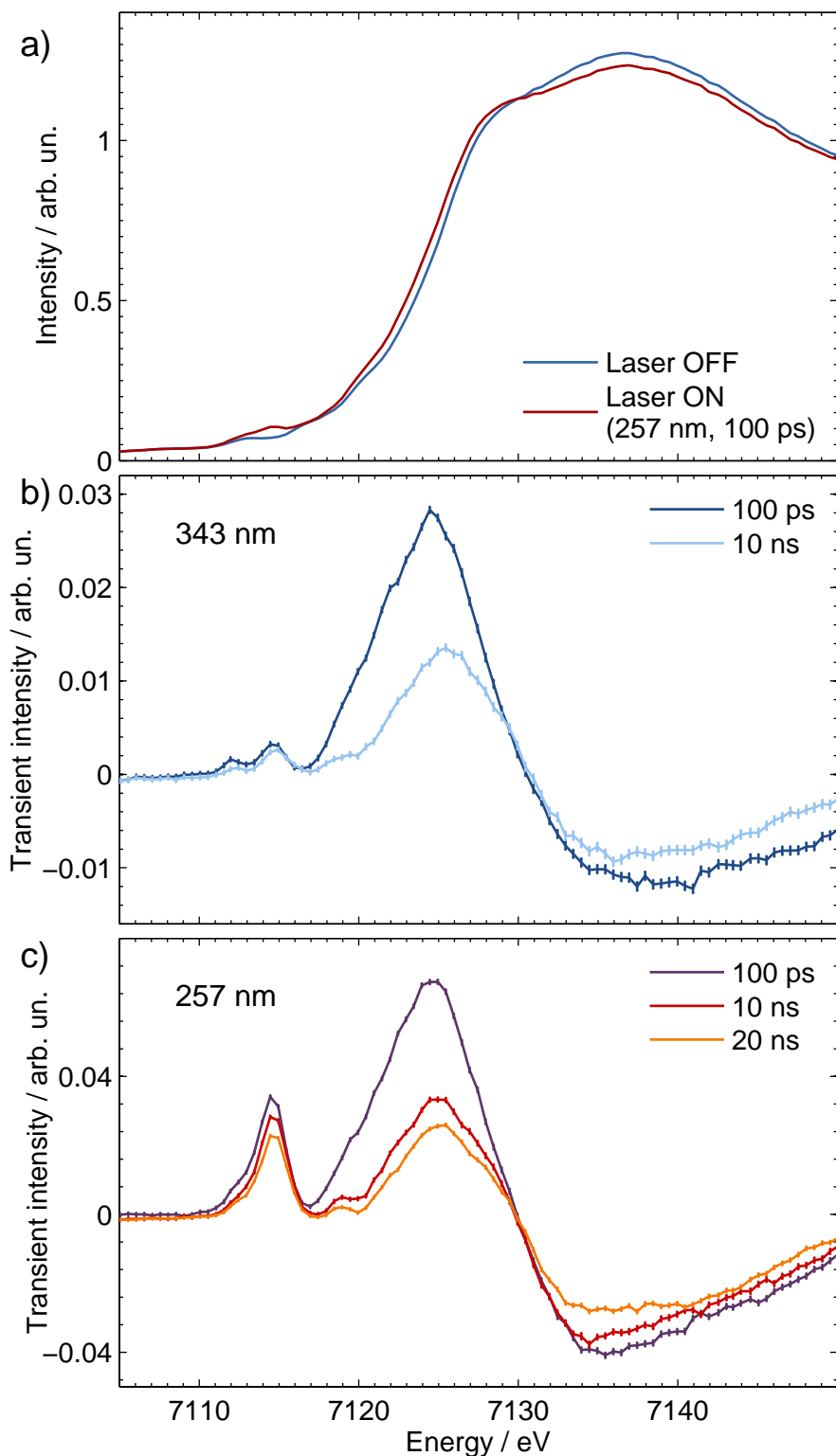


Figure 7.6: a) XANES of $trans[(cyclam)Fe^{III}(N_3)_2]^+$ in CH_3CN in the ground state (static) and 100 ps after 257 nm excitation. b) Transient XANES spectra after photoexcitation at 257 nm, c) those after 343 nm excitation.

X-ray energy of ~ 7124 eV) 100 ps after 343 nm excitation is $S/N \approx 70$ and 100 ps after 257 nm excitation $S/N \approx 100$. This is an improvement of about one order of magnitude compared to the APS measurements in Fig. 7.4, which yield a $S/N \approx 10$ at a delay of 100 ps after excitation at both wavelengths, 266 nm and 355 nm.

7.2.3 Picosecond XAS Analysis

Pre-edge Peak Position and Intensities

To determine the exact intensities and energies of the pre-edge features A and B we have decomposed the pre-edge region of the XANES transients in Fig. 7.6. We have used a sum of two Voigt profiles. Their Gaussian broadening was fixed to $\sigma_{\text{mono}} = (1/2.35)$ eV, which corresponds to the Si(111) resolution of 1.4×10^{-4} at 7112 eV. The Lorentzian broadening has been set to $\Gamma = 0.625$ eV, which corresponds to the core-hole lifetime broadening of the Fe K-shell [139].

The results of these fits for the transient XANES pre-edge for each two delays of 100 ps and 10 ns and two excitation wavelengths 266 nm and 355 nm are shown in Fig. 7.7. The resulting peak areas and energies are summarized in Table 7.4.

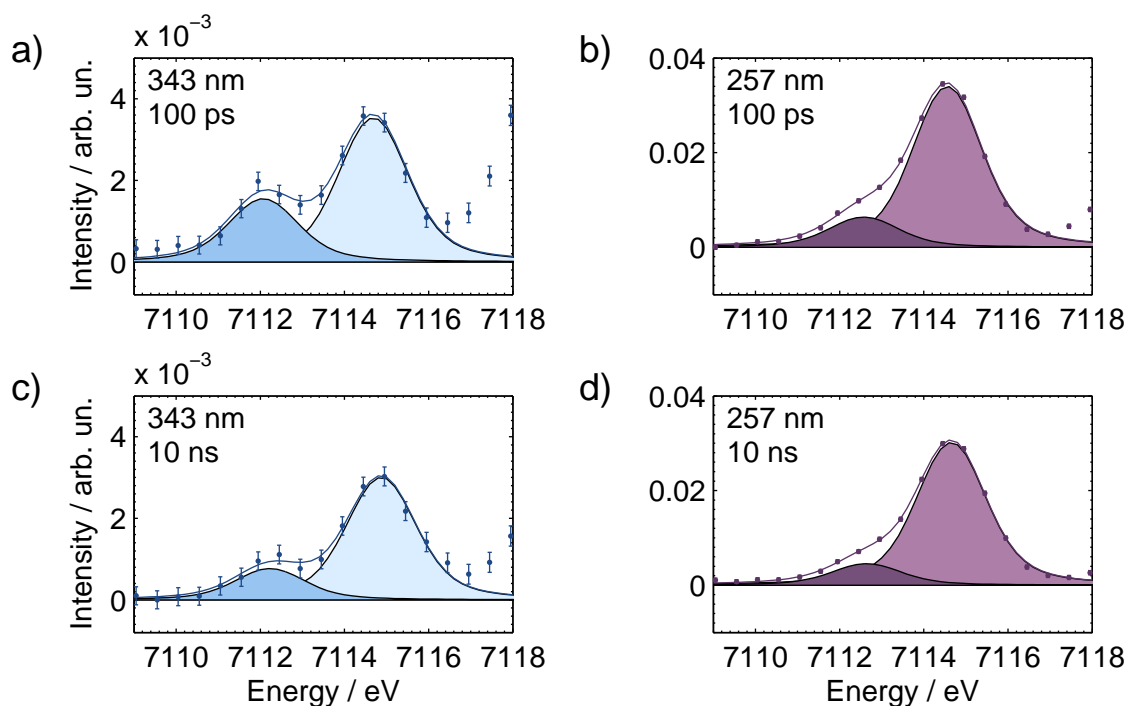


Figure 7.7: Decomposition of transient pre-edge peaks of *trans*[(cyclam)Fe^{III}(N₃)₂]⁺ in CH₃CN a) 100 ps and c) 10 ns after 343 nm excitation and b) 100 ps and d) 10 ns after 257 nm excitation. The shaded areas show the fitted Voigt peaks.

Table 7.4: Energies and areas of pre-edge peaks resulting from the fits in Fig. 7.7 (the values for the 20 ns, 257 nm transient are not explicitly shown). All energies are given in eV, all areas in arbitrary units. The fits were performed in Matlab using the *lsqcurvefit* function and the error bars correspond to the 95 % confidence interval which is calculated with the *nlparci* function.

λ	Delay	$E_{PE,1}$	$E_{PE,2}$	$A_{PE,1}$	$A_{PE,2}$
343 nm	100 ps	7112.1 ± 0.3	7114.7 ± 0.2	3.9 ± 0.8	8.9 ± 0.9
343 nm	10 ns	7112.2 ± 0.4	7114.9 ± 0.2	1.9 ± 0.6	7.5 ± 0.6
257 nm	100 ps	7112.2 ± 0.2	7114.6 ± 0.1	16.0 ± 1.6	85.2 ± 1.6
257 nm	10 ns	7112.6 ± 0.2	7114.7 ± 0.1	11.4 ± 1.2	75.6 ± 1.2
257 nm	20 ns	7112.6 ± 0.3	7114.7 ± 0.1	8.5 ± 1.4	61.5 ± 1.4

Comparison of XANES Spectra to Literature

The XANES spectra following 266 nm excitation containing the fingerprints of the high-valent Fe(V) complex in solution phase at room temperature are compared to experimental XANES spectra of a cryo-cooled octahedral Fe(V)-nitrido complex [234]. The energy of the pre-edge peak is further compared to the energies of other high-valent complexes with oxidation states up to +VI [83]. In addition, the pre-edge region is compared to time-dependent density functional theory (TDDFT) calculated pre-edge peaks of a model octahedral Fe(V)-nitrido complex [103].

The high-valent Fe(V)-nitrido complex $[(\text{cyclam-ac})\text{Fe}^{\text{V}}(\text{N})]^+$ (=Fe(V)-cryo) is generated from its precursor $[(\text{cyclam-acetato})\text{Fe}^{\text{III}}(\text{N}_3)]^+$ (=Fe(III)-cryo) under cryogenic conditions via flash-photolysis [234]. XANES spectra of these two complexes have been published about a decade ago and are (digitized and) presented together with our experimental data in Fig. 7.8a). Here, the experimental GS spectrum of the pure complex **1** (in the plot labeled Fe(III)-this work) corresponds to the static XANES trace measured at PETRA III (see Fig. 7.6a)), the spectrum of our high-valent Fe(V) complex **3** (labeled Fe(V)-this work) has been obtained from the XANES transient 20 ns after 257 nm excitation (Fig. 7.6c)). Here we applied Equation 3.21 and assumed an excited state fraction of $f = 20\%$ to reconstruct the XANES spectrum of complex **3**. The $f = 20\%$ has been chosen in order to match the intensity of the Fe(V)-cryo sample pre-edge peak.

In this comparison, special care has been taken to match the energy axis of the different XAS spectra. In this work we calibrated the spectra by setting the first inflection point, i.e. the maximum of the first derivative, of an Fe foil spectrum to the tabulated value of 7112 eV [243]. In the measurements of the cryo-cooled samples from Ref. [234] this first inflection point was set to 7111.2 eV, thus the literature data was shifted by +0.8 eV to match the calibration of the data measured in this thesis.

The XANES spectra of both Fe(V) complexes agree almost perfectly with each other, both in spectral shape as well as in edge position. This shows that indeed we have demonstrated

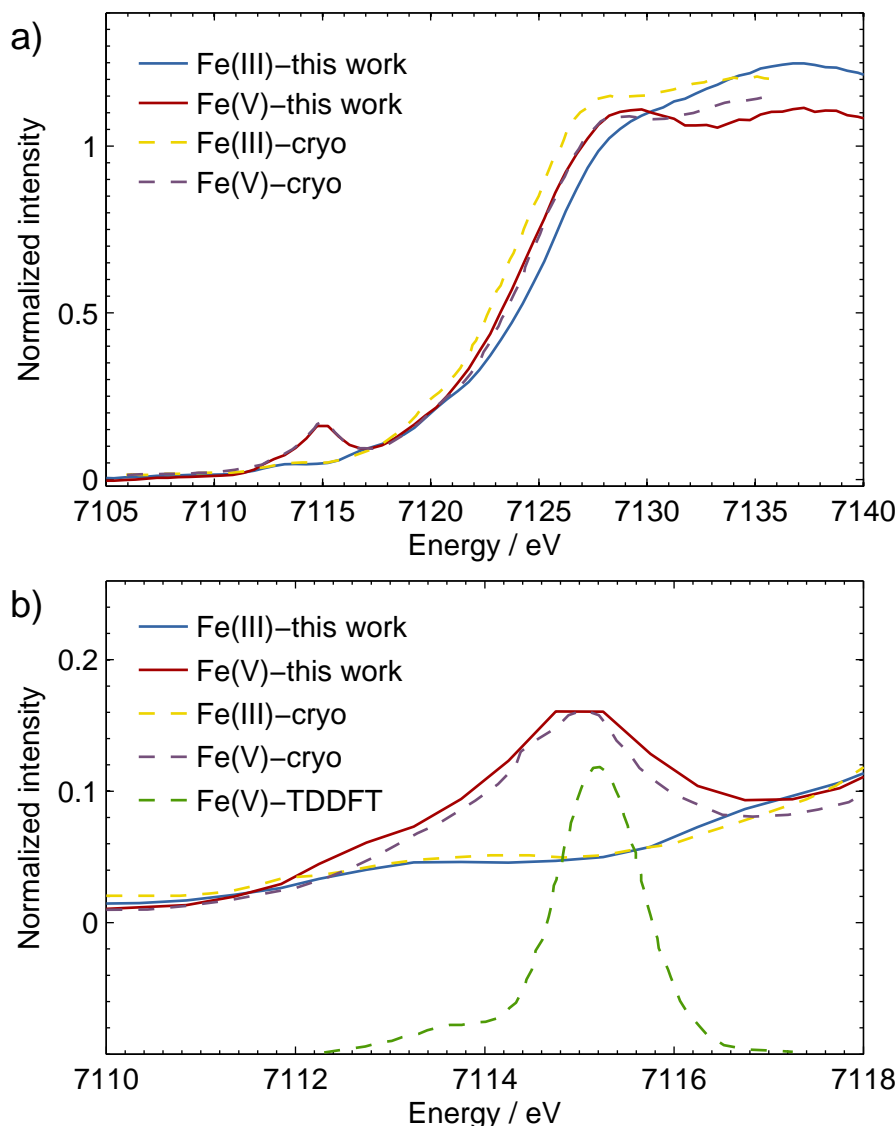


Figure 7.8: a) XANES spectrum of complex **1** (blue solid line), reconstructed XANES of **3** with anticipated excited state fraction of 20 % (red solid line) together with literature reference XANES spectra of cryo-cooled [(cyclam-ac)Fe^V(N)]⁺ and its Fe(III) precursor (data digitized from [234]). b) Pre-edge region of the spectra in a) together with TDDFT calculated pre-edges of Fe(V)-nitrido model complex from literature (data digitized from [103]).

the Fe(V) formation at ambient conditions. The XANES spectra of the parent Fe(III) complexes do not agree, the edge position of the cryo-cooled [(cyclam-acetato)Fe^{III}(N₃)₂]⁺ sample is located at 2 eV lower energy than the one of *trans*[(cyclam)Fe^{III}(N₃)₂]⁺ at ambient conditions. This results in a relative blue shift of the cryo-cooled sample after laser irradiation and formation of the Fe(V) complex. In contrast to this, our measurements revealed a red shift of the absorption edge when forming the Fe(V) complex from the parent Fe(III)

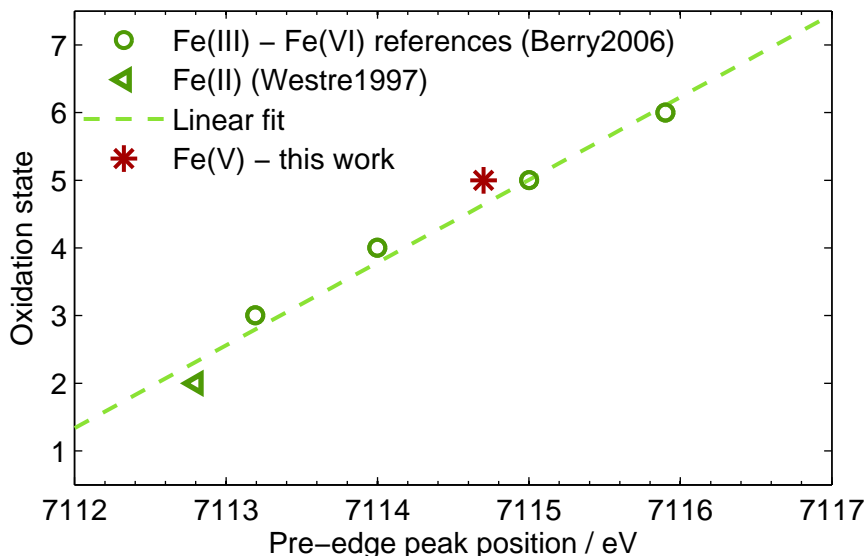


Figure 7.9: Oxidation state as a function of the pre-edge peak position of **3** (red cross) compared to references (green marks) with oxidation state +II (from [79]), +III, +IV, +V and +VI (all from [83]).

complex. We will discuss this mismatch and reason why the edge position can not be used to determine the oxidation state in the discussion in Section 7.2.3.

The result of the comparison of the pre-edge region to the TDDFT calculated pre-edge of a model Fe(V)-nitrido complex from Ref. [83] is shown in Fig. 7.8 b). The TDDFT calculated pre-edge feature was originally presented with the cryo-cooled Fe(V) data[234], thus it has also to be shifted by the according 0.8 eV. The TDDFT calculated Fe(V)-nitrido pre-edge also reproduces the general shape of the experimental Fe(V) pre-edge peaks.

In [83], a linear relationship between the oxidation state of Fe and the K-edge XAS pre-edge peak position of Fe complexes with oxidation states from +III to +VI has been established. A plot of the oxidation state as a function of the peak position is shown in Fig. 7.9. Additionally, the corresponding value of a low-spin Fe(II) pre-edge peak position from Ref. [79] has been added. Once again, the absolute energy calibration has been corrected to match the calibration of the measurements as presented in this work. The pre-edge peak position of the Fe(V) complex **3** from this work is found at 7114.7 eV, which is in excellent agreement with the expected value for an Fe(V) complex of ~ 7115 eV.

Timescale of Diffusion-driven Azide Recombination

We can estimate a diffusion driven recombination rate of complex **2** and N_3 , analogous to the ET rate calculated in Section 5.3.3.

The azide ligand has a length of ~ 2.35 Å and the whole complex **2** has a diameter of ~ 8 Å, thus the radii of the two recombining complexes are $R_{N_3} \approx 1.2$ Å and $R_{C_2} \approx 4.0$ Å

and the distance of closest approach is $R_C = R_{C2} + R_{N3} \approx 5.2 \text{ \AA}$. Using the viscosity of CH_3CN of $\eta = 3.43 \times 10^{-4} \text{ kg (ms)}^{-1}$ [214], we can calculate the diffusion rate constant according to Equation 5.3

$$k_D = 4\pi N_A R_C \frac{k_B T}{6\pi\eta} \left(\frac{1}{R_{C2}} + \frac{1}{R_{N3}} \right) \approx 2.7 \times 10^{10} \text{ (M s)}^{-1}. \quad (7.1)$$

For a back-of-the-envelope estimation we assume the laser excitation leads to an azide dissociation and formation of **2** from every second molecule in the laser excited volume (i.e. an excited state fraction of 50 %). Thus in the sample with a concentration of 10 mM a free azide concentration of 5 mM is produced in the laser excited volume. Consequently, the rate of an encounter of a free azide with the photoproduct **2** is

$$k_{\text{rec}} = 2.7 \times 10^{10} \text{ (M s)}^{-1} \times 5 \text{ mM} \approx 1.35 \times 10^8 \text{ s}^{-1}. \quad (7.2)$$

If every encounter of an azide ligand with a photoproduct **2** leads to a recombination, the recombination time is at the assumed experimental conditions $\tau_{\text{rec}} = 1/k_{\text{rec}} = 7.4 \text{ ns}$. This timescale matches the timescale found in the delay scans in Fig. 7.5, thus the decay of the transient on these timescales could be due to the recombination of complex **2** with a free azide ligand in the solution. This would be another ligand exchange reaction (the reverse reaction of the reaction pathway leading to complex **2**) where the CH_3CN solvent molecule is exchanged for the N_3^- .

Discussion

The outcome of the picosecond-resolved XANES measurements conducted at the APS and at PETRA III can be summarized briefly as follows.

The most important result is obtained from the XANES measurements following 266/257 nm photoexcitation. Their comparison to XANES measurements of a cryo-cooled Fe(V) sample [234] as well as to TDDFT calculations [103] allowed us to assign a spectral fingerprint to the high-valent Fe(V). We were able to unambiguously identify the pre-edge peak feature B at $\sim 7115 \text{ eV}$ as a marker of this high-valent Fe(V) complex **3** and thus we are able to detect the existence high-valent Fe(V) photoproduct **3** at our experimental conditions.

The time delay scans showed that I_B decreases only marginally by 25% within the timescales ($>10 \text{ ns}$) presented in Fig. 7.5. This further justifies our assignment of B to the high-valent complex **3**, as its lifetime is expected to be $350 \text{ }\mu\text{s}$ [53]. Furthermore, the delay scans revealed a $\sim 5 \text{ ns}$ component, which we have tentatively attributed to a diffusion driven process, such as the azide recombination.

The pre-edge peak feature A between 7112-7113 eV is present in all transient spectra and its origin has not yet been discussed. Due to the energy position we can assign it to a low-valent Fe(II) or Fe(III) species. The most obvious origin would be complex **2**, which

is also distorted from octahedral, resulting in an increased pre-edge peak intensity. The experimental S/N does not allow us to determine if the feature consists of only a single peak. Thus this pre-edge peak could be related to more than one species, e.g. it could also contain an additional peak due to an additional reductive pathway, where the Fe(II) equivalent to **2** is formed.

Nevertheless, it is not clear yet, why Fe(V)-cryo yielded a blue shifted absorption edge compared to its pre-cursor Fe(III)-cryo, while our XANES measurements of complex **1** yielded a red shift of the absorption edge upon laser excitation at 266 nm and thus predominant formation of complex **3**.

One explanation could be, that a blue shift is actually hidden underneath the red shift associated with complex **2**. The XANES measurements after 355/343 nm excitation with predominant formation of **2** indeed revealed a very strong red shift of the absorption edge. A clear assignment of the edge features and a definite interpretation of the edge shift is difficult. Next to the oxidation state the edge position depends strongly on the structure of the molecule and numerous examples of structural changes leading to strong edge shifts without a change in oxidation state exist. An example of a red shift of the absorption edge due to the optically induced LS-HS transition and the concomitant structural changes can be found in Chapter 6.

Further examples of strong edge-shifts between transition metal complexes of equal oxidation state are ubiquitous in literature. The edge position depends on the coordination number and thus the symmetry, e.g. high-spin Fe(II) complexes can vary by ~ 2 eV in their edge position between 4-coordinated and 6-coordinated complexes [244]. Furthermore, the edge position strongly depends on the ligation state. In Ref. [245], the X-ray absorption edge position of a series of Cr^{III}Cl₃L complexes with different tridentate ligands L, yielding either three nitrogen or three sulfur donor atoms, have been compared. The edge-positions spanned a range of 8 eV within the single Cr oxidation state +III.

The last example of a study of the correlation of K-edge positions of 3d transition metal complexes of different oxidation states was found in Ref. [246]. There, the XANES spectra of a pair of an octahedral Mn(III)-azide complex and its high-valent Mn(V)-nitrido form, where the azide (N₃) was substituted with a single Nitrogen (N), are compared. Here the Mn(V)-nitrido complex exhibits a very strong pre-edge peak in contrast to the Mn(III)-azide complex. Most interestingly though, the edge position of both complexes is almost identical. This example of a pair of Mn complexes is very similar to our pair of complexes **1** and **3** and the comparison of both measurements further supports our assignment of the spectral features, especially of pre-edge feature B.

7.3 Results II - Femtosecond-resolved X-ray Spectroscopy

We have measured TR XAS, XES and XDS of *trans*[(cyclam)Fe^{III}(N₃)₂]⁺ in CH₃CN at the Japanese XFEL SACLA. In this thesis only the spectroscopic measurements are presented. The sample consisted of a 100 mL solution of 20 mM concentration, twice as concentrated as during the synchrotron measurements. The experimental setup at SACLA is described in Section 3.8.4. The specific experimental laser and X-ray parameters are summarized in Table 7.5. The data presented here has been acquired during two campaigns: In May 2015 the TR XAS following 266 nm excitation, and in November 2015 the TR XES and XDS (not part of this thesis) following 355 nm photoexcitation have been measured.

The main goal of these experiments were to observe the real-time formation process of the high-valent complex **3** upon photo-dissociation of a dinitrogen from one of the azide ligands of **1** and triple bonding of the terminal N⁻ ligand. Furthermore, the experiments aimed at advancing the understanding of the ligand exchange mechanism comprising the distinct steps of the azide dissociation and the subsequent solvent molecule attachment, with eventually proving the existence of a penta-coordinated intermediate complex **2_{int}**. In the following subsections, the TR XAS after 266 nm photoexcitation and the TR XES after 355 nm excitation will be presented.

Table 7.5: Experimental conditions of XAS and XES measurements performed at the SACLA XFEL on *trans*[(cyclam)Fe^{III}(N₃)₂]⁺ in CH₃CN. The 266 nm measurements have been conducted in May 2015, the 355 nm measurements in November 2015.

Wavelength / nm	266	355
X-ray spot size / μm^2	5×5	$<(10 \times 10)$
X-ray repetition rate / Hz	30	30
X-ray flux ^a / photons/pulse	$\sim 2 \times 10^9$	$\sim 10^{11}$
X-ray spectral bandwidth / eV	1 ^b	$\sim 35^c$
Laser spot size ^d / μm^2 (VxH, FWHM)	$\sim 140 \times 100$	55×75
Laser repetition rate / Hz	15	15
Laser pulse duration ^e / fs	~ 200	~ 200
Laser pulse energy / μJ	15	13
Laser fluence / mJ/cm^2	~ 136	~ 400
Laser intensity / GW/cm^2	~ 680	~ 2000

^aThe X-ray photon flux presented here is merely a rough estimate: The pulse energy at SACLA is up to 0.5 mJ, which corresponds to 4×10^{11} photons / pulse at a photon energy of ~ 7.5 keV. To the sample, losses of a factor >2 are possible. The monochromatization leads to a decrease in flux of a factor of ~ 50 .

^bwith 4 bounce Si(111) mono

^cpink beam

^dThe 355 nm laser beam profile was measured with a 100 μm diameter pinhole, see Appendix C.1 for details

^eThe laser pulse duration is estimated in Section 7.3.2

7.3.1 TR XAS after 266 nm Excitation

The XANES spectra measured statically, 5 ps after 266 nm excitation, as well as the transient difference of the two is plotted in Fig. 7.10 a), the transient differences 1 ps, 5 ps, 20 ps and 100 ps after photoexcitation in Fig. 7.10 b).

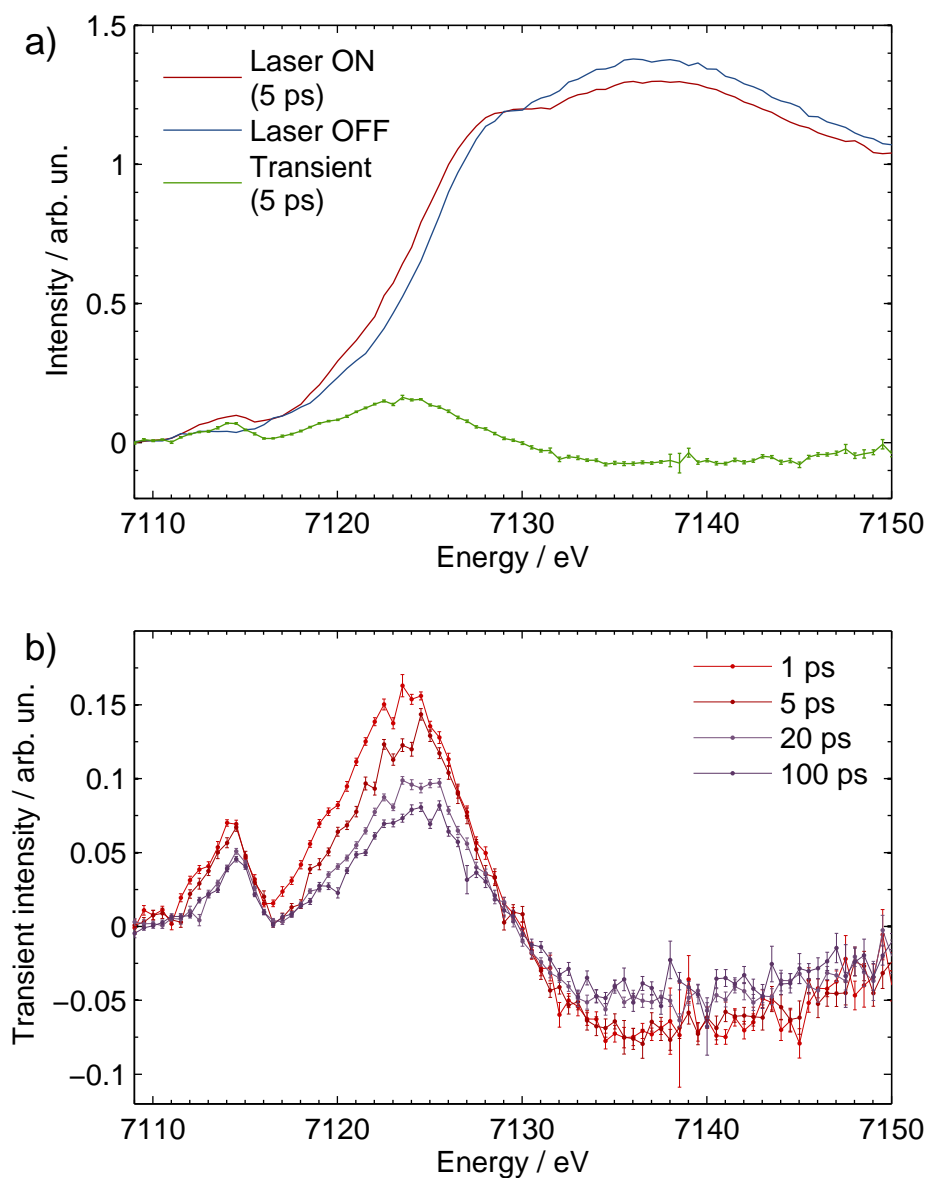


Figure 7.10: a) XANES of $trans[(cyclam)Fe^{III}(N_3)_2]^+$, static (blue), 5 ps after 266 nm excitation (red) and transient difference of both. b) Transient XANES spectra 1 ps, 5 ps, 20 ps and 100 ps after 266 nm excitation.

The transient XANES spectrum 100 ps after photoexcitation resembles very well the 100 ps spectra following 266 nm excitation measured at both the APS and PETRA III, comprising the discussed features A-E. The transient spectra at short delays of 1 ps and

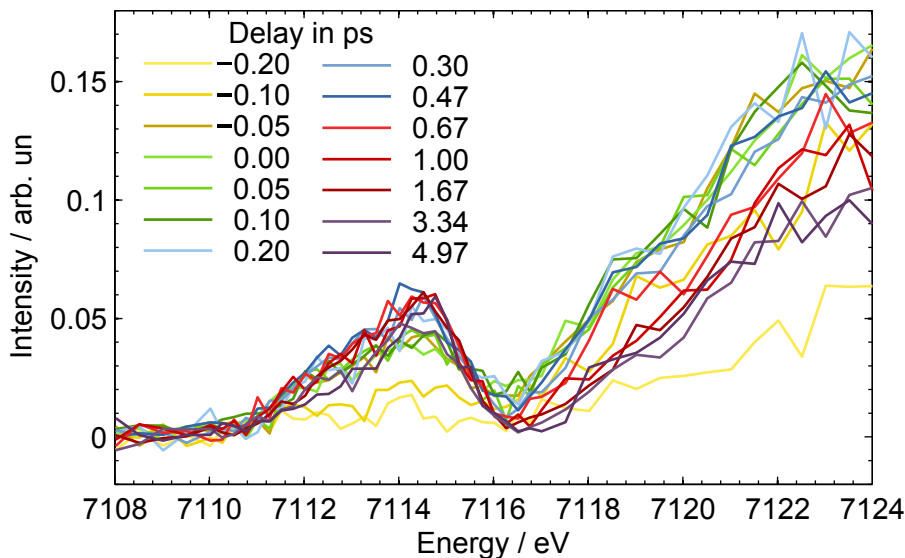


Figure 7.11: Transient XANES traces of $trans[(cyclam)Fe^{III}(N_3)_2]^+$ in CH_3CN . The pre-edge to half-rise region has been scanned after 266 nm excitation for 14 different delays between -200 fs to 5 ps.

5 ps do not show any additional features compared to the 100 ps spectra. Furthermore we can make the following observations about the temporal evolution of the XANES transients within the first 100 ps after photoexcitation: i) The two pre-edge features A and B appear within the first picosecond and the intensity of both pre-edge peaks decays within the first 100 ps only slightly. Feature A appears to decrease more than feature B, but due to the relative weakness of A compared to B and due to the experimental errorbars, a quantitative statement is not possible. ii) The edge shift (features C and D) appears within the temporal resolution and decreases in intensity within the first 100 ps. Here we observe a difference in the kinetics of C and D. While C seems to decay almost completely within the first 100 ps, D decays only to about half its intensity in the same amount of time. The time constant of this decay can only very vaguely be quantified to ~ 10 ps, which interestingly corresponds to the timescale found for the VER as well as for the dynamic build-up of complex **3** found in Ref. [242].

To obtain more detailed information about the behavior of these features within the first hundreds of femtoseconds after photoexcitation we have mapped the XANES region from 7108 eV to 7124 eV (which contains the pre-edge region up to about the half-rise of the absorption edge) in finer time steps from -200 fs to 5 ps. The transient differences measured at 14 different delays are plotted in Fig. 7.11. These scans show that both pre-edge peaks appear on sub-picosecond timescales and stay at almost constant intensity until 5 ps delay, only A appears to decay slightly within the first 5 ps. The edge shift appears promptly after photoexcitation, reaches its maximum at about 200 fs delay and immediately decays to about 50 % of its maximum after 5 ps.

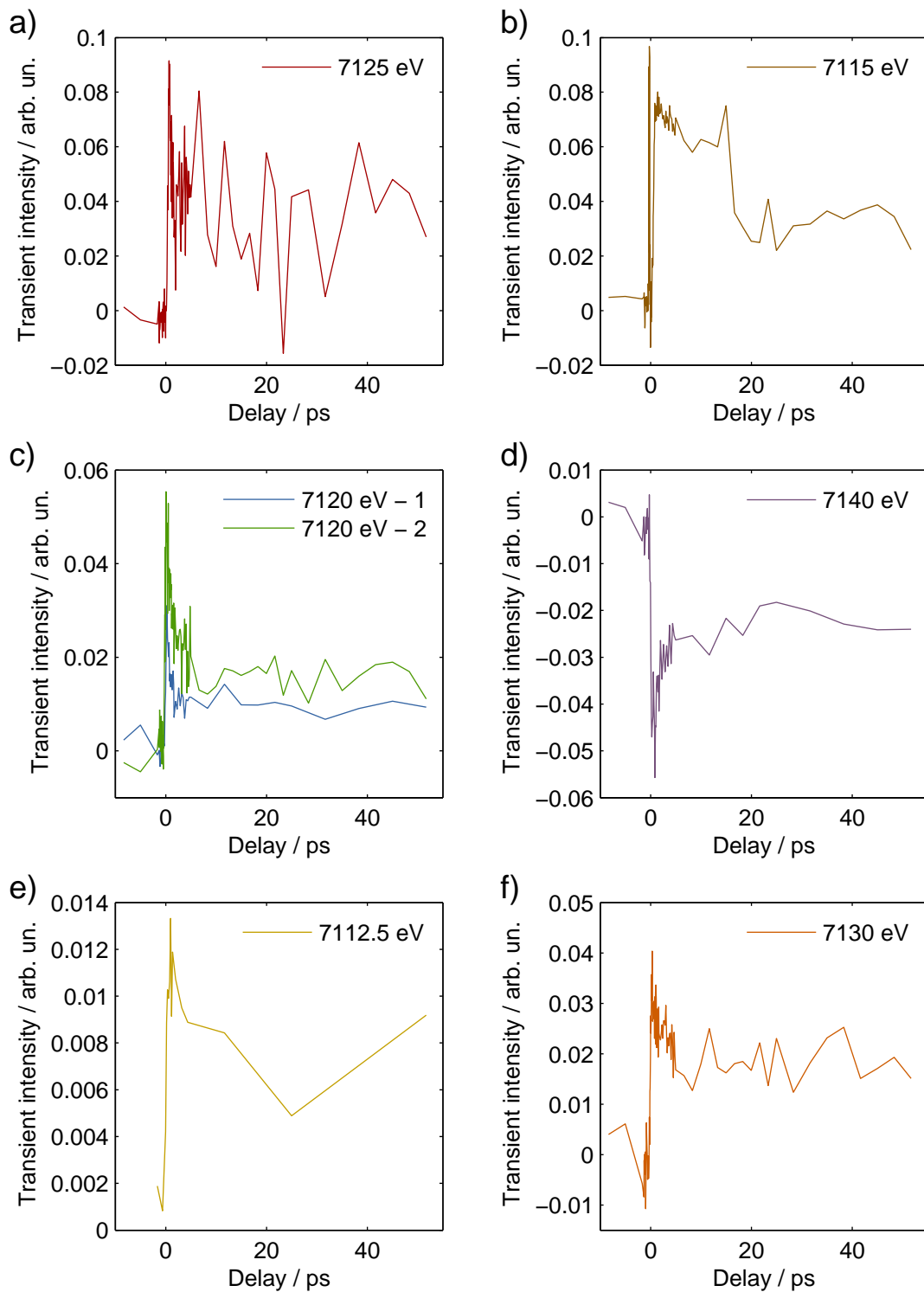


Figure 7.12: Time delay scans of transient XAS intensity at six selected incident X-ray energies.

We have also measured time delay scans at selected XANES features (see Fig. 7.12). These scans confirm the general trends of the dynamics of the features A, B, C and D discussed in the previous paragraphs. Nonetheless, as these scans suffer from large statistical noise as well as from additional artifacts, we do not analyze them further here.

7.3.2 Femtosecond XAS Analysis

Timing Tool Correction

We have used the SACLA timing tool [247], which applies the so-called spatial encoding, similar to the timing tool routinely available at LCLS [248]. This timing tool is used to measure and post correct the laser-X-ray timing jitter for each single X-ray pulse. Here, mainly the 14 XANES scans in Fig. 7.11 could benefit from the timing tool. But before applying the jitter correction to these scans, we test the post correction algorithm using the example of a delay scan.

We have chosen the second delay scan at the C feature (7120 eV) in Fig. 7.12c) (green solid line). At each delay point, the transient intensity has been measured for a total of 500 X-ray pulses consisting of 250 pulses with laser excitation and 250 without laser excitation. Without timing tool correction, this delay scan is visualized by taking the average of each of the 250 laser ON and OFF pulses and plotting their respective difference as a function of the uncorrected delay (see brown points with error bars in Fig. 7.13). The uncorrected (=raw) delay corresponds to the laser-X-ray delay which has been experimentally applied by elongating the laser beam path using a translation stage.

To correct for the timing jitter, this raw uncorrected delay value is corrected by the laser-X-ray delay which has been measured for each single pulse by the timing tool. After this correction the corrected delays are not sorted into discrete bins anymore. Furthermore, the actual delay values of two initially distinct raw delay points may overlap. Thus the set of data points for each single X-ray pulse in the whole delay scan, consisting of pairs of values for the transient intensity and corresponding delay, are re-binned into a new set of delay bins. After re-binning, the laser ON and OFF values in each of the new bins are averaged and the difference of laser ON and OFF for each delay bin is calculated, yielding the transient difference at each corrected delay point. Additionally, the standard error of each point is calculated. In Fig. 7.13 the delay scan after timing tool correction is plotted (blue points with error bars).

The improvement in temporal resolution is apparent. The rise time is shortened and the exponential decay at longer delays appears sharper.

To further quantify the improvement in temporal resolution we use a kinetic model consisting of two components to describe the temporal evolution of the transient intensity. The first component with transient intensity $I_{es1,max}$ is generated within the instrument response function time σ_{lx} and decays with a time constant of τ_{es1} to a second component of intensity $I_{es2,max}$. The lifetime of the second component is much larger than the 4 ps

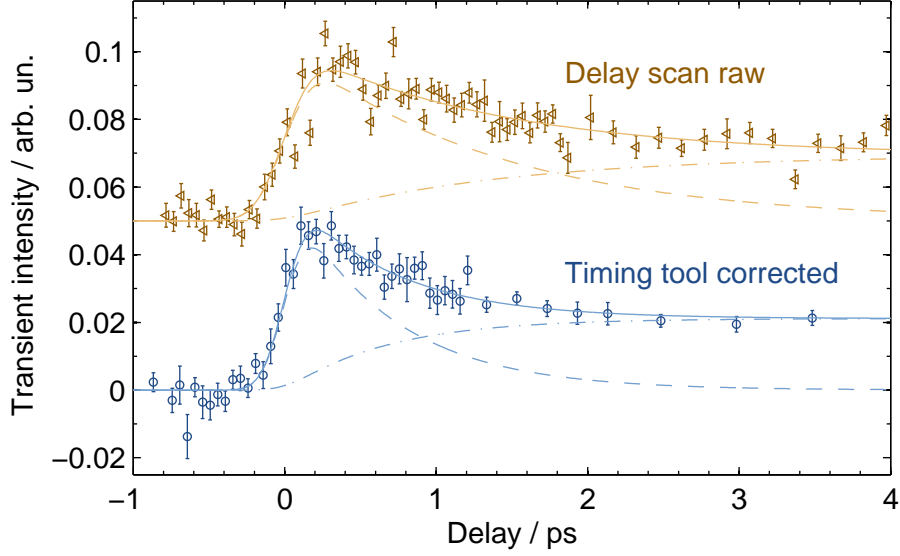


Figure 7.13: Delay scan at 7120 eV before (red) and after (blue) timing tool correction. The transient intensity consists of a superposition of two states, an intermediate state with intensity $I_1(t)$ (dashed lines) is created within the instrument response time σ_{lx} and decays with a time constant τ_{es1} to a longer lived state with intensity $I_2(t)$ (dashed-dotted lines). The fit of the raw data yielded $2.35 \times \sigma_{lx} = (360 \pm 130)$ fs (FWHM) and $\tau_{es1} = (1.36 \pm 0.64)$ ps, the fit of the timing tool corrected data results in $2.35 \times \sigma_{lx} = (278 \pm 76)$ fs (FWHM) and $\tau_{es1} = (0.67 \pm 0.27)$ ps.

window which is fitted in Fig. 7.13. The transient intensity as a function of the delay according to this kinetic model is then given by

$$I_{es,tot}(t) = I_{es1}(t) + I_{es2}(t) \quad \text{with} \quad (7.3)$$

$$I_{es1}(t) = I_{es1,max} \int_{-\infty}^{\infty} \frac{\exp\left(\frac{-x^2}{2\sigma^2}\right)}{\sigma_{lx}\sqrt{2\pi}} H(t - t_0 - x) \exp\left(\frac{-t}{\tau}\right) dx \quad \text{and} \quad (7.4)$$

$$I_{es2}(t) = I_{es2,max} \int_{-\infty}^{\infty} \frac{\exp\left(\frac{-x^2}{2\sigma^2}\right)}{\sigma_{lx}\sqrt{2\pi}} H(t - t_0 - x) \left(1 - \exp\left(\frac{-t}{\tau}\right)\right) dx. \quad (7.5)$$

Here $H(t - t_0 - x)$ is the Heaviside function, which is a Gaussian broadened step function. This kinetic model is fitted to the uncorrected (raw) delay scan and to the delay scan after timing tool correction. The results are plotted as solid lines in Fig. 7.13. The fit resulted in instrument response function of $2.35 \times \sigma_{lx} = (360 \pm 130)$ fs (FWHM) before and $2.35 \times \sigma_{lx} = (278 \pm 76)$ fs (FWHM) after timing tool correction. The decay times before and after the the timing tool corrections were found to be $\tau_{es1} = (1.36 \pm 0.64)$ ps and $\tau_{es1} = (0.67 \pm 0.27)$ ps, respectively.

Thus, due to the timing tool correction we are able to improve the temporal resolution of the experiment from ~ 380 fs (FWHM) to ~ 300 fs (FWHM).

Pre-edge Features and Rising Edge

The timing tool correction has also been applied to each point of the 14 XANES scans in Fig. 7.11. Here we also had to corrected for the energy-dependent path length difference through the four-bounce mono. This correction is explained in the Appendix C. There, the delay distribution before and after the timing tool correction is displayed in Fig. C.7. The re-binned data with laser excitation, without laser excitation, the transient difference as well as the standard error of the transient difference is plotted as 2D color maps in Fig. 7.14.

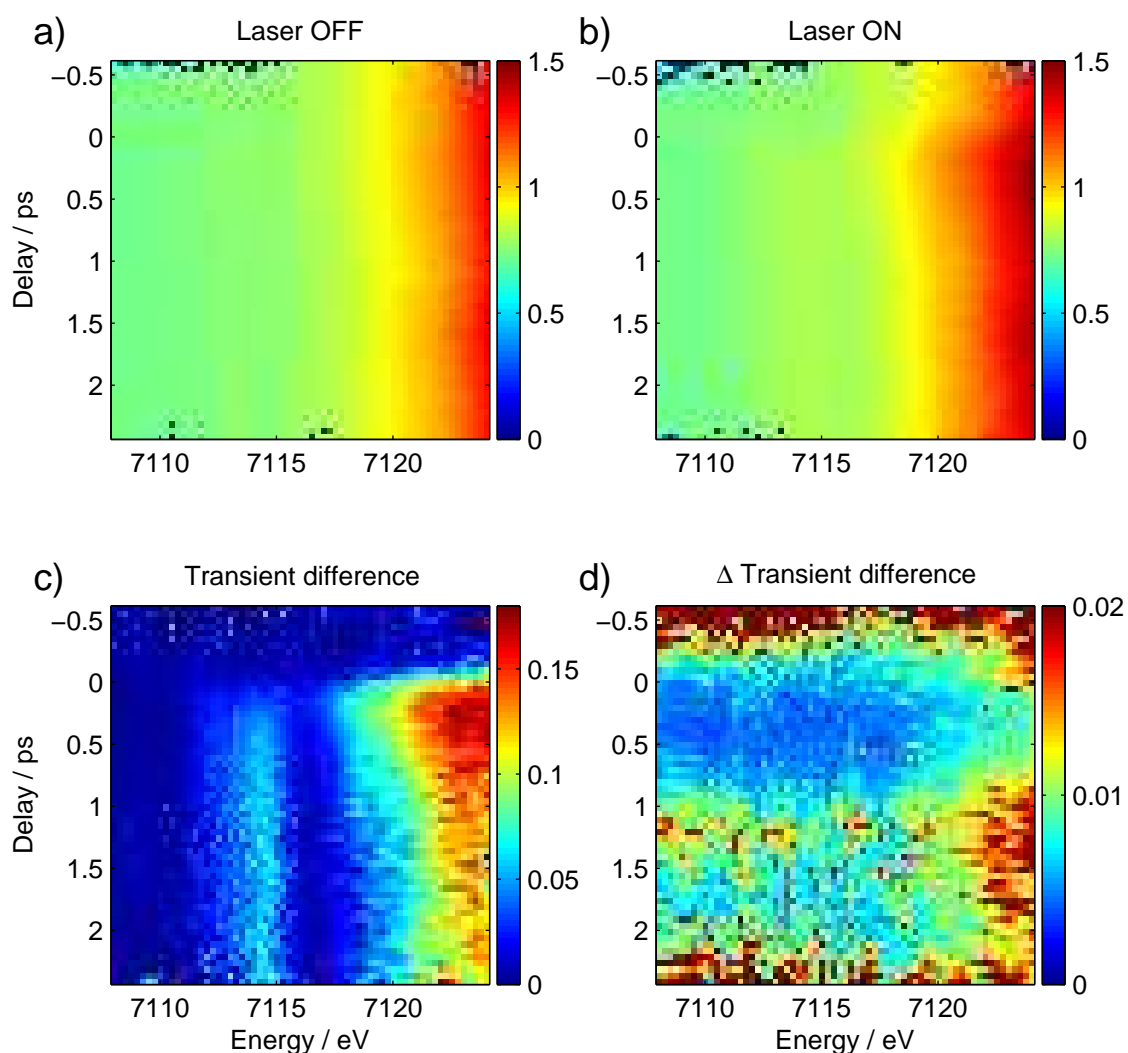


Figure 7.14: Colormaps showing the XANES spectra for a delay range from -0.5 ps to 2.5 ps. The timing-tool correction has been applied, leading to a temporal resolution of 280 fs. In a) the Laser OFF spectra, in b) the laser ON spectra, in c) the transient difference and in d) the error of the transient difference are shown.

To obtain kinetic information about the transient features A-D, line-outs along the delay axis have been taken. For feature A, the line-outs between 7111 eV and 7113 eV are summed up, for B those between 7114 eV and 7116 eV, for C the ones from 7117 eV to 7121 eV and for D the ones from 7122 eV to 7124 eV. These line-outs deliver kinetic traces which are plotted in Fig. 7.15.

The transient intensity of the pre-edge features A and B appears to grow in with the temporal resolution of the experiment and stays constant within the 2.5 ps shown in Fig. 7.15. Thus we can use a kinetic model to describe the pre-edge transient intensity $I_{pe}(t)$ by a single component $I_{pe,max}$ which grows in within the temporal resolution τ and stays constant during the first 2.5 ps. The transient intensity according to this model is

$$I_{pe}(t) = I_{pe,max} \int_{-\infty}^{\infty} \frac{1}{\sigma_{lx}\sqrt{2\pi}} \exp(-x^2/2\sigma^2) H(t - t_0 - x) dx . \quad (7.6)$$

For C and D, the kinetic model in Equation 7.3 has been applied. Using these two models we have performed a global fit of all four line-outs, the result is depicted with solid lines in Fig. 7.15. In this fit, t_0 as well as σ_{lx} were locked to the same value for all four features. Furthermore, the decay constant τ of C and D has been assumed to be equal. The fit results yielded an instrument response function of $2.35 \times \sigma_{lx} = 317$ fs and a decay time of C and D of $\tau = 730$ fs.

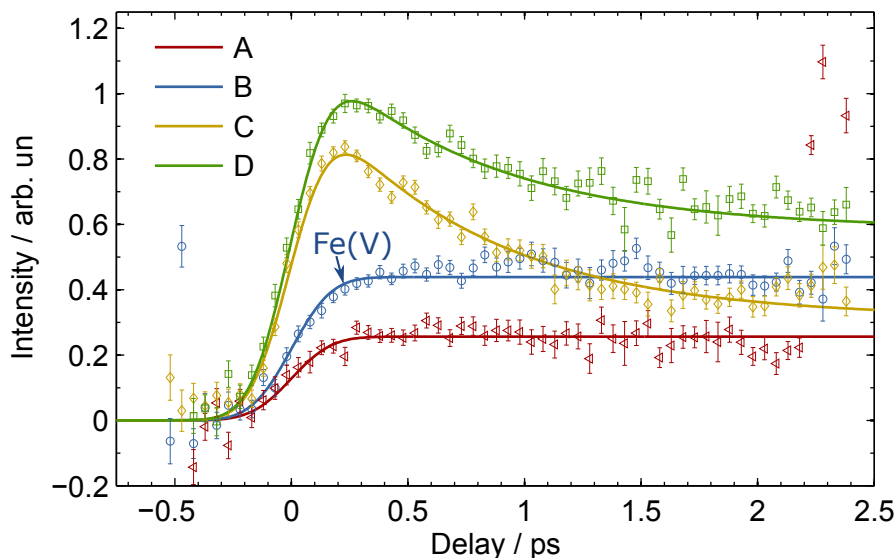


Figure 7.15: Lineouts of the transient XANES intensity in Fig. 7.14 along the delay axis of features A, B, C and D together with fits of a kinetic model described in the text. This fit yielded for all components a rise time of 317 fs and a decay time for C and D with a time constant of 730 fs. Few outliers are visible, which could eventually be discarded by setting stricter limits in the filtering process of the raw data.

As the fingerprint (feature B) of the high-valent Fe(V) appears within the temporal resolution, we can conclude that the high-valent Fe(V) formation is completed within these ~ 300 fs. The 700 fs decay of C and D could be attributed to several electronic or geometric changes, such as a structural relaxation of the newly formed complex **3**. Nevertheless, advanced modeling of the XANES region is required for a definite assignment of C and D. A further statistical analysis will be necessary to determine the confidence intervals on the obtained rise and decay times. Determining these confidence intervals is difficult due to the large parameter space of the fit. As a rough estimate, the confidence intervals from the single delay scan in Fig. 7.13 could be used.

Expected Temporal Resolution

To understand the temporal resolution of the experiment we consider two main broadening mechanisms: The group-velocity mismatch G_{VM} between the laser and the X-rays in the liquid jet and the pulse duration of the laser excitation pulse, which is additionally broadened due to group-velocity dispersion (GVD) in transmissive optical elements.

We have calculated the G_{VM} in the liquid jet with thickness t_{jet} between the optical (UV) laser and the X-rays with

$$G_{VM} = \frac{t_{\text{jet}}}{c}(n_{\text{laser}} - n_{\text{xray}}). \quad (7.7)$$

Here the indices of refraction are n_{xray} for the X-rays and n_{laser} for the 266 nm laser light. Using $t_{\text{jet}} \approx 150 \mu\text{m}$ (100 μm nozzle turned to $\sim 45^\circ$), $n_{\text{xray}} = 1$ and $n_{\text{laser}} = 1.4$ [249] we obtain

$$G_{VM} \approx 200 \text{ fs}. \quad (7.8)$$

Furthermore, we estimate the pulse duration of the laser pulse due to the GVD. Assuming a Gaussian pulse shape with a transform limited FWHM pulse duration $\tau_{o,p}$, the pulse duration after passing through a distance z of a material with group velocity dispersion k_l'' is given by [250]

$$\tau_p(z) = \tau_{o,p} \sqrt{1 + \left(\frac{(4 \ln(2) z k_l'')^2}{(\tau_{o,p})^4} \right)}. \quad (7.9)$$

After the third harmonic generation crystal, few transmissive optical elements have been inserted in the beam path, which are: i) a ND filter of thickness $\sim 2 \text{ mm}^1$, ii) the entrance window to the Helium filled sample chamber of thickness $\sim 2 \text{ mm}$ and iii) a focusing lens with a diameter of 50 cm^2 with thickness of $\sim 6 \text{ mm}$. Thus the beam passes through a total thickness of $z \sim 10 \text{ mm}$ of fused silica. Using the group velocity dispersion of fused silica of $k_l'' = 198 \text{ fs}^2/\text{mm}$ [249] and an initially transform limited pulse with $\tau_{o,p} = 25 \text{ fs}$ we obtain

$$\tau_p(10\text{mm}) \approx 220 \text{ fs}. \quad (7.10)$$

¹e.g. Thorlabs NDL-10C-2 or similar

²e.g. Thorlabs LA4984-UV or similar

This can only be seen as a very rough estimate of the pulse duration. A more precise calculation would require the spectrum and the initial phase of the laser pulse, which we were not able to retrieve yet. In Appendix C.1 we have calculated the GVD of laser pulses 20 fs to 100 fs long Fourier-transform limited pulses. Their respective duration after passing through 1 cm fused silica is between 100 and 300 fs, which shows that the 200 fs estimate is valid. We have done the same calculation for 355 nm laser light in Appendix C.1. Here the GVD is less dramatic, but due to the OPA we can assume that the laser pulse has a larger initial chirp. For this reason we also use the 200 fs estimate for the 355 nm pump laser pulse duration in Table 7.5. Especially in the case of 355 nm excitation the pulse duration is not crucial, here it is merely used to estimate the laser fluence and intensity at the sample position.

Using the pulse duration of the optical pump laser at the sample position and the G_{VM} in the liquid jet we can estimate the total experimental resolution via the squared sum of both broadening mechanisms,

$$IRF = \sqrt{\tau_p^2 + G_{VM}^2} \approx 297 \text{ fs} . \quad (7.11)$$

This estimate is in excellent agreement with the observed instrument response time.

7.3.3 TR XES after 355 nm Excitation

While the precursor complex **1** and the long-lived products **2**, **3** are of doublet spin multiplicity, the intermediate state $\mathbf{2}_{int}$ is expected to have a quartet spin multiplicity (see supplementary information in Ref. [53]). Thus we can use $K\beta$ XES to identify $\mathbf{2}_{int}$ (see Section 3.4).

$K\beta$ XES of $trans[(cyclam)Fe^{III}(N_3)_2]^+$ in CH_3CN was measured with a von Hamos spectrometer using a cylindrically bent Ge(440) analyzer crystal. The spectra without laser excitation, about 1 ps after 355 nm photoexcitation and their respective transient difference are shown in Fig. 7.16. In addition to the experimental data, the doublet and quartet static reference spectra (from Fig. 3.9) and the quartet-doublet reference difference (scaled by 0.68) are presented in Fig. 7.16.

The transient difference is in excellent agreement with the scaled reference difference, which allows us to assign the excited state 1 ps after photoexcitation (or at least the dominant one amongst several excited states) to have a quartet spin multiplicity. Furthermore, we can quantify the excited state fraction to $\sim 68\%$. In conclusion, we have found a fingerprint of the penta-coordinated complex $\mathbf{2}_{int}$ which is present after dissociation of an azide ligand and before incorporation of a solvent CH_3CN molecule.

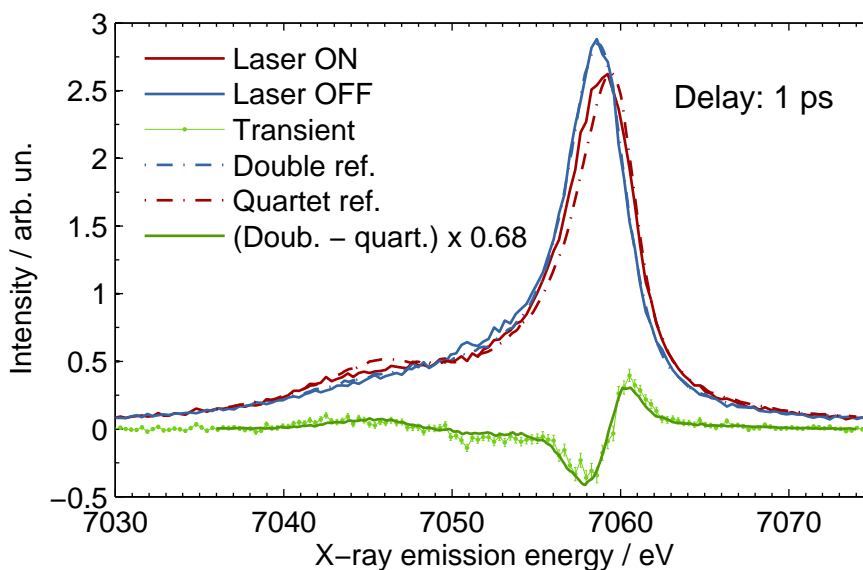


Figure 7.16: $K\beta$ XES of $trans[(cyclam)Fe^{III}(N_3)_2]^+$ in CH_3CN without laser excitation (solid blue line), 1 ps after 355 nm photoexcitation (solid red line) and their respective transient difference (green points with error bars), together with doublet reference (dashed blue line), quartet reference (dashed red line) and to 68 % scaled quartet-doublet reference difference (dashed green line). The reference spectra are taken from [39].

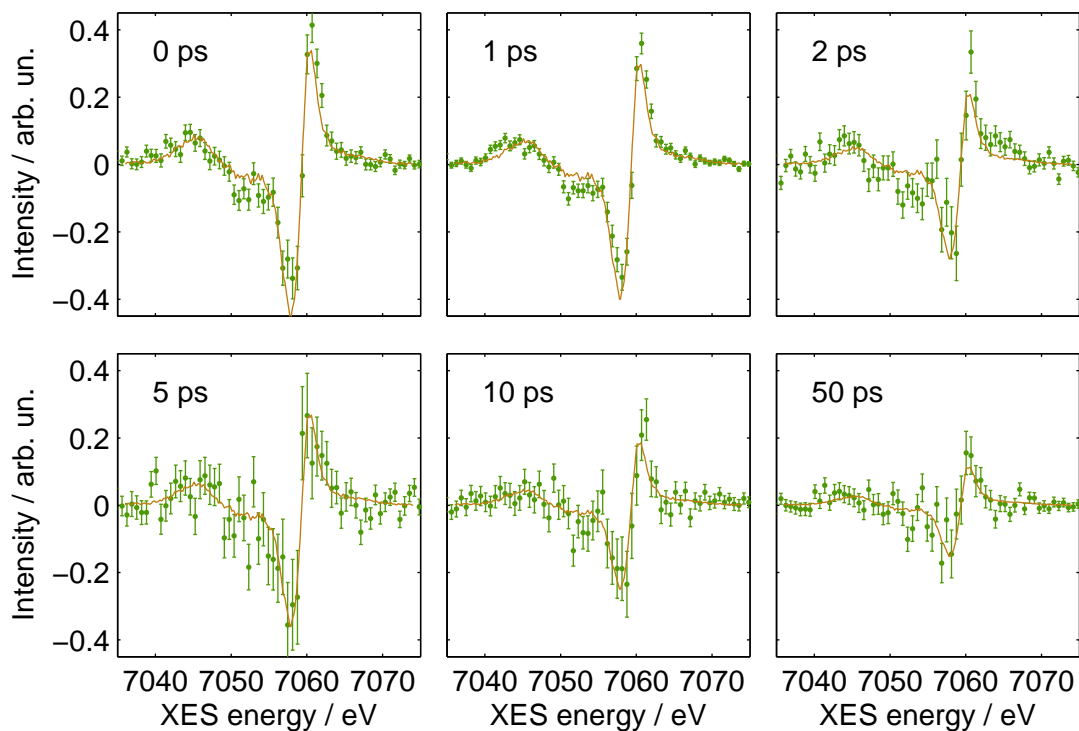


Figure 7.17: Transient K β XES for different delays after photoexcitation (green points with error bars) together with scaled quartet-doublet reference transients (brown solid lines). The reference spectra are taken from [39].

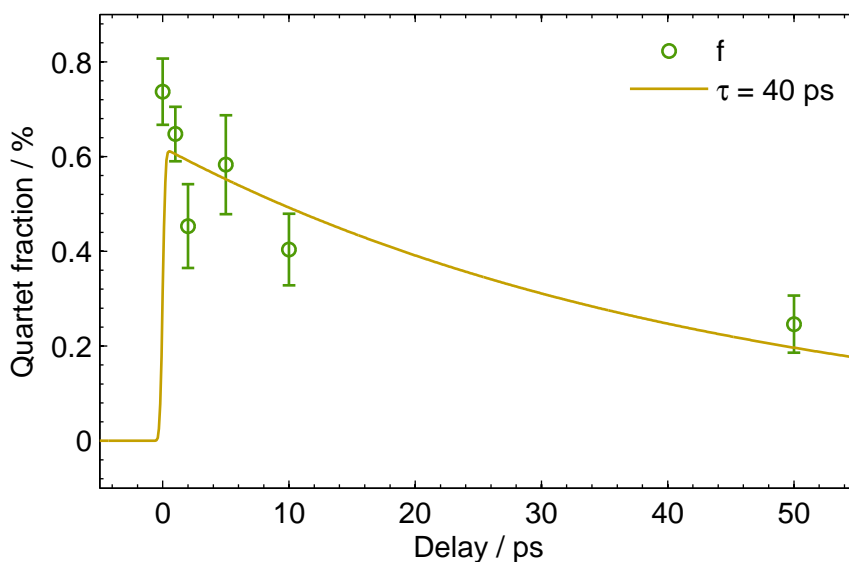


Figure 7.18: Excited state fraction as from transient XES in Fig. 7.17 plotted as a function of the delay. The fit of an exponential decay results in a quartet spin state lifetime of $\tau \approx 40$ ps.

We have measured $K\beta$ XES at five additional delays: 0 ps, 2 ps, 5 ps, 10 ps and 50 ps. The transient spectra together with scaled quartet-doublet reference differences to determine the excited state fraction at each delay point are displayed in Fig. 7.17. The obtained excited state fractions are plotted as a function of the delay in Fig. 7.18. The fit of an exponential decay to these points yields a time constant of $\tau \approx 40$ ps.

Thus we can conclude that the azide dissociation happens within the first ps after photoexcitation, the exact dissociation time cannot be determined due to the few delay points at which XES is measured. Furthermore, the coordination happens on a ~ 40 ps timescale. This timescale is in good agreement with the 28 ps time constant of CH_3CN solvent binding of $[\text{Ru}(\text{bpy})_2(\text{CH}_3\text{CN})]^{2+}$ in CH_3CN found in Ref. [251].

Here we would like to give an outlook on first attempts towards a new von Hamos X-ray emission spectrometer design (by J. Szlachetko) which has been implemented to increase the covered solid (and thus to boost the photon count rate). It applies a 7 cm focal length (and small Bragg angle) cylindrically bent Si(220) analyzer crystal which covers the $K\beta$ as well as the vtc XES and disperses the spectra onto a 2D detector (see Fig. 3.15).

Simultaneously to the measurements in Fig. 7.17 we have acquired XES spectra with this short focal length spectrometer. A TR $K\beta$ spectrum 1 ps after photoexcitation together with a set of reference spectra is shown in Fig. 7.19a). The broadening is clearly visible, which is due to the compromised spectrometer resolution caused by the small Bragg angle and the short focal length. Thanks to the increased count rate we were also able to obtain TR vtc XES. The vtc spectrum without laser excitation, 1 ps after 355 nm excitation and the transient difference are depicted in Fig. 7.19b). Here spectra at low and high laser intensity have been summed up. In the same plot, DFT calculated spectra (by G. Vankó) for complex **1** and a calculated difference corresponding to a transient $\mathbf{2}_{int}$ species are shown. The measured vtc XES spectra are extremely broadened but agree qualitatively with the DFT calculation.

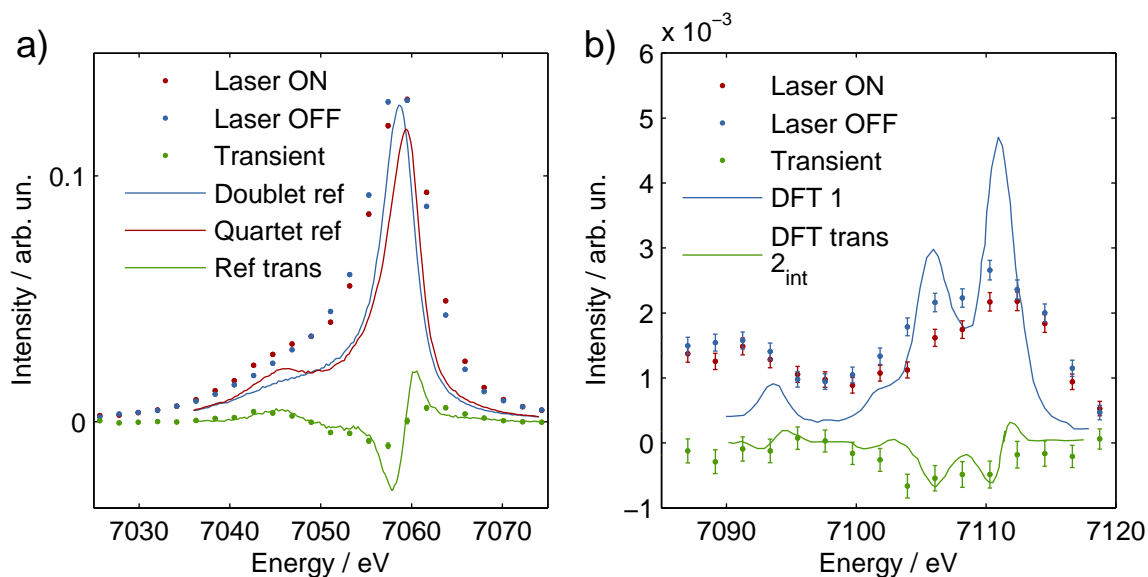


Figure 7.19: a) $K\beta$ XES of $trans[(cyclam)Fe^{III}(N_3)_2]^+$ in CH_3CN without laser excitation (blue points), 1 ps after 355 nm photoexcitation (red points) and their respective transient difference (green points). Additionally, a doublet reference (blue line), quartet reference (red line) and quartet-doublet reference difference (green line) is shown. The reference spectra are taken from [39]. b) vtc XES of $trans[(cyclam)Fe^{III}(N_3)_2]^+$ in CH_3CN without laser excitation (blue points), 1 ps after photoexcitation at 355 nm (red points) and transient difference (green points), together with DFT simulations (by G. Vankó) of vtc XES of **1** and transient difference between **2_{int}** and **1**. The experimental spectra shown here are strongly distorted and with low energy resolution as they are measured with a 7 cm radius Si(220) von Hamos crystal.

Table 7.6: Summary of the observed timescales from 300 fs to 5 ns and their respective assignment in the photochemical reaction pathways of $trans[(cyclam)Fe^{III}(N_3)_2]^+$ in CH_3CN .

Timescale	Wavelength	Description	Assignment
< 300 fs	266 nm	Risetime of XAS transient including pre-edge	Formation time of 3
~700 fs	266 nm	Partial decay of edge-shift	Structural or electronic rearrangements of 3
< 1 ps	355 nm	Formation of doublet-quartet XES transient	Formation of 2_{int}
~10 ps	266 nm	Partial decay of XAS transient	Further structural relaxation (same timescale as vibrational cooling)
~40 ps	355 nm	Decay of quartet-doublet XES transient	CH_3CN ligation / formation of 2
~5 ns	266/355 nm	Decay of edge-shift	Further (diffusion driven) chemical reactions of 2 and 3 , e.g. azide recombination

Furthermore, we have measured TR XANES of **1** following 266 nm excitation at the SACLA XFEL. The measurements revealed a partial decay of the edge-shift features C and D on a ~10 ps timescale, which could be due to structural relaxation. This timescale is in agreement with the timescale observed for VER found in the fs IR experiments [242]. The transient XANES pre-edge and edge shift features have been mapped with higher temporal resolution also applying the timing tool to remove the laser-X-ray temporal jitter. This improved the temporal resolution to ~300 fs and revealed that all transient features are formed within this time, including the pre-edge feature B. Thus we conclude that the Fe(V) formation is completed within ≤ 300 fs. A decay of C and D with a 700 fs time constant has been observed, which could be due to ultrafast electronic or structural relaxation.

We have also measured fs-resolved XES following 355 nm excitation at SACLA. The measurements revealed a short lived intermediate state of higher (presumably quartet) spin multiplicity. This intermediate state can be attributed to the pentacoordinated complex **2_{int}**, which is formed after the N_3^- dissociation and before incorporation of a solvent CH_3CN molecule. The formation of the higher spin intermediated is observed at shortest time delays <1 ps and decays with a ~40 ps time constant. Thus **2_{int}** is formed promptly after laser excitation and the solvation is completed in ~40 ps.

The TR XAS and XES at SACLA facilitated further insights into the photochemical pathways leading to the formation of photoproducts **2** and **3** and the established reaction scheme showing their ultrafast formation processes are summarized in Fig. 7.20. Table 7.6 furthermore summarizes the observed spectroscopic features and the timescales of their temporal evolution together with their respective interpretation.

8 General Conclusions and Outlook

Time-resolved (TR) X-ray absorption (XAS) and emission (XES) spectroscopies can be used to monitor the changes of the electronic and spin state as well as of the molecular structure of transition metal (TM) complexes during the ongoing process of a chemical reaction. With this thesis we have taken the next steps towards applying these TR X-ray spectroscopies towards answering urgent questions in current TM chemistry research, with the focus on catalytically relevant systems. The efforts here can be trisected into technical developments to optimize the signal-to-noise ratio (S/N) in transient X-ray absorption measurements, into the utilization of the TR XAS and XES to study (potential) photosensitizers (PS) and further into the application of these techniques to a model system for enzymatic reactions. These achievements will be summarized and possible follow-up research projects will be outlined in this chapter. Furthermore, the longer-term perspectives of the field, especially in the context of the advent of European XFEL, will be discussed.

8.1 Summary and Conclusions

We have developed a setup to measure TR XAS at the P01 beamline at PETRA III, which has been designed to fully exploit the high X-ray photon flux per pulse available at the P01 beamline as well as the high X-ray pulse repetition rate of PETRA III in 40- and 60-bunch modes (see Chapter 4). This setup is composed of a synchronized and repetition-rate-tunable MHz fiber amplifier laser system and a data acquisition scheme capable of multi-photon counting with single photon resolution in a single X-ray pulse. With this we are able to increase the achievable S/N by a factor >20 at equivalent acquisition times compared to state-of-the-art setups for TR XAS.

The data acquisition as well as the MHz fiber amplifier laser system will be implemented at European XFEL. Here, especially the data acquisition system which is capable of measuring multi-photon events with single photon sensitivity will be crucial, as the X-ray pulse repetition rate in the burst will be 4.5 MHz and the photon flux per pulse will be about two to three orders of magnitude higher than at PETRA III.

The iridium-based photosensitizer (IrPS) $[\text{Ir}(\text{ppy})_2(\text{bpy})]^+$ is used to generate molecular hydrogen when contained in a homogeneous solution with a sacrificial reductant (SR) and a water reduction catalyst (WRC) [49]. In Chapter 5 we have determined the changes in the electronic structure of the IrPS after optical excitation. Here, next to conventional 100-ps-resolved L-edge XAS, TR high energy resolution fluorescence detection (HERFD) L-edge XAS has been exploited to circumvent the ~ 5 eV core-hole lifetime broadening

of the Ir L-edge. The increased resolution of ~ 3 eV allowed to precisely determine the energies of the $2p \rightarrow 5d$ transitions, and thus to map the unoccupied valence orbitals of IrPS. This facilitated determining its electronic structure (e.g. we quantified the ligand field splitting to $10Dq = (4.6 \pm 0.4)$ eV) as well as to follow the iridium valence shell occupation during the photocatalytic cycle. Applying this to the IrPS as part of the fully functioning photocatalytic system facilitated directly observing the electron transfer (ET) process from the SR to the photoexcited IrPS*.

Many PSs based on $4d$ and $5d$ TMs exist, but the goal is to develop cheaper solutions based on $3d$ TMs such as iron. A possible candidate towards this new class of low spin iron(II) complexes is $[\text{Fe}(\text{dcpp})_2]^{2+}$ [52]. We have used combined 100-ps-resolved XAS and XES to characterize the excited state (ES) structure and spin state of $[\text{Fe}(\text{dcpp})_2]^{2+}$ in CH_3CN solution (see Chapter 6). The ES spin was found to be $S_{\text{ES}}=2$ and the first coordination shell ES structure with an average Fe-N bond length of 2.16 \AA is typical for the $^5\text{T}_2$ high spin state of Fe(II) complexes. The ES structure is strongly Jahn-Teller distorted, with axial bond lengths 0.16 \AA shorter than the equatorial ones. The extremely short (280 ps) ES lifetime of $[\text{Fe}(\text{dcpp})_2]^{2+}$ can be explained by a barrier-less transition between the $^5\text{T}_2$ ES and the $^1\text{A}_1$ ground state (GS).

As a follow-up project we intend to also apply our techniques to the last step of the photocatalytic reaction in Chapter 5 in order to observe the electron arrival at the WRC as well as its catalytic reaction in water splitting. Furthermore, we envisage to investigate other photosensitizers, especially $3d$ TM based systems. For example a copper PS has been found to function in hydrogen-generating systems [252]. In parallel to the study on $[\text{Fe}(\text{dcpp})_2]^{2+}$, other groups succeeded to generate low-spin Fe(II) complexes with long-lived ($> \text{ps}$) metal-to-ligand charge transfer states [71, 72, 220, 221], which bear great potential as PSs.

This thesis culminates in the study of $\textit{trans}[(\text{cyclam})\text{Fe}^{\text{III}}(\text{N}_3)_2]^+$ in CH_3CN (see Chapter 7), which can undergo two (main) distinct wavelength dependent photochemical reaction pathways: i) A complete azide can be dissociated with a subsequent coordination of a solvent CH_3CN molecule and ii) the dissociation of a dinitrogen leads to a triple bonded terminal nitride ligand, which superoxidizes the Fe center to +V. Using 100-ps-resolved XAS at distinct wavelengths in the visible and UV spectral range, we found a $1s \rightarrow 3d$ pre-edge feature as an X-ray absorption spectral fingerprint of the Fe(V) complex. Using 300-fs-resolved XAS at SACLA we found the formation of the Fe(V) complex to occur within the 300-fs-resolution of the XANES experiment. 1-ps-resolved XES at SACLA showed that the azide dissociation is prompt (faster than 1 ps) and the coordination of a CH_3CN molecule occurs within ~ 40 ps.

With the investigation of $\textit{trans}[(\text{cyclam})\text{Fe}^{\text{III}}(\text{N}_3)_2]^+$ we have entered a completely new class of molecules to be investigated with ultrafast X-ray spectroscopies. Here an incredible amount of further experiments could be thought of. First of all, an increased temporal resolution to beyond 300 fs is highly desired. The limitation due to the group velocity

dispersion of the pump pulse can be overcome using reflective optics and the broadening due to the group velocity mismatch can be decreased by means of thinner liquid jets. Liquid jets with thicknesses $\ll 10 \mu\text{m}$ are available [253], which could decrease the group velocity mismatch broadening by a factor greater ten, and thus to <20 fs. This should in principle allow temporal resolutions on the order of ~ 30 fs. At equal sample concentrations though, this would also require a ten-fold increase in number of accumulated incident X-ray photons to achieve equivalent S/N. An increased X-ray flux would also be required to collect more than the six data points in the fs-resolved XES spectra (which required several hours of data acquisition at SACLA). These possible extensions and improvements of the experiments presented in this thesis require a higher average photon flux, especially at XFELs.

As the main X-ray absorption spectroscopic feature of the Fe(V) complex was found in the (in principle dipole-forbidden) $1s \rightarrow 3d$ transition pre-edge peaks, one could consider to include TR soft X-ray spectroscopies and measure TR XAS on the Fe L-edge or even the nitrogen K-edge. Including the soft X-ray domain has already proven its potential to investigate Fe(II) spin transition systems [254–256] as well as to understand ligand exchange mechanisms of iron-carbonyls [257, 258].

8.2 Perspectives and Outlook

The European XFEL, which will start user operation in 2017, will revolutionize the field of ultrafast X-ray spectroscopies. With its >100 -fold increased number of X-ray pulses/s, and thus also >100 -fold increase in average photon flux compared to SACLA and LCLS, it will facilitate establishing the TR X-ray spectroscopies as a standard tool in the investigation of chemical dynamics of transition metal complexes. Advanced TR spectroscopies such as HERFD, resonant XES and valence-to-core XES have already shown their potential, but were mainly limited to samples which were tailored to the experiment (highly concentrated, strong optical absorption with large electronic and structural changes, etc...). Thanks to European XFEL, these techniques will also become standard for (dilute) biological samples or samples of technological interest.

The higher average photon flux will also allow to decrease the optical excitation energies, and thus to "tickle and probe" the sample. Many recent experiments, especially those conducted at XFELs, where beamtime is scarce, suffer from excessively high pump laser intensities $> \text{TW}/\text{cm}^2$ [41, 42] (This applies also to the SACLA experiments presented in Chapter 7). Decreasing the laser intensity requires to decrease the laser fluence. The option to elongate, i.e. by chirping or stretching, the laser pulses is not desired, as this would compromise the temporal resolution. A lower laser fluence is, in the case of linear absorption, directly proportional to the excited state fraction f . The S/N of a TR XAS measurement in total fluorescence yield scales with square-root of the number of incident X-ray photons I_0 and linear with f , thus $\text{S/N} \propto f\sqrt{I_0}$ (see Section 3.3.3). To compensate

for an order of magnitude lower laser fluence requires a 100-fold larger accumulated number of incident X-ray photons, which corresponds exactly to the increase in average flux at European XFEL compared to LCLS or SACLA.

The Femtosecond X-ray Experiments (FXE) instrument at the European XFEL will be a dedicated instrument for combined XAS, XES and also X-ray diffuse scattering (XDS) experiments. There, almost all the techniques described in this thesis will be available. (The exception could be the extended X-ray absorption fine structure, which requires scanning the incident X-ray energy over a large energy range > 100 eV and it is unclear to date if this will be possible at European XFEL). Although all experiments described in this thesis have been done on molecular systems in solution, the techniques can also be applied to solids and gases. Here, catalytically relevant examples include TiO_2 [36] and ZnO [259, 260] nanoparticles.

A MHz DAQ at P01 User's Guide

Written with the help of Christina Bömer, Patrick Gessler, Andreas Beckmann, Hamed Sotoudi Namin, Frank Babies and many more.

A.1 Preparing Input Signals for MHz DAQ

A plot showing the bunch clock (trigger) and laser gate (laser trigger) traces, the APD trace as well as the trace of a laser photodiode (which sits in this case inside the tangerine fiber amplifier) can be found in Fig. A.1 and a schematic showing the connections to set up these signals is shown in Fig. A.2.

With the rising edge of the bunch clock (BC) trigger signal the MHz DAQ is triggered to start the acquisition at 0 ns and sample the APD trace. Due to a mismatch of the internal delays between the BC trigger signal, the laser trigger signal and the signal trace to be digitized, the trigger signal has to be additionally delayed by about 80 ns and the laser trigger by about 120 ns. In the following we describe how the signals are to be fed into the MHz DAQ:

- **Trigger:** As a trigger signal the single bunch trigger of the bunch clock (~ 130 kHz) is used. As trigger signals positive signals of about 3 V are required. Attenuator(s) can be used to decrease the signal height to the desired 3 V. Due to internal delays of the MHz DAQ the trigger signal has to be shifted 80 ns later than the actual start of the acquisition. Therefore we use the delay option of the BC electronics. In Fig. A.1 the signal before shifting is shown as a dashed purple line, the actual trigger shifted by 80 ns as it is sent to the MHz DAQ is shown with a solid purple line.
- **Laser trigger:** The laser trigger (which is in reality a laser ON gate) is derived from the photodiode (PD) signal monitoring the optical laser pulses, see solid green line in Fig. A.1. As a laser trigger signal a positive signal of about 3 V is required as well. Here we used the PD inside the tangerine amplifier which delivers a positive signal and we derive a laser trigger gate from the PD signal as follows: The PD signal is inverted in the Philips Scientific fan-in/out and then discriminated in the Ortec 935 CFD to a logic signal. This signal is sent to the Ortec GG8020 gate generator to prepare a TTL signal gate of right length and to delay this gate to the desired position in time. The gate width should be slightly smaller than the inter bunch spacings of 192 ns in 40 bunch mode and 128 ns in 60 bunch mode. The center of

the shifted laser trigger should be 120 ns after the start position of the pulse trace integral of the laser ON X-ray pulse (which is usually set to just before the start of the rising edge of the X-ray pulse). The laser trigger before being shifted is shown as a yellow dashed line in Fig. A.1 and as a solid yellow line after being shifted by 120 ns (which is send to the MHz DAQ). An additional attenuator can be used to decrease the signal height of the laser trigger.

- APDs: The APD signal is the raw signal coming from the APD and an example can be seen as a blue solid line in Fig. A.1. The APD pulse which corresponds to the laser excited pulse is highlighted red and arrives more than 200 ns later than the laser diode pulse, which is due to the fact that long (50 m) cables have been used to transmit the APD signals. The APD signals can be attenuated to match the strict maximum of 0.8 V peak-to-peak, which the digitizer accepts.

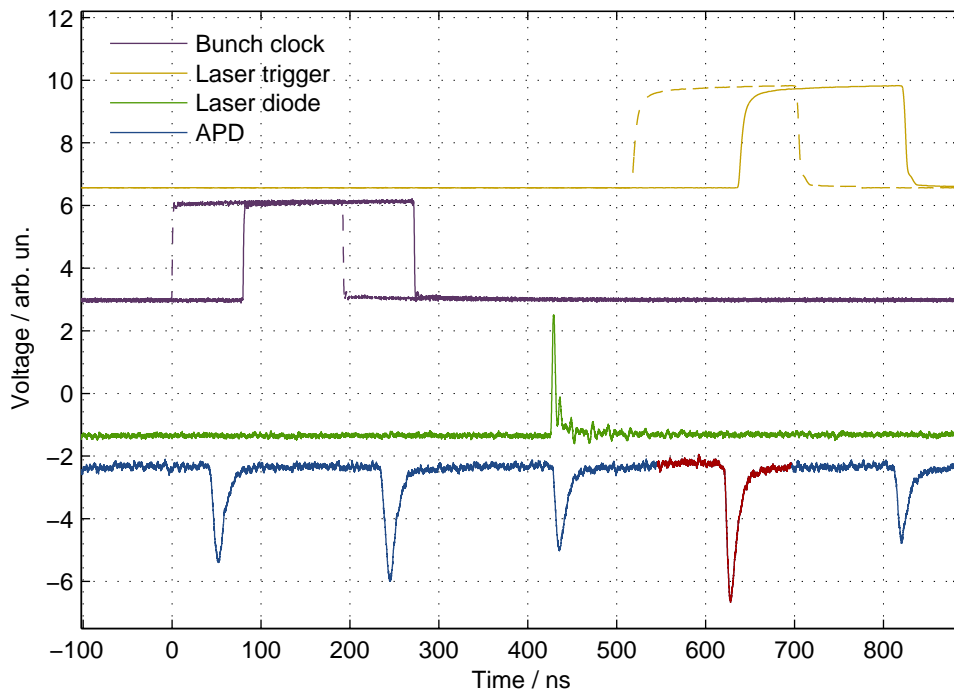


Figure A.1: Example of input signals for MHz DAQ: Bunch clock signal (purple solid line) used for triggering the acquisition, laser trigger (yellow solid line) derived from the laser photodiode signal (green solid line) and APD signal measuring TFY of the sample (blue solid line). The third APD pulse corresponding to the laser excited one is highlighted red.

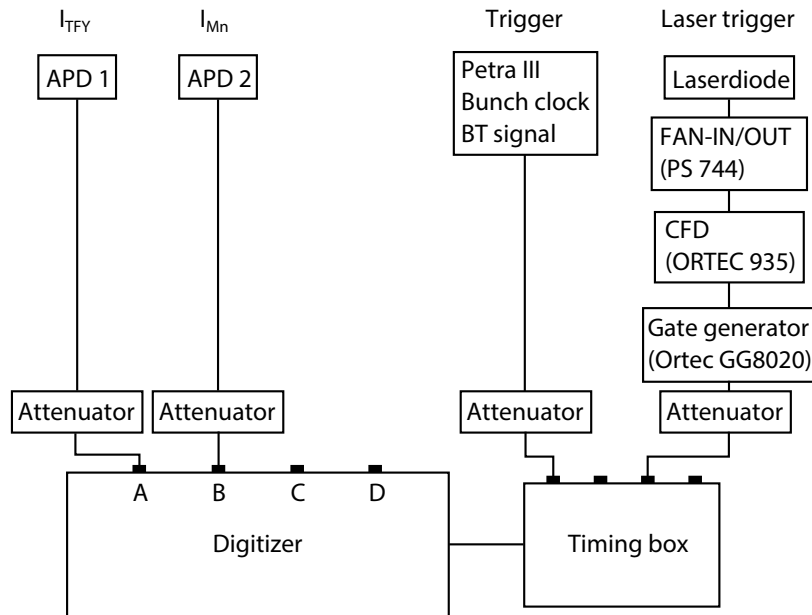


Figure A.2: Scheme showing an example of the input signal connections for the MHz DAQ. Two APD signals are fed into the digitizer, e.g. to channels A and B to measure the fluorescence signal of the sample I_{TFY} and the normalization signal I_{Mn} .

A.2 Software Starting Procedure

Start of Karabo Framework

The Karabo framework has to run on the MHz DAQ control PC. To start the framework open a terminal and enter:

```
kenv start
```

One can check if all servers are running using the command

```
kenv status
```

If so, the GUI can be started using

```
kenv gui
```

The Karabo framework can be stopped using (this command needs to be repeated until all servers are stopped)

```
kenv stop
```

Start of Device Server

The device server is executed on the crate. To start it, log in to the crate with the user name "utcaadm" and the password "ADMIN4every1" via ssh by entering into a (second) terminal

```
ssh utcaadm@exflutcafxe
```

Now one can start the device server by entering

```
kenv start
```

Start of Karabo Project

The starting procedure for data acquisition with Karabo is as follows:

- Use the "wall plug" icon in the Karabo GUI (see screenshot in Fig. A.3) to log on
- In the "Navigation" window the two devices, i.e. the control PC and the crate, should show up. Then we can open the pre-configured Karabo project called "digitizer_fxe" in the "Projects" window and the the project "digitizer_fxe" will show up in the "Projects" window.
- Left click on the project "digitizer_fxe" to load it into the "Configurator" window. Now we can change the parameters of the project to our needs before instantiating the project.
- Instantiate the project with parameter **Data Type** under **Acquisition** set to "raw". Now we can set the values for *baseline begin*, *baseline end*, *pulse begin*, *pulse end* and *upper limit* correctly by monitoring the signal traces within Karabo (see Fig. A.3). If the baseline before the first pulse is a little longer or shorter than desired, the trigger signal from the bunch clock can still be fine tuned (shifts less than tens of ns).
- Shutdown instance and change parameter **Data Type** under **Acquisition** to "APD". Check all parameters if they are at the desired values (see next chapter for detailed description).
- Instantiate again. Now we are ready to scan with SPOCK.

Start of TCP/IP Server

The MHz DAQ is connected to the beamline control at PETRA III (SPOCK) via a TCP/IP server, which has to be started on the control PC in the Karabo command line by executing the following commands:

```
cd /karabo/karaboRun/bin
./startCli
import rdcserver
d = DeviceClient()
s = rdcserver.Server(2500, d, 'digitizer_fxe')
s.start()
```

A.3 Parameters of the Karabo project for data acquisition

In this section describe the parameters of the Karabo project which can be used to tailor the data acquisition to ones needs. A selection of the more important parameters as used for an example configuration can be found in Tab. A.1 and I will comment in the following on the most relevant parameters.

- **Data Type** under **Acquisition**:

The most important parameter is the **Data Type** in the parameter group **Acquisition** as it is used to select one of the fundamentally different acquisition modes. The two acquisition modes which we use are:

1. **raw**: In "raw" mode the digitizer sampled voltage, i.e. the detector signal trace, is saved for a number of samples which can be set in the configurator. The "raw" mode also allows to directly monitor the signal trace within Karabo, which is useful to check the correct preparation of the input signal traces and trigger signals, as described in the previous section.
2. **APD**: In "APD" mode the signal trace is digitized and further processed to obtain a single pulse integral by integrating over the APD pulse and correcting background to remove a possible offset. A *baseline begin* and *baseline end* as well as *pulse begin* and *pulse end* have to be set (all in units samples usually corresponding to 0.5 ns when the the digitizer is-set up to work at 2 GS/s). Furthermore, an *upper limit* has to be defined, which corresponds to the inter-bunch spacing of the X-rays in samples. This needs to be set to distinguish the X-ray pulses within one acquisition cycle, as the data acquisition is only triggered at a sub-harmonic of the X-ray repetition rate, the single bunch roundtrip frequency. The laser trigger is further used to mark each pulse integral as laser ON or OFF.

Both software- and hardware(fpga)-based integration algorithms are implemented to calculate the mean value and standard deviation of the laser ON and OFF pulse integrals. The "APD" mode is the one frequently used at Petra III, as the mean values and standard deviations can be streamed via the TCP/IP server to the beamline control (SPOCK) and are written into the data file of the executed scan.

- **Triggers/Run** under **Acquisition**:

Number of triggers used per acquisition cycle. For example in the case of the 130 kHz trigger, 130000 corresponds to 1 s data acquisition. This value can be set via the TCP/IP server to synchronize the data acquisition time of a scan in SPOCK to the one in the MHz DAQ.

- **Channel A** under **Acquisition**:
 Activate *true* to select **Channel A** for acquisition. The same works for **Channel B**, **Channel C** and **Channel D**. In the usual configuration, **Channel A** is used for the TFY of the sample, **Channel B** for the I_0 .
- **Samples/Trigger** under **Acquisition/Raw Data**:
 Defines the number of samples which are acquired per trigger when the **Data Type** parameter under **Acquisition** is set to *raw*.
- **Correction** under **Acquisition/APD**:
 Select either software-based or hardware(=fpga)-based integration algorithm when the **Data Type** parameter under **Acquisition** is set to *APD*. The software-based algorithm is the accurate but slower one. When using the MHz DAQ at PETRA III, we usually use the software based algorithm, as only the mean values and standard deviation are recorded and we wish to have an accurate value.
- **Pulses/Trigger** under **Acquisition/APD**:
 Sets the number of pulses/trigger when **Data Type** parameter under **Acquisition** is set to *APD*. In the example in the Tab. A.1 it is set to 4, which would mean that with the 130 kHz trigger 520000 pulses/second are acquired. This values should be smaller than the total number of X-ray pulses available in an acquisition cycle, e.g. it should be set to a maximum of 39 in 40 bunch mode and 59 in 60 bunch mode, to prevent problems due to overlaps of acquisition cycles.
- **Mode** under **Output**:
 Choose if data is written by MHz DAQ to internal storage. If only mean and stdv are recorded in SPOCK, this is set to *none*. Set to *file* to record either single pulse integrals or full sampled traces (see **Data Type** under **Acquisition**).
- **Triggers/File** under **Output**:
 Set number of triggers which are written into one file. If it is smaller than **Triggers/Run**: under **Acquisition**, one acquisition cycle will be split into multiple files.

A.4 TCP/IP server to connect MHz DAQ with SPOCK

In the current configuration a TCP/IP server is used to connect the MHz DAQ with SPOCK.

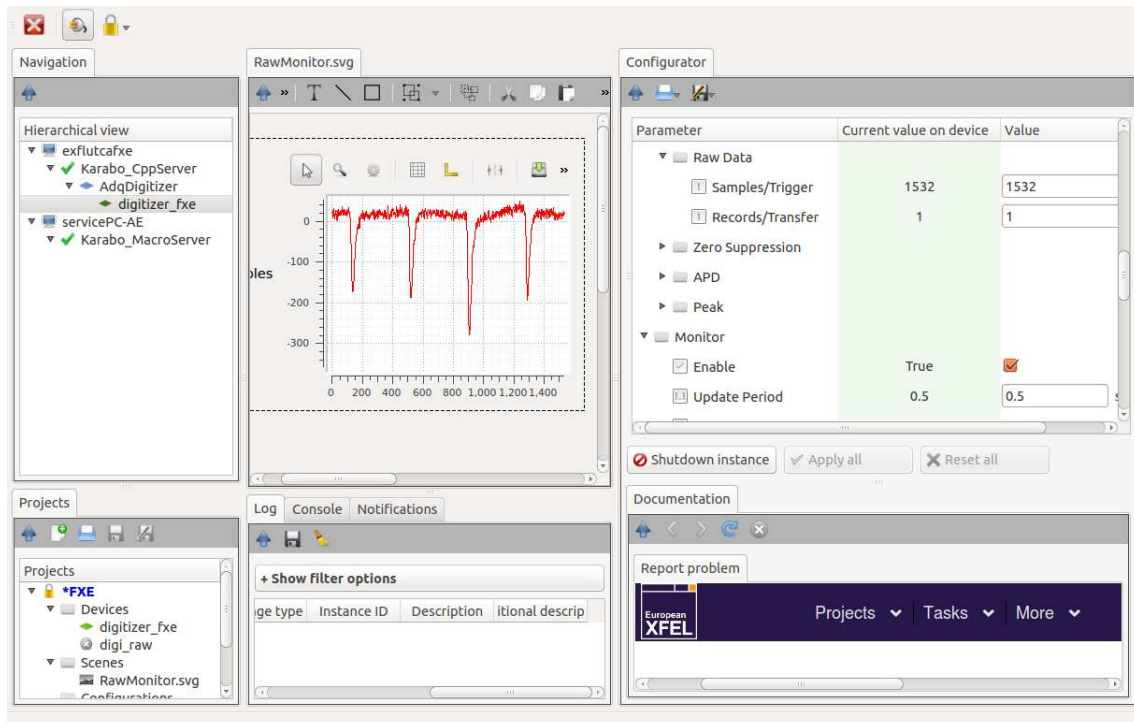


Figure A.3: Screenshot of Karabo with opened "digitizer_fxe" project within "raw" mode.

Table A.1: List of important parameters of the Karabo project "digitizer_fxe". The configuration shown below is used to measure TR XAS in 40 bunch mode at Petra III with the laser repetition rate set to 130 kHz. A total of 4 pulses out of 40 per round trip are acquired, 3 laser off and 1 laser on using the signal traces as shown in Fig. A.1. The scheme is used to measure XAS of samples with long($>1\mu\text{s}$)-lived photoproducts. The 36 X-ray pulses, corresponding to $\approx 7\mu\text{s}$, which are not recorded between the laser ON and following 3 laser OFF pulses are long enough to replenish the the sample, given the laser spot size is small($\sim 20\ \mu\text{m}$).

Parameter group	Parameter name	Example value	Comment
Trigger	Mode	External	
Trigger	Source of ID	Internal	
Trigger/Master	Input	RX18	
Trigger/Master	Output	None	
Trigger/Slave	Input	RX18	
Trigger/Laser On/Off	Input	TX18	
Trigger	Edge	Rising	
Trigger	Level	100	
Trigger	Channel A	True	
Trigger	Channel B	True	
Trigger	Channel C	True	
Trigger	Channel D	True	
Trigger	Pretrigger	0	
Trigger	Trigger Hold Off	0	
Trigger	Timeout	2.0	
Acquisition	Triggers/Run	130000	
Acquisition	Channel A	True	
Acquisition	Channel B	True	
Acquisition	Channel C	False	
Acquisition	Channel D	False	
Acquisition	Interleaved	False	
Acquisition	Signal Offset	1580	
Acquisition	Data Type	APD	
Acquisition/Raw Data	Samples/Trigger	1532	
Acquisition/Raw Data	Records/Transfer	1	
Acquisition/Zero Suppression	Polarity	positive	
Acquisition/Zero Suppression	Samples	8	
Acquisition/Zero Suppression	Threshold	5.0	
Acquisition/Zero Suppression	Limiter	4	
Acquisition/APD	Correction	Software	
Acquisition/APD	Pulses/Trigger	4	
Acquisition/APD/Channel A	Base Begin	1	
Acquisition/APD/Channel A	Base End	100	
Acquisition/APD/Channel A	Pulse Begin	101	
Acquisition/APD/Channel A	Pulse End	300	
Acquisition/APD/Channel A	Initial Delay	0	
Acquisition/APD/Channel A	Upper Limit	384	
Acquisition/APD/Channel A	Calibration Factor	1.0	
Acquisition/APD/Channel B	<i>same as for Ch. A</i>		
Acquisition/APD/Channel C	<i>same as for Ch. A</i>		
Acquisition/APD/Channel D	<i>same as for Ch. A</i>		
Monitor	Slot/Channel	1A	
Output	Mode	None	
Output	Path		
Output	Filename Prefix		
Output	Overwrite Mode	UseRunNumber	
Output	Triggers/File	100	

B Iridium L₃-edge - Gaussian vs. Lorentzian Broadening

We have noticed, that the broadening of the L-edges of $[\text{Ir}(\text{ppy})_2(\text{bpy})]^+$ has a large Gaussian contributions (see Fig. B.1). This is in contrast to the expectations for a mainly lifetime broadened absorption edge.

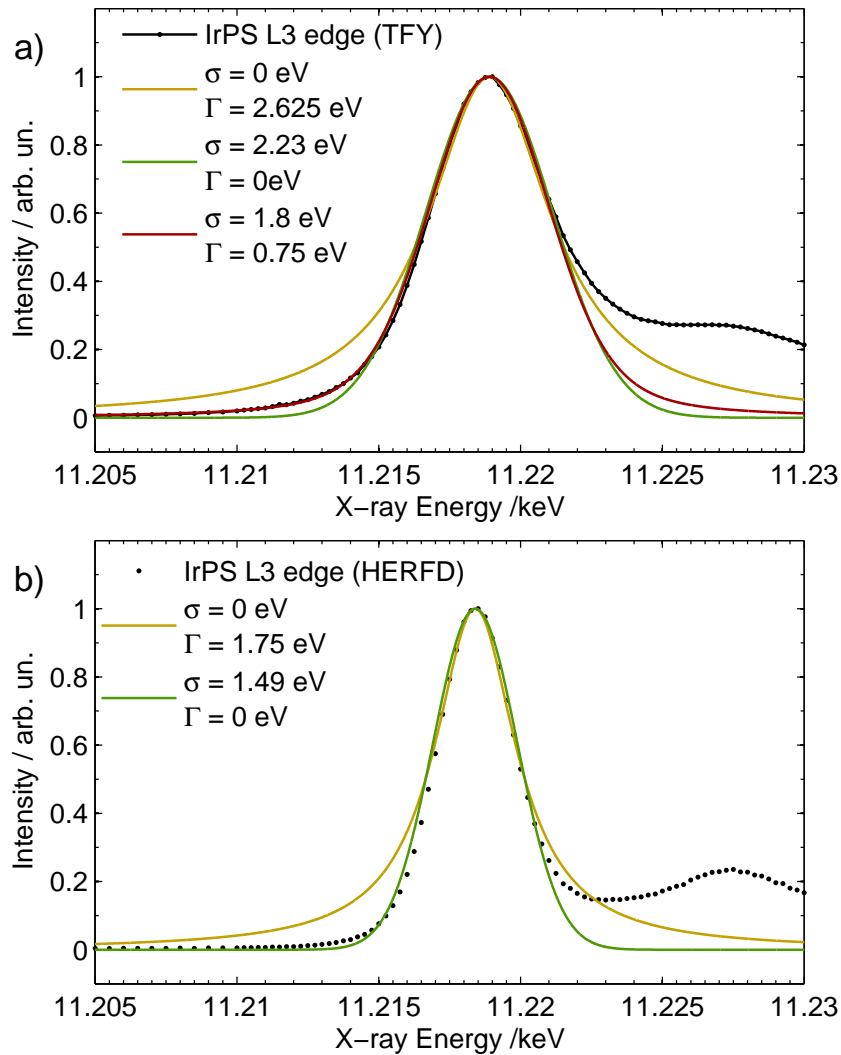


Figure B.1: Comparison of Gaussian (σ) and Lorentzian (γ) broadening of the L₃-edge measured in TFY (a) and HERFD (b).

C Supplementary Info - SACLA Experiments

C.1 Dispersive Pulse Broadening and Spot Size Measurements

Dispersive Pulse Broadening

The minimum duration of a laser pulse τ_0 (FWHM) is determined by the time-bandwidth product

$$P_{tb} = \Delta\nu \times \tau_0 , \quad (\text{C.1})$$

where $\Delta\nu$ is the spectral bandwidth (FWHM) of the laser pulse centered at a frequency $\nu = c/\lambda$. For a Gaussian pulse $P_{tb} \approx 0.44$ [261]. Using this, we have calculated the required spectral bandwidth $\Delta\lambda$ of a Gaussian pulse to generate Fourier-transform limited laser pulses with a center wavelength of 266 nm (see Fig. C.1a)) and with a center wavelength of 355 nm (see Fig. C.1b)).

Due to the group velocity dispersion an initially transform limited pulse of duration $\tau_{o,p}$ is broadened and the pulse duration after passing through a distance z of a material with group velocity dispersion k_l'' is given by [250]

$$\tau_p(z) = \tau_{o,p} \sqrt{1 + \left(\frac{(4 \ln(2) z k_l'')^2}{(\tau_{o,p})^4} \right)}. \quad (\text{C.2})$$

For fused silica at $\lambda = 266$ nm avlenegth the group velocity dispersion is $k_l'' = 198$ fs²/mm and at $\lambda = 355$ nm it is $k_l'' = 117$ fs²/mm [249].

We have used this to calculate the pulse duration after traveling a distance z through fused silica. The result for initially Fourier-transform limited laser pulses of several different durations at a central wavelength of 266 nm is shown in Fig. C.1c) and for a central wavelength of 355 nm in Fig. C.1d).

Laser Spot Size Measurements

The laser spot size has been measured using a 100 μm diameter pinhole. This has been translated through the laser beam and the transmitted power has been measured. These scans in X-direction (horizontal) and Z-direction (vertical) are shown in Fig. C.2.

A fit of a convolution of a Gaussian beam shape with a 140×100 μm^2 diameter (V \times H, FWHM) pinhole yielded a best fit to the data.

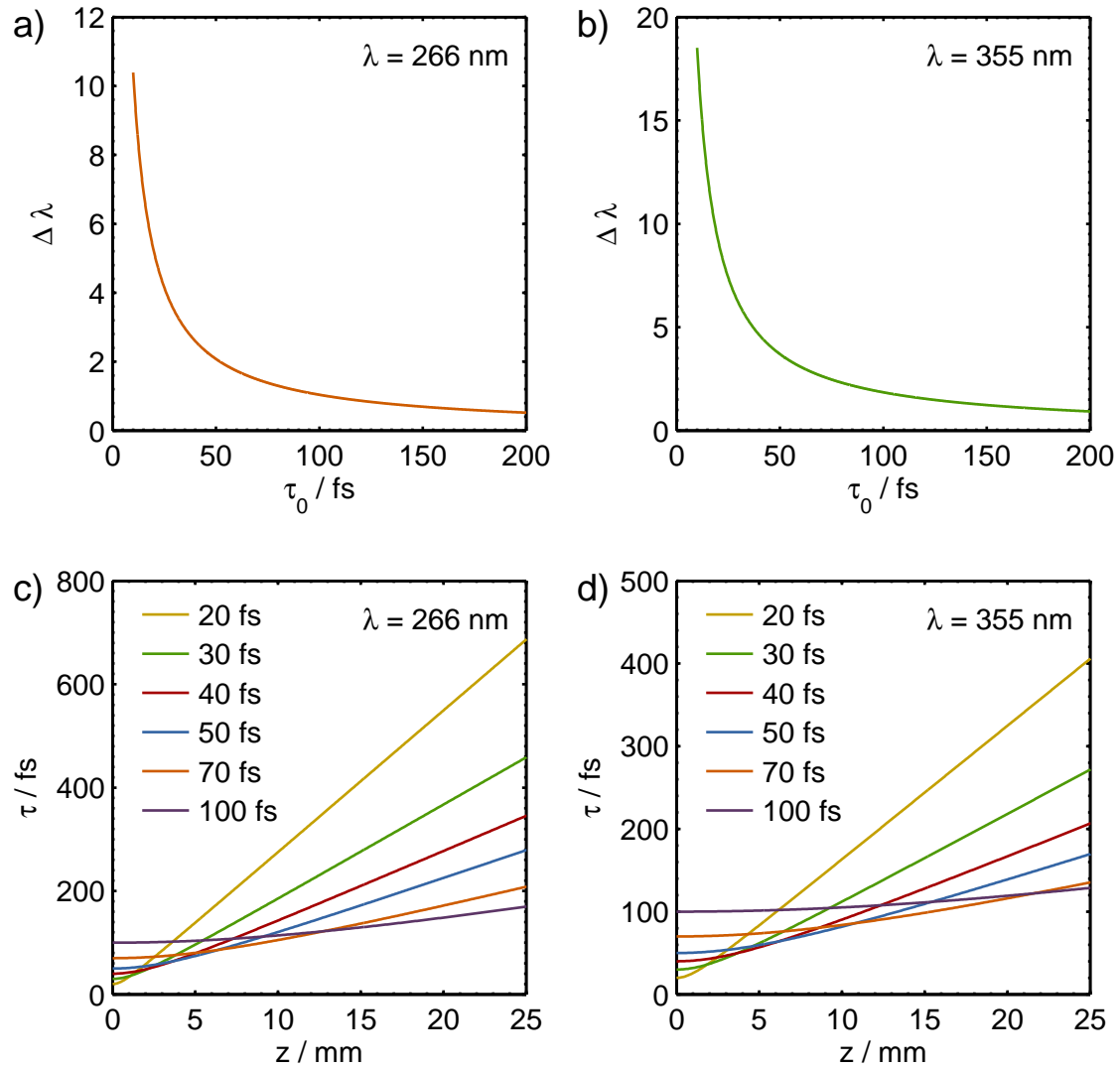


Figure C.1: Required spectral bandwidth to generate a Fourier-transform limited laser pulse as a function of the the pulse duration at a central wavelength of 266 nm (a) and 355 nm (b). Pulse duration of initially Fourier-transform limited laser pulses after group velocity dispersion as a function of the path length z traveled through fused silica for a central wavelength of 266 nm (c) and 355 nm (d).

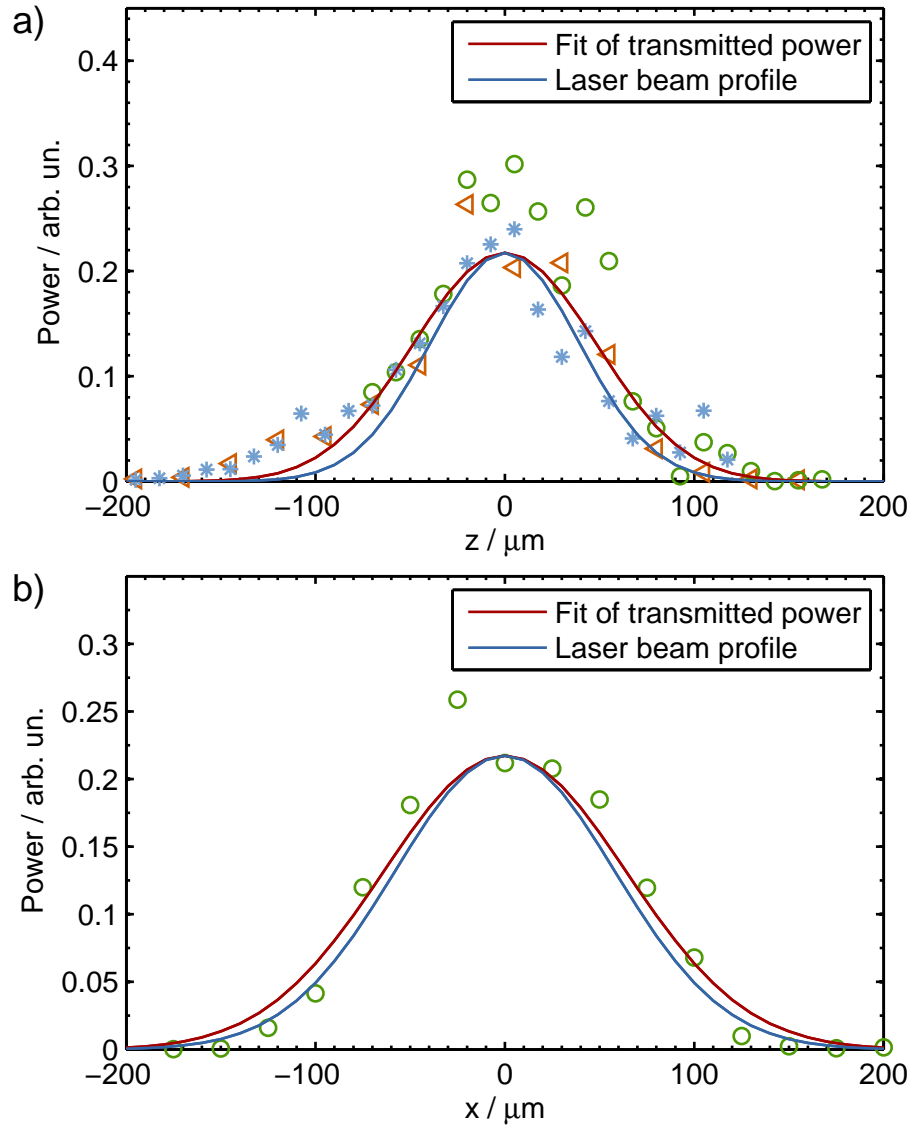


Figure C.2: Laser pinhole scans using 100 μm diameter pinhole in a) X-direction (stars, circles and triangles) and b) Z-direction (circles). A Gaussian laser beam profile has been convoluted with a 100 μm diameter pinhole to fit the data (red solid line). The best fit was obtained for a laser beam profile with $\sim 140 \mu\text{m}$ diameter (FWHM) in X-direction (horizontal) and $\sim 100 \mu\text{m}$ diameter (FWHM) in Z-direction (vertical). These laser beam profiles in both directions are plotted as a solid blue line.

C.2 Low vs. High Laser Intensity

Low vs. High Laser Intensity during XES Measurements

The $K\beta$ XES of $trans[(cyclam)Fe^{III}(N_3)_2]^+$ in CH_3CN was measured at SACLA at comparably high laser pump pulse energies of $13 \mu J$. We have measured one single scan at about half the excitation energy ($6 \mu J$). The transient here is identical to the high power transient. This means that we have already reached a remarkable ground state bleach at the lower excitation energies. Most importantly though, the effective shape of the transient is identical and we assume that this allows us to conclude that the investigated photochemistry is not affected by the excessively high laser pulse energy in the rest of the measurements. Both transient XES are shown in Fig. C.3

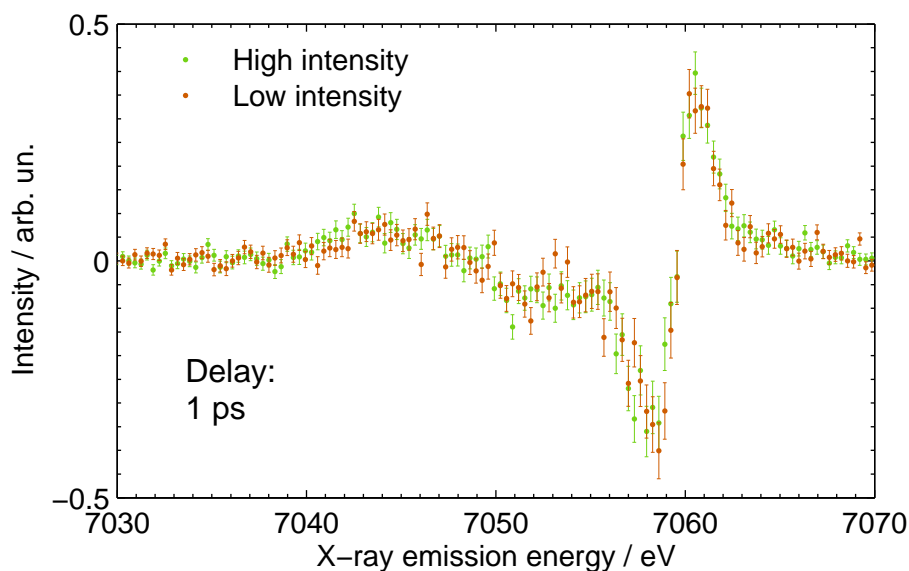


Figure C.3: Transient $K\beta$ XES of $trans[(cyclam)Fe^{III}(N_3)_2]^+$ in CH_3CN 1 ps after 355 nm excitation at high ($13 \mu J$ laser pulse energy corresponding to an intensity of $\sim 2 \text{ TW/cm}^2$) and ($6 \mu J$ laser pulse energy corresponding to an intensity of $\sim 1 \text{ TW/cm}^2$) laser intensity.

Low vs. High Laser Intensity during XAS Measurements

The low intensity transient XANES of $trans[(cyclam)Fe^{III}(N_3)_2]^+$ in CH_3CN 100 ps after 266 nm photoexcitation from the APS is compared to the higher intensity transient measured at SACLA in Fig. C.4

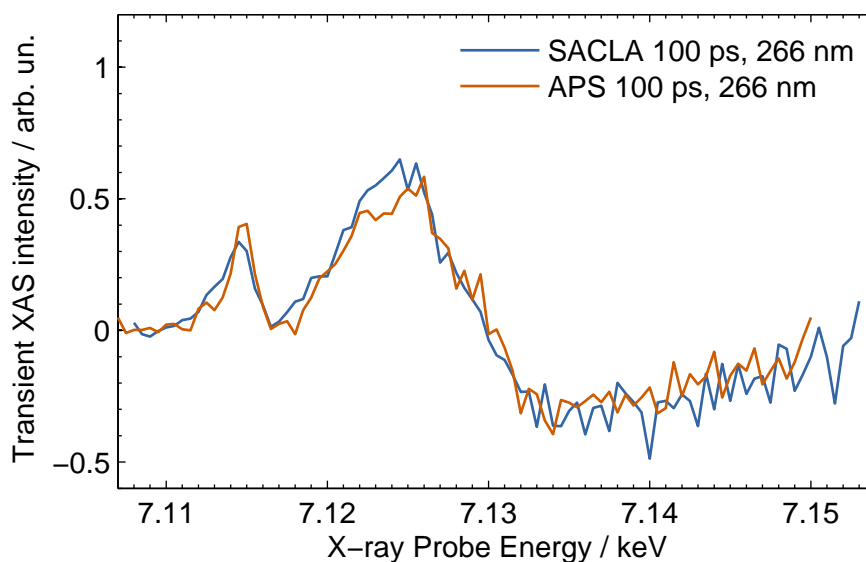


Figure C.4: Transient XANES of $trans[(cyclam)Fe^{III}(N_3)_2]^+$ in CH_3CN 100 ps after 266 nm photoexcitation measured at SACLA with high laser intensity (680 GW/cm^2) and measured at the APS at low laser intensity (300 GW/cm^2). The transients agree very well, showing that the photophysics of $trans[(cyclam)Fe^{III}(N_3)_2]^+$ are not affected by the relatively high laser intensity at SACLA. The transients are arbitrarily scaled for comparison.

C.3 Channel Cut Si(111) Monochromator and Timing Tool Correction

Channel Cut Si(111)

We have used the channel cut Si(111) monochromator at SACLA, the X-ray beam path through these 2 channel cut crystals is depicted in Fig. C.5. When the X-rays are monochromatized, are reflected four times by an angle of θ (see green solid line). Due to the two identical channel cut crystals, the monochromatization does not lead to a horizontal offset compared to the X-ray beam path without monochromator (blue dashed line). Nevertheless, the monochromatization of the X-rays leads to a path elongation of Δl_{mono} and thus an additional delay Δt_{mono} , which can be calculated via

$$\Delta t_{\text{mono}} = \frac{\Delta l_{\text{mono}}}{c} \quad \text{with} \quad \Delta l_{\text{mono}} = 2d \frac{1 - \cos(2\theta)}{\sin \theta}. \quad (\text{C.3})$$

Here c is the speed of light and d the channel width of the channel cut Si(111) crystal, see Fig. C.5. In the Fig., the path length difference with and without mono corresponds to $\Delta l_{\text{mono}} = 2a + b - c$. In Fig. C.6 the Bragg angle θ and the additional delay caused by the monochromator Δt_{mono} as a function of the incident X-ray energy are plotted.

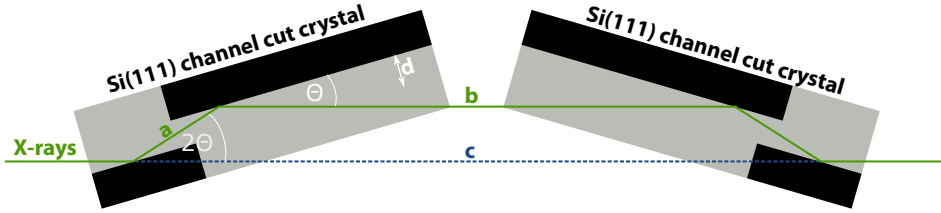


Figure C.5: Channel cut 4-bounce Si(111) monochromator at SACLA.

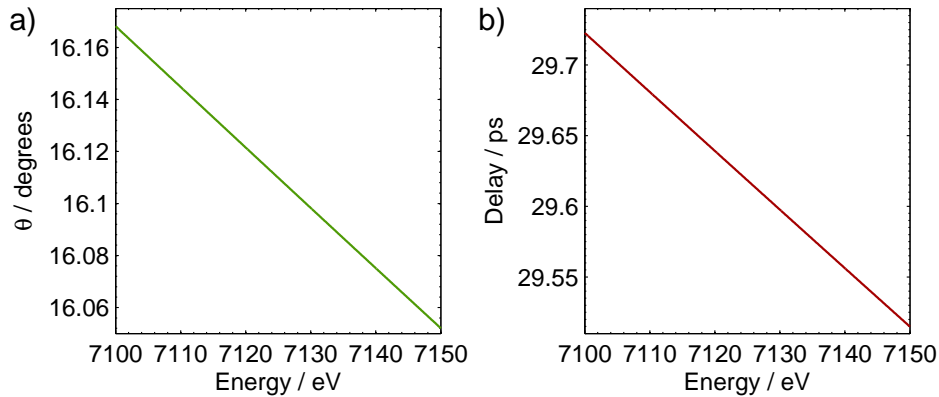


Figure C.6: a) Bragg angle θ of Si(111) monochromator as a function of the X-ray energy, b) additional laser-X-ray delay due to elongated beam path through Si(111) four-bounce mono in Fig. C.5

Timing Tool Jitter Correction

In Fig .C.7, the delay distribution before and after timing tool correction of the 14 XANES scans of $trans[(cyclam)Fe^{III}(N_3)_2]^+$ shown in Fig. 7.11 are plotted. Before the timing jitter correction, the distribution contains 14 discrete values, after correction the distribution is spread out. Due to the jitter, a more or less continuous distribution from -1 ps to 2 ps is obtained.

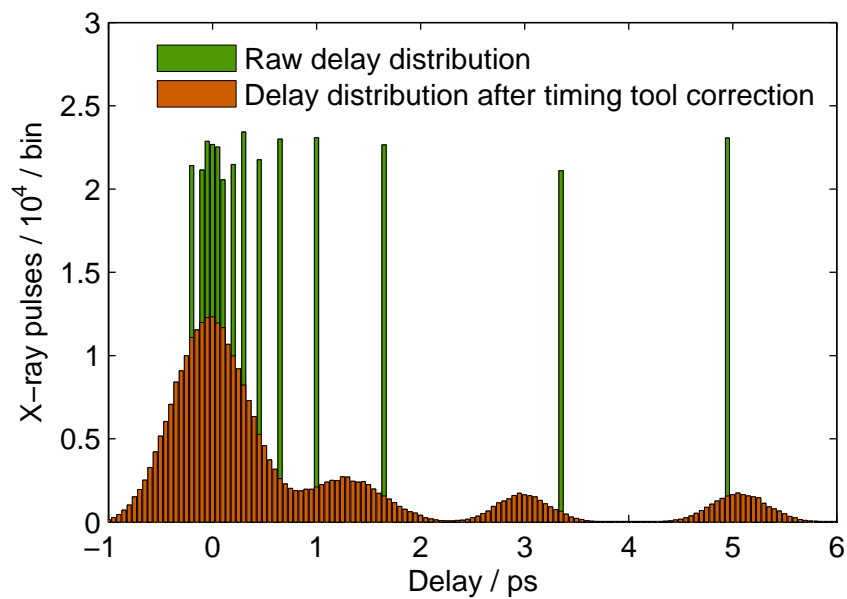


Figure C.7: Delay distribution before and after timing tool correction.

D FEFF Input File for $[\text{Fe}(\text{dcpp})_2]^{2+}$ Ground State

*TITLE S=0 Fe(dcpp) singlet ground state spectrum

*britza 22042014

CONTROL 1 1 1 1 1 1

PRINT 1 0 0 1 0 3

EDGE K

S02 1.0

SCF 5 1 30 0.2

EXAFS

RPATH 6

EXCHANGE 0 0 0.35 0

POTENTIALS

0 26 Fe 2 2 1.0

1 8 O -1 1 4.0

2 7 N -1 1 6.0

3 6 C -1 1 34.0

ATOMS

0.000016671	0.000000283	-0.000002238	0	Fe
3.48355901	-2.443509172	-0.05959316	1	O
-3.483510759	-2.443560184	0.058451241	1	O
1.41403748	-0.013400399	1.442593274	2	N
1.409106395	0.909562047	2.419671495	3	C
2.469636487	1.080521052	3.300462918	3	C
3.596910112	0.279188826	3.159188066	3	C
3.599195475	-0.699361974	2.169689822	3	C
2.483956128	-0.833218947	1.349130937	3	C
0.000031881	-1.998857142	-0.000529456	2	N

Appendix D. FEFF Input File for $[\text{Fe}(\text{dcpp})_2]^{2+}$ Ground State

2.455136094	-1.982681365	0.388432279	3	C
1.147601391	-2.693192833	0.143203833	3	C
1.18765002	-4.086241536	0.114883633	3	C
0.000019289	-4.796351581	-0.000699764	3	C
-1.187592636	-4.086213347	-0.116203313	3	C
-1.147532222	-2.693157103	-0.144343128	3	C
-2.455068741	-1.982575984	-0.389374379	3	C
-1.414025573	-0.012718551	-1.442516554	2	N
-2.483905475	-0.83264788	-1.349516654	3	C
-3.599176753	-0.698315241	-2.169957877	3	C
-3.596986171	0.280930311	-3.158768375	3	C
-2.469788122	1.082457846	-3.299536143	3	C
-1.409200313	0.91092725	-2.418936606	3	C
3.483545463	2.443531201	0.059592456	1	O
-3.48352346	2.44354098	-0.058450845	1	O
1.414039819	0.013408694	-1.442595793	2	N
1.409116793	-0.909554972	-2.419673072	3	C
2.469653119	-1.080513352	-3.300457134	3	C
3.596924569	-0.279179169	-3.159175609	3	C
3.599201005	0.699373775	-2.169679493	3	C
2.483955927	0.83323006	-1.349128307	3	C
0.000021367	1.998858259	0.000525735	2	N
2.455126342	1.982695446	-0.388433711	3	C
1.147586987	2.693199871	-0.143209383	3	C
1.187628075	4.086248786	-0.114891902	3	C
-0.000006173	4.796352893	0.000691707	3	C
-1.187614147	4.08620833	0.116198547	3	C
-1.147546267	2.693152467	0.144340175	3	C
-2.45507816	1.982564364	0.389374841	3	C
-1.414023869	0.012710097	1.442512707	2	N
-2.48390603	0.832637143	1.349519486	3	C
-3.599171482	0.698302117	2.169967683	3	C
-3.596972724	-0.28094367	3.158777869	3	C
-2.469772866	-1.082470324	3.299537509	3	C
-1.409191037	-0.910937267	2.418931335	3	C

END

Bibliography

- [1] M. Chergui, A. H. Zewail, *ChemPhysChem* **2009**, *10*, 28–43.
- [2] A. H. Zewail, *Science* **1988**, *242*, 1645–1653.
- [3] A. H. Zewail, *The Journal of Physical Chemistry A* **2000**, *104*, 5660–5694.
- [4] M. Dantus, P. Gross, *Encyclopedia of Applied Physics* **1998**, *22*, 431–456.
- [5] R. Berera, R. V. Grondelle, J. T. M. Kennis, *Photosynthesis Research* **2009**, *101*, 105–118.
- [6] <https://www.newport.com> (accessed 10.10.2016).
- [7] J Takeda, K Nakajima, S Kurita, *Physical Review B* **2000**, *62*, 83–87.
- [8] E Pomarico, M Silatani, F Messina, O Braem, A Cannizzo, E Barranoff, J. H. Klein, C Lambert, M Chergui, *The Journal of Physical Chemistry C* **2016**, *120*, 1645916469.
- [9] M. Khalil, N Demirdöven, A. Tokmakoff, *Journal of Physical Chemistry A* **2003**, *107*, 5258–5279.
- [10] S. Mukamel, *Annual Review of Physical Chemistry* **2000**, *51*, 691–729.
- [11] M. C. Hoffmann, J. A. Fülöp, *Journal of Physics D: Applied Physics* **2011**, *44*, 83001.
- [12] E. Goulielmakis, Z.-h. Loh, A. Wirth, R. Santra, N. Rohringer, V. S. Yakovlev, S. Zherebtsov, T. Pfeifer, A. M. Azzeer, M. F. Kling, S. R. Leone, F. Krausz, *Nature* **2010**, *466*, 739–744.
- [13] F. Krausz, M. Ivanov, *Reviews of Modern Physics* **2009**, *81*, 163.
- [14] A. H. Zewail, *Annu. Rev. Phys. Chem.* **2006**, *57*, 65–103.
- [15] K. J. Gaffney, H. N. Chapman, *Science* **2007**, *316*, 1444–1448.
- [16] C. Bressler, M. Chergui, *Chemical Reviews* **2004**, *104*, 1781–1812.
- [17] L. X. Chen, X. Zhang, J. V. Lockard, A. B. Stickrath, K. Attenkofer, G. Jennings, D.-J. Liu, *Acta Crystallographica Section A* **2010**, *66*, 240–251.
- [18] C. Bressler, M. Chergui, *Annual Review of Physical Chemistry* **2010**, *61*, 263–282.
- [19] L. X. Chen, W. J. Jäger, G Jennings, D. J. Gosztola, A Munkholm, J. P. Hessler, *Science* **2001**, *292*, 262–264.
- [20] L. X. Chen, G. B. Shaw, I. Novozhilova, T. Liu, G. Jennings, K. Attenkofer, G. J. Meyer, P. Coppens, *Journal of the American Chemical Society* **2003**, *125*, 7022–7034.
- [21] W. Gawelda, M. Johnson, F. M. F. D. Groot, R. Abela, C. Bressler, M. Chergui, *Journal of the American Chemical Society* **2006**, 5001–5009.

- [22] W. Gawelda, V.-T. Pham, M. Benfatto, Y. Zaushitsyn, M. Kaiser, D. Grolimund, S. Johnson, R. Abela, A. Hauser, C. Bressler, M. Chergui, *Physical Review Letters* **2007**, *98*, 057401.
- [23] M. Khalil, M. a. Marcus, A. L. Smeigh, J. K. McCusker, H. H. W. Chong, R. W. Schoenlein, *Journal of Physical Chemistry A* **2006**, *110*, 38–44.
- [24] W. Gawelda, V.-T. Pham, R. M. van der Veen, D. Grolimund, R. Abela, M. Chergui, C. Bressler, *The Journal of Chemical Physics* **2009**, *130*.
- [25] G. Vankó, A. Bordage, M. Pápai, K. Haldrup, P. Glatzel, A. M. March, G. Doumy, A. Britz, A. Galler, T. A. Assefa, D. Cabaret, T. B. V. Driel, K. S. Kjær, A. O. Dohn, K. B. Moller, H. T. Lemke, M. Rovezzi, Z. Németh, E. Rozsályi, T. Rozgonyi, J. Uhlig, V. Sundstrom, M. M. Nielsen, L. Young, S. H. Southworth, C. Bressler, W. Gawelda, *Journal of Physical Chemistry C* **2015**, *119*, 5888–5902.
- [26] G. Vankó, P. Glatzel, V.-T. Pham, R. Abela, D. Grolimund, C. N. Borca, S. L. Johnson, C. J. Milne, C. Bressler, *Angewandte Chemie - International Edition* **2010**, *49*, 5910–5912.
- [27] G. Vankó, A. Bordage, P. Glatzel, E. Gallo, M. Rovezzi, W. Gawelda, A. Galler, C. Bressler, G. Doumy, A. M. March, E. P. Kanter, L. Young, S. H. Southworth, S. E. Canton, J. Uhlig, G. Smolentsev, V. Sundström, K. Haldrup, T. B. van Driel, M. M. Nielsen, K. S. Kjaer, H. T. Lemke, *Journal of Electron Spectroscopy and Related Phenomena* **2013**, *188*, 166–171.
- [28] K. Haldrup, G. Vankó, W. Gawelda, A. Galler, G. Doumy, A. M. March, E. P. Kanter, A. Bordage, A. Dohn, T. B. van Driel, K. S. Kjær, H. T. Lemke, S. E. Canton, J. Uhlig, V. Sundström, L. Young, S. H. Southworth, M. M. Nielsen, C. Bressler, *The Journal of Physical Chemistry A* **2012**, *116*, 9878–9887.
- [29] C. Bressler, W. Gawelda, A. Galler, M. M. Nielsen, V. Sundström, G. Doumy, A. M. March, S. H. Southworth, L. Young, G. Vankó, *Faraday Discussions* **2014**, *171*.
- [30] M. Saes, F. van Mourik, W. Gawelda, M. Kaiser, M. Chergui, C. Bressler, D. Grolimund, R. Abela, T. E. Glover, P. a. Heimann, R. W. Schoenlein, S. L. Johnson, A. M. Lindenberg, R. W. Falcone, *Review of Scientific Instruments* **2004**, *75*, 24–30.
- [31] F. A. Lima, C. J. Milne, D. C. V. Amarasinghe, M. H. Rittmann-Frank, R. M. van der Veen, M. Reinhard, V.-T. Pham, S. Karlsson, S. L. Johnson, D. Grolimund, C. Borca, T. Huthwelker, M. Janousch, F. van Mourik, R. Abela, M. Chergui, *The Review of Scientific Instruments* **2011**, *82*, 063111.
- [32] A. M. March, A. Stickrath, G. Doumy, E. P. Kanter, B. Krässig, S. H. Southworth, K. Attenkofer, C. A. Kurtz, L. X. Chen, L. Young, *The Review of Scientific Instruments* **2011**, *82*, 73110.
- [33] A. Britz, T. A. Assefa, A. Galler, W. Gawelda, M. Diez, P. Zalden, D. Khakhulin, B. Fernandes, P. Gessler, H. S. Namina, A. Beckmann, M. Harder, H. Yava, C. Bressler, *Journal of Synchrotron Radiation* **2016**, *23*.
- [34] C. Bressler, C. J. Milne, V.-T. Pham, A. ElNahas, R. M. van der Veen, W. Gawelda, S. L. Johnson, P. Beaud, D. Grolimund, M. Kaiser, C. N. Borca, G. Ingold, R. Abela, M. Chergui, *Science* **2009**, *323*, 489–492.

-
- [35] C. J. Milne, V.-T. Pham, W. Gawelda, R. M. V. D. Veen, A. E. Nahhas, S. L. Johnson, P. Beaud, G. Ingold, F. Lima, D. a. Vithanage, M. Benfatto, D. Grolimund, C. Borca, M. Kaiser, A. Hauser, R. Abela, C. Bressler, M. Chergui, *Journal of Physics: Conference Series* **2009**, *190*, 12052.
- [36] F. G. Santomauro, A Lübcke, J Rittmann, E Baldini, A Ferrer, M Silatani, P. Zimmermann, S. Grübel, J. A. Johnson, S. Mariager, P. Beaud, D. Grolimund, C. Borca, G. Ingold, S. L. Johnson, M. Chergui, *Scientific Reports* **2015**, *5*, 14834 —.
- [37] H. T. Lemke, C. Bressler, L. X. Chen, D. M. Fritz, K. J. Gaffney, A. Galler, W. Gawelda, K. Haldrup, R. W. Hartsock, H. Ihee, J. Kim, K. H. Kim, J. H. Lee, M. M. Nielsen, A. B. Stickrath, W. Zhang, D. Zhu, M. Cammarata, *The Journal of Physical Chemistry A* **2013**, *117*, 735–740.
- [38] T. Katayama, Y. Inubushi, Y. Obara, T. Sato, T. Togashi, K. Tono, T. Hatsui, T. Kameshima, A. Bhattacharya, Y. Ogi, N. Kurahashi, K. Misawa, T. Suzuki, M. Yabashi, *Applied Physics Letters* **2013**, *103*, 131105.
- [39] W. Zhang, R. Alonso-Mori, U. Bergmann, C. Bressler, M. Chollet, A. Galler, W. Gawelda, R. G. Hadt, R. W. Hartsock, T. Kroll, K. S. Kjær, K. Kubiček, H. T. Lemke, H. W. Liang, D. a. Meyer, M. M. Nielsen, C. Purser, J. S. Robinson, E. I. Solomon, Z. Sun, D. Sokaras, T. B. van Driel, G. Vankó, T.-C. Weng, D. Zhu, K. J. Gaffney, *Nature* **2014**, *509*, 345–348.
- [40] S. E. Canton, K. S. Kjaer, G. Vanko, T. B. van Driel, S.-i. Adachi, A. Bordage, C. Bressler, P. Chabera, M. Christensen, A. O. Dohn, A. Galler, W. Gawelda, D. Gosztola, K. Haldrup, T. Harlang, Y. Liu, K. B. Moller, Z. Nemeth, S. Nozawa, M. Papai, T. Sato, T. Sato, K. Suarez-Alcantara, T. Togashi, K. Tono, J. Uhlig, D. A. Vithanage, K. Warnmark, M. Yabashi, J. Zhang, V. Sundstrom, M. M. Nielsen, *Nature Communications* **2015**, *6*, 359.
- [41] K. Haldrup, W. Gawelda, R. Abela, R. Alonso-Mori, U. Bergmann, A. Bordage, M. Cammarata, S. E. Canton, A. O. Dohn, T. B. van Driel, D. M. Fritz, A. Galler, P. Glatzel, T. Harlang, K. S. Kjær, H. T. Lemke, K. B. Møller, Z. Németh, M. Pápai, N. Sas, J. Uhlig, D. Zhu, G. Vankó, V. Sundström, M. M. Nielsen, C. Bressler, *The Journal of Physical Chemistry B* **2016**, *120*, 1158–1168.
- [42] E. Biasin, T. B. V. Driel, K. S. Kjær, A. O. Dohn, M. Christensen, T. Harlang, P. Chabera, Y. Liu, J. Uhlig, M. Pápai, Z. Németh, R. Hartsock, W. Liang, J. Zhang, R. Alonso-mori, M. Chollet, J. M. Glowonia, S. Nelson, D. Sokaras, T. A. Assefa, A. Britz, A. Galler, W. Gawelda, C. Bressler, K. J. Gaffney, H. T. Lemke, K. B. Møller, M. M. Nielsen, V. Sundström, G. Vankó, K. Wärmmark, S. Canton, K. Haldrup, *Physical Review Letters* **2016**, *117*, 013002.
- [43] P Emma, R Akre, J Arthur, R Bionta, C Bostedt, J Bozek, A. Brachmann, P Bucksbaum, R Coffee, F.-J. Decker, Y Ding, D Dowell, S Edstrom, A. Fisher, J Frisch, S Gilevich, J Hastings, G Hays, P. Hering, Z Huang, R Iverson, H Loos, M Messerschmidt, A. Miahnahri, S Moeller, H.-D. Nuhn, G Pile, D Ratner, J Rzepiela, D Schultz, T Smith, P Stefan, H Tompkins, J Turner, J Welch, W White, J Wu, G Yocky, J Galayda, *Nature Photonics* **2010**, *4*, 641–647.

- [44] H. Tanaka, M. Yabashi, T. Ishikawa, H. Aoyagi, T. Asaka, Y. Asano, N. Azumi, T. Bizen, H. Ego, K. Fukami, T. Fukui, Y. Furukawa, S. Goto, H. Hanaki, T. Hara, T. Hasegawa, T. Hatsui, A. Higashiya, T. Hirono, N. Hosoda, M. Ishii, T. Inagaki, Y. Inubushi, T. Itoga, Y. Joti, M. Kago, T. Kameshima, H. Kimura, Y. Kirihara, A. Kiyomichi, T. Kobayashi, C. Kondo, T. Kudo, H. Maesaka, X. M. Marechal, T. Masuda, S. Matsubara, T. Matsumoto, T. Matsushita, S. Matsui, M. Nagasono, N. Nariyama, H. Ohashi, T. Ohata, T. Ohshima, S. Ono, Y. Otake, C. Saji, T. Sakurai, T. Sato, K. Sawada, T. Seike, K. Shirasawa, T. Sugimoto, S. Suzuki, S. Takahashi, H. Takebe, K. Takeshita, K. Tamasaku, H. Tanaka, R. Tanaka, T. Tanaka, T. Togashi, K. Togawa, A. Tokuhisa, H. Tomizawa, K. Tono, S. Wu, M. Yabashi, M. Yamaga, A. Yamashita, K. Yanagida, C. Zhang, T. Shintake, H. Kitamura, N. Kumagai, *Nature Photonics* **2012**, *6*, 540–544.
- [45] M. Altarelli, *High Power Laser Science and Engineering* **2015**, *3*.
- [46] H. Dau, M. Haumann, *Coordination Chemistry Reviews* **2008**, *252*, 273–295.
- [47] M Grätzel, *Inorganic Chemistry* **2005**, *44*, 6841–6851.
- [48] J. I. Goldsmith, W. R. Hudson, M. S. Lowry, T. H. Anderson, S. Bernhard, *Journal of the American Chemical Society* **2005**, *127*, 7502–7510.
- [49] F. Gärtner, B. Sundararaju, A. E. Surkus, A. Boddien, B. Loges, H. Junge, P. H. Dixneuf, M. Beller, *Angewandte Chemie - International Edition* **2009**, *48*, 9962–9965.
- [50] G. Smolentsev, V. Sundström, *Coordination Chemistry Reviews* **2015**, *304-305*, 117–132.
- [51] S. Canton, X. Zhang, J. Zhang, T. B. van Driel, K. S. Kjaer, K. Haldrup, P. Chabera, T. Harlang, K. Suarez-Alcantara, Y. Liu, J. Pérez, A. Bordage, M. Papai, G. Vankó, G. Jennings, C. A. Kurtz, M. Rovezzi, P. Glatzel, G. Smolentsev, J. Uhlig, A. O. Dohn, M. Christensen, A. Galler, W. Gawelda, C. Bressler, H. T. Lemke, K. B. Moller, M. M. Nielsen, R. Lomoth, K. Wärnmark, V. Sundström, *Physical Chemistry Letters* **2013**, *4*, 1972–1976.
- [52] L. L. Jamula, A. M. Brown, D. Guo, J. K. McCusker, *Inorganic Chemistry* **2014**, *53*.
- [53] J. Torres-Alacan, U. Das, A. C. Filippou, P. Vöhringer, *Angewandte Chemie - International Edition* **2013**, *52*, 12833–12837.
- [54] B Meunier, S. P. de Visser, S Shaik, *Chemical Reviews* **2004**, *104*, 3947–3980.
- [55] M. Gerloch, E. Constable, *Transition Metal Chemistry*, **1994**.
- [56] IUPAC, *Compendium of Chemical Terminology Gold Book*, **2012**.
- [57] G. A. Lawrance, *Introduction to Coordination Chemistry*, **2010**.
- [58] <https://iupac.org/> (accessed 23.10.2016).
- [59] M. F. Perutz, M. G. Rossmann, A. F. Cullis, H Muirhead, G Will, A. C. T. North, *Nature* **1960**, *185*, 416–422.
- [60] J. C. Kendrew, R. E. Dickerson, B. E. Strandberg, H. R. G. D. R. Davies, D. C. Phillips, V. C. Shore, *Nature* **1960**, *185*, 422–427.

- [61] P. S. Wagenknecht, P. C. Ford, *Coordination Chemistry Reviews* **2011**, *255*, 591–616.
- [62] P. Gütllich, H. A. Goodwin, *Spin Crossover in Transition Metal Compounds I*, **2004**.
- [63] H. Yersin, W. J. Finkenzeller, *Highly Efficient OLEDs with Phosphorescent Materials*, **2007**.
- [64] V. E. Balzani, S. E. Campagna, *Photochemistry and photophysics of coordination compounds: Rhenium, Vol. 281*, **2007**, pp. 45–100.
- [65] W. Gawelda, PhD thesis, EPFL Lausanne, **2006**.
- [66] B. Valeur, *Molecular Fluorescence: Principles and Applications*, **2001**.
- [67] M. Reinhard, PhD thesis, EPFL Lausanne, **2013**.
- [68] C. Sousa, C. de Graaf, A. Rudavskiy, R. Broer, J. Tatchen, M. Etinski, C. M. Marian, *Chemistry - A European Journal* **2013**, *19*, 17541–17551.
- [69] C. Bressler, M. Saes, M. Chergui, R. Abela, P. Pattison, *Nuclear Instruments and Methods in Physics Research Section A: Accelerators Spectrometers Detectors and Associated Equipment* **2001**, *467-468*, 1444–1446.
- [70] C. Bressler, M. Saes, M. Chergui, D. Grolimund, R. Abela, P. Pattison, *The Journal of Chemical Physics* **2002**, *116*, 2955–2966.
- [71] Y. Liu, T. Harlang, S. E. Canton, P. Chábera, K. Suárez-Alcántara, A. Fleckhaus, D. a. Vithanage, E. Göransson, A. Corani, R. Lomoth, V. Sundström, K. Wärnmark, *Chem. Commun.* **2013**, *49*, 6412–6414.
- [72] W. Zhang, K. S. Kjær, R. Alonso-Mori, U. Bergmanna, M. Chollet, L. A. Fredin, R. G. Hadt, R. W. Hartsock, T. Harlang, T. Kroll, K. Kubiček, H. T. Lemke, H. W. Liang, Y. Liu, M. M. Nielsen, P. Persson, J. S. Robinson, E. I. Solomon, Z. Sun, D. Sokaras, T. B. van Driel, T.-C. Weng, D. Zhu, K. Wärnmark, V. Sundström, K. J. Gaffney, *Chemical Science (in press)* **2016**.
- [73] J. H. Dawson, M. Sono, *Chemical Reviews* **1987**, *87*, 1255–1276.
- [74] J. H. Hubbell, H. A. Gimm, I Overbo, *Journal of Physical and Chemical Reference Data* **1980**, *9*, 1023–1148.
- [75] D. Meschede, *Gerthsen Physik*, **2003**.
- [76] A. Thompson, D. Attwood, E. Gulliksen, M. Howells, K.-J. Kim, J. Kirz, J. Kortright, I. Lindau, Y. Liu, P. Pianetta, A. Robinson, J. Scofield, J. Underwood, G. Williams, H. Winick, *X-ray data booklet*, **2009**.
- [77] <http://physics.nist.gov/PhysRefData/Xcom/html/xcom1.html> (accessed 10.10.2016).
- [78] J. Als-Nielsen, D. McMorrow, *Elements of Modern X-ray Physics*, 2nd ed., **2011**.
- [79] T. E. Westre, P. Kennepohl, J. G. Dewitt, B. Hedman, K. O. Hodgson, E. I. Solomon, *Journal of the American Chemical Society* **1997**, *119*, 6297–6314.
- [80] J Wong, F. W. Lytle, R. P. Messmer, D. H. Maylotte, *Physical Review B* **1984**, *30*, 5596–5610.

- [81] E. Cottrell, K. A. Kelley, A. Lanzirrotti, R. A. Fischer, *Chemical Geology* **2009**, *268*, 167–179.
- [82] S Bajt, S. R. Sutton, J. S. Delaney, *Geochimica et Cosmochimica Acta* **1994**, *58*, 5209–5214.
- [83] J. F. Berry, E. Bill, E. Bothe, S. D. George, B. Mienert, F. Neese, K. Wieghardt, *Science* **2006**, *312*, 1937–1941.
- [84] M. Wilke, F. Farges, P.-E. Petit, G. E. Brown Jr, F. Martin, *American Mineralogist* **2001**, *86*, 714–730.
- [85] W. Gawelda, C. Bressler, M. Saes, M. Kaiser, A. Tarnovsky, D. Grochimund, S. L. Johnson, R. Abela, M. Chergui, *Physica Scripta* **2005**, *T115*, 102–106.
- [86] A El Nahhas, R. M. van der Veen, T. J. Penfold, V. T. Pham, F. a. Lima, R Abela, a. M. Blanco-Rodriguez, S Záliš, A Vlček, I Tavernelli, U Rothlisberger, C. J. Milne, M Chergui, *The Journal of Physical Chemistry A* **2013**, *117*, 361–369.
- [87] X. Zhang, S. E. Canton, G. Smolentsev, C.-j. Wallentin, Y. Liu, Q. Kong, K. Attenkofer, A. B. Stickrath, M. W. Mara, L. X. Chen, K. Wärnmark, V. Sundström, *Journal of the American Chemical Society* **2014**, *136*, 8804–8809.
- [88] X. Zhang, M. Pápai, K. B. Møller, J. Zhang, S. E. Canton, *Molecules* **2016**, *21*.
- [89] D. Goeries, PhD thesis, Uni Hamburg, **2014**.
- [90] J. Yano, V. K. Yachandra, *Photosynthesis Research* **2009**, *102*, 241–254.
- [91] G. R. Shulman, Y Yafet, P Eisenberger, W. E. Blumberg, *Proceedings of the National Academy of Sciences* **1976**, *73*, 1384–1388.
- [92] A. Bianconi, M. Dell’Ariccia, P. J. Durham, J. B. Pendry, *Physical Review B* **1982**, *26*, 6502–6508.
- [93] M Reinhard, T. J. Penfold, F. A. Lima, J Rittmann, M. H. Rittmann-Frank, R. Abela, I. Tavernelli, U. Rothlisberger, C. J. Milne, M. Chergui, *Structural Dynamics* **2014**, *1*, 024901.
- [94] A Bianconi, E Fritsch, G Calas, J Petiau, *Physical Review B* **1985**, *32*, 4292–4295.
- [95] J. L. DuBois, P. Mukherjee, T. D. P. Stack, B. Hedman, E. I. Solomon, K. O. Hodgson, *Journal of the American Chemical Society* **2000**, *122*, 5775–5787.
- [96] N. Kosugi, T. Yokoyama, K. Asakura, H. Kuroda, *Chemical Physics* **1984**, *91*, 249–256.
- [97] M. Calandra, J. Rueff, C. Gougoussis, M. Gorgoi, S. Benedetti, P. Torelli, A. Shukla, D. Chandresris, C. Brouder, *Physical Review B* **2012**, *86*, 165102.
- [98] J. L. Dehmer, D. Dill, *Physical Chemistry Letters* **1975**, *35*, 213–215.
- [99] D. Kleppner, J. C. Lewis Cocke, A. Dalgarno, R. W. Field, T. W. Hänsch, N. F. LANE, J. Macek, F. M. Pipikin, I. A. Sellin, *Physics through the 1990s: Atomic, Molecular, and Optical Physics*, **1987**.
- [100] P. A. Lee, J. B. Pendry, *Physical Review B* **1975**, *11*, 2795–2811.
- [101] C. J. Milne, T. J. Penfold, M. Chergui, *Coordination Chemistry Reviews* **2014**, *277-278*, 44–68.

- [102] S. D. George, T. Petrenko, F. Neese, *Journal of Physical Chemistry A* **2008**, *112*, 12936–12943.
- [103] J. F. Berry, S. D. George, F. Neese, *Physical Chemistry Chemical Physics* **2008**, *10*, 4361–4374.
- [104] F. Neese, *WIREs Comput Mol Sci* **2012**, *2*, 73–78.
- [105] J. J. Rehr, R. C. Albers, *Reviews of Modern Physics* **2000**, *72*, 621–654.
- [106] J. D. Bourke, C. T. Chantler, Y. Joly, *Journal of Synchrotron Radiation* **2016**, *23*, 551–559.
- [107] S. A. Guda, A. A. Guda, M. A. Soldatov, K. A. Lomachenko, A. L. Bugaev, C. Lamberti, W. Gawelda, C. Bressler, G. Smolentsev, A. V. Soldatov, Y. Joly, Guda2015_{_}FDMNES.pdf, **2015**.
- [108] P.-A. Malmqvist, A. Rendell, B. Roos, *Journal of Physical Chemistry* **1990**, *a*, 5411–5482.
- [109] P. A. Malmqvist, B. O. Roos, B. Schimmelpfennig, *Chemical Physics Letters* **2002**, *357*, 230–240.
- [110] E. Stavitski, F. M. F. de Groot, *Micron* **2010**, *41*, 687–694.
- [111] R. Stumm von Bordwehr, *Ann. Phys. Fr.* **1989**, *14*, 377–465.
- [112] D. E. Sayers, E. A. Stern, F. Lytle, *Physical Chemistry Letters* **1971**, *27*, 1204.
- [113] E. A. Stern, *Physical Review B* **1974**, *10*, 3027–3037.
- [114] A. L. Ankudinov, J. J. Rehr, S. D. Conradson, *Physical Review B* **1998**, *58*, 7565–7576.
- [115] G. Bunker, Errors in fluorescence EXAFS, tech. rep., **1988**.
- [116] J. Jaklevic, J. A. Kirby, M. P. Klein, A. S. Robertson, *Solid State Communications* **1977**, *23*, 679–682.
- [117] FMB Oxford Datasheet - Ver. 1 - Aug 2009, tech. rep., **2009**.
- [118] G. Vankó, T. Neisius, G. Molnar, F. Renz, S. Karpati, A. Shukla, F. M. F. de Groot, *The Journal of Physical Chemistry B* **2006**, *110*, 11647–11653.
- [119] P. Glatzel, U. Bergmann, *Coordination Chemistry Reviews* **2005**, *249*, 65–95.
- [120] U. Bergmann, P. Glatzel, *Photosynthesis Research* **2009**, *102*, 255–266.
- [121] E. Gallo, P. Glatzel, *Advanced Materials* **2014**.
- [122] G. Smolentsev, A. V. Soldatov, J. Messinger, K. Merz, T. Weyhermu, U. Bergmann, Y. Pushkar, J. Yano, V. K. Yachandra, P. Glatzel, *Journal of the American Chemical Society* **2009**, *131*, 13161–13167.
- [123] V. A. Safonov, L. N. Vykhodtseva, Y. M. Polukarov, O. V. Safonova, G. Smolentsev, M. Sikora, S. G. Eeckhout, P. Glatzel, *The Journal of Physical Chemistry B* **2006**, *110*, 23192–23196.
- [124] M. Bauer, *Phys. Chem. Chem. Phys.* **2014**, *16*, 13827–13837.

- [125] J. Kern, R. Alonso-Mori, R. Tran, J. Hattne, R. J. Gildea, N. Echols, C. Glöckner, J. Hellmich, H. Laksmono, R. G. Sierra, B. Lassalle-Kaiser, S. Koroidov, A. Lampe, G. Han, S. Gul, D. Difiore, D. Milathianaki, A. R. Fry, A. Miahnahri, D. W. Schafer, M. Messerschmidt, M. M. Seibert, J. E. Koglin, D. Sokaras, T.-C. Weng, J. Sellberg, M. J. Latimer, R. W. Grosse-Kunstleve, P. H. Zwart, W. E. White, P. Glatzel, P. D. Adams, M. J. Bogan, G. J. Williams, S. Boutet, J. Messinger, A. Zouni, N. K. Sauter, V. K. Yachandra, U. Bergmann, J. Yano, *Science* **2013**, *340*, 491–495.
- [126] A. M. March, T. A. Assefa, C. Bressler, G. Doumy, A. Galler, W. Gawelda, E. P. Kanter, Z. Németh, M. Pápai, S. H. Southworth, L. Young, G. Vankó, *Journal of Physical Chemistry C* **2015**, *119*, 14571–14578.
- [127] L. v. Hámos, *Die Naturwissenschaften* **1932**, *38*, 705–706.
- [128] H. H. Johann, *Zeitschrift für Physik* **1931**, *69*, 185–206.
- [129] T. Johansson, *Zeitschrift für Physik* **1933**, *82*, 507–528.
- [130] J Szlachetko, M Nachtegaal, E de Boni, M Willimann, O Safonova, J Sa, G Smolentsev, M Szlachetko, J. a. van Bokhoven, J.-C. Dousse, J Hozzowska, Y Kayser, P Jagodzinski, A Bergamaschi, B Schmitt, C David, A Lücke, *The Review of Scientific Instruments* **2012**, *83*, 103105.
- [131] R. Alonso-Mori, J. Kern, D. Sokaras, T. C. Weng, D. Nordlund, R. Tran, P. Montanez, J. Delor, V. K. Yachandra, J. Yano, U. Bergmann, *Review of Scientific Instruments* **2012**, *83*, 073114.
- [132] <https://www.psi.ch/sls/superxas/johann-xes-spectrometer> (accessed 10.10.2016).
- [133] P. Glatzel, M. Sikora, G. Smolentsev, M. Fernández-García, *Catalysis Today* **2009**, *145*, 294–299.
- [134] W. Schülke, *Electron Dynamics by Inelastic X-ray Scattering*, **2007**.
- [135] K Hämäläinen, D Siddons, J Hastings, L Berman, *Physical Chemistry Letters* **1991**, *67*, 2850–2853.
- [136] J. Szlachetko, J. Sá, M. Nachtegaal, U. Hartfelder, J.-C. Dousse, J. Hozzowska, D. L. A. Fernandes, H. Shi, C. Stampfls, *The Journal of Physical Chemistry Letters* **2013**, *5*, 80–84.
- [137] F. de Groot, *Chemical Reviews* **2001**, *101*, 1779–1808.
- [138] F de Groot, M Krisch, J Vogel, *Physical Review B* **2002**, *66*, 195112.
- [139] M. O. Krause, J. H. Oliver, *J. Phys. Chem. Ref. Data* **1979**, *8*, 329–338.
- [140] D. H. Bilderback, P. Elleaume, E. Weckert, *Journal of Physics B: Atomic Molecular and Optical Physics* **2005**, *38*, S773–S797.
- [141] M Altarelli, *Nuclear Instruments and Methods in Physics Research Section B: Beam Interactions with Materials and Atoms* **2011**, *269*, 2845–2849.
- [142] B. W. J. McNeil, N. R. Thompson, *Nature Photonics* **2010**, *4*, 814–821.
- [143] G Margaritondo, P. R. Ribic, *Journal of Synchrotron Radiation* **2011**, *18*, 101–108.
- [144] J Feikes, M von Hartrott, G Wüstefeld, A Hoehl, R Klein, R Müller, G Ulm, *Proceedings of PAC09 Vancouver BC Canada* **2009**, 1093–1095.

-
- [145] S. Ibrahimkuty, D. Issenmann, S. Schleef, A. S. Müller, Y. L. Mathis, B. Gasharova, E. Huttel, R. Steininger, J. Göttlicher, T. Baumbach, A. Bartels, C. Janke, A. Plech, *Journal of Synchrotron Radiation* **2011**, *18*, 539–545.
- [146] A Lindenberg, I Kang, S Johnson, T Missalla, P Heimann, Z Chang, J Larsson, P Bucksbaum, H Kapteyn, H Padmore, R Lee, J Wark, R Falcone, *Physical Review Letters* **1999**, *84*, 111–114.
- [147] C Stamm, T Kachel, N Pontius, R Mitzner, T Quast, K Holldack, S Khan, C Lupulescu, E. F. Aziz, M Wietstruk, H. A. Dürr, W Eberhardt, *Nature Materials* **2007**, *6*, 740–743.
- [148] M. Wulff, F. Schotte, G. Naylor, Dominique Burgeois, K. Moffat, G. Mourouc, *Nuclear Instruments and Methods in Physics Research Section A* **1997**, *398*, 69–84.
- [149] T Graber, S Anderson, H Brewer, Y. S. Chen, H. S. Cho, N Dashdorj, R. W. Henning, I Kosheleva, G MacHa, M Meron, R Pahl, Z Ren, S Ruan, F Schotte, V Srajer, P. J. Viccaro, F Westferro, P Anfinrud, K Moffat, *Journal of Synchrotron Radiation* **2011**, *18*, 658–670.
- [150] www.lightsources.org (accessed 10.10.2016).
- [151] <http://photon-science.desy.de/> (accessed 14.10.2016).
- [152] www.aps.anl.gov (accessed 14.10.2016).
- [153] <http://www.esrf.eu> (accessed 14.10.2016).
- [154] <http://www.synchrotron-soleil.fr/portal/page/portal/SourceAccelateur> (accessed 14.10.2016).
- [155] <http://als.lbl.gov/machine-information/> (accessed 14.10.2016).
- [156] M. Saes, W. Gawelda, M. Kaiser, A. Tarnovsky, C. Bressler, M. Chergui, S. L. Johnson, D. Grolimund, R. Abela, *Synchrotron Radiation News* **2003**, *16*, 12–20.
- [157] M. Yabashi, H. Tanaka, T. Ishikawa, *Journal of Synchrotron Radiation* **2015**, *22*, 477–484.
- [158] M Altarelli, R. Brinkmann, M. Chergui, W. Decking, B. Dobson, S. Düsterer, G. Grübel, W. Graeff, H. Graafsma, J. P. Janos Hajdu, Jonathan Marangos, H. Redlin, D. Riley, I. Robinson, J. Rossbach, A. Schwarz, K. Tiedtke, T. Tschentscher, I. Vartaniants, H. Wabnitz, H. Weise, R. Wichmann, A. W. Karl Witte, M. Wulff, M. Yurkov, *The European X-ray Free-Electron Laser*, **2006**.
- [159] W. E. White, A. Robert, M. Dunne, *Journal of synchrotron radiation* **2015**, *22*, 472–476.
- [160] K Tono, T Togashi, Y Inubushi, T Sato, T Katayama, K Ogawa, H Ohashi, H Kimura, S Takahashi, K Takeshita, H Tomizawa, S Goto, T Ishikawa, M Yabashi, *New Journal of Physics* **2013**, *15*.
- [161] B. D. Patterson, R Abela, H.-H. Braun, U Flechsig, R Ganter, Y Kim, E Kirk, A Oppelt, M Pedrozzi, S Reiche, L Rivkin, T. Schmidt, B Schmitt, V. N. Strocov, S Tsujino, A. F. Wrulich, *New Journal of Physics* **2010**, *12*, 035012.
- [162] J Han, H Kang, I. S. Ko, S.-b. Pc, *Proceedings of IPAC2012* **2012**, 1735–1737.

- [163] M Altarelli, *Crystallography Reports* **2010**, *55*, 1145–1151.
- [164] P. Schmäser, M. Dohlus, J. Rossbach, *Ultraviolet and Soft X-Ray Free-Electron Lasers*, **2008**.
- [165] J. Ullrich, A. Rudenko, R. Moshhammer, *Annual Review of Physical Chemistry* **2012**, *63*, 635–660.
- [166] T Ejdrup, H. T. Lemke, K Haldrup, T. N. Nielsen, D. A. Arms, D. A. Walko, A Miceli, E. C. Landahl, E. M. Dufresne, M. M. Nielsen, *Journal of Synchrotron Radiation* **2009**, *16*, 387–390.
- [167] Y. Obara, T. Katayama, Y. Ogi, T. Suzuki, S. Karashima, Y. Chiba, Y. Isokawa, T. Togashi, Y. Inubushi, M. Yabashi, T. Suzuki, K. Misawa, *Optics Express* **2014**, *22*, 61–63.
- [168] G. Cerullo, S. De Silvestri, *Review of Scientific Instruments* **2003**, *74*, 1–18.
- [169] T. Kameshima, S. Ono, T. Kudo, K. Ozaki, Y. Kirihara, K. Kobayashi, Y. Inubushi, M. Yabashi, T. Horigome, A. Holland, K. Holland, D. Burt, H. Murao, T. Hatsui, *Review of Scientific Instruments* **2014**, *85*, 033110.
- [170] J Larsson, P. A. Heimann, A. M. Lindenberg, P. J. Schuck, P. H. Bucksbaum, R. W. Lee, H. A. Padmore, J. S. Wark, R. W. Falcone, *Applied Physics A* **1998**, *66*, 587–591.
- [171] P. A. Heimann, A. M. Lindenberg, I. Kang, S. Johnson, T. Missalla, Z. Chang, R. W. Falcone, R. W. Schoenlein, T. E. Glover, H. A. Padmore, *Nuclear Instruments and Methods in Physics Research Section A: Accelerators Spectrometers Detectors and Associated Equipment* **2001**, *467-468*, 986–989.
- [172] F. Schotte, M. Lim, T. a. Jackson, A. V. Smirnov, J. Soman, J. S. Olson, G. N. Phillips, M. Wulff, P. a. Anfinrud, *Science* **2003**, *300*, 1944–1947.
- [173] R. Neutze, R. Wouts, S. Techert, J. Davidsson, M. Kocsis, A. Kirrander, F. Schotte, M. Wulff, *Physical Review Letters* **2001**, *87*, 195508.
- [174] E. A. Stern, D. L. Brewster, K. M. Beck, S. M. Heald, Y Feng, *Physica Scripta T* **2005**, *T115*, 1044–1046.
- [175] L Stebel, M Malvestuto, V Capogrosso, P Sigalotti, B Ressel, F Bondino, E Maggano, G Cautero, F Parmigiani, *The Review of Scientific Instruments* **2011**, *82*, 123109.
- [176] H Navirian, R Shayduk, W Leitenberger, J Goldshteyn, P Gaal, M Bargheer, *The Review of Scientific Instruments* **2012**, *83*, 63303.
- [177] D Issenmann, S Ibrahimkutty, R Steininger, J Göttlicher, T Baumbach, N Hiller, A-S Müller, A Plech, *Journal of Physics: Conference Series* **2013**, *425*, 92007.
- [178] U. Bergmann, A. Di Cicco, P. Wernet, E. Principi, P. Glatzel, A. Nilsson, *Journal of Chemical Physics* **2007**, *127*, 174504.
- [179] T. T. Fister, K. P. Nagle, F. D. Vila, G. T. Seidler, C. Hamner, J. O. Cross, J. J. Rehr, *Physical Review B* **2009**, *79*, 174117.
- [180] U Bergmann, P Glatzel, S Cramer, *Microchemical Journal* **2002**, *71*, 221–230.
- [181] M. Krisch, F. Sette, *Surface Review and Letters* **2002**, *9*, 969–976.

- [182] C. Sternemann, H. Sternemann, S. Huotari, F. Lehmkuhler, M. Tolan, J. S. Tse, *Journal of Analytical Atomic Spectrometry* **2008**, *23*, 807–813.
- [183] C. J. Sahle, A. Mirone, J. Niskanen, J. Inkinen, M. Krisch, S. Huotari, *Journal of Synchrotron Radiation* **2015**, *22*, 400–409.
- [184] D. Goeries, B. Dicke, P. Roedig, N. Stübe, J. Meyer, A. Galler, W. Gawelda, A. Britz, P. Geßler, H. Sotoudi Namin, A. Beckmann, M. Schlie, M. Warmer, M. Naumova, C. Bressler, M. Rübhausen, E. Weckert, A. Meents, *Review of Scientific Instruments* **2016**, *87*, 053116.
- [185] H.-C. Wille, H. Franz, R. Röhlberger, W. a. Caliebe, F.-U. Dill, *Journal of Physics: Conference Series* **2010**, *217*.
- [186] R. Röhlberger, H.-C. Wille, K. Schlage, B. Sahoo, *Nature* **2012**, *482*, 199–203.
- [187] D. Ketenoglu, M. Harder, K. Klementiev, M. Upton, M. Taherkhani, M. Spiwek, F.-U. Dill, H.-C. Wille, H. Yava, *Journal of Synchrotron Radiation* **2015**, *22*, 961–967.
- [188] Y. Zaouter, J. Boulet, E. Mottay, E. Cormier, *Optics Letters* **2008**, *33*, 1527.
- [189] A. Q. R. Baron, S. Kishimoto, J. Morse, J. M. Rigal, *Journal of Synchrotron Radiation* **2006**, *13*, 131–142.
- [190] H.-C. Schröder, A. Affeldt, H.-P. Gausepohl, G. Kube, G. Priebe in Proceedings of DIPAC2011, Hamburg, Germany, **2011**, pp. 113–115.
- [191] T. Reusch, M. Osterhoff, J. Agricola, T. Salditt, *Journal of Synchrotron Radiation* **2014**, *21*, 708–715.
- [192] C. Milne, V. Pham, W. Gawelda, A. E. Nahhas, R. M. V. D. Veen, S. L. Johnson, P. Beaud, G. Ingold, C. Borca, D. Grolimund, R. Abela, M. Chergui, C. Bressler, *Acta Physica Polonica A* **2010**, *117*, 391–393.
- [193] W. Gawelda, A. Cannizzo, V.-T. Pham, F. van Mourik, C. Bressler, M. Chergui, *Journal of the American Chemical Society* **2007**, *129*, 8199–8206.
- [194] A. Cannizzo, C. J. Milne, C. Consani, C. Bressler, F. Van Mourik, M. Chergui, *Coordination Chemistry Reviews* **2010**, *254*, 2677–2686.
- [195] M. A. Scandola, F. Scandola, *Journal of the American Chemical Society* **1971**, *94*, 1805–1810.
- [196] M. Nishazawa, P. C. Ford, *Inorganic Chemistry* **1981**, *128*, 294–295.
- [197] S. J. Milder, H. B. Gray, V. M. Miskowski, *Journal of the American Chemical Society* **1984**, *106*, 3764–3767.
- [198] S. Fischer, O. S. Bokareva, E. Barsch, S. I. Bokarev, O. Kühn, R. Ludwig, *ChemCatChem* **2016**, *8*, 404–411.
- [199] F. Gärtner, A. Boddien, E. Barsch, K. Fumino, S. Losse, H. Junge, D. Hollmann, A. Brückner, R. Ludwig, M. Beller, *Chemistry - A European Journal* **2011**, *17*, 6425–6436.
- [200] F. Gärtner, S. Denurra, S. Losse, A. Neubauer, A. Boddien, A. Gopinathan, A. Spannenberg, H. Junge, S. Lochbrunner, M. Blug, S. Hoch, J. Busse, S. Gladiali, M. Beller, *Chemistry - A European Journal* **2012**, *18*, 3220–3225.

- [201] A. Neubauer, G. Grell, A. Friedrich, S. I. Bokarev, P. Schwarzbach, F. Gärtner, A.-E. Surkus, H. Junge, M. Beller, O. Kühn, S. Lochbrunner, *Journal of Physical Chemistry Letters* **2014**, *5*, 1355–1360.
- [202] S. I. Bokarev, O. S. Bokareva, O. Kühn, *Coordination Chemistry Reviews* **2015**, *304-305*, 133–145.
- [203] <http://www.chemaxon.com> (accessed 24.10.2016).
- [204] E. F. Pettersen, T. D. Goddard, C. C. Huang, G. S. Couch, D. M. Greenblatt, E. C. Meng, T. E. Ferrin, *Journal of Computational Chemistry* **2004**, *25*, 1605–1612.
- [205] S. I. Bokarev, O. S. Bokareva, O. Kühn, *The Journal of Chemical Physics* **2012**, *136*, 214305.
- [206] S. I. Bokarev, D. Hollmann, A. Pazidis, A. Neubauer, J. Radnik, O. Kühn, S. Lochbrunner, H. Junge, M. Beller, A. Brückner, *Physical Chemistry Chemical Physics* **2014**, *16*, 4789–4796.
- [207] Private communication with Sergey Bokarev (23.5.2016).
- [208] J. P. Clancy, N. Chen, C. Y. Kim, W. F. Chen, K. W. Plumb, B. C. Jeon, T. W. Noh, Y. J. Kim, *Physical Review B* **2012**, *86*, 195131.
- [209] M. Saes, **2004**, *2970*, 121.
- [210] P. Glatzel, T.-c. Weng, K. Kvashnina, J. Swarbrick, M. Sikora, E. Gallo, N. Smolentsev, R. Alonso, *Journal of Electron Spectroscopy and Related Phenomena* **2013**, *188*, 17–25.
- [211] P. Glatzel, F. M. F. de Groot, O. Manoilova, D. Grandjean, W. B.M., U. Bergmann, R. Barrea, *Physical Review B* **2005**, *72*, 014117.
- [212] M. Kavcic, M. Zitnik, K. Bucar, A. Mihelic, M. Stuhec, J. Szlachetko, W. Cao, R. Alonso Mori, P. Glatzel, *Physical Review Letters* **2009**, *102*, 143001.
- [213] T. K. Sham, *Journal of Chemical Physics* **1985**, *83*, 3222–3224.
- [214] <http://www.viscopedia.com> (accessed 14.10.2016).
- [215] www.sigmaaldrich.com (accessed 14.10.2016).
- [216] www.chemicalbook.com (accessed 14.10.2016).
- [217] D. N. Bowman, A. Bondarev, S. Mukherjee, E. Jakubikova, *Inorganic Chemistry* **2015**, *54*, 8786–8793.
- [218] J. K. McCusker, K. N. Walda, R. C. Dum, J. D. Simon, D. Magde, D. N. Hendrickson, *Journal of the American Chemical Society* **1993**, *115*, 298–307.
- [219] G. Auböck, M. Chergui, *Nature Chemistry* **2015**, *7*, 629–633.
- [220] Y. Liu, K. S. Kjaer, L. A. Fredin, P. Chabera, T. Harlang, S. E. Canton, S. Lidin, J. Zhang, R. Lomoth, K.-E. Bergquist, P. Persson, K. Warnmark, V. Sundstrom, *Chemistry - A European Journal* **2015**, *21*, 3628–3639.
- [221] T. C. B. Harlang, Y. Liu, O. Gordivska, L. A. Fredin, C. S. Ponseca, P. Huang, P. Chábera, K. S. Kjaer, H. Mateos, J. Uhlig, R. Lomoth, R. Wallenberg, S. Styring, P. Persson, V. Sundström, K. Wärnmark, *Nature Chemistry* **2015**, *7*, 883–889.

- [222] T. Duchanois, T. Etienne, C. Cebrian, L. Liu, A. Monari, M. Beley, X. Assfeld, S. Haacke, P. C. Gros, *European Journal of Inorganic Chemistry* **2015**, 2469–2477.
- [223] R. Marcus, *Nobel lecture* **1992**.
- [224] N. Sutin, *Accounts of Chemical Research* **1982**, *15*, 275–282.
- [225] S. E. Canton, X. Zhang, M. L. Lawson Daku, A. L. Smeigh, J. Zhang, Y. Liu, C.-j. Wallentin, K. Attenkofer, G. Jennings, C. A. Kurtz, D. Gosztola, A. Hauser, V. Sundström, *Journal of Physical Chemistry C* **2014**, *118*, 4536.
- [226] X Zhang, M. L. Lawson Daku, J Zhang, K Suarez-Alcantara, G Jennings, C. A. Kurtz, S. E. Canton, *Journal of Physical Chemistry C* **2015**, *119*, 3312–3321.
- [227] P. R. Bevington, D. K. Robinsin, *Data Reduction and Error Analysis*, **2003**.
- [228] B Ravel, M Newville, *Journal of synchrotron radiation* **2005**, *12*, 537–541.
- [229] B. Ravel, ATHENA User's Guide, Document version 2.0, for athena version 0.9.19, January 9, 2014, **2014**.
- [230] J. K. McCusker, Private communication, 28.6.2016, **2016**.
- [231] M. H. Lim, J.-U. Rohde, A. Stubna, M. R. Bukowski, M. Costas, R. Y. N. Ho, E. Münck, W. Nam, L. Que, *Proceedings of the National Academy of Sciences of the United States of America* **2003**, *100*, 3665–3670.
- [232] F. T. de Olivera, A. Chanda, D. Banerjee, X. Shan, S. Mondal, L. Que, E. L. Bominaar, E. Münck, T. J. Collins, *Science* **2007**, *315*, 835.
- [233] K. Meyer, E. Bill, B. Mienert, T. Weyhermu, K. Wieghardt, *Journal of the American Chemical Society* **1999**, *121*, 4859–4876.
- [234] N. Aliaga-Alcalde, S. DeBeer George, B. Mienert, E. Bill, K. Wieghardt, F. Neese, *Angewandte Chemie - International Edition* **2005**, *44*, 2908–2912.
- [235] C. Vogel, F. W. Heinemann, J. Sutter, C. Anthon, K. Meyer, *Angewandte Chemie - International Edition* **2008**, *47*, 2681–2684.
- [236] H. Vennekate, D. Schwarzer, J. Torres-Alacan, O. Krahe, A. C. Filippou, F. Neese, P. Vöhringer, *Phys. Chem. Chem. Phys.* **2012**, *14*, 6165–6172.
- [237] H. Vennekate, D. Schwarzer, J. Torres-alacan, P. Vöhringer, *Journal of the American Chemical Society* **2014**, *136*, 1009510103.
- [238] J. J. Scepaniak, C. S. Vogel, M. M. Khusniyarov, F. W. Heinemann, K. Meyer, J. M. Smith, *Science* **2011**, *331*, 1049.
- [239] J. T. Groves, *Journal of Inorganic Biochemistry* **2006**, *100*, 434–447.
- [240] M. E. Ener, Y.-T. Lee, J. R. Winkler, H. B. Gray, L. Cheruzel, *Proceedings of the National Academy of Sciences of the United States of America* **2010**, *107*, 18783–18786.
- [241] J. Torres-Alacan, P. Vöhringer, *International Reviews in Physical Chemistry* **2014**, *33*, 37–41.
- [242] J. Torres-Alacan, J. Lindner, P. Vöhringer, *ChemPhysChem* **2015**, *16*, 2289–2293.
- [243] J. A. Bearden, A. F. Burr, *Reviews of Modern Physics* **1967**, *39*, 125–142.

- [244] C. R. Randall, L. Shu, Y.-m. C. Karl, S. H. Masami, N. Kitajima, R. J. Lachicotte, Y. Zang, L. Que, *Inorganic Chemistry* **1995**, *34*, 1036–1039.
- [245] M. Tromp, J. Moulin, G. Reid, J. Evans, *AIP Conference Proceedings* **2007**, *822*, 699.
- [246] P Glatzel, G Smolentsev, G Bunker, *Journal of Physics: Conference Series* **2009**, *190*, 012046.
- [247] T. Katayama, S. Owada, T. Togashi, K. Ogawa, P. Karvinen, I. Vartiainen, A. Eronen, C. David, T. Sato, K. Nakajima, Y. Joti, H. Yumoto, H. Ohashi, M. Yabashi, *Structural Dynamics* **2016**, *3*, 034301.
- [248] M Harmand, R Coffee, M. R. Bionta, M Chollet, D French, D Zhu, D. M. Fritz, H. T. Lemke, N Medvedev, B Ziaja, S Toleikis, M Cammarata, *Nature Photonics* **2013**, *7*, 215–218.
- [249] M. N. Polyanskiy, Refractive index database, <http://refractiveindex.info> (accessed 21.10.2016).
- [250] J.-C. Diels, W. Rudolph, *Ultrashort Laser Pulse Phenomena*, **2006**.
- [251] Y. Liu, D. B. Turner, T. N. Singh, A. M. Angeles-Boza, A. Chouai, K. R. Dunbar, C. Turro, *Journal of the American Chemical Society* **2009**, *131*, 26–27.
- [252] S. Fischer, D. Hollmann, S. Tschierlei, M. Karnahl, N. Rockstroh, E. Barsch, P. Schwarzbach, S.-P. Luo, H. Junge, M. Beller, S. Lochbrunner, R. Ludwig, A. Brückner, *ACS Catalysis* **2014**, *4*, 1845–1849.
- [253] M. Ekimova, W. Quevedo, M. Faubel, P. Wernet, E. T. J. Nibbering, *Structural Dynamics* **2015**, *2*, 054301.
- [254] N. Huse, T. K. Kim, L. Jamula, J. K. McCusker, F. M. F. de Groot, R. W. Schoenlein, *Journal of the American Chemical Society* **2010**, *132*, 6809–6816.
- [255] N. Huse, H. Cho, K. Hong, L. Jamula, F. M. F. D. Groot, T. K. Kim, J. K. Mccusker, R. W. Schoenlein, *Physical Chemistry Letters* **2011**, *2*, 880–884.
- [256] B. E. Van Kuiken, H. Cho, K. Hong, M. Khalil, R. W. Schoenlein, T. K. Kim, N. Huse, *Journal of Physical Chemistry Letters* **2016**, *7*, 465–470.
- [257] P. Wernet, M Scholz, K Kunnus, I Josefsson, I Rajkovic, W Quevedo, M Beye, S Schreck, S Grübel, D Nordlund, W Zhang, R. W. Hartsock, W. F. Schlotter, J. J. Turner, B Kennedy, F Hennies, F. M. F. de Groot, K. J. Gaffney, S Techert, M Odelius, A Föhlich, *Nature* **2015**, *520*, 78–81.
- [258] K Kunnus, I Josefsson, I Rajkovic, S Schreck, W Quevedo, M Beye, C Weniger, S Grübel, M Scholz, D Nordlund, W Zhang, R. W. Hartsock, K. J. Gaffney, W. F. Schlotter, J. J. Turner, B Kennedy, F Hennies, F. D. Groot, S Techert, M Odelius, P. Wernet, A Föhlich, *Structural Dynamics* **2016**, *3*, 094307.
- [259] T. J. Penfold, J. Szlachetko, W. Gawelda, F. Santomauro, A. Britz, T. B. V. Driel, L. Sala, S. Ebner, S. H. Southworth, G. Doumy, A. M. March, C. S. Lehmann, T. Katayama, M. Mucke, D. Iablonskyi, Y. Kumagai, G. Knopp, Koji Motomura, T. Togashi, S. Owada, M. Yabashi, J. Rittmann, M. M. Nielsen, M. Pajek, K. Ueda, M. Chergui, R. Abela, C. J. Milne in International Conference on Ultrafast Phenomena, **2016**.

- [260] T Rossi, T. J. Penfold, M. H. Rittmann-Frank, M Reinhard, J Rittmann, C. N. Borca, D Grolimund, C. J. Milne, M Chergui, *The Journal of Physical Chemistry C* **2014**, *118*, 19422–19430.
- [261] R. Paschotta, The Encyclopedia of Laser Physics and Technology, <https://www.rp-photonics.com/encyclopedia.html> (accessed 21.10.2016).

Bibliography

Acknowledgements

First of all I would like express my deepest gratitude to my supervisor Christian Bressler for letting me become a member of the FXE group at European XFEL and introducing me to the fascinating world of femtochemistry and ultrafast X-ray spectroscopies. His constantly open door lead to innumerable exciting and valuable discussions, which is one of the key ingredients to the results presented in this thesis. I would also like to thank Wilfried Wurth for co-supervising my PhD thesis. His frequent and clear feedback were extremely helpful making this PhD a success. I also express my gratitude to Daniela Pfannkuche, Angel Rubio and Nils Huse for agreeing to evaluate this PhD thesis and the upcoming PhD defense.

This thesis would have not been possible without the enormous help of all other members of the FXE group: Wojciech Gawelda, Andreas Galler, Dmitry Khakhulin, Peter Zalden, Sebastian Schulz, Martin Knoll as well as my fellow FXE PhD students, Tadesse Assefa, Manuel Harder, Michael Diez and Christina Bömer. The numerous and fruitful discussions on our research projects within the group as well as their constant feedback on my individual work were of incredible value. Here I would like to highlight Wojciech Gawelda and Andreas Galler who guided me, together with Christian Bressler, through my PhD from day one on.

At this point I would also like to appreciate at European XFEL my scientific director Thomas Tschentscher and the rest of the staff for helping me whenever support was needed, also in many non-scientific issues. It is worth pointing out the tremendous effort by Patrick Gessler, Bruno Fernandes, Hamed Sotoudi Namin, Andreas Beckmann and Frank Babies in developing and improving the MHz DAQ.

The presented results in this thesis could have not been thought of without the help of many collaborators all around the world. Here I would like to thank Shin-ichi Adachi, Eva Bajnoczi, Matthias Beller, Elisa Biasin, Sergey Bokarev, Hana Cho, Asmus Dohn, Gilles Doumy, Tim Brandt van Driel, Dennis Goeries, Alexander Guda, Kristoffer Haldrup, Nils Huse, Elena Jakubikova, Henrik Junge, Marcin Klepka, Oliver Kühn, Stefan Lehmann, Stefan Lochbrunner, Anne Marie March, James McCusker, Lars Mewes, Chris Milne, Dooshaye Moonshiram, Maria Naumova, Zóltan Németh, Martin M. Nielsen, Shunsuke Nozawa, Miguel Ochmann, Jochen Rittmann, Nils Rockstroh, Philip Roedig, Fabio Santomauro, Tokushi Sato, Ryszard Sobierajski, Stephen Southworth, Dorottya Szemes, Jakub Szlachetko, Joel Torres-Alacan, György Vankó, Peter Vöhringer, Anna Wolska, Hasan Yavas, Linda Young, and many more.

The numerous beamtimes in Hamburg, France, the USA and Japan would have not been

possible without the excellent local support: I express my deepest gratitude to Hans-Christian Wille and Frank-Uwe Dill for their support at beamline P01 of PETRA III, Don Walko and everybody else at sector 7 of the APS, Tetsuo Katayama and the SACLA team as well as Michael Wulff and the ID09 staff at ESRF.

I would like to thank my fellow PhD students of the International Max Planck Research School for Ultrafast Imaging and Structural Dynamics (IMPRS-UFAST), of the graduate school of the Hamburg Centre for Ultrafast Imaging (CUI) and of the Partnership for Innovation, Education and Research (PIER) graduate school. Especially the frequent meetings with my IMPRS fellow students were extremely valuable, both socially as well as scientifically. Next to the students, the IMPRS coordinators Anja Bleidorn, Sonia Utermann and Julia Quante deserve to be highlighted with their excellent support in managing all non-scientific obstacles in a PhD students life.

I would like to acknowledge the discussion about HERFD with Pieter Glatzel and Frank de Groot. I equally acknowledge Steffen Hauf, Matthias Michels, Moritz Hambach and Johann Haber for feedback on my thesis from outside of the TR XAS and XES community. I thank European XFEL as my main source of funding as a PhD student, equally I thank IMPRS, CUI, PIER, PSI, EUCALL and the EAgLE project for additional travel funds and workshop/conference invitations.

Letztendlich möchte ich auch meinen Eltern, meiner Schwester und dem Rest meiner Familie danken, dass sie mich immer unterstützt haben. Ausserdem danke ich meinen Freunden. Zum Beispiel denen, mit denen ich im Saarland aufgewachsen und zur Schule gegangen bin, mit denen in ich in Darmstadt, Badajoz und Barcelona studiert habe, und zuletzt denen, die Hamburg nicht nur wegen der Wissenschaft lebenswert gemacht haben.

List of Publications

1. A. M. March, T. A. Assefa, C. Boemer, C. Bressler, **A. Britz**, M. Diez, G. Doumy, A. Galler, M. Harder, D. Khakhulin, Z. Németh, M. Pápai, S. Schulz, S. H. Southworth, H. Yavas, L. Young, W. Gawelda and G. Vankó: *Probing Transient Valence Orbital Changes with Picosecond Valence-to-Core X-ray Emission Spectroscopy*, J. Phys. Chem. C, in press (2017)
2. **A. Britz**, T. A. Assefa, A. Galler, W. Gawelda, M. Diez, P. Zalden, D. Khakhulin, B. Fernandes, P. Gessler, H. Sotoudi Namin, A. Beckmann, M. Harder, H. Yavas and C. Bressler: *A multi-MHz single-shot data acquisition scheme with high dynamic range: pumpprobe X-ray experiments at synchrotrons*, J. Synchrotron Rad. 23 (2016)
3. E. Biasin, T. B. v. Driel, K. S. Kjær, A. O. Dohn, M. Christensen, T. Harlang, P. Chabera, Y. Liu, J. Uhlig, M. Pápai, Z. Németh, R. Hartsock, W. Liang, J. Zhang, R. Alonso-Mori, M. Chollet, J. M. Glowina, S. Nelson, D. Sokaras, T. A. Assefa, **A. Britz**, A. Galler, W. Gawelda, C. Bressler, K. J. Gaffney, H. T. Lemke, K. B. Moller, M. M. Nielsen, V. Sundström, G. Vankó, K. Wärnmark, S. E. Canton, and K. Haldrup: *Femtosecond X-Ray Scattering Study of Ultrafast Photoinduced Structural Dynamics in Solvated $[Co(terpy)_2]^{2+}$* , Phys. Rev. Lett. 117, 013002 (2016)
4. D. Göries, B. Dicke, P. Roedig, N. Stübe, J. Meyer, A. Galler, W. Gawelda, **A. Britz**, P. Gessler, H. Sotoudi Namin, A. Beckmann, M. Schlie, M. Warmer, M. Naumova, C. Bressler, M. Rübhausen, E. Weckert, and A. Meents: *Time-resolved pump and probe x-ray absorption fine structure spectroscopy at beamline P11 at PETRA III*, Rev. Sci. Instrum. 87, 053116 (2016)
5. G. Vankó, A. Bordage, M. Pápai, K. Haldrup, P. Glatzel, A. M. March, G. Doumy, **A. Britz**, A. Galler, T. Abebaw Assefa, D. Cabaret, A. Juhin, T. B. v. Driel, K. S. Kjær, A. O. Dohn, K. B. Moller, H. T. Lemke, E. Gallo, M. Rovezzi, Z. Németh, E. Rozsályi, T. Rozgonyi, J. Uhlig, V. Sundström, M. M. Nielsen, L. Young, S. H. Southworth, Ch. Bressler, and W. Gawelda: *Detailed characterization of a nanosecond-lived excited state: X-ray and theoretical investigation of the quintet state in photoexcited $[Fe(terpy)_2]^{2+}$* J. Phys. Chem. C, 119, 58885902 (2015)
6. J. Dura, N. Camus, A. Thai, **A. Britz**, M. Hemmer, M. Baudisch, A. Senftleben, C. D. Schröter, J. Ullrich, R. Moshhammer, J. Biegert: *Ionization with low-frequency fields in the tunneling regime*, Sci. Rep. 3, 2675 (2013)

7. M. M. Günther, **A. Britz**, R. J. Clarke, K. Harres, G. Hoffmeister, F. Nürnberg, A. Otten, A. Pelka, M. Roth, and K. Vogt: *NAIS: Nuclear activation-based imaging spectroscopy*, Rev. Sci. Instrum. 84, 073305 (2013)
8. M. M. Günther, J. Schütrumpf, **A. Britz**, K. Vogt, K. Sonnabend, M. Roth: *Development of High-Power Laser Based Nuclear Applications*, Fus. Sci. and Technol., 61, 1 (2012)

Eidesstattliche Versicherung

Hiermit erkläre ich an Eides statt, dass ich die vorliegende Dissertationsschrift selbst verfasst und keine anderen als die angegebenen Quellen und Hilfsmittel benutzt habe.

Hamburg, Oktober 2016